Rare-Earth-Containing Selenides and Oxyselenides

by

Vidyanshu Mishra

A thesis submitted in partial fulfillment of the requirements for the degree of

Doctor of Philosophy

Department of Chemistry
University of Alberta

Abstract

In this thesis, rare-earth-containing chalcogenides and oxychalcogenides were sought with the aims to identify new crystal structures and to evaluate their potential as optical and thermoelectric materials. They were synthesized in the form of pure microcrystalline powders and single crystals through high-temperature reactions. To address frequently made claims that the bonding in oxychalcogenides can be partitioned separately within the more ionic oxide vs. the more covalent chalcogenide blocks within their structures, electron localization function maps were examined carefully to evaluate the bonding character.

Many ternary chalcogenides *RE*–*Tr*–*Ch* (*RE* = rare-earth metal; *Tr* = Ga, In, Tl; *Ch* = S, Se, Te) are known, but most of them (about 75%) are sulfides, while the corresponding selenides and tellurides are still underexplored. Among the series of chalcogenides RE_3TrCh_6, there remain some ambiguities in the existence of several members and their structures. Several new compounds in the RE_3InSe_6 series were prepared. They exhibit an unusual structural evolution in which the In atoms occupy tetrahedral or octahedral sites, depending on the *RE*. They have relatively narrow band gaps in the attractive range of 1.2–1.4 eV, making them suitable as potential photovoltaic materials.

The major portion of the thesis was motivated by an initially naive hypothesis that oxychalcogenides could be prepared by successively substituting O for *Ch* atoms within existing series of chalcogenides. In this way, Sm_3GaSe_5O was obtained; however, its structure is new and unrelated to RE_3GaSe_6. Instead, it contains unprecedented $GaSe_5$ units in trigonal pyramidal geometry. Attempts to substitute other *RE* components led to two series of oxychalcogenides: $La_4Ga_2Se_6O_3$ and $RE_4Ga_2Se_7O_2$ (*RE* = Pr, Nd). They adopt new framework structures that can be contrasted with the layered structures more commonly associated with oxychalcogenides. They

have relatively small band gaps of 1.7–1.8 eV, as determined from optical diffuse reflectance spectra, which suggests that they could be viable candidates as thermoelectric materials. To evaluate this potential application, electronic and thermal properties were calculated from first principles.

Preface

This thesis encompasses six chapters from research work during my graduate studies (September 2017 to August 2022) conducted in the laboratory of Dr. A. Mar at the Department of Chemistry, University of Alberta. My contributions and those of others in the presented work are described below. Dr. A. Mar was the corresponding author and he was involved in all stages of manuscript editing, preparation, and submission.

Chapter 2 was published as Mishra, V.; Mumbaraddi, D.; Iyer, A. K.; Mar, A. Rare-earth indium selenides RE_3InSe_6 (*RE* = La−Nd, Sm, Gd, Tb): Structural evolution from tetrahedral to octahedral sites. *J. Solid State Chem.* **2021**, 297, 122096. My contribution includes conceptualization, synthesis, data collection, crystal structure determination, characterization, electronic structure calculation, and preparation of the initial draft of the manuscript. D. Mumbaraddi and Dr. A. K. Iyer assisted in the synthesis and powder X-ray data collection.

Chapter 3 was published as Mishra, V.; Mumbaraddi, D.; Iyer, A. K.; Yin, W.; Mar, A. Semiconducting Sm_3GaSe_5O with trigonal bipyramidal $GaSe_5$ units. *J. Solid State Chem.* **2022**, 308, 122901. My contribution includes conceptualization, synthesis, data collection, crystal structure determination, characterization, electronic structure calculation, and preparation of the initial draft of the manuscript. Dr. A. K. Iyer and Dr. W. Yin assisted in synthesis, and D. Mumbaraddi assisted in powder X-ray data collection.

Chapter 4 was published as Mishra, V.; Zabolotnii, A.; Mar, A. $La_4Ga_2Se_6O_3$: A rare-earth oxyselenide built from one-dimensional strips. *Inorg. Chem.* **2022**. 61, 12458–12465. My contribution includes conceptualization, synthesis, data collection, crystal structure determination, characterization, electronic structure, thermal properties calculation, and preparation of the initial draft of the manuscript. A. Zabolotnii assisted in synthesis.

Chapter 5 has been prepared as a draft for publication as Mishra, V.; Mumbaraddi, D.; Jomaa M.; Guérin, L.; Mar, A. Structure, optoelectronic, and thermal properties of $RE_4Ga_2Se_7O_2$ (*RE* = Pr, Nd) containing trigonal bipyramidal $GaSe_5$ units. My contribution includes conceptualization, synthesis, data collection, crystal structure determination, characterization, electronic structure, thermal properties calculation, and preparation of the initial draft of the manuscript. D. Mumbaraddi, M. Jomaa, and L. Guérin assisted in synthesis.

Appendix 1 was published as Mishra, V.; Iyer, A. K.; Mumbaraddi, D.; Oliynyk, A. O.; Zuber, G.; Boucheron, A.; Dmytriv, G.; Bernard, G. M.; Michaelis, V. K.; Mar, A. Coloured intermetallic compounds $LiCu_2Al$ and $LiCu_2Ga$. *J. Solid State Chem.* **2020**, 292, 121703. My contribution includes synthesis, powder X-ray data collection, crystal structure determination, characterization, electronic structure calculation, and preparation of the initial draft of the manuscript. Dr. A. K. Iyer proposed the idea, D. Mumbaraddi assisted in synthesizing the standards, Dr. A. O. Oliynyk assisted in electronic structure calculation, G. Zuber, A. Boucheron, and Dr. G. Dmytriv assisted in synthesis, G. M. Bernard collected NMR data, and Dr. V. K. Michaelis edited the NMR section.

Acknowledgements

First and foremost, I sincerely express my gratitude to my research supervisor, Prof. Arthur Mar, an extraordinary teacher. I feel privileged to have learned from him. He has been an inspiring mentor who prepared me beyond academics to life. His availability to guide and support whenever I needed has been a life-learning lesson. His pleasant and approachable persona has made him a friend to me than a supervisor. His belief in giving hints rather than straightforward solutions helped me develop new skills and has made me an independent researcher. I desire to adopt these qualities in my lifestyle forever.

I express my gratitude to my parents, Mr. Prem Narayan Mishra and Mrs. Shashi Kala Devi, and family who understood the importance of education and provided me with a favorable environment of freedom to grow independently. I am very thankful to my wife, Shaivya, for her constant support and patience during my random late-night work schedule. She has been a remarkable woman. My Ph.D. research journey would not have been this memorable without her love and care. I would also like to extend my gratitude to my in-laws, Dr. Mahendra Prakash Pathak, Mrs. Prema Pathak, and Mr. Devesh Pathak, for their unconditional love, trust, and support. I express my deep love to my grandfather, who always wished for me to pursue higher education.

School and college days have been memorable, where I developed scientific curiosity. I thank my school teachers, especially Mr. S. B. Singh and the late Mr. Hanuman Prasad Ji, who believed in me and improved my public speaking skills. I want to thank Prof. Sebastian C. Peter and the research group at JNCASR, Bangalore, during 2015–2017, who instilled a passion for solid-state chemistry in me. I sincerely thank Dr. Udumula Subbarao, who taught me to operate the single-crystal X-ray diffractometer, a bread-and-butter instrument for solid-state chemists.

I will always cherish the sense of friendship with Dr. Saurav Chandra Sarma and Dundappa Mumbaraddi, with whom I often discuss my research and personal life experiences. I have been fortunate to have friends like Dr. Abishek K. Iyer, Dr. Sahil Malhotra, Dr. Piyush Mishra, Pushpendra Kumar, Aman Chaturvedi, Vinayshri Tripathi, Dr. Gururaj Hosmani, Sachin, Felix, and Abhishek. Their unconditional support strengthened me whenever I needed it. Also, I thank past and present group members for the fruitful discussions and gossip: postdocs Anton, Yuqiao, Lawrence, Frank, Bala, Brett, and Max; graduate students Ebru, Alex, Dong, Amit, Mohammed, Arkadii, and Ritobroto.

The research work in this thesis would not have been in shape without fruitful discussions with Dr. Michael Ferguson, Dr. Guy Bernard, Dr. Guibin Ma, Dr. Nathan Gerein, Dr. Wayne Moffat, Jennifer Jones, and Rebecca Funk. I am grateful to Dr. Yoram Apelblat for his kind support and guidance in my teaching assistantship. I am thankful to my supervisory committee members, Prof. Vladimir Michaelis and Prof. Yunjie Xu, for their valuable suggestions. I thank Prof. Julianne Gibbs, Prof. Karthik Shankar, and Prof. R. B. Jordan for serving as arm lengths members in my candidacy exam. I am grateful to Paul and Dirk for fixing the instruments, and to Anita and Laura for administrative support.

I thank the Department of Chemistry for teaching assistantship appointments, and Future Energy Systems and the Natural Sciences and Engineering Research Council of Canada for the financial support during the spring and summer term research. I want to thank the undergraduate and graduate students I supervised, and I appreciate the assistance I received from them during their internships.

Table of Contents

List of Tables

List of Figures

List of Symbols and Abbreviations

Absorption coefficient (Kubelka-Munk)	α
Angle of reflection	θ
Atomic number	Z
Atomic sphere approximation	ASA
Bond valence sum	BVS
Cell volume	V
Chalcogenides	Ch
Chemical potential	μ
Critical temperature	T_c
Crystal orbital Hamilton population	COHP
Density	ρ
Density functional theory	DFT
Density of states	DOS
d-spacing	d_{hkl}
Effective magnetic moment	μ_{eff}
Electrical conductivity	σ
Electron	e^-
Electronegativity; Magnetic susceptibility	χ
Energy dispersive X–ray spectroscopy	EDX
Fermi level	E_F
Kubelka-Munk (K-M) function	$F(R_\infty)$
Linear muffin-tin orbital	LMTO

Local density approximation	LDA
Magnetic field	H
Miller indices	hkl
One-, two-, three-dimensional	1D, 2D, 3D
Perdew, Burke, and Ernzerhof	PBE
Physical property measurement system	PPMS
Rare-earth	RE
Reflectance	R
Relaxation time	τ
Scanning electron microscope	SEM
Seebeck coefficient, Goodness-of-fit, Scattering coefficient	S
Structure factor	F_{hkl}
Temperature	T
Thermal conductivity	k
Triels (Group-13 elements)	Tr
Ultraviolet	UV
Unit cell parameters	$a\ b\ c\ \alpha\ \beta\ \gamma$
Wavelength	λ
X-ray diffraction	XRD

Chapter 1.

Introduction

Solid state chemistry deals with the study of synthesis, structures, properties, and applications of solids. Depending on the synthetic route, many types of solid state compounds can be formed by reactions of starting materials, but predicting even the compositions of these compounds remains an unsolved problem. These compounds adopt a wide variety of crystal structures and exhibit diverse physical properties. In this thesis, the structures and properties of several important classes of solids, namely chalcogenides and oxychalcogenides, are investigated.

1.1. Inorganic solid-state materials

Substances can be categorized into those that are molecular and non-molecular. Most inorganic solids are non-molecular and adopt extended structures in which atoms are bonded in an infinite fashion. Elemental metals such as Cu, Au, Al, and Fe contain a regular arrangement of atoms whose valence electrons are distributed in a delocalized manner; ionic solids such as NaCl and KBr contain cations and anions held by electrostatic attractions; and covalent network solids such as silicon and some forms of phosphorus contain atoms held by directed covalent bonds. The atoms can be in ordered arrangements, as found in crystalline materials, or they can be disordered, as found in amorphous materials. Knowing the detailed atomic arrangements within these structures is essential because they dictate the properties of materials. Then, it becomes possible to think of ways to manipulate their compositions and structures to obtain desired properties. For example, substitution of one element for another allows many physical properties to be controlled, such as optical band gaps, magnetic behaviour, and thermal conductivity.[1]

The history of solid state chemistry has long been dominated by the study of oxides and halides, perhaps because they were easier to synthesize. However, there are many other combinations of elements that lead to interesting classes of solids, including chalcogenides (compounds of S, Se, Te), pnictides (compounds of P, As, Sb, Bi), and intermetallics (compounds of more than one metal). The study of how elements react to form these compounds is far from exhausted because the number of combinations is immense (e.g., out of ~1.6×10^6 combinations of three elements, only ~2×10^5 ternary systems have been discovered to date).[2] This also means that there are still plenty of opportunities to discover compounds with desired physical properties. The focus of this thesis is on compounds that straddle both oxides and non-oxides, namely a potentially large class of mixed-anion compounds known as oxychalcogenides.

1.2. Chalcogenides

The group-16 elements are called the chalcogens, a term derived from *χαλκός* (Greek for copper) and *genēs* (Latinized Greek for born or produced), in reference to their common occurrence in copper-containing minerals. In accordance with trends within the periodic table, the metallic character of these elements increases and electronegativity decreases going down the group (χ^{Pauling} = 3.5 for O, 2.5 for S, 2.4 for Se, and 2.1 for Te), so that O is a typical nonmetal whereas Te is a metalloid. The term chalcogenides is often reserved for compounds of S, Se, and Te when one wishes to draw a distinction from oxides, which behave quite differently in terms of their structures and bonding character. Given the greater difference in electronegativities between metal atoms and group-16 elements, metal oxides tend to exhibit more ionic bonding, whereas metal chalcogenides exhibit more covalent bonding, or in the case of tellurides, perhaps even strong metallic character. As a result, the structures of metal oxides vs. chalcogenides are also

generally different. Many metal oxides can be described in terms of arrangements of close packed O^{2-} anions with metal cations placed within interstitial sites. In contrast, metal chalcogenides are more prone to form low-dimensional structures, such as layers, because the lower electronegativity of the heavier chalcogens does not preclude contact between *Ch* atoms; in fact, homoatomic *Ch*–*Ch* bonds can be found in many structures because of the greater propensity for catenation. The low-dimensional structures of such chalcogenides can lead to highly anisotropic physical properties.[3–6] For example, although they both consist of edge-sharing metal-centred octhaedra, TiO_2 (rutile) has a 3D framework whereas TiS_2 has a 2D layered structure (**Figure 1-1**).[2]

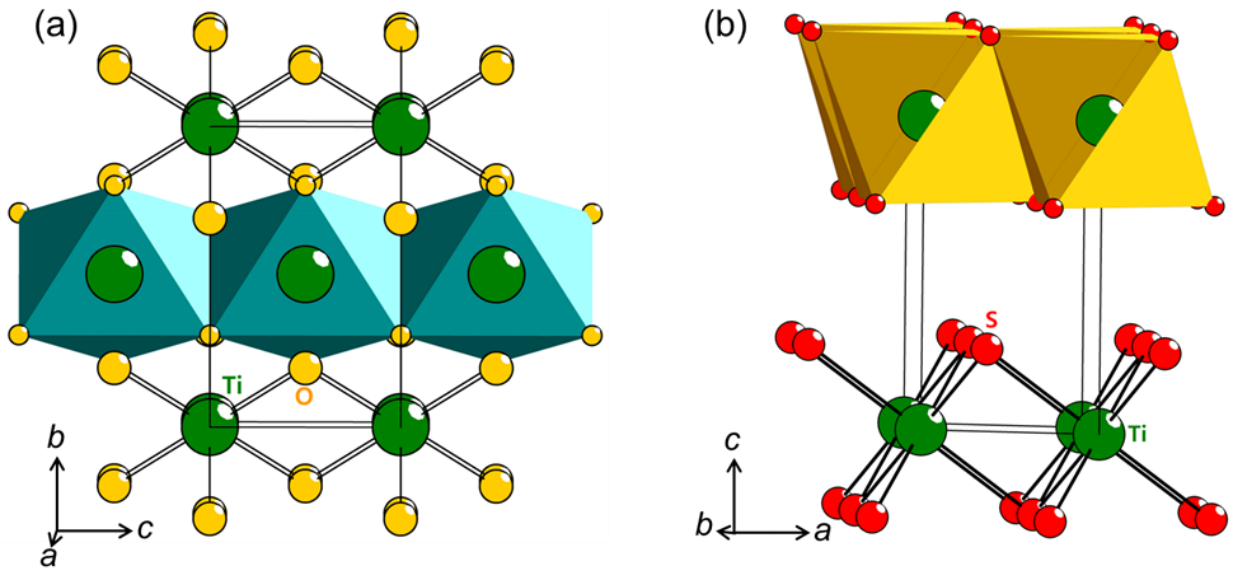

Figure 1-1. (a) 3D framework structure of TiO_2 (rutile) and (b) 2D layered structure of TiS_2.

Metal chalcogenides have numerous applications, and many of them are biocompatible, nontoxic, and easy to synthesize.[7,8] Compared to oxides, they tend to have smaller band gaps, which leads to various applications involving light absorption in the visible region, such as MoS_2 in solar cells and photodetectors.[9,10] Other applications include light emitting diodes (CdSe–ZnS, ZnSe, CdSe–CdS),[11] water splitting catalysts (MoS_2, $MoSe_2$),[12] Li-ion batteries (WS_2),[13] sensors ($Pb_{1-x}SnSe$),[14] superconductivity (Mo_5SnS_6 and $PbMo_6S_8$),[15,16] charge density waves ($NbSe_3$),[17]

potassium storage ($TiSe_2$, MoSSe alloys),[18] nonlinear optics ($AgGaS_2$, $CuGaS_2$),[19] and thermoelectrics (PbTe, Bi_2Te_3).[20]

1.3. Rare-earth chalcogenides

The rare-earth elements (*RE*) refer to the 4f block (La–Lu) of elements, as well as Sc and Y.[21,22] Chalcogenides containing these elements provide a wide space for diversity in structures and control of properties. The large *RE* atoms are typically surrounded by *Ch* atoms in their coordination environment in complex and often highly distorted geometries, within structures exhibiting frameworks, layers, or clusters.[3] The 4f electrons of *RE* atoms are highly localized and do not generally participate in orbital overlap for bonding. Electronic optical, and magnetic structures of these compounds can be highly complex.[23–26]

Ternary rare-earth chalcogenides *RE–M–Ch* comprise a very large group: several thousand compounds are already known, many having been discovered within only the past two or three decades.[2] They are of interest for unusual bonding motifs ($Er_7Ni_2Te_2$),[27] magnetic properties ($Eu_{1-x}Gd_xSe$),[28] nonlinear optical behaviour (RE_3GaS_6),[29] and thermoelectric properties ($A_xRE_2Cu_{6-x}Te_6$).[30] Some of these compounds, in which *M* is restricted to p-block metals, have been identified as suitable candidates for luminescent materials, originating from f-f transitions within the *RE* atoms (e.g., $RE_xBi_{2-x}Se_3$),[31] and as photovoltaic materials, originating from narrow band gaps (e.g., $EuGa_2S_4$).[32]

For the particular subset of compounds *RE–M–Ch* restricted to *M* = Al, Ga, In and *Ch* = S, Se, Te, most known representatives are sulfides, while there are still large gaps in knowledge about the corresponding selenides and tellurides (**Table 1-1**).[2] Three of the most common structure types among these compounds are highlighted: $Ce_3Al_{1.67}S_7$ (space group $P6_3$), Er_3GaS_6 (space group

*Cmc*2$_1$), and U_3ScS_6 (space group *Pnnm*) (**Figure 1-2**). The $Ce_3Al_{1.67}S_7$-type structure is particularly prevalent, adopted by 230 ternary and 40 quaternary chalcogenides;[2] interest in these compounds has recently been revived because of their nonlinear optical and photoelectric properties.[33]

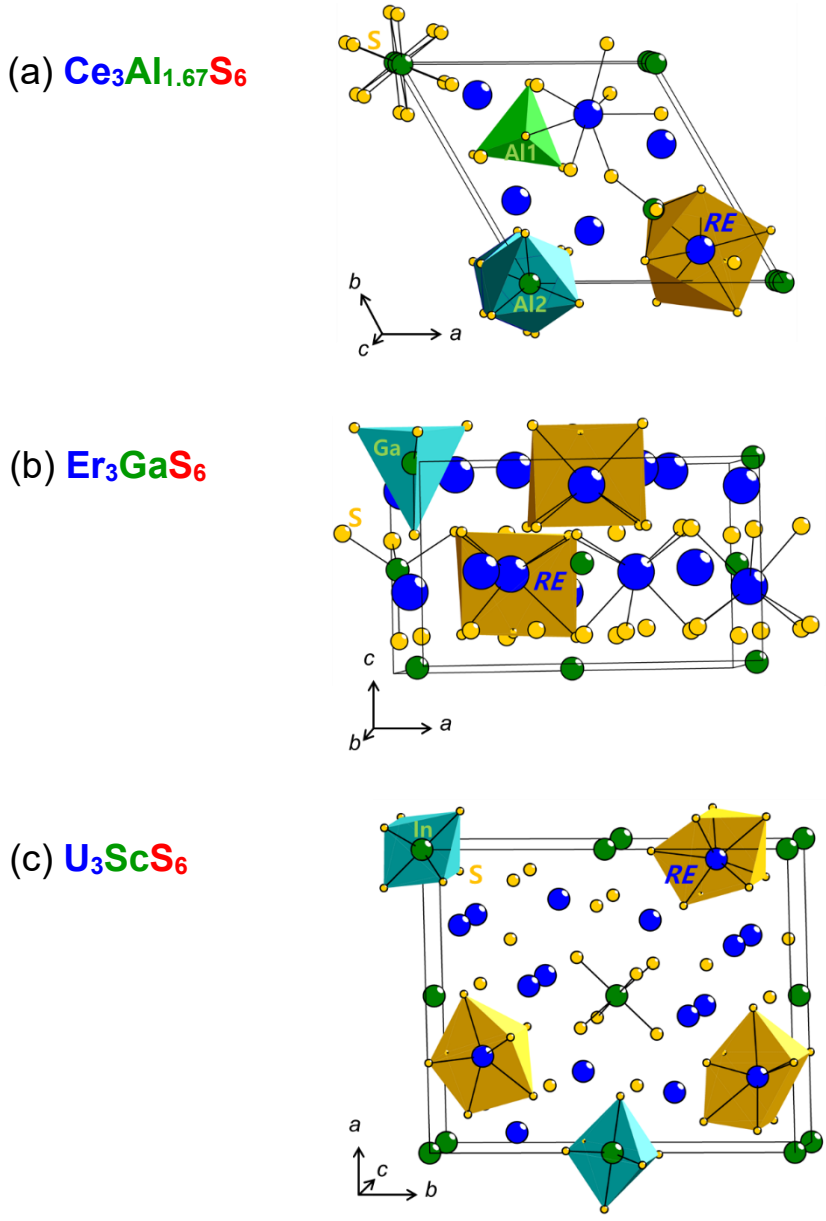

Figure 1-2. Three common structure types adopted by *RE*–*M*–*Ch* (*M* = Al, Ga, In; *Ch* = S, Se, Te): (a) $Ce_3Al_{1.67}S_6$, (b) Er_3GaS_6, and (c) U_3ScS_6.

Table 1-1. Known representatives of ternary chalcogenides *RE–M–Ch* (*M* = Al, Ga, In; *Ch* = S, Se, Te) and their structure types.[2]

Structure type	Composition	Rare earth element													
		La	Ce	Pr	Nd	Sm	Eu	Gd	Tb	Dy	Ho	Er	Tm	Yb	Lu
Sulfides															
$Ce_3Al_{1.67}S_7$[#]	$RE_3Al_{1.67}S_7$	+	+	+	+	+	+	+	+	+	+	+	–	–	–
	$RE_3Ga_{1.67}S_7$	+	+	+	+	+	–	+	+	+	+	–	–	–	–
	$RE_3In_{1.67}S_7$	–	–	–	–	–	–	–	–	–	–	–	–	–	–
$NaFeO_2$	$RETlS_2$	–	+	+	+	+	+	+	+	+	+	–	+	+	+
$EuGa_2S_4$	$REAl_2S_4$	–	–	–	–	–	+	–	–	–	–	–	–	–	–
	$REGa_2S_4$	–	–	–	–	–	+	–	–	–	–	–	–	+	–
	$REIn_2S_4$	–	–	–	–	–	–	–	–	–	–	–	–	–	–
U_3ScS_6	RE_3InS_6	–	–	–	–	+	–	+	–	–	–	–	–	–	–
$SrAl_2Se_4$	$REGa_2S_4$	–	–	–	–	–	–	–	–	–	–	–	–	+	–
	$REIn_2S_4$	–	–	–	–	–	–	–	–	–	–	–	–	+	–
$Nd_4In_5S_{13}$	$RE_4In_5S_{13}$	+	+	+	+	+	–	+	+	+	+	+	–	–	–
La_3InS_6[#]	RE_3InS_6	+	+	+	+	+	–	+	+	+	+	+	+	+	+
Er_3GaS_6[#]	RE_3GaS_6	–	–	–	–	–	–	–	–	+	+	+	–	–	–
Selenides															
$Ce_3Al_{1.67}S_7$	$RE_3Al_{1.67}Se_7$	+	+	+	+	+	–	+	+	+	+	–	–	–	–
	$RE_3Ga_{1.67}Se_7$	+	+	+	+	+	–	+	–	–	–	–	–	–	–
	$RE_3In_{1.67}Se_7$	+	–	–	–	–	–	–	–	–	–	–	–	–	–
$NaFeO_2$	$RETlSe_2$	–	–	–	+	+	–	+	+	+	+	+	+	+	+
$EuGa_2S_4$	$REAl_2Se_4$	–	–	–	–	+	+	–	–	–	–	–	–	–	–
	$REGa_2Se_4$	–	–	–	–	+	+	–	–	–	–	–	–	–	–
	$REIn_2Se_4$	–	–	–	–	–	+	–	–	–	–	–	–	+	–
U_3ScS_6	RE_3InSe_6	–*	–*	+*	–*	+*	–	+*	–*	–	–	–	–	–	–
$SrAl_2Se_4$	$REGa_2Se_4$	–	–	–	–	–	–	–	–	–	–	–	–	+	–
	$REIn_2Se_4$	–	–	–	–	–	+	–	–	–	–	–	–	–	–
$Nd_4In_5S_{13}$	$RE_4In_5Se_{13}$	+	–	–	–	–	–	–	–	–	–	–	–	+	–
Tellurides															
$NaFeO_2$	$RETlTe_2$	–	–	–	+	+	–	+	+	+	+	+	+	–	+
$PbTl_4Te_3$	$RETl_4Te_3$	+	+	+	+	+	–	+	+	–	–	+	–	–	–

+ compound is known to form; – compound does not form or is unknown; # noncentrosymmetric; * reported in Chapter 2.

Although the RE_3MCh_6 series has been known for 50 years, there were still unresolved ambiguities about the existence of many specific members and their structures. Prior to the work in this thesis, only a few RE_3GaS_6 compounds were reported for smaller *RE* atoms (Dy, Ho Er, Y),[34–37] whereas RE_3InS_6 compounds were known for almost the entire range of *RE* elements.[38–44] The RE_3GaS_6 compounds adopt the noncentrosymmetric Er_3GaS_6-type structure (space group $P6_3$). $DyGaS_6$ has been evaluated for the non-linear optical properties showing higher thresholds for laser induced damages.[37] Surprisingly, the corresponding selenides were unknown for RE_3GaSe_6, and very few were known for RE_3InSe_6.[45–48] Another puzzling observation is that RE_3InS_6 adopts a noncentrosymmetric La_3InS_6-type structure (space group $P2_12_12$) for the earlier *RE* members (La–Nd), but a centrosymmetric U_3ScS_6-type structure (space group *Pnnm*) for the later *RE* members (Sm, Gd, Tb) (**Figure 1-2c**). These structures are closely related but differ in the coordination environment around the In atoms: both tetrahedral and octahedral in La_3InS_6-type, but only octahedral in U_3ScS_6-type. A key point is that most reports were based on powder X-ray diffraction methods, and the structures were assigned without strong evidence. For the RE_3InSe_6 series, the U_3ScS_6-type structure was assigned for the *RE* members (Pr, Sm, Gd) using single crystal X-ray diffraction techniques. However, close inspection of the structure determination of Pr_3InSe_6 shows unusual features around the In sites, which exhibit large thermal displacement parameters. Chapter 2 addresses all of the problems noted above through new syntheses of the selenides RE_3GaSe_6 and RE_3InSe_6, and careful structure determination studies.

1.4. Rare earth oxychalcogenides

Metal oxides are plentiful and usually stable in air; they have been extensively explored for many years for their interesting physical properties, such as high temperature superconductivity and solid oxide fuel cells.[49, 50] Of course, there are other classes of materials containing anions besides O^{2-}, but they are not as numerous (**Figure 1-3**).[2] There has been revived interest in discovering new materials containing two or more anions, known as mixed anion compounds, after various oxypnictides were reported to be superconducting two decades ago.[51,52] The major portion of this thesis focuses on oxychalcogenides, which contain O in combination with heavier *Ch* anions.

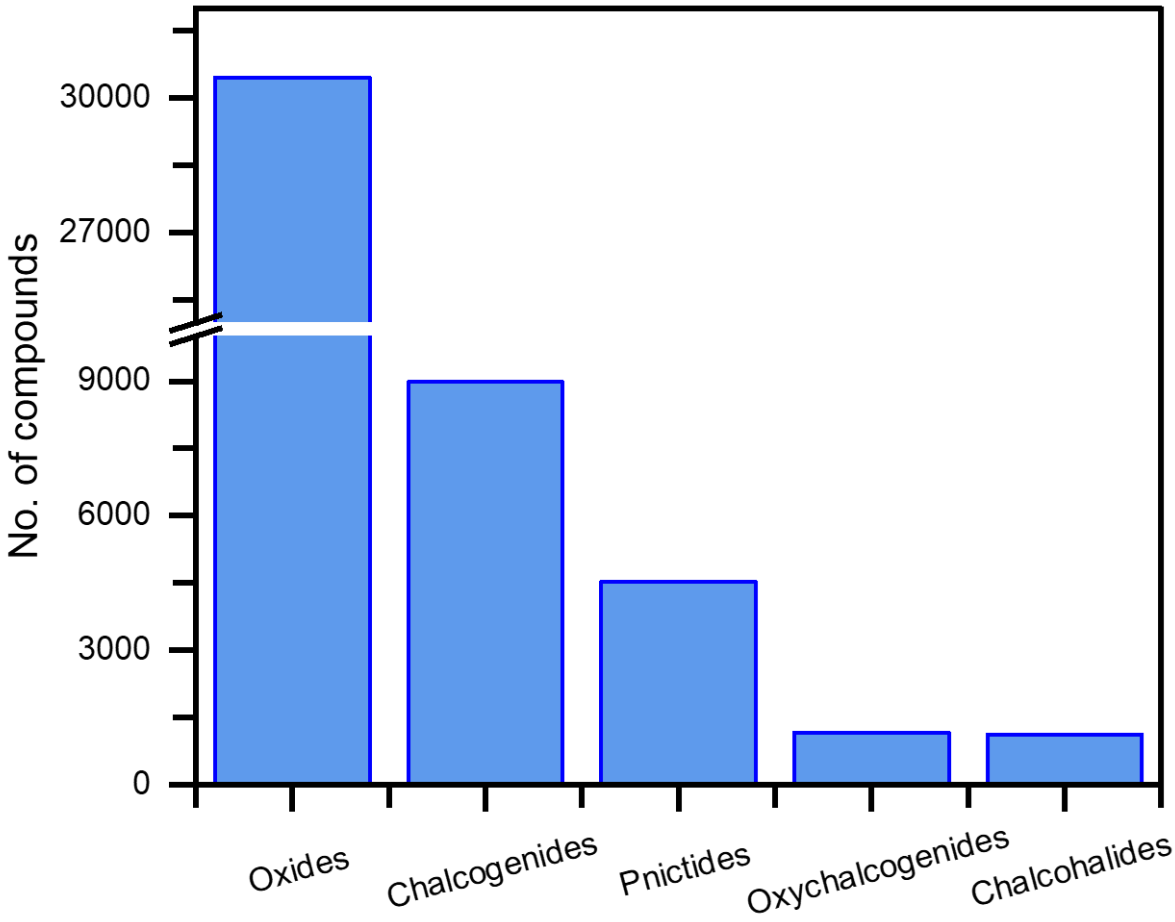

Figure 1-3. Reports for unique compounds containing various anions for which complete structure has been determined.[2]

It is important to appreciate that the definition of a mixed-anion compound truly implies the presence of two or more types of anions, where both O and *Ch* atoms are in formally negative oxidation states. Thus, oxychalcogenides are not the same as more mundane compounds that contain oxyanions such as SO_4^{2-} or SeO_4^{2-}. Introducing anions with different characteristics (e.g., size, electronegativity) provides additional degrees of freedom that can be imparted to structures and properties. The hypothesis is that O and *Ch* atoms will surround metal centres in coordination geometries that are heteroleptic (a term borrowed from organometallic chemistry, a field that tends to be fond of abstruse language), leading to greater structural diversity. There is also an assumption that mixed anions are more likely to order than mixed cations, enabling better control of structures. Existing oxychalcogenides often exhibit 2D layered structures consisting of separate blocks containing O vs. *Ch* atoms. The segregation into more insulating oxide vs. more semiconducting chalcogenide layers has led to lofty descriptions of such layered chalcogenides as "multiple quantum wells."[53] Similarly, other chalcogenides that have 3D framework structures can often be viewed in terms of fragments of more familiar rocksalt, fluorite, or perovskite-type blocks.[54]

To anticipate later discussions of bonding within these oxychalcogenides, it is useful to examine the atomic properties (e.g., size, electronegativity, polarizability) (**Table 1-2**).[55,56] Based on the hard-soft acid-base (HSAB) principle,[57] the simplistic expectation is that O anions will prefer to bond to more highly charged and more electropositive metal cations whereas the heavier *Ch* anions will prefer to bond to less highly charged and less electropositive metal cations. (Notwithstanding its persistence in undergraduate courses, like a guest who has overstayed their welcome, HSAB theory has long since been outdated and its reliability has been shown to be questionable,[58] but it serves as a starting point for discussions about bonding.) That is, there should be a greater tendency for O and *Ch* anions to order within the structures of oxychalcogenides, in

contrast to the disorder of O and N atoms often found in oxynitrides, or O and F atoms in oxyfluorides.[54,59–63] This argument reinforces the frequent depiction of oxychalcogenides into distinct fragments, noted above. Then, the hope is that these fragments can be manipulated separately (or "rationally designed," as phrased by some carnival barkers) through chemical substitution to vary the physical properties. In this way, oxychalcogenides have been considered as candidates for optoelectronic materials, thermoelectrics, photocatalysts (water splitting), and *p*-type transparent semiconductors.[54,62,64–70]

Table 1-2. Atomic radius, electronegativity, and polarizability of atoms.

Element	Atomic radius (pm)	Electronegativity ($\chi^{Pauling}$)	Polarizability (a.u.)	Element	Atomic radius (pm)	Electronegativity ($\chi^{Pauling}$)	Polarizability (a.u.)
La	195	1.10	215(20)	O	60	3.44	5.3(2)
Ce	185	1.12	205(20)	S	100	2.58	19.4(1)
Pr	185	1.13	216(20)	Se	115	2.55	29(1)
Nd	185	1.14	208(20)	Te	140	2.10	38(4)
Sm	185	1.17	192(20)	Al	125	1.61	57.8(1)
Eu	185	1.20	184(20)	Ga	130	1.81	50(3)
Gd	180	1.20	158(20)	In	155	1.78	65(4)
Tb	175	1.10	170(20)	Tl	190	1.62	50(2)
Dy	175	1.22	165(15)				
Ho	175	1.23	156(10)				
Er	175	1.24	150(15)				
Tm	175	1.25	144(15)				
Yb	175	1.10	139(6)				
Lu	175	1.27	137(7)				
Sc	160	1.36	97(10)				
Y	180	1.22	162(12)				

Most oxychalcogenides to date have been prepared synthetically. Naturally occurring minerals (e.g., $CaSb_{10}O_{10}S_6$, $Na_{3.6}(Sb_2O_3)_3(SbS_3)(OH)_{0.6}\cdot 2.4H_2O$) are rare.[71,72] Among rare-earth-containing oxychalcogenides *RE*–*Ch*–O, the most well studied have the composition RE_2ChO_2, with sulfides and selenides known for nearly all *RE*, and tellurides are known for La–Dy.[2] Their structure consist of layers formed by distorted ORE_4 tetrahedra, separated by chalcogenide ions. The sulfides RE_2SO_2 are candidates for oxygen storage materials.[73,74] Another class has the composition $RE_4Se_3O_4$ (*RE* = La–Lu), whose structure consists of fluorite-type $[RE_2O_2]^{2+}$ layers separated by discrete $[Se{-}Se]^{2-}$ units.[75] Among quaternary rare-earth oxychalcogenides, perhaps the most popular oxychalcogenides are the equiatomic phases *REMCh*O (*M* = d- or p-block metal or metalloid), which adopt layered structures (ZrCuSiAs-type).[76,77] The characteristic features are fluorite-type blocks built from edge-sharing ORE_4 tetrahedra and antifluorite-type blocks built from edge-sharing *MCh* tetrahedra. These compounds have been well investigated and reviewed in the literature. Instead, we focus on other families of quaternary rare-earth oxychalcogenides that deserve further attention.

1.4.1. $CeBiS_2O$-type

The tetragonal $CeBiS_2O$-type (space group *P*4/*nmm*)[78,79] is most frequently observed structure among rare earth oxychalcogenides $REMCh_2O$ (*M* = As, Sb, Bi; *Ch* = S, Se). It consists of separate layers, [CeO] and $[BiS_2]$, stacked alternately along the *c*-axis (**Figure 1-4a**). The [CeO] layers consist of edge-sharing OCe_4 tetrahedra, whereas the $[BiS_2]$ layers consist of edge-sharing BiS_6 octahedra. Because one of the axial Bi–S bonds is much longer (3.3 Å) than the other five (2.5–2.8 Å), the coordination around the Bi atoms is better described as being square pyramidal (CN5). Given the resemblance to structures of layered oxypnictide superconductors,[76,77,80] it has

been proposed that $CeBiS_2O$ and related compound could also be superconducting, with the [CeO] layers acting as a charge reservoir. The results are controversial, with some reports of superconductivity in $CeBiS_2O$ and others indicating non-metallic behaviour.[81,82] Single crystals of $CeBiS_2O$ grown in CsCl flux were demontrated to exhibit superconductivity, with evidence for valence fluctuation of the Ce atoms.[83] Substitution of O by F atoms within the [BiS_2] layers in $REBiS_2O_{1-x}F_x$ (*RE* = La, Ce, Pr, Nd, Yb) introduces electron carriers which enhance the superconductivity in the range of 1.9–10.6 K.[84–88]

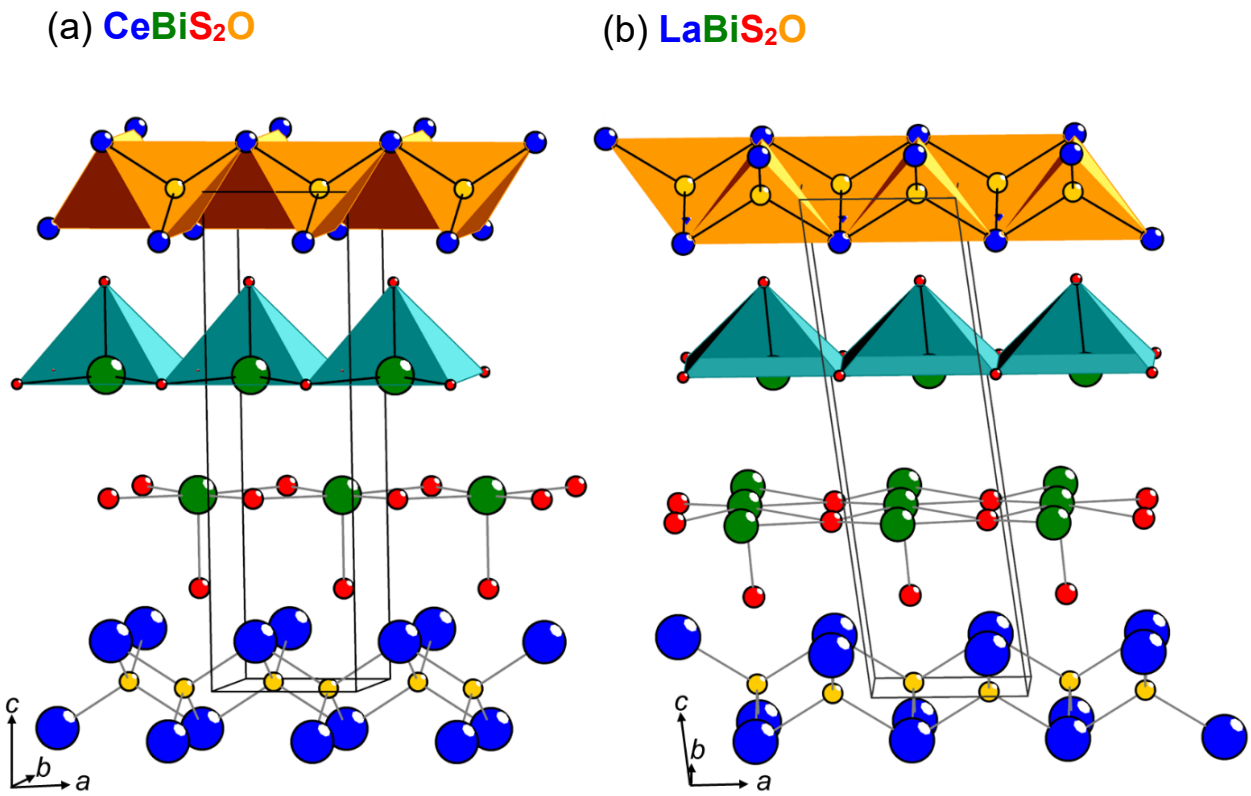

Figure 1-4. Structures of (a) $CeBiS_2O$ (*P*4/*nmm*) and (b) $LaBiS_2O$ (*P*2$_1$/*m*).

Single crystals of $LaBiS_2O$ grown in the same way were found to exhibit a symmetry-lowered structure (monoclinic $P2_1/m$), with a shift in the [BiS_2] layers (**Figure 1-4b**). The pressure dependence of the superconductivity and electronic structure calculations have also been investigated.[89] Other applications of *RE*Bi*Ch*$_2$O include thermoelectrics and photocatalysis.[90,91]

1.4.2. $Ce_2GaS_{2.5}O_2$ and $La_2SnS_3O_2$-type

The $Ce_2GaS_{2.5}O_2$-type structure (tetragonal, $I4/mmm$) is adopted by many compounds: $La_2AsS_{2.5}O_2$, $Ce_2GaS_{2.5}O_2$, $La_2Ga_{0.94}Se_{2.41}O_2$, $RE_4As_2S_5O_4$ (*RE* = La–Nd), $RE_4Sb_2S_5O_4$ (*RE* = La–Pr), $RE_2SbS_{2.5}O_2$ (*RE* = La–Nd, Sm, Eu, Dy–Er, Yb), and $Pr_4Bi_2S_5O_4$.[2] Most of them were characterized by powder XRD only. The related $La_2SnS_3O_2$-type structure (orthorhombic, *Pnma*) is adopted by $RE_4Sn_2S_6O_4$ (*RE* = La–Nd) and $La_4Sn_2Se_6O_4$, again mostly through powder XRD characterization.[2] Both structures consist of [*RE*O] layers, seen earlier, alternating with ribbons built from MS_4 tetrahedra (**Figure 1-5**). The *M* atoms are disordered within partially occupied (0.25) tetrahedral sites in $Ce_2GaS_{2.5}O_2$; correspondingly, the four coplanar S sites are also partially occupied (0.50) (**Figure 1-6**).

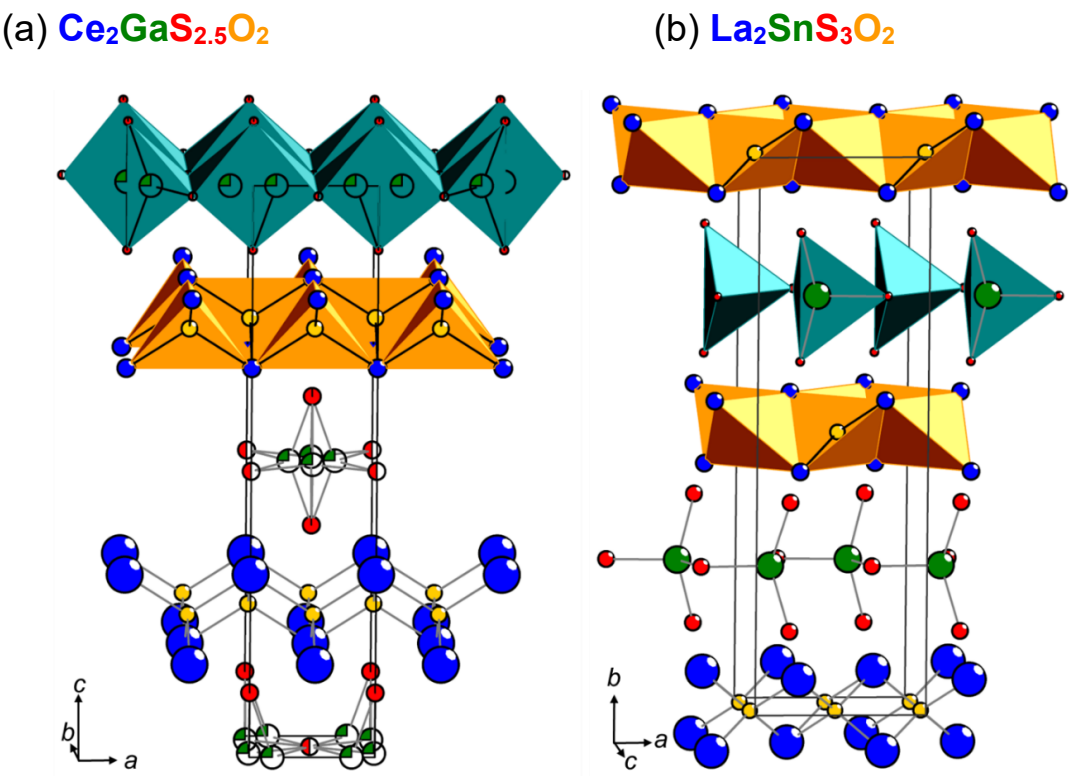

Figure 1-5. Structures of (a) $Ce_2GaS_{2.5}O_2$ and (b) $La_2SnS_3O_2$

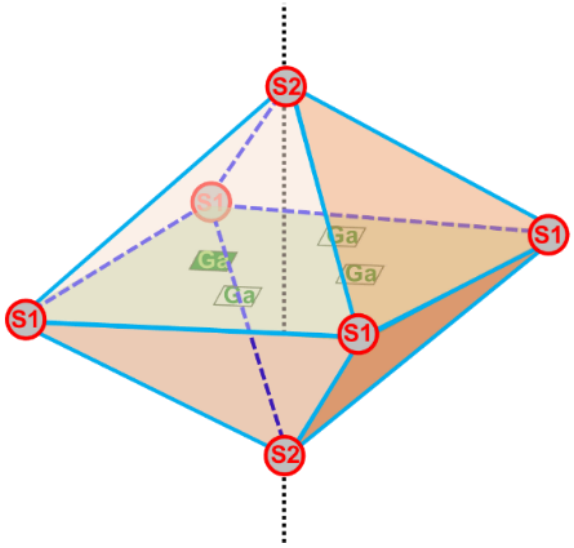

Figure 1-6. Environment of partially occupied Ga sites, each in tetrahedral geometry, in $Ce_2GaS_{2.5}O_2$.

1.4.3. $Nd_4Ga_2S_5O_4$-type

The $Nd_4Ga_2S_5O_4$-type structure (orthorhombic, *Pbca*) is adopted by $RE_4Ga_2S_5O_4$ (*RE* = Pr, Nd, Sm), $RE_4Ge_{1.5}S_5O_4$ (*RE* = La–Nd), $La_4Ga_2Se_5O_4$, and $La_4Ge_{1.5}Se_5O_4$. Only $Nd_4Ga_2S_5O_4$ has been characterized by single-crystal X-ray diffraction.[2] The structure consists of undulating [*RE*O] layers built from RE_4O tetrahedra, alternating with ribbons of corner-sharing MCh_4 tetrahedra (**Figure 1-7**).

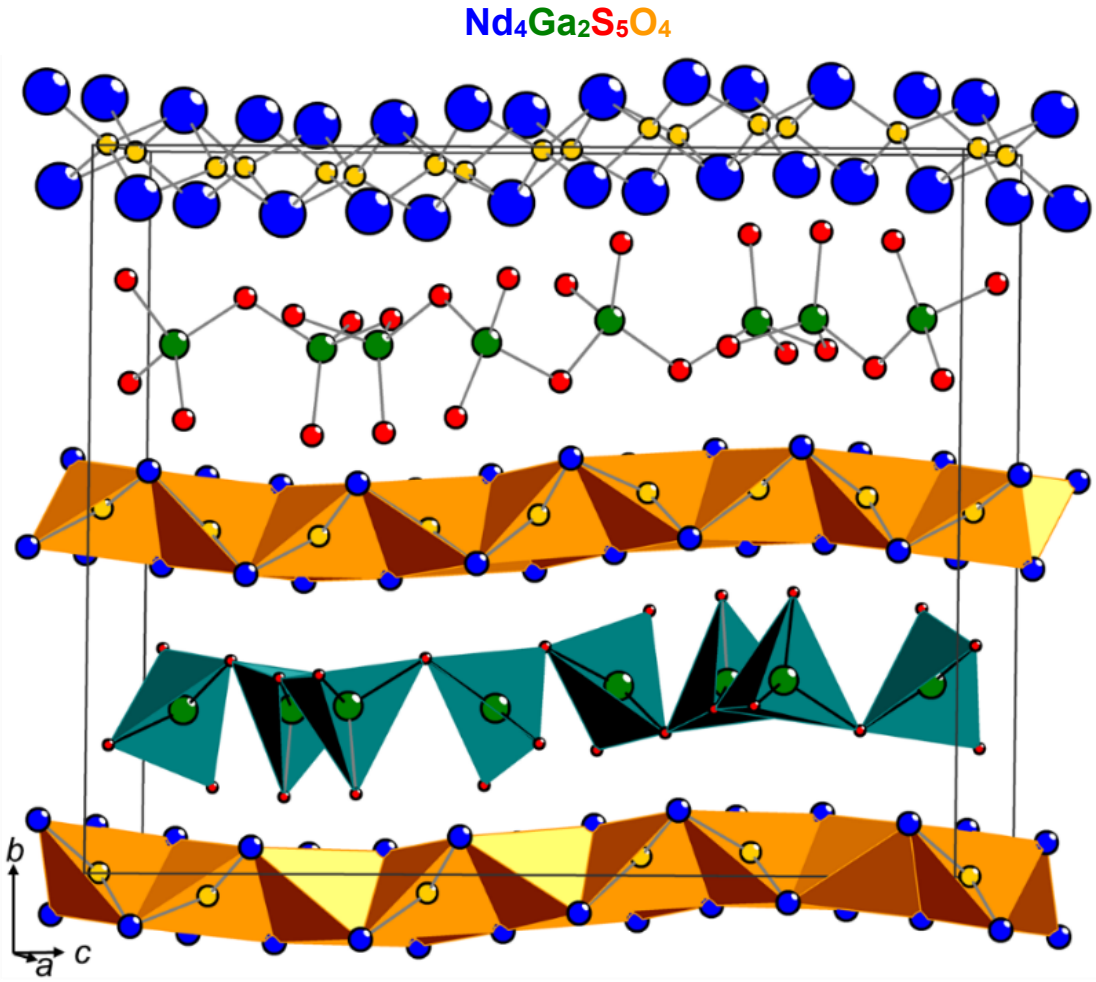

Figure 1-7. Structure of $Nd_4Ga_2S_5O_4$.

1.4.4. $LaGaSe_2O$-type

Only two compounds, $LaGaSe_2O$ and $LaInOSe_2$, adopt this structure (orthorhombic, $Pca2_1$).[92] Resembling the $CeBiS_2O$-type structure, it contains [*RE*O] layers alternating with zigzag ribbons of corner-sharing $GaSe_4$ tetrahedra (**Figure 1-8**).

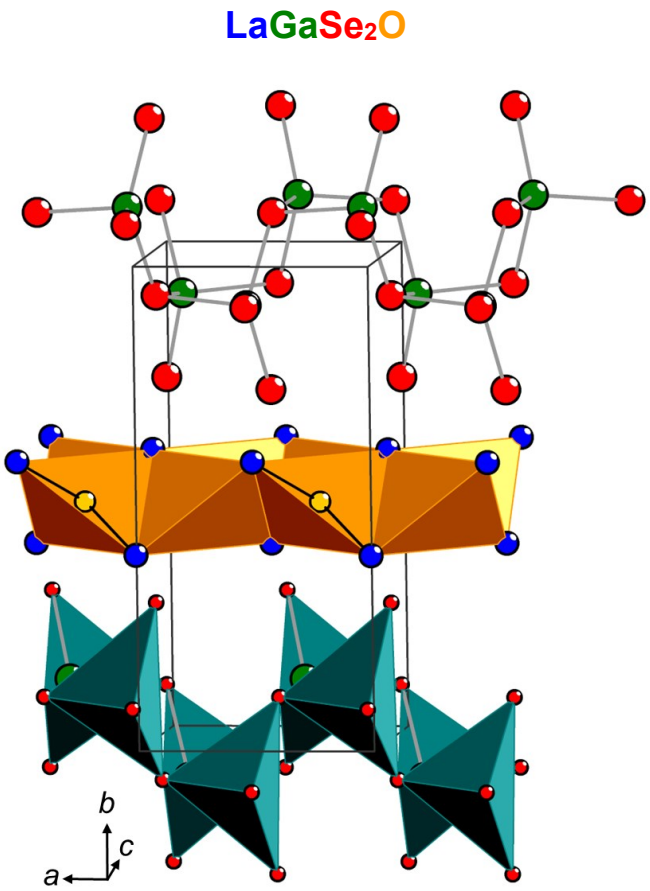

Figure 1-8. Structure of $LaGaSe_2O$.

1.4.5. *RE*–In–*Ch*–O compounds

There are relatively few quaternary In-containing oxychalcogenides *RE*–In–*Ch*–O: $La_5In_3S_9O_3$,[93] $La_{10}In_6S_{17}O_6$,[93] $LaInS_2O$,[92] and $LaInSe_2O$.[92] Their structures are idiosyncratic. $La_5In_3S_9O_3$ consists of 3-unit-wide fragments of the familiar fluorite-type [LaO] blocks, separated by layers of both In-centred tetrahedra and octahedra (**Figure 1-9a**).[93] $La_{10}In_6S_{17}O_6$ contains the

same motifs, but in different arrangements; furthermore, the In-centred octahedra are highly distorted, and unusually, one of the axially coordinated ligands is another In atom instead of a S atom, resulting in In–In bonds (**Figure 1-9b**). The octahedral In sites are half-occupied. These octahedra are connected together by the In-centred tetrahedra.

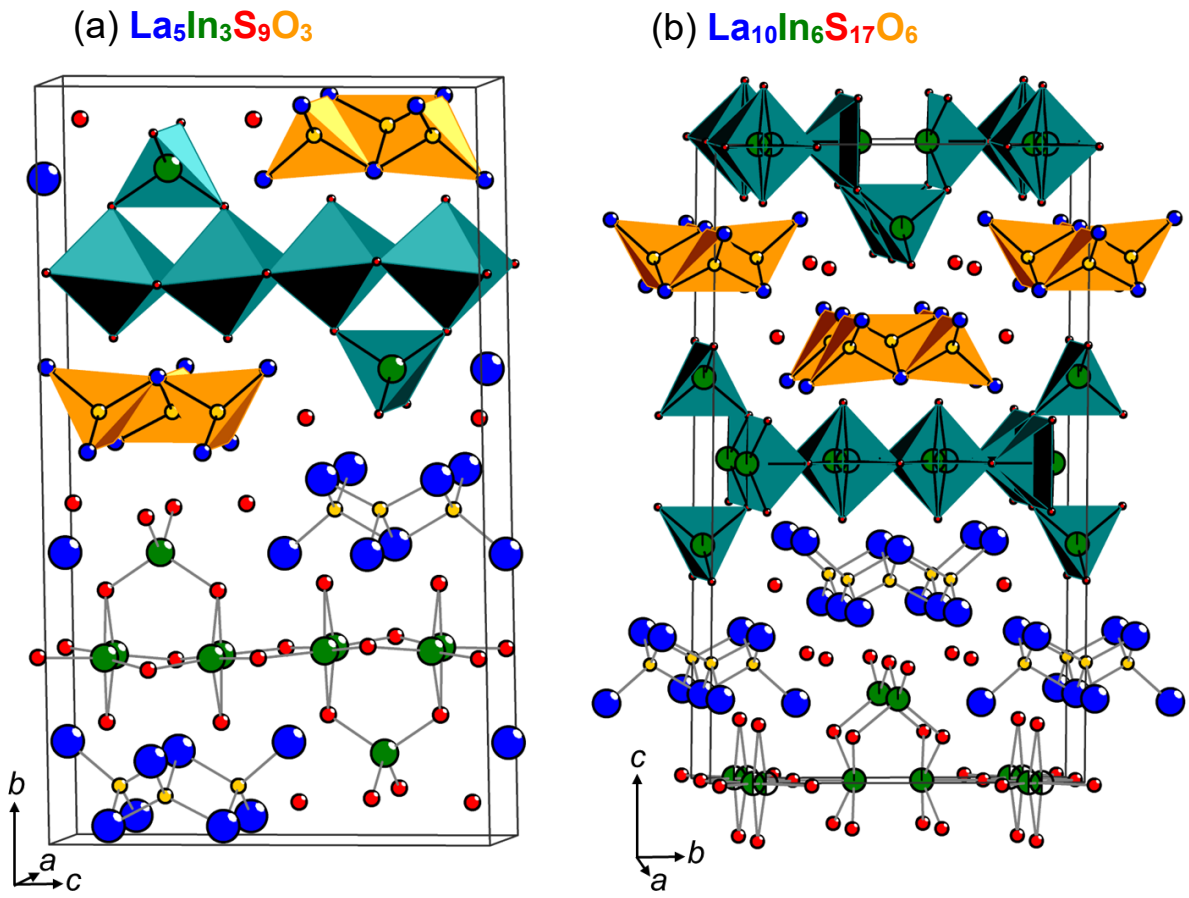

Figure 1-9. Structures of (a) $La_5In_3S_9O_3$ and (b) $La_{10}In_6S_{17}O_6$, consisting of In-centred tetrahedra or octahedra alternating with fragments of [LaO] blocks.

In the course of investigating La–In–S–O systems, the two compounds $La_5In_3S_9O_3$ (described above) and $LaInS_2O$ were identified.[93] $LaInS_2O$ exists as two polymorphs. The stable one (orthorhombic, *Pnma*) (**Figure 1-10**) contains six-tetrahedra-wide fragments of the familiar [LaO] blocks, capped by unusual La_3InO units at both ends, rendering the In coordination to be InS_5O. These fragments are connected together by InS_6 octahedra. This polymorph has been

shown to be a good photocatalyst for visible light water splitting.[95] A metastable form was obtained by metathesis reaction. Its structure (monoclinic, $P2_1/m$) is similar to $LaBiS_2O$ (**Figure 1-4b**), and its photocatalytic activity was evaluated.[96,97]

The structures of all existing quaternary rare-earth chalcogenides *RE*–*M*–*Ch*–O (*M* = p-block metal or metalloid) are summarized in **Table 1-3**.

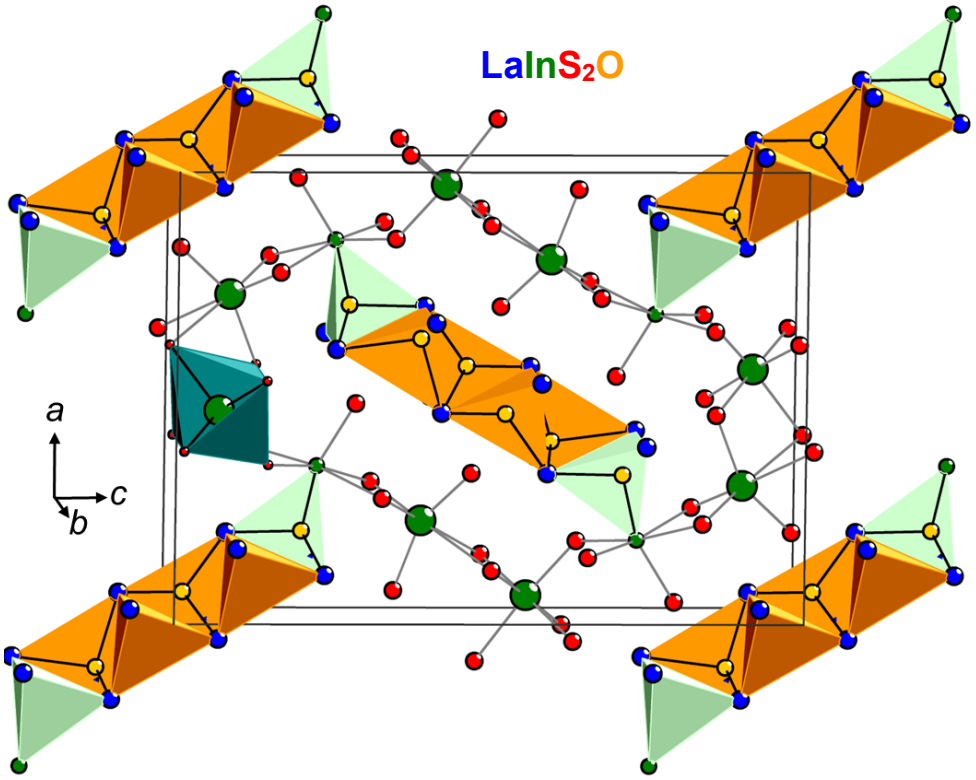

Figure 1-10. Structure of $LaInS_2O$.

Table 1-3. Reported oxychalcogenides *RE*–*M*–*Ch*–O (*M* = p-block metal or metalloid).[2]

Structure, space group	Compounds		
	Sulfides	**Selenides**	**Tellurides**
$CeBiS_2O$, *P*4/*nmm*	*RE*BiS_2O (*RE* = La – Nd, Sm, Gd, Dy, Yb) *RE*SbS_2O (*RE* = La – Lu, except Pm) **RE*AsS_2O (*RE* = La – Nd)	$LaBiOSe_2$ *RE*$SbSe_2O$ (*RE* = La, Ce)	
$Ce_2GaS_{2.5}O_2$, *I*4/*mmm*	$La_2AsS_{2.5}O_2$ $Ce_2GaS_{2.5}O_2$ **RE*$_4As_2S_5O_4$ (*RE* = La – Nd) **RE*$_4Sb_2S_5O_4$ (*RE* = La – Pr) **RE*$_2SbS_{2.5}O_2$ (*RE* = La – Nd, Sm, Eu, Dy – Er, Yb) *$Pr_4Bi_2S_5O_4$	$La_2Ga_{0.94}Se_{2.41}O_2$	
$LaBiS_2O$, *P*2$_1$/*m*	*RE*BiS_2O (*RE* = La, Pr) *RE*InS_2O (*RE* = La – Pr) $CeSbS_2O$		
$La_2SnS_3O_2$, *Pnma*	$La_2SnS_3O_2$ **RE*$_4Sn_2S_6O_4$ (*RE* = La – Nd)	*$La_4Sn_2Se_6O_4$	
$Nd_4Ga_2S_5O_4$, *Pbca*	$Nd_4Ga_2S_5O_4$ **RE*$_4Ga_2S_5O_4$ (*RE* = Pr, Nd, Sm) **RE*$_4Ge_{1.5}S_5O_4$ (*RE* = La – Nd)	*$La_4Ga_2Se_5O_4$ *$La_4Ge_{1.5}Se_5O_4$	
$La_4Ga_{1.33}S_4O_4$, *P*4/*mmm*	**RE*$_4Ga_{1.33}S_4O_4$ (*RE* = La, Ce)		
$LaGaS_2O$, *Pbcm*	$LaGaS_2O$		
La_3GaS_5O, *Pnma*	La_3GaS_5O		
$LaInS_2O$, *Pnma*	$LaInS_2O$		
$La_{1.67}Ga_3S_6O$, *P*$\bar{4}$2$_1$*m*	$La_{1.67}Ga_3S_6O$		
Ga_2S_3, *Cc*	$Sm_{0.4}Ga_{1.6}S_{2.4}O_{0.6}$		
$La_{10}In_6S_{17}O_6$, *Immm*	$La_{10}In_6S_{17}O_6$		
$La_4As_2S_6O_3$, *Ibam*	$La_4As_2S_6O_3$		
$La_4Ga_{1.72}S_{4.58}O_4$, *P*4/*mmm*	$La_4Ga_{1.72}S_{4.58}O_4$		
$La_5In_3S_9O_3$, *Pbcm*	$La_5In_3S_9O_3$		
$La_6Sb_4S_3O_{12}$, *I*4$_1$/*amd*	$La_6Sb_4S_3O_{12}$		
$LaBiS_2O_{0.93}$, *P*4/*n*	$LaBiS_2O_{0.93}$		
$Sm_8CrTe_{13}Cl$, *Cmc*2$_1$	$Dy_8SnS_{13.61}O_{0.39}$		
$NdBi_2ClO_4$, *P*4/*mmm*	$CeBi_2SeO_4$		
$LaGaSe_2O$, *Pca*2$_1$		La*M*Se_2O (*M* = Ga, In)	
$(Li_{0.25}Bi_{0.75})_2ClO_2$, *I*4/*mmm*		$La_{0.04}$ $Bi_{1.96}$ SeO_2	
Na_2SiF_6, *P*321			$La_xIn_{2-x}TeO_6$
Bi_2TeO_5, *Aem*2			*RE*$_x$$Bi_{2-x}TeO_5$ (*RE* = Ce, Eu)

* Compounds have been tentatively assigned to structure types, but no experimental data are available.

1.5. Synthesis

Solid state reactions are often performed at high temperatures and over lengthy times to ensure that the atoms within the starting materials diffuse at reasonable rates to form products. Typical temperatures may exceed 800 °C and typical times could range from a few days to even months. Thermodynamically stable phases are usually obtained. Non-experts sometimes disparage this approach as being unsophisticated, betraying their own misconceptions and prejudices. First, notwithstanding this simplistic caricature of how solid state reactions are often portrayed, complex reaction mechanisms are at play in which not only various solid phases are at play, but also liquid and gas phases. There remains relatively poor understanding of how these reactions proceed, largely because of the absence of good characterization tools at such extreme conditions of temperature. Experiments to probe such reactions through *in situ* characterization are highly cumbersome to set up, but offer glimpses into the details of solid state reaction mechanisms.[98] Second, the investigation of solid state reactions through traditional methods is far from exhausted, and literally untold numbers of even thermodynamic phases are ripe for discovery. Why build a rocketship to travel to distant universes when our own immediate worlds have hardly been explored? Third, high-temperature reactions are a mainstay of numerous industrial processes, such as the fabrication of steel. A high-temperature furnace need not be regarded as some strange piece of equipment that seems out of place in a lab: the stereotypical image of dissolved reactants stirring within round-bottom flasks is more a reflection of how molecular chemists have pushed their own narrow conception of how chemical reactions "should" proceed over other areas of chemistry.

Varying the conditions of solid state reactions enables access to phases that may not be thermodynamically stable. For example, metastable phases could be obtained depending on

heating or cooling rates, or use of a flux. Synthetic variables such as the choice of precursors, the temperature profile, and the dimensions and type of container (e.g. fused silica or alumina) could all influence the outcome of a reaction. Depending on the compound being targeted, careful considerations are also made to avoid deleterious reactions with the container. For example, it is prudent to apply a protective pyrolyzed carbon coating on the inner side of fused silica tubes, to avoid reaction with alkali and alkaline-earth metals. Alternatively, a binary starting material containing these active metals could be used in lieu of the elemental form. Some starting materials (such as chalcogens, pnictogens) will have high vapour pressure when heated, posing a risk of explosion; in this instance, a larger or thicker tube would be advisable. Use of such precursors also means that control of composition may be difficult because of volatilization losses that need to be compensated. In a typical procedure, the starting materials are combined in a desired ratio, finely ground and mixed, and often cold-pressed into pellets to maximize surface contact. For target materials that are not oxides, the tubes must be evacuated and then sealed. A prevailing thought in solid state synthesis is that ternary and quaternary phases are more difficult to access, even when they may be thermodynamically stable, because competing binary or ternary phases on the reaction pathway may form. The usual strategy is to remove the products at this stage, regrind them to expose more contacting surfaces, and apply the heat treatment again, repeating this procedure as necessary to improve phase purity (**Figure 1-11**).

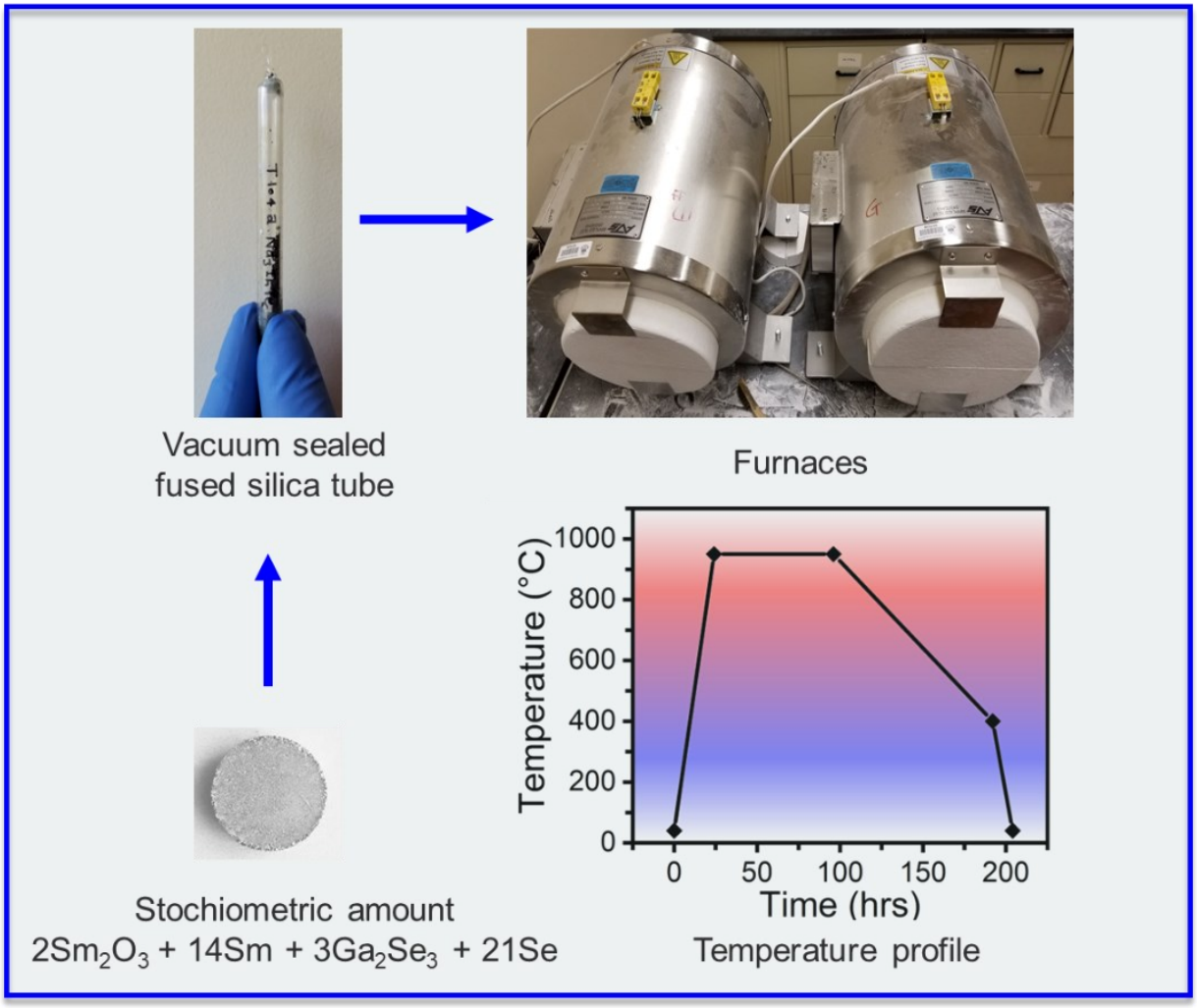

Figure 1-11. Steps involved in typical solid-state synthesis of Sm_3GaSe_5O.

To illustrate the typical synthetic considerations discussed above, a quaternary oxychalcogenide *RE*–Ga–*Ch*–O could be prepared by an appropriate combination of elemental and binary phase reactants (*RE*, RE_2O_3, Ga_2Ch_3, *Ch*). A large thick-walled fused-silica tube (length of 15 cm, diameter of 9–12 mm) would be suitable for a reaction on a 300-mg scale, taking into account the high vapour pressures and relatively low melting points for elemental chalcogens (**Figure 1-12**). If the reactions are run at 850–950 °C, there may be some volatilization loss of elemental chalcogens (unless they have largely reacted with the other components at a lower

temperature), but this is only known after several reactions have been attempted, by observing their deposition at the opposite end of the tube. From these observations, a typical weight excess of 10% S or 5% Se is added to compensate for these losses. The heating (or cooling) rates may also be adjusted as another synthetic variable.

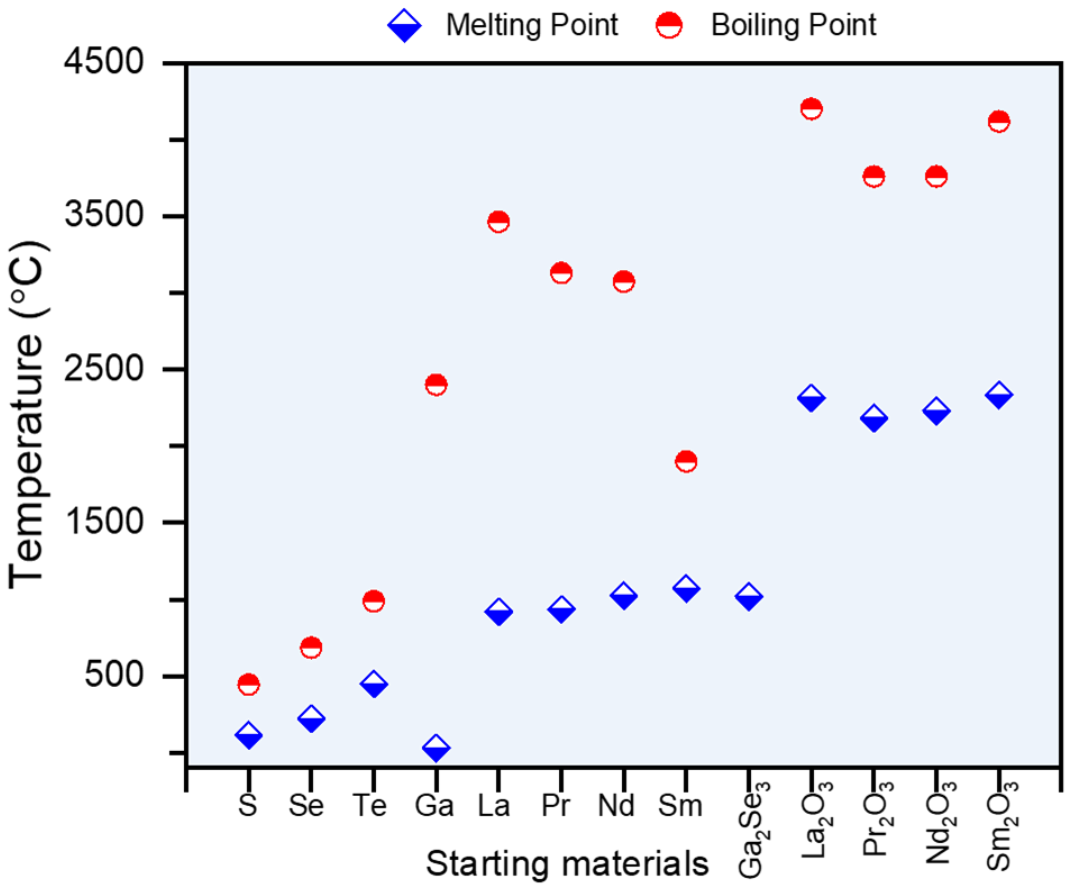

Figure 1-12. Melting and boiling points of precursors.

Of utmost importance in solid state chemistry is the growth of single crystals. The structures of solid state compounds are definitively determined through single-crystal X-ray diffraction, the most important characterization technique in this research area. Moreover, physical properties can be unambiguously attributed to a compound in question if it is in the form of a single crystal, rather than a microcrytalline sample in which the potential presence of impurity phases is always a nagging concern. Single crystals suitable for structure determination must be

of sufficient size (thankfully, advances in crystallographic instrumentation now permit routine investigation of crystals as small as <0.1 mm) and of good quality, meaning that they give clean diffraction patterns. Despite many bold and perhaps unjustifiably overconfident claims for "design" (as manifested even in the titles of certain journals), crystal growth largely remains an artform. Among various techniques, slow cooling of the melt is a straightforward technique, although success is not guaranteed and may be thwarted by incongruent melting behaviour. It is popular to add fluxes, which are high-temperature solvents that helps dissolve reactants through their colligative properties, to promote crystal growth and to lower melting temperatures. An appropriate flux could simply be an excess of one of the precursors themselves, especially if they are low-melting (e.g., Ga, In, Ge, Al), acting as a self-flux. For crystal growth of chalcogenides, molten halide salts (e.g., NaCl, KCl, KBr) have been previously used.[99] Some fluxes may become incorporated into the product; if this is a desirable result, they are termed "reactive fluxes" in a face-saving attempt to pretend that this was intentional (or better yet, "rational design!"). To be fair, how fluxes operate is still largely a mystery because of the experimental challenges in monitoring these reactions: many have tried but failed.[100] To promote growth of large crystals, whether of the melt or within a flux, slow cooling (over days or even weeks) is generally helpful. A flux can be removed by washing with solvent, chosen appropriately to ensure that the desired crystals themselves are not destroyed, or in some cases, it could be centrifuged and filtered while still molten at high temperature. Crystals of some compounds in this thesis were easily obtained by slow cooling of the melt, whereas others required addition of KBr or NaCl flux. There are, of course, many other techniques of crystal growth, but they often require specialized equipment (e.g., Bridgman-Stockbarger) that does not fall into the purview or capabilities of most laboratories.

1.6. Characterization

Successful synthesis of a new compound is arguably the most challenging part of solid state chemistry, but the hard work has only just begun. The next steps are to characterize it as thoroughly as possible through various techniques. Single-crystal and powder X-ray diffraction techniques are the most important, and are used for identifying phases and determining crystal structures.[101] Compositions were analyzed by energy-dispersive X-ray analysis, although other techniques such as inductively coupled plasma optical emission or mass spectroscopy (ICP-OES or ICP-MS) are also possible. Because optical properties were of interest, band gaps were measured experimentally by optical diffuse reflectance spectroscopy. Other techniques, such as X-ray photoelectron or absorption near-edge spectroscopy could be helpful in identifying the valence of certain rare-earth atoms (e.g., Ce, Sm, Eu, Yb).[102]

1.6.1. X-ray diffraction

Because X-ray diffraction is the major technique used here, it is helpful to review the properties of X-rays and how they are generated. Discovered by Röntgen, X-rays are a high-energy form of electromagnetic radiation (5–10 keV). Hard X-rays with short wavelengths, similar to the spacings of atoms within a crystal, are highly penetrating and have practical applications in medical diagnostics, security screening, and crystallography.

X-rays are generated within an evacuated tube operated a high voltage (30–50 kV). Electrons accelerated by the hot cathode strike a water-cooled metal target anode (usually Cu or Mo) over a small area (0.4 × 8 mm for a fine focus tube, 1 × 10 mm for a normal tube). The X-ray emission spectrum consists of a broad continuous background, known as white radiation or Bremsstrahulung, caused by inelastic collisions of the bombarding electrons with the atoms in the

metal anode, and sharp and intense characteristic lines caused by electronic transitions specific to the element in the metal anode (**Figure 1-13**). When electrons ejected from the *K* shell ($n = 1$), electrons from higher energy levels relax down to the generated hole, emitting X-rays in the process. Transitions from the *L* to *K* shell give rise to the more intense *K*α line, and transitions from the *M* to *K* shell to the less intense *K*β line. The X-rays are monochromatized by removing the background radiation and the *K*β line, through absorption by an appropriate filter (Ni filter for Cu source, or Nb filter for Mo source), leaving only the *K*α line. This line is actually split into a doublet, $K\alpha_1$ and $K\alpha_2$, due to spin-orbit coupling. In careful crystallographic work, the $K\alpha_1$ line can be specifically selected through monochromatization with a quartz or germanium crystal.

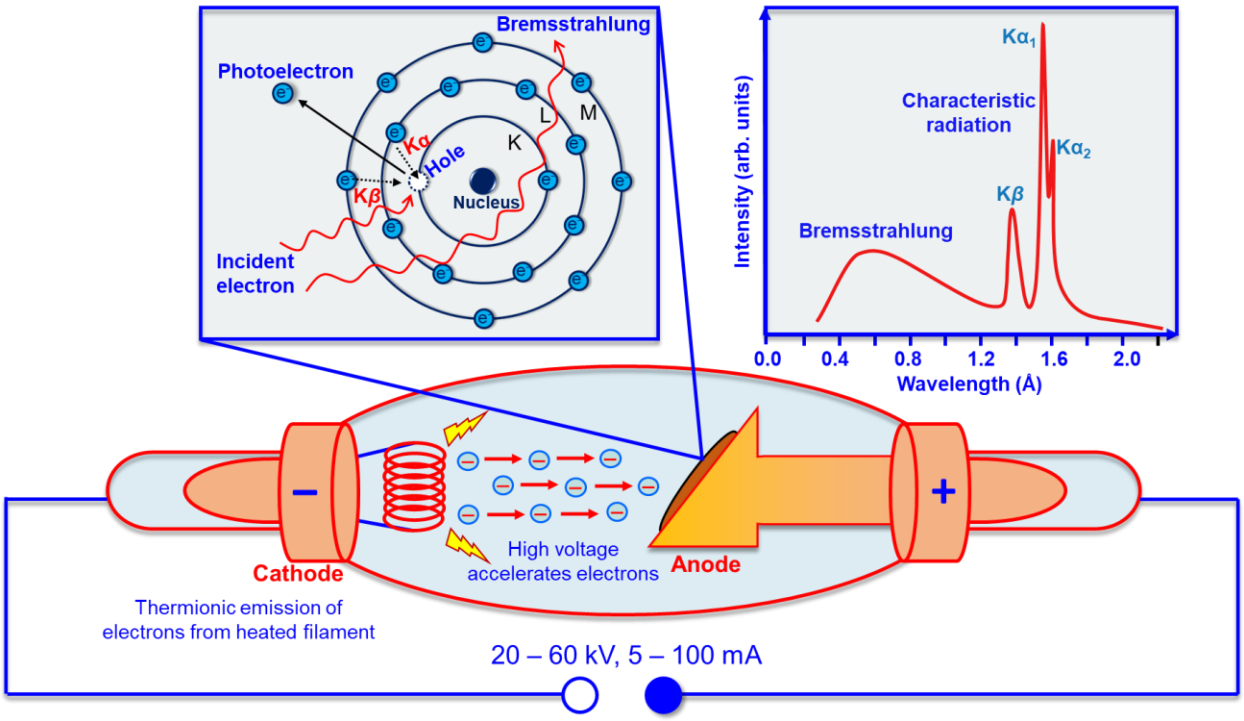

Figure 1-13. Generation of X-rays within an evacuated tube. Electrons emitted by the cathode strike a metal anode, ejecting core electrons. The characteristic Kα and Kβ X-rays are produced by electronic transitions to the resulting hole in the K-shell of the atom.

When a monochromatic X-ray beam strikes a crystalline sample, the elastically scattered radiation forms a diffraction pattern: the directions reveal the lattice and the intensities reveal the position and types of atoms. Generally speaking, powder XRD is used to evaluate phase identity, particle sizes, and degree of crystallinity, whereas single-crystal XRD is used to determine crystal structures accurately. The diffraction pattern results from constructive and destructive interference of X-rays as they strike a crystal. The scattering process can be modeled as reflection by imaginary lattice planes (*hkl*) separated by a constant spacing *d*, so that the geometry of diffraction is governed by Bragg's law, $2d \sin \theta = \lambda$, which gives the condition for constructive interference (**Figure 1-14**).

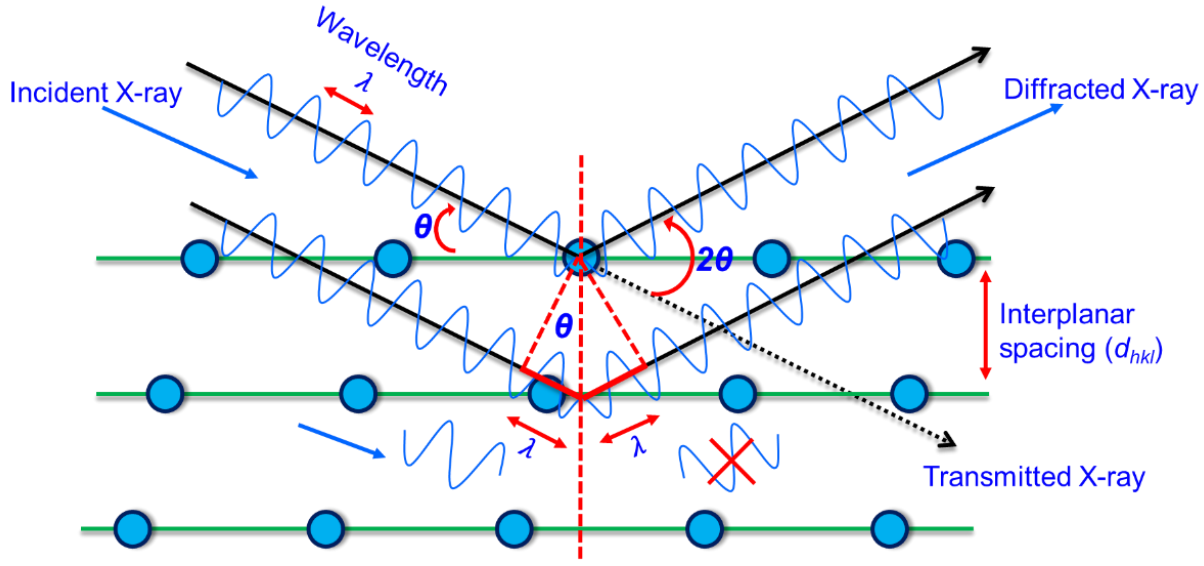

Figure 1-14. Bragg's law.

An equivalent derivation of diffraction geometry by visualizing the intersection of Laue cones, formed by satisfying the conditions for constructive interference within by a three-dimensional lattice, with repeat distances *a*, *b*, and *c* (**Figure 1-15**). These conditions are very restrictive: To observe diffraction, the crystal and the detector must be oriented at very specific angles to satisfy these conditions.

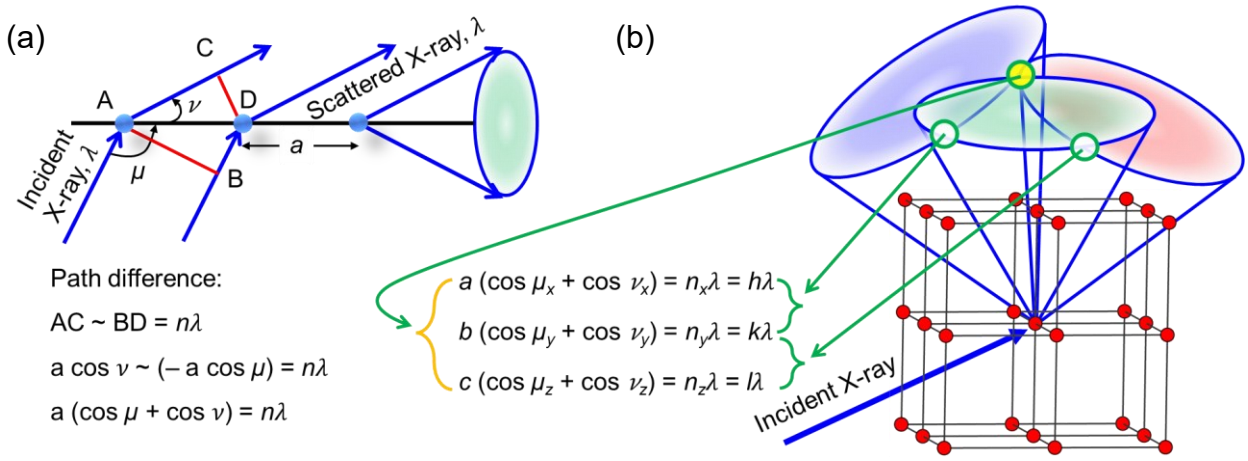

Figure 1-15. Laue conditions.

1.6.1.1 Single Crystal X-ray Diffraction

Modern X-ray diffractometers are highly automated and enable diffraction data to be collected efficiently. Crystallography has progressed so much that many non-practitioners will accept crystallographic results at face value; while this faith is touching, uncritical acceptance is not really a virtue. A brief description of how structures are routinely solved and refined is presented.

The first and perhaps most important step is to select a good crystal. What constitutes "good" is not necessarily obvious until some preliminary frames of diffraction data are inspected. Typical crystals of inorganic solids have dimensions of 0.01–0.5 mm. They are mounted to the tip of a glass fiber or within a loop by adhesive, transferred to a goniometer head, and centred on a four-circle diffractometer. The reflections (referring to the diffraction spots, the terminology being a holdover from Bragg's law) are measured as photographic frames on a CCD area detector (**Figure 1-16**),[103] as the crystal is moved in different orientations through a data collection strategy suggested by automated software. In a typical data set, frames of reflection data are collected at 7–8 different ϕ angles, using ω-scans with a frame width of 0.3° and an exposure time of 10–60 s per frame, depending on how well the crystal diffracts. The instrument used was a Bruker D8

PLATFORM diffractometer equipped with a SMART APEX II CCD area detector and a graphite-monochromated Mo *K*α radiation source.

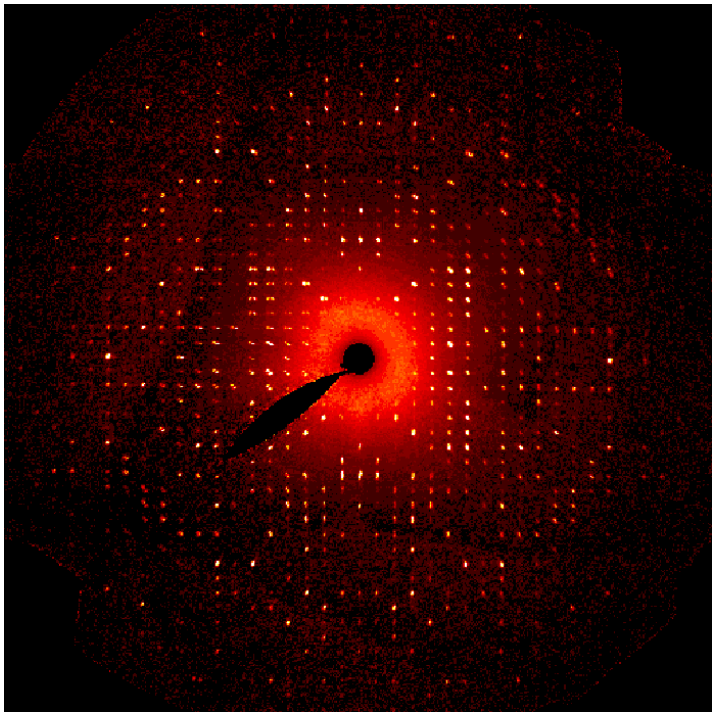

Figure 1-16. Typical precession image showing reflections from a single crystal of La_3InSe_6.

The data set consists of thousands of reflections with intensities I_{hkl}, obtained by integration of the diffraction peaks, and corrected for scaling and absorption. For rare-earth-containing compounds, absorption correction is especially important for good structure determinations. Although often inexplicably neglected by others, face-indexed numerical absorption corrections are rigorously and routinely applied in our practice. The diffraction intensities are proportional to the square of the structure factors, F_{hkl}, which are Fourier transforms of the electron density function $\rho(x,y,z)$, according to:

$$\rho_{xyz} = \frac{1}{V}\sum_{hkl} F_{hkl}.\,\mathrm{e}^{-i2\pi(hx+ky+lz)}$$

where V is the volume of the unit cell.

Crystallography would be a simple mathematical process were it not for the problem that the structure factors are complex-valued, while the experimental measurement of intensities only gives their magnitude through the relationship $I_{hkl} = |F_{hkl}|^2$. In other words, the phases of these structure factors are experimentally inaccessible. Modern structure solution exploits statistical methods (direct methods or, more recently, charge flipping) to make very good guesses of these phases, and it is a tribute to their developers that structure determination is now considered more or less a routine process. For most molecular compounds, this perception is probably true, but for solid state compounds, automated structure determination programs often fail spectacularly. (Companies that sell diffractometers don't like to draw attention to the shortcomings of their products.)

The initially solved structure still needs to be refined; that is, the positions of atoms are adjusted iteratively in the structural model until they are accurately determined, by improving the agreement between observed and calculated structure factors. Other parameters, including atomic displacement parameters and site occupancies, may also need to be introduced into the model. There are different measures of the agreement between experiment and model, but two commonly encountered ones are the conventional *R*-factor and the goodness of fit:

$$\text{Conventional } R = \frac{\sum_{hkl} ||F_o| - |F_c||}{\sum_{hkl} |F_c|}$$

$$\text{Goodness of fit, } S = \sqrt{\frac{\sum_{hkl} w(F_o^2 - F_c^2)}{m-n}}$$

where F_o are observed structure factors, F_c are structure factors, $w = 1/\sigma^2$ are weighting factors, m is the number of reflections, and n is the number of parameters. Good structures usually have low values of *R*, goodness of fits close to unity, and clean residual electron density maps. Unfortunately, crystallography is not immune to the putridness of "fake news" that pervades much of social media, and there are always stories of unethical scientists who have fabricated good but

fake crystal structures.[104] A critical eye to evaluating the chemical reasonableness of crystal structures is the best antidote to limit the propagation of such untruths.

1.6.1.2 Powder X-ray Diffraction

Powder samples can also be examined by X-ray diffraction using the same working principle as before. X-rays striking a powder sample are diffracted by many small randomly oriented crystallites, as long as Bragg's law is satisfied. However, symmetry-equivalent reflections arising from lattice planes with the same interplanar spacing *d*, which would normally be resolved in single-crystal X-ray diffraction, are no longer distinguishable in powder X-ray diffraction. In fact, it is often possible for more than one set of planes to have similar or even identical sets of *d*-spacings, resulting in overlap of peaks so that it is difficult to extract intensities of individual reflections *hkl* accurately. For this reason, powder X-ray diffraction is mainly used as a non-destructive technique for phase identification and quantification rather than for full structure determination. For example, a typical powder pattern reveals that a sample of Sm_3GaSe_5O contains about ~17% of a secondary Sm_2SeO_2 phase, with some peaks overlapping (**Figure 1-17**).[105] Cell parameters can be accurately refined by measuring the peak positions. In more detailed analysis, Rietveld refinement can be performed to fit the profile of the powder XRD pattern to a structural model, so that cell parameters and atomic positions can be obtained similar to a single-crystal analysis. For the work performed here, a Bruker D8 Advance diffractometer equipped with a Cu Kα radiation source operated at 40 kV and 40 mA was used.

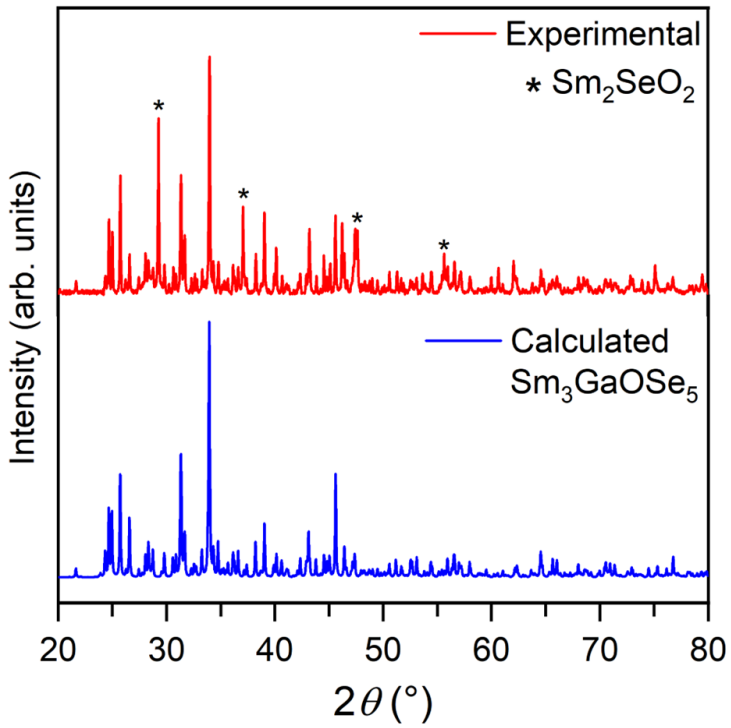

Figure 1-17. Experimental powder XRD pattern (red), compared with a pattern simulated from a structural model (blue).

1.6.2. Electron microscopy

When a beam of electrons strikes the surface of a solid, many processes can take place, some of which can be exploited to reveal information about morphology, topology, and chemical properties. The interaction volume depends on the incident angle and energy of the electron beam, but typically the penetration depth is a few micrometers. The incident electrons could be scattered, secondary electrons could be ejected, and characteristic X-rays could be emitted (**Figure 1-18**). For this work, electron microscopy is mainly used to image samples of single crystals and to determine elemental compositions.

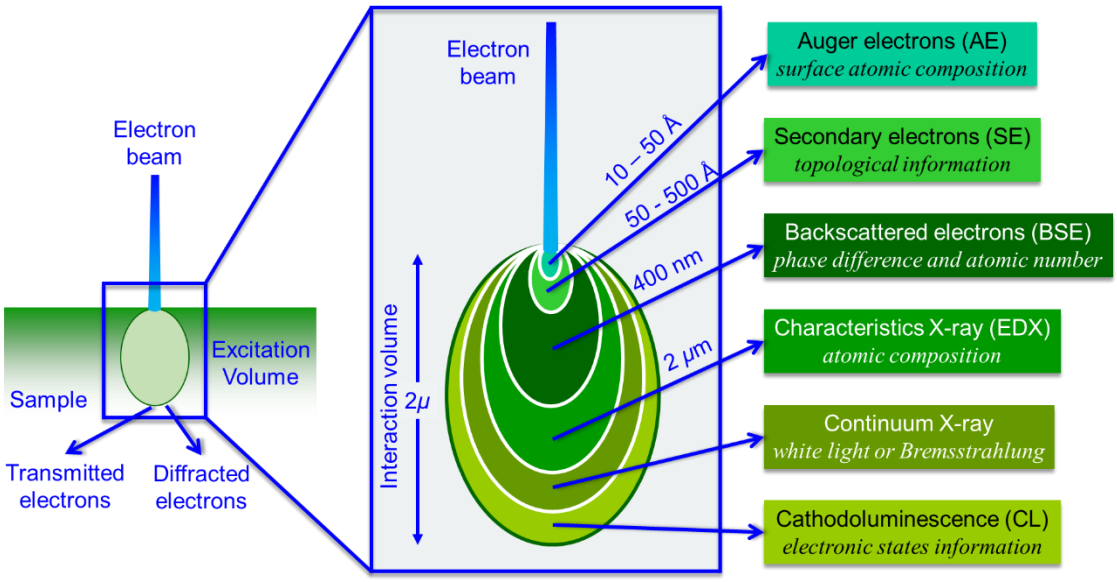

Figure 1-18. Interaction of an electron beam with the surface of a solid.

1.6.2.1 Scanning electron microscopy (SEM)

Secondary electrons can be generated from inelastic scattering of incoming electrons, within a depth of 50–500 Å of the sample surface. These electrons can then be detected at various directions to image the surface morphology. In this work, a Zeiss Sigma 300 VP field emission scanning electron microscope or a JEOL JSM-6010LA scanning electron microscope was used to analyze single crystals of various rare-earth chalcogenides and oxychalcogenides, as shown in a typical image (**Figure 1-19**).[106] Samples are mounted on electrically conductive carbon tape attached to an aluminum sample holder.

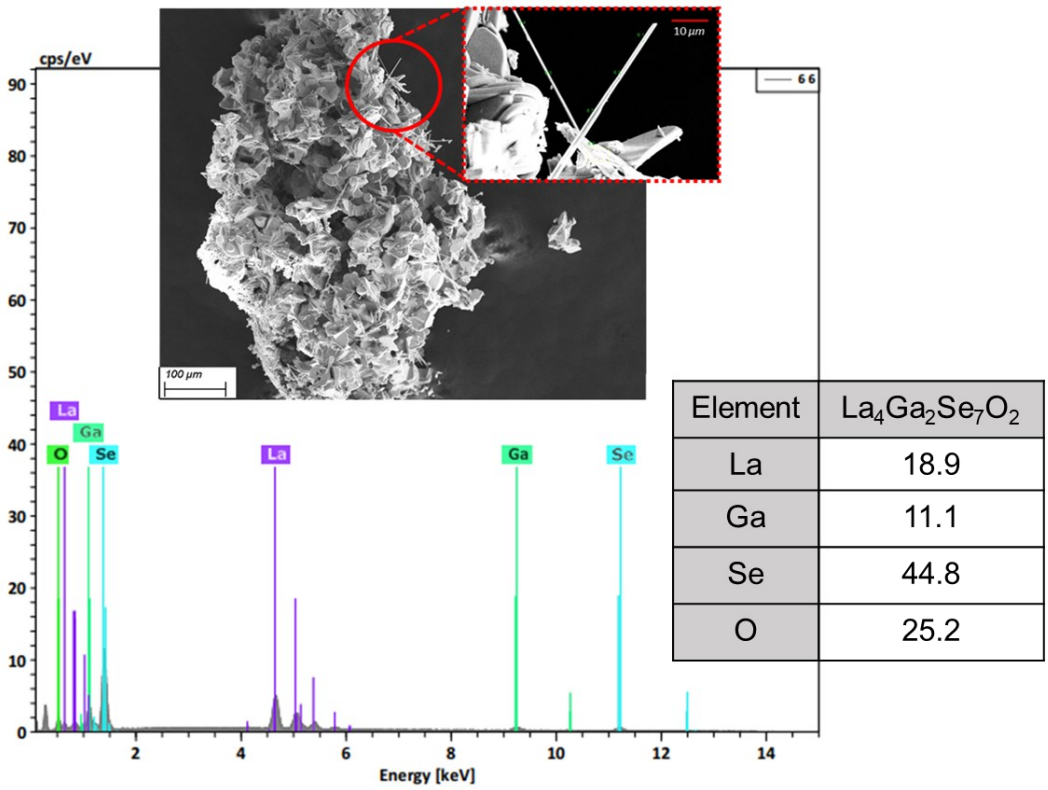

Element	$La_4Ga_2Se_7O_2$
La	18.9
Ga	11.1
Se	44.8
O	25.2

Figure 1-19. SEM image of $La_4Ga_2Se_7O_2$ obtained from secondary electron imaging and composition obtained from relative peak intensities by EDX analysis.

1.6.2.2 Energy-dispersive X-ray spectroscopy (EDX)

Among the processes that take place when an electron beam strikes a surface, characteristic X-rays can also be generated involving the same principle as described earlier (**Figure 1-20**). Because the wavelengths of the emitted X-rays are characteristic of the elements in question, they can be used to determine the chemical composition.[107] Usually, heavier elements are detected without difficulty, whereas lighter elements (with atomic number lower than 10) can be detected if more sophisticated instrumentation is available. A Bruker Quantax 600 system with appropriate dual X-Flash 6/60 detectors, capable of detecting lighter elements such as oxygen, which are present in oxychalcogenides, was used in combination with the Zeiss Sigma 300 VP scanning electron microscope.

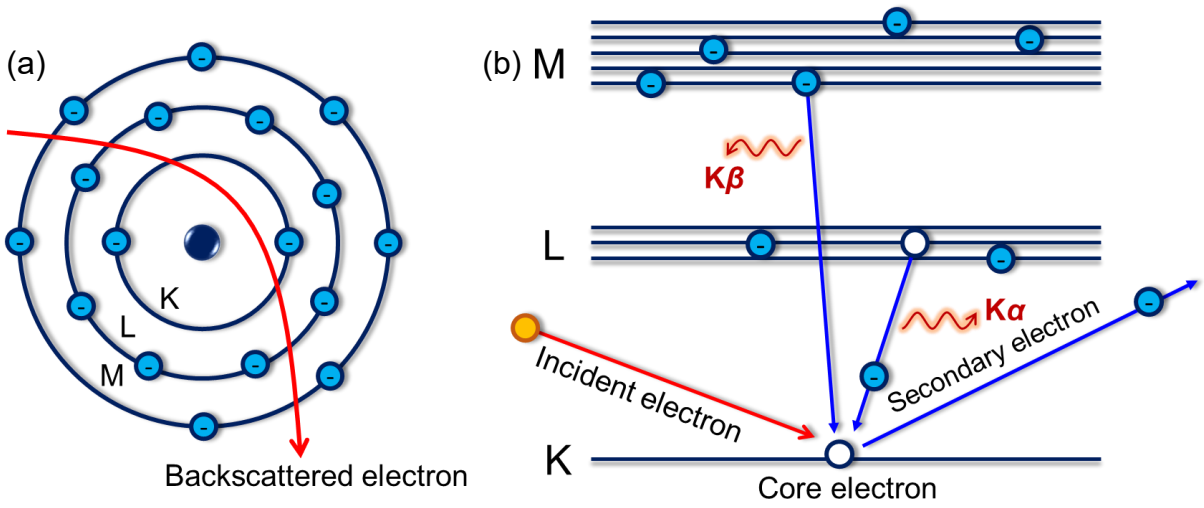

Figure 1-20. Generation of (a) backscattered electrons due to elastic scattering and (b) secondary electrons due to inelastic scattering, and characteristics X-rays.

A typical EDX spectrum show characteristic lines assigned to specific elements (**Figure 1-19**). The amounts of each element can be quantified through the relative intensities of the peaks.[107] The accuracy of EDX analysis depends on many factors (sample topography, morphology, orientation and matrix, concentration — ≥0.1% for heavier elements and ≥1% for lighter elements (F to Be), and accelerating voltage), but a serious problem can arise when peaks overlap. For example, Cu and Ga can be difficult to quantify if they occur in the same sample.[108–110] Elements lighter than Be can not be detected.[109,111,112] In general, unless careful calibration is performed with standards, an accuracy of a few weight percent (up to ~5%) can be estimated for most elements.

1.7. Optical diffuse reflectance spectroscopy

Most metal chalcogenides are semiconducting. Their band gaps can be determined experimentally by measuring the temperature dependence of the electrical conductivity, or by monitoring the absorption of light in optical diffuse reflectance spectra, as performed here. Light of varying wavelengths strikes the surface of the sample and the reflectance is measured. The

reflection is specular if the surface is smooth, as is the case for single crystals, but it is diffuse if the surface is rough, as is the case for powder samples, which contains small, randomly oriented particles reflecting light in all possible directions (**Figure 1-21**). Depending on the sizes of the particles, especially if they are small, the intensity of the scattered light has various contributions from reflection, refraction, and diffraction processes. From a detailed treatment of multiple scattering processes, the absorption coefficient can be related to the reflectance according to:[113]

$$\frac{\alpha}{S} = \frac{(1 - R_\infty)^2}{2R_\infty} = F\,(R_\infty)$$

where α is the absorption coefficient, S is the scattering coefficient, R is the reflectance, and $F(R_\infty)$ is the Kubulka-Munk function, also called the remission.

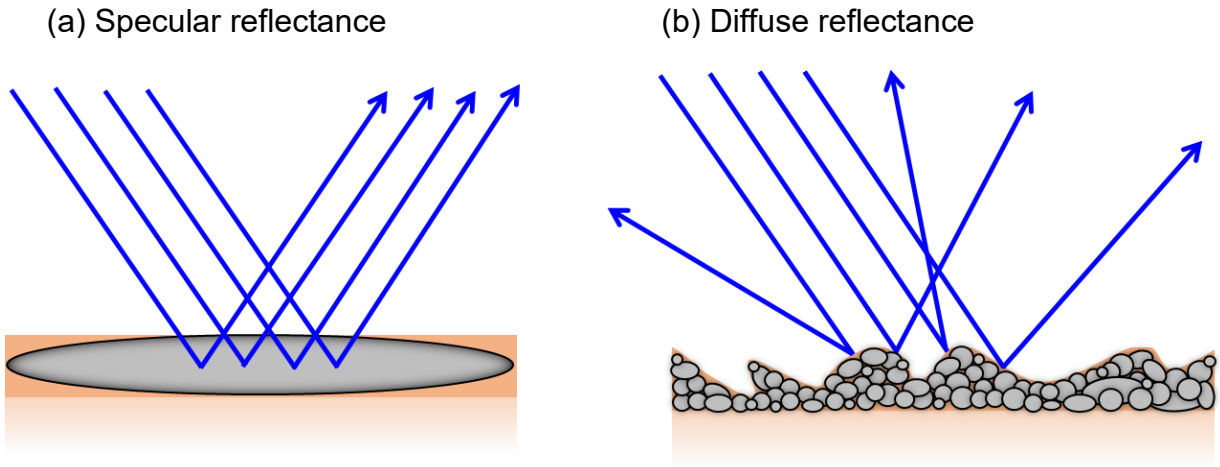

Figure 1-21. (a) Specular reflectance from a smooth surface vs. (b) diffuse reflectance from a rough surface.

Diffuse reflectance was measured on a Cary 5000 UV-vis-NIR spectrophotometer equipped with a diffuse reflectance accessory with an optical polytetrafluoroethylene disk used as a reflectance standard (>98% reflectivity in the range of 200–2200 nm). The reflectance was converted to absorption coefficients, and plotted as a function of energy of light. To extract band gaps, the absorption edges were extrapolated from plots of $(F(R_\infty)\cdot E)^n$ vs. E. A linear fit to an

exponent $n = 2$ implies a direct band gap, whereas a fit to an exponent $n = 1/2$ implies an indirect band gap. A more accurate procedure is to fit the Urbach tail, which arises from fluctuations in band energies, caused by lattice vibrations, and from disorder, caused by structural defects.[114] Linear fits are made to the absorption edge and to the abscissa for the slope below the absorption edge, and the intersection is assumed to the band gap (**Figure 1-22**).

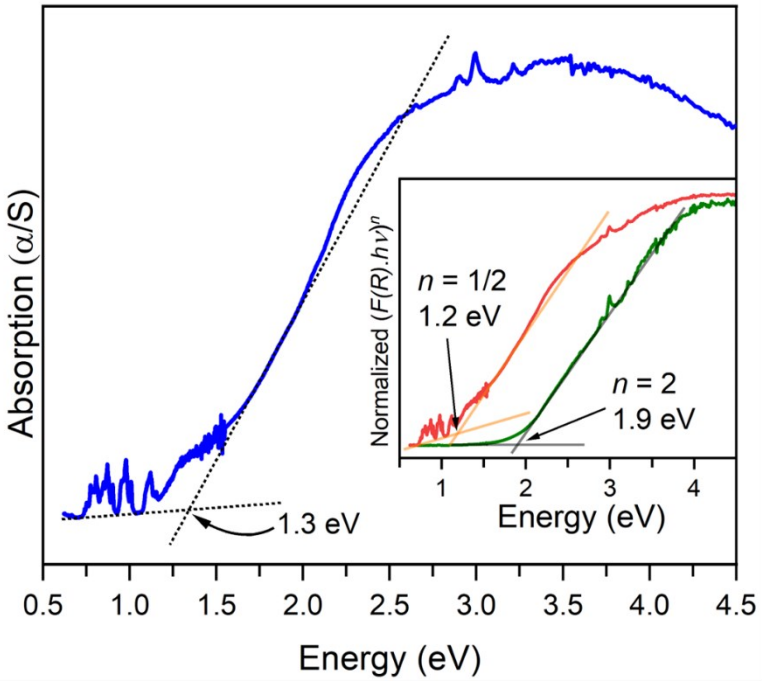

Figure 1-22. Diffuse reflectance spectra collected on powder sample semiconducting Sm_3GaOSe_5.

1.8. Electronic structure calculations

First-principles calculations of the electronic structure are helpful to understand the bonding in solids, including orbital contributions and degree of covalent vs. ionic character, and to ascertain the type of band gaps (direct vs. indirect) in semiconducting chalcogenides and oxychalcogenides. These calculations can be performed through empirical, semiempirical, or ab initio methods. Empirical and semiempirical methods, such as tight-binding and pseudopotential approaches, employ a minimal number of parameters, which can be adjusted to fit to known

features.[115] In contrast, ab initio methods do not require any experimental input and employ first principles to calculate the band structure, such as density functional theory (DFT) and non-equilibrium Greens function (NEGF). Although ab initio methods are more computationally expensive, they are becoming more commonly applied as computational power becomes more available.[115] For this work, DFT was applied to calculate the electronic structure of compounds using the projector augmented wave method as implemented in the Vienna Ab initio Simulation Package (VASP).

In contrast to molecules, which contain a finite number of atoms that interact to form discrete energy levels, extended solids contain a very large number of atoms (effectively infinite) that interact to form many closely spaced energy levels that are represented as continua called bands. It may seem challenging to solve the Schrödinger equation for something that contains an infinite number of atoms, but because crystals contain a periodic arrangement of atoms, they can be treated by imposing periodic boundary conditions. Just as atomic orbitals can be combined to form molecular orbitals, the electronic wavefunctions in a solid are represented as linear combinations of the basis functions (i.e. individual atomic orbitals), symmetry-adapted according to the periodic repeat of the lattice. For a one-dimensional lattice with repeat distance *a* and a set of basis functions χ_n for atoms within the unit cell, these wavefunctions, called Bloch functions, [116] are given by:

$$\psi_k = \sum_n e^{ikna} \chi_n$$

where the wavevector *k* is quantized within the boundaries of the first Brillouin zone, $-\frac{\pi}{a} \leq k \leq \frac{\pi}{a}$, which can be thought of as a unit cell in reciprocal space. A plot of the energy of these Bloch functions versus the wavevector *k* is known as a band dispersion diagram (**Figure 1-23b**). It

suffices to plot over positive values of k because the bands are symmetric around the reciprocal lattice origin. Because the energy levels are so numerous and spaced so closely, it is convenient to plot the density of states (DOS), corresponding to the number of states present over infinitesimally small energy increments. The DOS can also be viewed as the reciprocal of the slopes of bands. By weighting over elements of the Hamiltonian matrix for interactions between two different atoms, the crystal orbital Hamilton population (COHP) acts as a measure for the strength of bonding interactions. For real solids, which contain many types of atoms interacting in 3D, the band dispersion diagram and the DOS curves can be very complex. Most chalcogenides and oxychalcogenides follow "normal valence" rules and are electron-precise, within the implication that the electronic structure typically consists of filled valence and empty conduction bands separated by a gap.

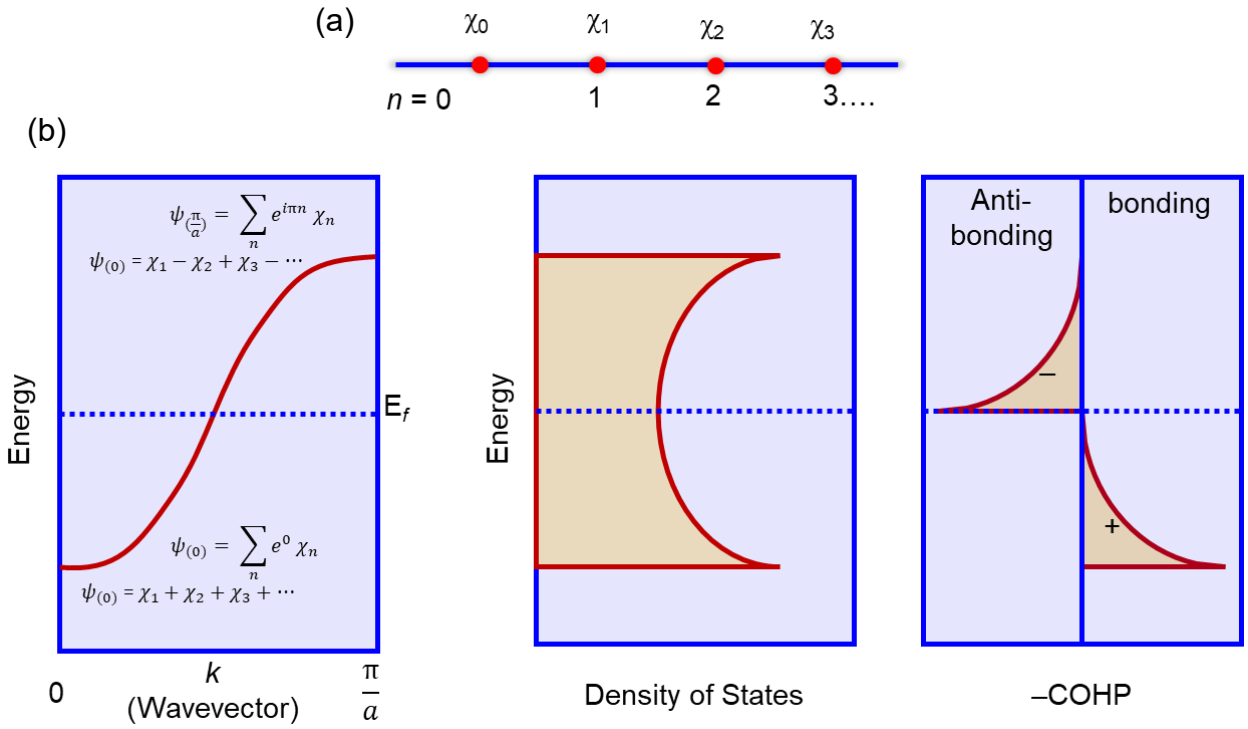

Figure 1-23. (a) Basis functions within a 1D lattice. (b) Band dispersion, density of states, and crystal orbital Hamilton populations.

DFT has been influential in facilitating modern electronic structure calculations on solids. It makes use of an initial assumption that electrons do not interact with each other, but move within a fictitious potential that attempts to model the detailed interactions with all the remaining electrons and nuclei. The Schrödinger equation is then expressed through Kohn-Sham equations with this potential (**Figure 1-24**).[117] The idea of DFT is to iteratively model the same electron density, which is a function of 3D space, as would the real solid with individually interacting electrons, in a self-consistent way. When the ground state energies of successive iterations are lower than a defined threshold (such as 10^{-8} eV), the calculation is assumed to have converged to a desired accuracy. Once the correct electron density of the ground state is obtained, the corresponding Hamiltonian operator contains the information about the quantum states (wavefunctions and energies), which can be used to evaluate band structure, density of states, and electron localization functions (ELF).

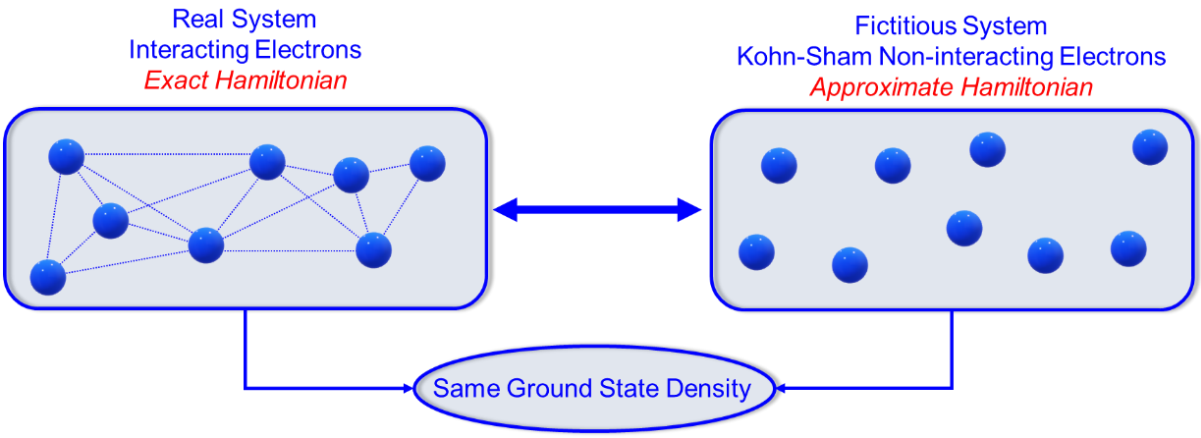

Figure 1-24. Representation of real system containing interacting electrons with fictitious system with non-interacting electrons using an approximate Hamiltonian.

In reality, of course, electrons do interact with each other and with nuclei through complex mechanisms, and their behaviour is correlated.[118–120] Because the exact correlation energy cannot

be obtained within DFT, these complex interactions are treated by introducing exchange and correlation functionals, based on several approximations (such as the local density approximation (LDA) and the generalized gradient approximation (GGA)). To further reduce computational cost, core electrons within atoms are approximated through pseudopotentials, and only valence electrons are treated in the actual calculations (**Figure 1-25**). Some properties, especially the magnitudes of band gaps, depend sensitively on the approximations made to prepare the exchange correlation functionals. In this work, the PBE functional has been used to improve the accuracy of band gap predictions.[119,120]

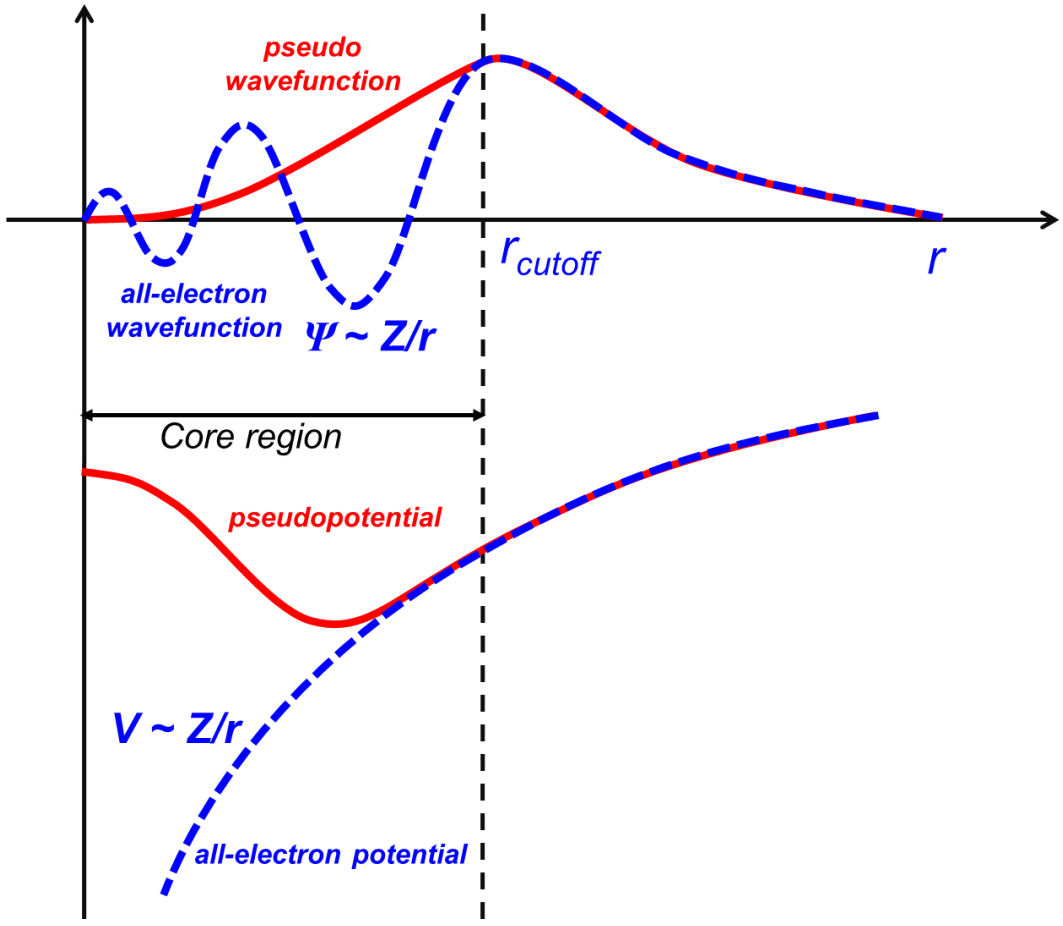

Figure 1-25. Comparison of pseudowavefunction and pseudopotentials (red) with real wavefunction and Coulomb potentials (blue). Both real and pseudo wavefunctions and potentials are the same above a particular cutoff radius (r_{cutoff}).

The typical results of a band structure calculation include a band dispersion diagram showing bands drawn as continuous lines, a DOS curve showing the number of states per unit energy (over a unit cell volume), and a COHP curve showing the bonding or antibonding character for interactions between specified pairs of atoms (**Figure 1-26**). A recent development is the conception of a crystal orbital bond in index (COBI), which attempts to quantify the degree of covalency vs. ionicity within bonds of a solid, following the approach of Wiberg and Mayer.[121–123]

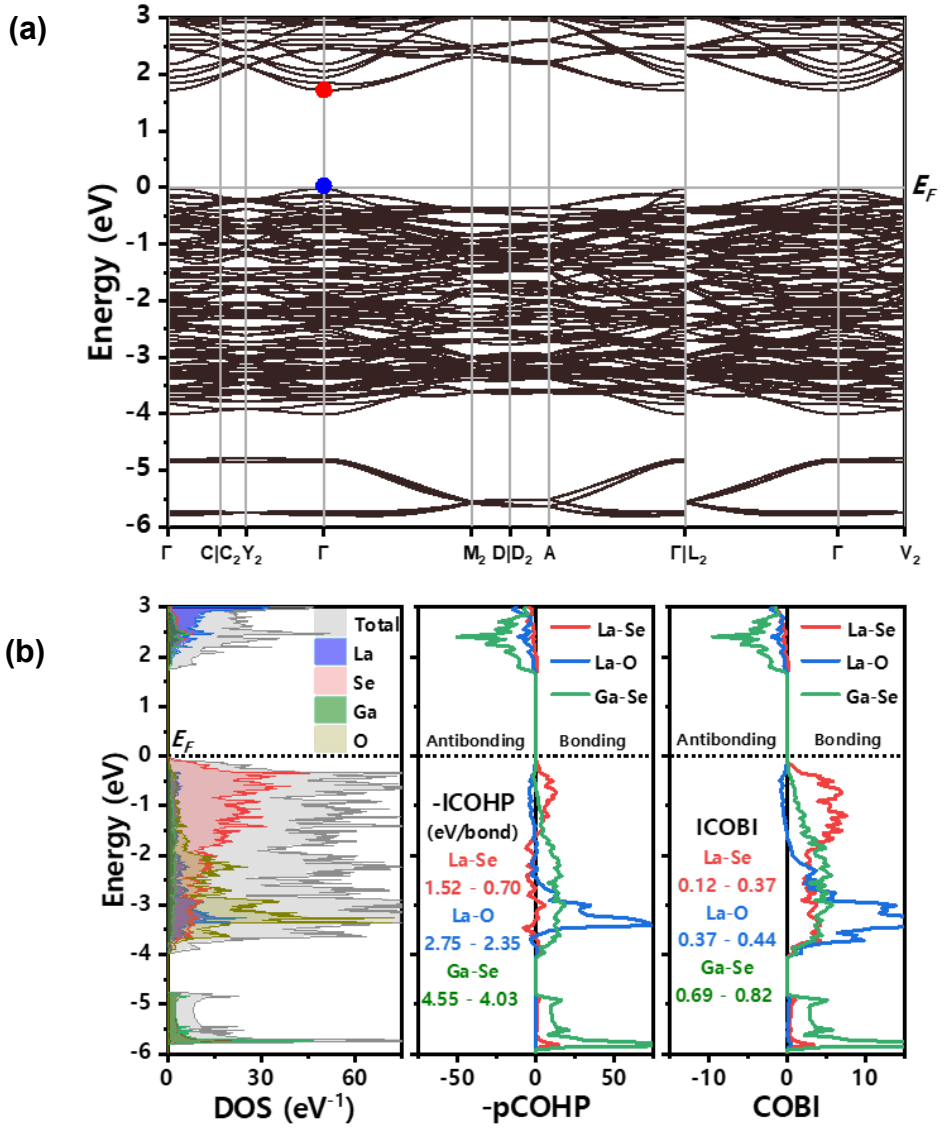

Figure 1-26. (a) Band dispersion, with valence band maximum (blue) and conduction band minimum (red) noted. (b) DOS (left), –COHP (center), and COBI (right) curves for $La_4Ga_2Se_6O_3$.

1.9. Motivation and objectives

The primary goal of this thesis is to discover new ternary chalcogenides and quaternary oxychalcogenides containing rare-earth elements, and to evaluate their structural diversity. Unlike molecular chemistry, the structures of extended inorganic solids are not easily predictable, and it is not obvious that there are universal principles that govern them. Thus, structure determination is an important step to characterize such compounds and to discern their most common structural features. Conventionally, bonding within metal chalcogenides has assumed to be of covalent character. Similarly, the assertion that rare-earth oxychalcogenides *RE*–*M*–*Ch*–O can be segregated into more ionic *RE*–O and more covalent *M*–*Ch* building blocks, in accordance with the HSAB principle, has never really been tested. Thus, another goal is to quantify the degree of covalent vs. ionic character in such compounds. Because chalcogenides and oxychalcogenides exhibit varied physical properties, they are suitable candidates for photocatalysis, thermoelectrics, and semiconductors. A third goal is to measure or calculate some of the optical and electronic properties of these compounds to evaluate their potential for these applications.

Chapter 2 is motivated by the search for new ternary rare-earth chalcogenides *RE*–*M*–*Ch*. About 1200 representatives of such compounds have been known to date, especially those with *M* = d-block metals; many of these compounds have been of interest for their optical and electronic properties. In contrast, ternary chalcogenides containing *M* = p-block metals have been underexplored. Such compounds may be useful as optical materials. Most of these compounds are sulfides, followed by selenides, and very few are tellurides (Table 1-1). Furthermore, the structural characterization has been rudimentary, being limited to powder XRD data with no detailed location of atoms. The RE_3MCh_6 series was chosen for study because there were many unresolved ambiguities about their structures and physical properties.

Chapters 3 to 5 relate to the investigation of several new series of quaternary rare-earth oxychalcogenides *RE*–*M*–*Ch*–O, which are less numerous for *M* = p-block metals than for those with d-block metals. Related oxychalcogenides have drawn attention for their physical properties suitable for applications as thermoelectrics, photocatalysts, ionic conductors, and transparent semiconductors. A hypothesis was formulated that new oxychalcogenides $RE_3MCh_{6-x}O_x$ could be derived from the chalcogenides RE_3MCh_6 mentioned above by gradually substituting *Ch* with O atoms. Calling this "rational design," as the less scrupulous might be tempted to do, would be the height of hubris. Instead, as normally happens in science, unexpected results were obtained that led to productive new directions in research and revised hypotheses. In this way, the new oxychalcogenides $La_4Ga_2Se_6O_3$ and $RE_4Ga_2Se_7O_2$ were discovered. The persistent theme of *RE*–O and *M*–*Ch* blocks within their structures was evaluated through electronic structure calculations. Because these were found to be semiconducting, their transport properties were further calculated to assess their potential as thermoelectric materials.

1.10. References

(1) West, A. R. *Basic Solid State Chemistry*, 2nd ed.; Wiley: New York, 1999.

(2) Villars, P.; Cenzual, K. *Pearson's Crystal Data – Crystal Structure Database for Inorganic Compounds,* Release 2022/23, ASM International, Materials Park, OH, USA.

(3) Mitchell, K.; Ibers, J. A. *Chem. Rev.* **2002**, *102*, 1929–1952.

(4) Cody, J. A.; Mansuetto, M. F.; Pell, M. A.; Chien, S.; Ibers, J. A. *J. Alloys Compd.* **1995**, *219*, 59–62.

(5) Mar, A.; Jobic, S.; Ibers, J. A. *J. Am. Chem. Soc.* **1992**, *114*, 8963–8971.

(6) Rouxel, J. *Acc. Chem. Res.* **1992**, *25*, 328–336.

(7) Rahman, A.; Khan, M. M. *New J. Chem.* **2021**, *45*, 19622–19635.

(8) Choi, Y. I.; Lee, S.; Kim, S. K.; Kim, Y.-I.; Cho, D. W.; Khan, M. M.; Sohn, Y. *J. Alloys Compd.* **2016**, *675*, 46–56.

(9) Tsai, M.-L.; Su, S.-H.; Chang, J.-K.; Tsai, D.-S.; Chen, C.-H.; Wu, C.-I.; Li, L.-J.; Chen, L.-J.; He, J.-H. *ACS Nano* **2014**, *8*, 8317–8322.

(10) Tsai, D.-S.; Lien, D.-H.; Tsai, M.-L.; Su, S.-H.; Chen, K.-M.; Ke, J.-J.; Yu, Y.-C.; Li, L.-J.; He, J.-H. *IEEE J. Sel. Top. Quantum Electron.* **2014**, *20*, 30–35.

(11) Woods-Robinson, R.; Han, Y.; Zhang, H.; Ablekim, T.; Khan, I.; Persson, K. A.; Zakutayev, A. *Chem. Rev.* **2020**, *120*, 4007–4055.

(12) Yin, J.; Jin, J.; Lin, H.; Yin, Z.; Li, J.; Lu, M.; Guo, L.; Xi, P.; Tang, Y.; Yan, C.-H. *Adv. Sci.* **2020**, *7*, 1903070.

(13) Huang, J.; Wei, Z.; Liao, J.; Ni, W.; Wang, C.; Ma, J. *J. Energy Chem.* **2019**, *33*, 100–124.

(14) Zogg, H.; Maissen, C.; Masek, J.; Hoshino, T.; Blunier, S.; Tiwari, A. N. *Semicond Sci. Technol.* **1991**, *6*, C36–C41.

(15) Fischer, Ø.; Odermatt, R.; Bongi, G.; Jones, H.; Chevrel, R.; Sergent, M. *Phys. Lett. A* **1973**, *45*, 87–88.

(16) Matthias, B. T.; Marezio, M.; Corenzwit, E.; Cooper, A. S.; Barz, H. E. *Science* **1972**, *175*, 1465–1466.

(17) Francis, J. D. S.; Rice, T. M. *Phys. Today* **1979**, *32*, 32–38.

(18) Zhou, J.; Liu, Y.; Zhang, S.; Zhou, T.; Guo, Z. *InfoMat.* **2020**, *2*, 437–465.

(19) Boyd, G.; Kasper, H.; McFee, J. *IEEE J. Quantum Electron.* **1971**, *7*, 563–573.

(20) Shi, Y.; Sturm, C.; Kleinke, H. *J. Solid State Chem.* **2019**, *270*, 273–279.

(21) Balaram, V. *Geosci. Front.* **2019**, *4*, 1285–1303.

(22) Wall, F. Rare earth elements. In *Critical Metals Handbook*, Gunn G., Ed.; Wiley, 2014; pp 312–339.

(23) Petit, L.; Szotek, Z.; Lüders, M.; Svane, A. *J. Phys. Condens. Matter* **2016**, *28*, 223001.

(24) Wachter, P. *Crit. Rev. Solid State Mater. Sci.* **1972**, *3*, 189–241.

(25) Kumta, P.N., Risbud, S.H. *J. Mater. Sci*. **1994**, *29*, 1135–1158.

(26) Liu, W.; Zhang, Z.; Ji, J.; Liu, Y.; Li, J.; Wang, X.; Lei, H.; Chen, G.; Zhang, Q. *Chinese Phys. Lett.* **2018**, *35*, 117501.

(27) Meng, F.; Hughbanks, T. *Inorg. Chem.* **2001**, *40*, 2482–2483.

(28) Holtzberg, F.; McGuire, T. R.; Methfessel, S.; Suits, J. C. *Phys. Rev. Lett.* **1964**, *13*, 18–21.

(29) Chen, H.-Y.; Zhang, Y.-Y.; Yang, Y.-F.; Guo, S.-P. *J. Alloys Compd.* **2021**, *868*, 159112.

(30) Chen, M.-C.; Li, L.-H.; Chen, Y.-B.; Chen, L. *J. Am. Chem. Soc.* **2011**, *133*, 4617–4624.

(31) Alemi, A.; Klein, A.; Meyer, G.; Dolatyari, M.; Babalou, A. *Z. Anorg. Allg. Chem* **2011**, *637*, 87–93.

(32) Chi, Y.; Guo, S.-P.; Xue, H.-G. *RSC Adv.* **2017**, *7*, 5039–5045.

(33) He, J.; Wang, Z.; Zhang, X.; Cheng, Y.; Gong, Y.; Lai, X.; Zheng, C.; Lin, J.; Huang, F. *RSC Adv.* **2015**, *5*, 52629–52635.

(34) Lozac'h, A. M.; Jaulmes, S.; Guittard, M. *C. R. Seances Acad. Sci., Ser. C* **1971**, *272*, 1123–1126.

(35) Jaulmes, S.; Laruelle, P. *Acta Crystallogr. Sect. B Struct. Crystallogr. Cryst. Chem.* **1973**, *29*, 352–354.

(36) Loireau-Lozac'h, A. M.; Guittard, M.; Flahaut, J. *Mater. Res. Bull.* **1977**, *12*, 881–886.

(37) Zhang, M.-J.; Li, B.-X.; Liu, B.-W.; Fan, Y.-H.; Li, X.-G.; Zeng, H.-Y.; Guo, G.-C. *Dalton Trans.* **2013**, *42*, 14223–14229.

(38) Carré, D.; Guittard, M.; Adolphe, C. *Acta Crystallogr. Sect. B Struct. Crystallogr. Cryst. Chem.* **1978**, *34*, 3499–3501.

(39) Guittard, M.; Carré, D.; Kabré, T. S. *Mater. Res. Bull.* **1978**, *13*, 279–286.

(40) Aliev, O. M. *Izv. Akad. Nauk. SSSR, Neorg. Mater.* **1980**, *16*, 1514–1518.

(41) Akhmedova, D. A.; Agaev, A. B.; Rustamov, P. G. *Zh. Neorg. Khim.* **1992**, 37, 461–464.

(42) Ivashchenko, I.; Kozak, V.; Olekseyuk, I.; Daszkiewicz, M.; Halyan, V.; Tishchenko, P.; Shemet, V. Y.; Gulay, L. *J. Solid State Chem.* **2020**, *288*, 121339-1–121339-7.

(43) Messain, D.; Carré, D.; Laruelle, P. *Acta Crystallogr. Sect. B Struct. Crystallogr. Cryst. Chem.* **1977**, *33*, 2540–2542.

(44) Gulay, L. D.; Daszkiewicz, M.; Huch, M. R. *J. Solid State Chem.* **2008**, *181*, 2626–2632.

(45) Aleandri, L. E.; Ibers, J. A. *J. Solid State Chem.* **1989**, *79*, 107–111.

(46) Aleandri, L. E.; Ibers, J. A. *J. Solid State Chem.* **1989**, *81*, 317.

(47) Tougait, O.; Ibers, J. A. *Inorg. Chem.* **2000**, *39*, 1790–1794.

(48) Huch, M. R.; Gulay, L. D.; Olekseyuk, I. D. *J. Alloys Compd.* **2007**, *439*, 156–161.

(49) Rao, C. N. R.; Raveau, B. *Acc. Chem. Res.* **1989**, *22*, 106–113.

(50) Jacobson, A. J. *Chem. Mater.* **2010**, *22*, 660–674.

(51) Kamihara, Y.; Hiramatsu, H.; Hirano, M.; Kawamura, R.; Yanagi, H.; Kamiya, T.; Hosono, H. *J. Am. Chem. Soc.* **2006**, *128*, 10012–10013.

(52) Kamihara, Y.; Watanabe, T.; Hirano, M.; Hosono, H. *J. Am. Chem. Soc.* **2008**, *130*, 3296–3297.

(53) Ueda, K.; Hiramatsu, H.; Ohta, H.; Hirano, M.; Kamiya, T.; Hosono, H. *Phys. Rev. B* **2004**, *69*, 155305.

(54) Clarke, S. J.; Adamson, P.; Herkelrath, S. J. C.; Rutt, O. J.; Parker, D. R.; Pitcher, M. J.; Smura, C. F. *Inorg. Chem.* **2008**, *47*, 8473–8486.

(55) Schwerdtfeger, P.; Nagle, J. K. *Mol. Phys.* **2019**, *117*, 1200–1225.

(56) Slater, J. C. *J. Chem. Phys.* **1964**, *41*, 3199–3204.

(57) Pearson, R. G. *J. Chem. Educ.* **1968**, *45*, 581 and 643.

(58) Cárdenas, C.; Ayers, P. W. *Phys. Chem. Chem. Phys.* **2013**, 15, 13959–13968.

(59) Ebbinghaus, S. G.; Abicht, H.-P.; Dronskowski, R.; Müller, T.; Reller, A.; Weidenkaff, A. *J. Prog. Solid State Chem.* **2009**, *37*, 173–205.

(60) Tsujimoto, Y.; Yamaura, K.; Takayama-Muromachi, E. *J Appl. Sci.* **2012**, *2*, 206–219.

(61) Stock, C.; McCabe, E. *J. Condens. Matter Phys.* **2016**, *28*, 453001.

(62) Luu, S. D.; Vaqueiro, P. *J. Materiomics* **2016**, *2*, 131–140.

(63) Hiramatsu, H.; Yanagi, H.; Kamiya, T.; Ueda, K.; Hirano, M.; Hosono, H. *Chem. Mater.* **2008**, *20*, 326–334.

(64) Ueda, K.; Hiramatsu, H.; Hirano, M.; Kamiya, T.; Hosono, H. *Thin Solid Films* **2006**, *496*, 8–15.

(65) Wilmer, D.; Jorgensen, J. D.; Wuensch, B. J. *Solid State Ionics* **2000**, *136–137*, 961–966.

(66) Hiramatsu, H.; Kamihara, Y.; Yanagi, H.; Ueda, K.; Kamiya, T.; Hirano, M.; Hosono, H. *J. Eur. Ceram. Soc.* **2009**, *29*, 245–253.

(67) Tippireddy, S.; Prem Kumar, D. S.; Das, S.; Mallik, R. C. *ACS Appl. Energy Mater.* **2021**, *4*, 2022–2040.

(68) Muir, S.; Subramanian, M. A. *Prog. Solid State Chem.* **2012**, *40*, 41–56.

(69) Orr, M.; Hebberd, G. R.; McCabe, E. E.; Macaluso, R. T. *ACS Omega* **2022**, *7*, 8209–8218.

(70) Li, Z.; Xiao, C.; Xie, Y. *Appl. Phys. Rev.* **2022**, *9*, 011303.

(71) Nakai, I.; Koto, K.; Nagashima, K.; Morimoto, N. *Chem. Lett.* **1977**, *6*, 275–276.

(72) Sabelli, C.; Nakai, I.; Katsura, S. *Am. Miner.* **1988**, *73*, 398–404.

(73) Zhao, F.; Yuan, M.; Zhang, W.; Gao, S. *J. Am. Chem. Soc.* **2006**, *128*, 11758–11759.

(74) Yang, L.; Cai, Z.; Hao, L.; Xing, Z.; Dai, Y.; Xu, X.; Pan, S.; Duan, Y.; Zou, J. *ACS Appl. Mater. Interfaces* **2017**, *9*, 22518–22529.

(75) Strobel, S.; Choudhury, A.; Dorhout, P. K.; Lipp, C.; Schleid, T. *Inorg. Chem.* **2008**, *47*, 4936–4944.

(76) Johnson, V.; Jeitschko, W. *J. Solid State Chem.* **1974**, *11*, 161–166.

(77) Pöttgen, R.; Johrendt, D. *Z. Naturforsch. B* **2008**, *63*, 1135–1148.

(78) Céolin, R.; Rodier, N. *Acta Crystallogr. Sect. B Struct. Crystallogr. Cryst. Chem.* **1976**, *32*, 1476–1479.

(79) Pardo, M. P.; Céolin, R.; Guittard, M. *C. R. Seances Acad. Sci., Ser. C* **1976**, *283*, 735–738.

(80) Si, Q.; Rabello, S.; Ingersent, K.; Smith, J. L. *Nature* **2001**, *413*, 804–808.

(81) Nagao, M.; Miura, A.; Ueta, I.; Watauchi, S.; Tanaka, I. *Solid State Commun.* **2016**, *245*, 11–14.

(82) Higashinaka, R.; Asano, T.; Nakashima, T.; Fushiya, K.; Mizuguchi, Y.; Miura, O.; Matsuda, T. D.; Aoki, Y. *J. Phys. Soc. Jpn.* **2014**, *84*, 023702.

(83) Tanaka, M.; Nagao, M.; Matsumoto, R.; Kataoka, N.; Ueta, I.; Tanaka, H.; Watauchi, S.; Tanaka, I.; Takano, Y. *J. Alloys Compd.* **2017**, *722*, 467–473.

(84) Mizuguchi, Y.; Demura, S.; Deguchi, K.; Takano, Y.; Fujihisa, H.; Gotoh, Y.; Izawa, H.; Miura, O. *J. Phys. Soc. Jpn.* **2012**, *81*, 114725.

(85) Xing, J.; Li, S.; Ding, X.; Yang, H.; Wen, H.-H. *Phys. Rev. B* **2012**, *86*, 214518.

(86) Jha, R.; Kumar, A.; Kumar Singh, S.; Awana, V. P. S. *J. Supercond. Novel Magn.* **2013**, *26*, 499–502.

(87) Demura, S.; Mizuguchi, Y.; Deguchi, K.; Okazaki, H.; Hara, H.; Watanabe, T.; Denholme, S. J.; Fujioka, M.; Ozaki, T.; Fujihisa, H.; Gotoh, Y.; Miura, O.; Yamaguchi, T.; Takeya, H.; Takano, Y. *J. Phys. Soc. Jpn.* **2013**, *82*, 033708.

(88) Yazici, D.; Huang, K.; White, B. D.; Chang, A. H.; Friedman, A. J.; Maple, M. B. *Philos. Mag.* **2013**, *93*, 673–680.

(89) Tomita, T.; Ebata, M.; Soeda, H.; Takahashi, H.; Fujihisa, H.; Gotoh, Y.; Mizuguchi, Y.; Izawa, H.; Miura, O.; Demura, S.; Deguchi, K.; Takano, Y. *J. Phys. Soc. Jpn.* **2014**, *83*, 063704.

(90) Mizuguchi, Y.; Miura, A.; Nishida, A.; Miura, O.; Tadanaga, K.; Kumada, N.; Lee, C. H.; Magome, E.; Moriyoshi, C.; Kuroiwa, Y. *J Appl. Phys.* **2016**, *119*, 155103.

(91) Mizuguchi, Y. *Chem. Rec.* **2016**, *16*, 633–651.

(92) Guittard, M.; Bénazeth, S.; Dugué, J.; Jaulmes, S.; Palazzi, M.; Laruelle, P.; Flahaut, J. *J. Solid State Chem.* **1984**, *51*, 227–238.

(93) Kabbour, H.; Cario, L.; Moëlo, Y.; Meerschaut, A. *J. Solid State Chem.* **2004**, *177*, 1053–1059.

(94) Gastaldi, L.; Carré, D.; Pardo, M. P. *Acta Crystallogr. Sect. B Struct. Crystallogr. Cryst. Chem.* **1982**, *38*, 2365–2367.

(95) Kabbour, H.; Sayede, A.; Saitzek, S.; Lefèvre, G.; Cario, L.; Trentesaux, M.; Roussel, P. *Chem. Commun.* **2020**, *56*, 1645–1648.

(96) Miura, A.; Oshima, T.; Maeda, K.; Mizuguchi, Y.; Moriyoshi, C.; Kuroiwa, Y.; Meng, Y.; Wen, X.-D.; Nagao, M.; Higuchi, M.; Tadanaga, K. *J. Mater. Chem. A* **2017**, *5*, 14270–14277.

(97) Ito, H.; Miura, A.; Goto, Y.; Mizuguchi, Y.; Moriyoshi, C.; Kuroiwa, Y.; Azuma, M.; Liu, J.; Wen, X.-D.; Nishioka, S.; Maeda, K.; Masubuchi, Y.; Rosero-Navarro, N. C.; Tadanaga, K. *Dalton Trans.* **2019**, *48*, 12272–12278.

(98) Weiland, A.; Frith, M. G.; Lapidus, S. H.; Chan, J. Y. *Chem. Mater.* **2021,** *33*, 7657–7664.

(99) Kanatzidis, M. G. *Inorg. Chem.* **2017**, *56*, 3158–3173.

(100) Shoemaker, D. P.; Chung, D. Y.; Mitchell, J. F.; Bray, T. H.; Soderholm, L.; Chupas, P. J.; Kanatzidis, M. G. *J. Am. Chem. Soc.* **2012**, *134*, 9456–9463.

(101) Massa, W. *Crystal Structure Determination*, 2nd ed.; Springer: Berlin, 2004.

(102) Mishra, V.; Subbarao, U.; Roy, S.; Sarma, S. C.; Mumbaraddi, D.; Sarkar, S.; Peter, S. C. *Inorg. Chem.* **2018**, *57*, 12576–12587.

(103) Mishra, V.; Mumbaraddi, D.; Iyer, A. K.; Mar, A., *J. Solid State Chem.* **2021**, *297*, 122096.

(104) Else, H. *Nature* **2022**, *608*, 461.

(105) Mishra, V.; Mumbaraddi, D.; Iyer, A. K.; Yin, W.; Mar, A. *J. Solid State Chem.* **2022**, *308*, 122901.

(106) Mishra, V.; Zabolotnii, A.; Mar, A. *Inorg. Chem.* **2022**, *61*, 12458–12465.

(107) Russ, J. C. *Fundamentals of Energy Dispersive X-ray Analysis*; Butterworth: London, 1984.

(108) Mishra, V.; Oliynyk, A. O.; Subbarao, U.; Sarma, S. C.; Mumbaraddi, D.; Roy, S.; Peter, S. C. *Cryst. Growth Des.* **2018**, *18*, 6091–6099.

(109) Mishra, V.; Iyer, A. K.; Mumbaraddi, D.; Oliynyk, A. O.; Zuber, G.; Boucheron, A.; Dmytriv, G.; Bernard, G. M.; Michaelis, V. K.; Mar, A. *J. Solid State Chem.* **2020**, *292*, 121703.

(110) Mumbaraddi, D.; Mishra, V.; Lidin, S.; Mar, A. *J. Solid State Chem.* **2022**, *311*, 123157.

(111) Jomaa, M.; Mishra, V.; Mumbaraddi, D.; Chaudhary, M.; Dmytriv, G.; Michaelis, V. K.; Mar, A. *J. Solid State Chem.* **2022**, *306*, 122792.

(112) Jomaa, M.; Mishra, V.; Chaudhary, M.; Mumbaraddi, D.; Michaelis, V. K.; Mar, A. *J. Solid State Chem.* **2022**, *314*, 123372.

(113) Kubelka, P.; Munk, F. *Z. Tech. Phys.* **1931**, *12*, 259–274.

(114) Urbach, F. *Phys. Rev.* **1953**, *92*, 1324–1324.

(115) *Properties of Crystalline Silicon*, 4th ed.; Hull, R., Ed.; INSPEC: London, 1999.

(116) Bloch, F. *Z. Phys.* **1929**, *52*, 555–600.

(117) Kohn, W.; Sham, L. J. *Phys. Rev.* **1965**, *140*, A1133–A1138.

(118) Born, M.; Oppenheimer, R. *Ann. Phys.* **1927**, *389*, 457–484.

(119) Perdew, J. P.; Burke, K.; Ernzerhof, M. *Phys. Rev. Lett.* **1996**, *77*, 3865–3868.

(120) Perdew, J. P.; Ernzerhof, M.; Burke, K. *Chem. Phys.* **1996**, *105*, 9982–9985.

(121) Müller, P. C.; Ertural, C.; Hempelmann, J.; Dronskowski, R. *J. Phys. Chem. C* **2021**, *125*, 7959–7970.

(122) Wiberg, K. B. *Tetrahedron* **1968**, *24*, 1083–1096.

(123) Mayer, I. *Chem. Phys. Lett.* **1983**, *97*, 270–274.

Chapter 2.

Rare-earth indium selenides RE_3InSe_6 (*RE* = La–Nd, Sm, Gd, Tb): Structural evolution from tetrahedral to octahedral sites

A version of this chapter has been published.

Mishra, V.; Mumbaraddi, D.; Iyer, A. K.; Mar, A. J. Solid State Chem. ***2021****, 297, 122096.*

2.1. Introduction

Ternary rare-earth chalcogenides *RE*–*M*–*Ch* form a large group of compounds, now numbering several thousand, that exhibit diverse structures and physical properties. For *M* = d-block metals, the potential interactions of f and d electrons lead to interesting electronic and magnetic behaviour.[1] For *M* = p-block metals, the motivation has usually been to search for candidates with desirable optical properties related to localized f-f transitions from the *RE* atoms (useful for luminescent materials)[2] or to narrow band gaps (useful for photovoltaic materials).[3]

Within the *RE*–(Ga,In)–(S,Se) systems, the most commonly occurring phases have the compositions $RE_3M_{1.67}Ch_7$, RE_3MCh_6, $RE_4M_5Ch_{13}$, and $RE_3M_5Ch_{12}$, the vast majority (about 75%) of them being sulfides.[4] Among these, the RE_3MCh_6 series have been investigated since 50 years ago, but surprisingly there remain unresolved ambiguities about their existence and structures (**Table 2-1**). The Ga-containing sulfides RE_3GaS_6 are known for smaller *RE* atoms (Dy, Ho, Er, Y),[5–8] whereas the corresponding selenides RE_3GaSe_6 are unknown. The In-containing sulfides RE_3InS_6 are known for nearly the entire breadth of *RE*,[9–15] but the corresponding selenides RE_3InSe_6 have been reported for only a few larger *RE* atoms (Pr, Sm, Gd).[16–19] The

noncentrosymmetric structure of RE_3GaS_6 (Er_3GaS_6-type, space group $Cmc2_1$) has led to the evaluation of the infrared nonlinear optical properties of the Dy- and Y-containing members, which show high laser induced damage thresholds.[8] The compounds RE_3InS_6 adopt a noncentrosymmetric structure (La_3InS_6-type, space group $P2_12_12$) for *RE* = La–Nd, but a centrosymmetric structure (U_3ScS_6-type, originally called Sm_3InS_6-type, space group *Pnnm*) for *RE* = Sm, Gd, Tb; in most reports, only powder X-ray diffraction was performed and the structural assignment was often simply assumed without verification.[9–15] These two series of structures for RE_3InS_6 are closely related to each other, differing mainly in the occurrence of both tetrahedral and octahedral In sites in the La_3InS_6-type compounds, but only octahedral In sites in the U_3ScS_6-type compounds. The centrosymmetric U_3ScS_6-type structure has been confirmed by single-crystal X-ray diffraction studies on RE_3InSe_6 (*RE* = Pr, Sm, Gd), but a hint that something was unusual in the structure of Pr_3InSe_6 is an elevated displacement parameter in one of the In sites.[16–18]

Table 2-1. Formation of ternary chalcogenides RE_3MCh_6.

compound	La	Ce	Pr	Nd	Sm	Gd	Tb	Dy	Ho	Er	Tm	Yb	Lu	Y	Sc
RE_3GaS_6								a	a	a				a	
RE_3InS_6	b	b	b	b	b,c	b,c	b,c	b	b	b	b	b	b	b	b
RE_3GaSe_6															
RE_3InSe_6			c		c	c									

a. Er_3GaS_6-type ($Cmc2_1$).[5–8]

b. La_3InS_6-type ($P2_12_12$).[9–13]

c. U_3ScS_6-type (*Pnnm*).[14–19]

As part of ongoing studies to systematize the structures of ternary rare-earth chalcogenides, we present here an investigation of the RE_3InSe_6 series, with the aims to determine the extent of *RE* substitution and to clarify the relationship between the noncentrosymmetric La_3InS_6-type and centrosymmetric U_3ScS_6-type structures. Optical band gaps were measured for all members of RE_3InSe_6 prepared here, and magnetic measurements were made on two selected members.

2.2. Experimental

2.2.1. Synthesis

Freshly filed *RE* metal pieces (99.9%, Hefa), In powder (99.9%, Alfa-Aesar), and Se powder (99.99%, Sigma-Aldrich) were combined in a 3:1:6 molar ratio on a 300-mg scale, with a 5% weight excess of Se added. The mixtures were cold-pressed into pellets and placed into fused-silica tubes (12-mm diameter, 15-cm length), which were evacuated and sealed. The tubes were placed in a furnace where they were slowly heated to 850 °C in 48 h; the slow heating was a precaution to minimize risks of catastrophic failure of the tubes caused by rapid volatilization of selenium. The tubes were then held at 850 °C for 96 h, slowly cooled to 600 °C in 96 h, and then cooled to room temperature by shutting off the furnace. Powder X-ray diffraction (XRD) patterns of the samples were collected on a Bruker D8 Advance diffractometer equipped with a Cu $K\alpha_1$ radiation source operated at 40 kV and 40 mA. The desired compounds RE_3InSe_6 were found to form for *RE* = La–Nd, Sm, Gd, Tb (**Figure A2-1**). The XRD patterns were analyzed using the TOPAS-Academic software package,[20] with the background modeled by a ten-term polynomial function and the profile fitted by the Pawley method. Refined cell parameters are listed in **Table 2-2**, which includes data for some previously known members for comparison. These compounds are stable under ambient conditions, as confirmed by the absence of changes when the powder

XRD patterns were recollected after a few months. Attempts were made to prepare compounds containing other *RE* (specifically, Eu, Dy, Ho, Er, Tm, Yb, Lu) under the same synthetic conditions as described above, but these led to mixtures of other phases.

Crystals of La_3InSe_6, Ce_3InSe_6, and Nd_3InSe_6 were obtained in the presence of KBr flux (150 mg) added to the mixture of elements and treated as before. After the flux was removed by washing with methanol, black needle-shaped crystals were extracted and examined on a JEOL JSM-6010LA scanning electron microscope operated with an accelerating voltage of 15 kV (**Figure A2-2**). Energy-dispersive X-ray (EDX) analysis was performed on several points on these crystals with acquisition times of 60 s each. The observed compositions of these crystals (31(2)% La, 9(1)% In, 59(2)% Se for La_3InSe_6; 31(2)% Ce, 9(1)% In, 60(2)% for Ce_3InSe_6; 35(2)% Nd, 9(1)% In, 56(2)% Se for Nd_3InSe_6) were in good agreement with the expected composition of 30% *RE*, 10% In, and 60% Se.

Table 2-2. Cell parameters for RE_3InSe_6 (*RE* = La, Ce, Nd).[a]

compound	*a* (Å)	*b* (Å)	*c* (Å)	*V* (Å^3)	Reference
La_3InSe_6	14.3867(5)	17.5502(7)	4.1637(2)	1051.3(1)	This work
Ce_3InSe_6	14.3890(4)	17.5461(5)	4.1628(2)	1051.0(1)	This work
Pr_3InSe_6	14.3204(2)	17.4603(2)	4.1180(1)	1029.7(1)	This work
Pr_3InSe_6	14.275(1)	17.413(2)	4.109(1)	1021.4(1)	17
Nd_3InSe_6	14.2760(2)	17.4325(3)	4.0998(1)	1020.3(1)	This work
Sm_3InSe_6	14.1764(7)	17.3442(9)	4.0566(2)	997.4(1)	This work
Sm_3InSe_6	14.177(3)	17.352(4)	4.0625(8)	999.4(3)	18
Gd_3InSe_6	14.0924(4)	17.3041(5)	4.0248(1)	981.5(1)	This work
Gd_3InSe_6	14.071(3)	17.286(4)	4.0202(8)	977.9(3)	18
Tb_3InSe_6	14.043(1)	17.265(1)	4.0043(3)	970.8(1)	This work

[a] Cell parameters were refined from powder XRD data for compounds reported here, and from single-crystal data for compounds reported previously.

2.2.2. Structure determination

Intensity data were collected for RE_3InSe_6 (*RE* = La, Ce, Nd) at room temperature on a Bruker PLATFORM diffractometer equipped with a SMART APEX II CCD area detector and a graphite-monochromated Mo *K*α radiation source, using ω scans at 7–8 different ϕ angles with a frame width of 0.3° and an exposure time of 10–15 s per frame. Face-indexed numerical absorption corrections were applied. Structure solution and refinement were carried out with use of the SHELXTL (version 2018/3) program package.[21]

On the basis of Laue symmetry *mmm*, intensity statistics (mean $|E^2-1|$ = 0.98–1.02), and systematic absences indicating the presence of *n*-glide planes perpendicular to the *a* and *b* axes,

the centrosymmetric orthorhombic space group *Pnnm* was chosen for all three compounds. The structural models consisted of three *RE*, two In, and six Se sites, whose initial positions were determined by direct methods. For La_3InSe_6 and Ce_3InSe_6, one set of In atoms is located in Wyckoff position 4*e* (0, 0, *z*), where *z* is between 0.1 and 0.2, so that pairs of symmetry-equivalent sites related by a mirror plane are spaced at an unphysically short distance of about 1 Å apart. When refined, the occupancy of this 4*e* site (labeled In1) converged to 0.49(1) in both compounds. In subsequent refinements, this occupancy was fixed to be exactly 0.5. For Nd_3InSe_6, no splitting occurs and the corresponding site is located in Wyckoff position 2*a* (0, 0, 0). All other sites in the structures were confirmed to be fully occupied, with no unusual displacement parameters.

Subsequent refinements, including anisotropic displacement parameters, were based on atomic positions standardized with the program STRUCTURE TIDY[22] and proceeded without complications.**Table 2-3** lists crystal data, **Table 2-4** lists atomic and displacement parameters, and **Table 2-5** lists interatomic distances. CCDC 2054811–2054813 contain the supplementary crystallographic data for this paper. These data can be obtained free of charge from the Cambridge Crystallographic Data Centre via http://www.ccdc.cam.ac.uk/structures.

Table 2-3. Crystallographic data for RE_3InSe_6 (*RE* = La, Ce, Nd).

formula	La_3InSe_6	Ce_3InSe_6	Nd_3InSe_6
formula mass (amu)	1005.31	1008.94	1021.30
space group	*Pnnm* (No. 58)	*Pnnm* (No. 58)	*Pnnm* (No. 58)
a (Å)	14.4722(18)	14.3892(15)	14.2793(11)
b (Å)	17.636(2)	17.5331(18)	17.4401(14)
c (Å)	4.2123(5)	4.1616(4)	4.1013(3)
V (Å^3)	1075.1(2)	1049.9(2)	1021.36(14)
Z	4	4	4
T (K)	296(2)	296(2)	296(2)
ρ_{calcd} (g cm^{-3})	6.211	6.383	6.642
crystal dimensions (mm)	0.08 × 0.04 × 0.03	0.06 × 0.04 × 0.04	0.08 × 0.04 × 0.03
μ(Mo $K\alpha$) (mm^{-1})	34.04	35.66	38.53
transmission factors	0.172–0.391	0.224–0.485	0.143–0.512
2θ limits	3.64–57.53°	3.66–65.34°	3.69–66.76°
data collected	$-19 \le h \le 19$, $-23 \le k \le 23$, $-5 \le l \le 5$	$-21 \le h \le 21$, $-26 \le k \le 26$, $-6 \le l \le 6$	$-21 \le h \le 21$, $-26 \le k \le 26$, $-6 \le l \le 6$
no. of data collected	10692	14785	14818
no. of unique data, including $F_o^2 < 0$	1582 (R_{int} = 0.073)	2163 (R_{int} = 0.140)	2210 (R_{int} = 0.119)
no. of unique data, with $F_o^2 > 2\sigma(F_o^2)$	1258	1430	1491
no. of variables	65	65	64
$R(F)$ for $F_o^2 > 2\sigma(F_o^2)$ [a]	0.036	0.055	0.054
$R_w(F_o^2)$ [b]	0.088	0.146	0.148
goodness of fit	1.14	1.10	1.08
$(\Delta\rho)_{max}$, $(\Delta\rho)_{min}$ (e Å^{-3})	1.92, –2.18	4.00, –3.32	5.57, –4.45

[a] $R(F) = \sum||F_o| - |F_c|| / \sum|F_o|$. [b] $R_w(F_o^2) = [\sum[w(F_o^2 - F_c^2)^2] / \sum wF_o^4]^{1/2}$; $w^{-1} = [\sigma^2(F_o^2) + (Ap)^2 + Bp]$, where $p = [\max(F_o^2,0) + 2F_c^2] / 3$.

Table 2-4. Atomic coordinates and equivalent isotropic displacement parameters (Å^2) [a] for RE_3InSe_6 (*RE* = La, Ce, Nd).

Atom	Wyckoff position	*x*	*y*	*z*	U_{eq} (Å^2) [a]
La_3InSe_6					
La1	4*g*	0.31063(5)	0.14319(4)	0	0.0145(2)
La2	4*g*	0.53810(5)	0.27942(4)	0	0.0140(2)
La3	4*g*	0.74889(5)	0.10772(4)	0	0.0158(2)
In1 [b]	4*e*	0	0	0.1553(5)	0.0273(4)
In2	2*c*	0	1/2	0	0.0192(3)
Se1	4*g*	0.10815(8)	0.10709(7)	0	0.0163(3)
Se2	4*g*	0.11295(8)	0.74582(7)	0	0.0152(3)
Se3	4*g*	0.17799(8)	0.28264(7)	0	0.0148(3)
Se4	4*g*	0.18735(8)	0.51741(7)	0	0.0149(3)
Se5	4*g*	0.39943(9)	0.41240(8)	0	0.0187(3)
Se6	4*g*	0.52159(8)	0.10197(7)	0	0.0151(3)
Ce_3InSe_6					
Ce1	4*g*	0.31167(7)	0.14424(5)	0	0.0163(2)
Ce2	4*g*	0.53953(7)	0.27858(5)	0	0.0159(2)
Ce3	4*g*	0.75057(7)	0.10678(5)	0	0.0178(2)
In1 [b]	4*e*	0	0	0.1038(8)	0.0385(10)
In2	2*c*	0	1/2	0	0.0206(4)
Se1	4*g*	0.11031(12)	0.10982(10)	0	0.0180(4)
Se2	4*g*	0.11181(12)	0.74711(10)	0	0.0168(3)
Se3	4*g*	0.17967(12)	0.28357(9)	0	0.0158(3)
Se4	4*g*	0.18880(12)	0.51821(10)	0	0.0165(3)
Se5	4*g*	0.40239(13)	0.41371(10)	0	0.0197(4)
Se6	4*g*	0.52216(12)	0.10258(9)	0	0.0171(3)
Nd_3InSe_6					
Nd1	4*g*	0.31284(6)	0.14515(5)	0	0.0151(2)
Nd2	4*g*	0.54094(6)	0.27754(5)	0	0.0148(2)
Nd3	4*g*	0.75157(6)	0.10579(5)	0	0.0168(2)
In1	2*a*	0	0	0	0.0369(5)
In2	2*c*	0	1/2	0	0.0190(3)
Se1	4*g*	0.11253(12)	0.11280(9)	0	0.0162(3)
Se2	4*g*	0.11127(11)	0.74799(9)	0	0.0150(3)
Se3	4*g*	0.18157(11)	0.28503(9)	0	0.0147(3)
Se4	4*g*	0.19023(11)	0.51939(9)	0	0.0159(3)
Se5	4*g*	0.40496(11)	0.41464(9)	0	0.0165(3)
Se6	4*g*	0.52251(11)	0.10342(9)	0	0.0160(3)

[a] U_{eq} is defined as one-third of the trace of the orthogonalized U_{ij} tensor.

[b] Occupancy of 0.5.

Table 2-5. Interatomic distances (Å) in RE_3InSe_6 (*RE* = La, Ce, Nd).

	La_3InSe_6	Ce_3InSe_6	Nd_3InSe_6
*RE*1–Se2 (×2)	2.9892(10)	2.9657(14)	2.9319(12)
*RE*1–Se1	2.9986(14)	2.960(2)	2.9154(19)
*RE*1–Se4 (×2)	3.0589(11)	3.0352(14)	3.0030(13)
*RE*1–Se3	3.1198(14)	3.0944(19)	3.0764(17)
*RE*1–Se6	3.1385(14)	3.116(2)	3.0812(18)
*RE*2–Se1 (×2)	3.0772(11)	3.0324(14)	2.9847(13)
*RE*2–Se5	3.0867(15)	3.083(2)	3.0802(18)
*RE*2–Se2 (×2)	3.0929(10)	3.0621(15)	3.0323(13)
*RE*2–Se3 (×2)	3.1196(10)	3.0958(14)	3.0705(13)
*RE*2–Se6	3.1386(14)	3.0959(19)	3.0480(17)
*RE*3–Se3 (×2)	3.0377(10)	3.0111(14)	2.9716(13)
*RE*3–Se5 (×2)	3.0510(11)	3.0383(15)	3.0214(14)
*RE*3–Se4 (×2)	3.1779(11)	3.1499(15)	3.1206(13)
*RE*3–Se2	3.2663(14)	3.238(2)	3.2155(17)
*RE*3–Se6	3.2910(15)	3.287(2)	3.2710(19)
In1–Se1 (×2)	2.5387(13)	2.5325(18)	2.5400(16)
In1–Se5 (×2)	2.5715(16)	2.642(3)	2.8747(11)
In1–Se5 (×2)	3.482(2)	3.252(2)	2.8747(11)
In2–Se4 (×2)	2.7287(12)	2.7353(17)	2.7373(16)
In2–Se6 (×4)	2.7870(8)	2.7689(11)	2.7499(10)

2.2.3. Electronic structure calculations

Tight-binding linear muffin-tin orbital (TB-LMTO) band structure calculations were performed on La_3InSe_6 within the local density and atomic-spheres approximation with the use of the Stuttgart TB-LMTO program.[23] The cell parameters and atomic positions were taken from the single-crystal structure determination, except that an ordered model was considered in which the half-occupied In1 site is shifted slightly from 4*e* (0, 0, ~0.1) to become a fully occupied site at 2*a* (0, 0, 0). The basis set consisted of La 6s/6p/5d/4f, In 5s/5p/5d/4f, and Se 4s/4p/4d orbitals, with the La 6p/4f, In 5d/4f, and Se 4d orbitals being downfolded. Integrations in reciprocal space were carried out with an improved tetrahedron method over 63 irreducible *k* points within the first Brillouin zone. Crystal orbital Hamilton populations (COHP) were evaluated to analyze bonding interactions.[24]

2.2.4. Physical measurements

Optical diffuse reflectance spectra for ground samples of RE_3InSe_6 (*RE* = La–Nd, Sm, Gd, Tb) were measured from 200 nm (6.2 eV) to 1400 nm (0.89 eV) on a Cary 5000 UV-vis-NIR spectrophotometer equipped with a diffuse reflectance accessory. An optical polytetrafluoroethylene disc with >98% reflectivity in the range of 250 to 2200 nm was used as a reflectance standard. The reflectance spectra were converted to optical absorption spectra using the Kubelka-Munk function, $F(R) = \alpha/S = (1–R)^2/2R$, where α is the Kubelka–Munk absorption coefficient, S is the scattering coefficient, and R is the reflectance.[25]

Zero-field-cooled dc magnetic susceptibility measurements were made on La_3InSe_6 and Nd_3InSe_6 between 2 and 300 K on a Quantum Design 9T–PPMS magnetometer. The applied

magnetic field was 3 T for La_3InSe_6 and 0.5 T for Nd_3InSe_6. Susceptibility values were corrected for contributions from the holder and sample diamagnetism.

2.3. Results and discussion

The ternary selenides RE_3InSe_6, which were previously reported for three members (*RE* = Pr, Sm, Gd),[16–19] have now been extended to include four new members (*RE* = La, Ce, Nd, Tb). They could not be prepared beyond Tb, under the synthetic conditions (reactions of the elements at 850 °C) used here. Previous phase diagram investigations of the pseudobinary systems RE_2Se_3–In_2Se_3 at a lower temperature of 600 °C have confirmed the existence of Pr_3InSe_6 (corresponding to a composition of 1.5 Pr_2Se_3–0.5 In_2Se_3) but not the La, Er, or Y members.[19] These results imply that La_3InSe_6 is a high-temperature phase and that the selenides RE_3InSe_6 are unlikely to form with smaller *RE* atoms at any temperature, in contrast to the sulfides RE_3InS_6 which are known for nearly all *RE* members.[9–15] The cell parameters of the RE_3InSe_6 samples prepared here were refined from powder XRD patterns. In accordance with the lanthanide contraction, the unit cell volume decreases upon substitution with smaller *RE* atoms on proceeding from La to Tb (**Figure 2-1**); the plateau at the La member suggests an upper limit for the volume.

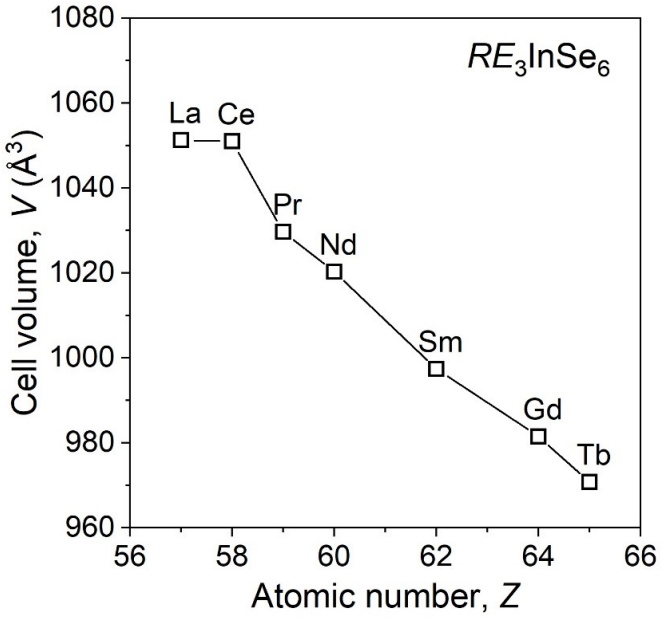

Figure 2-1. Plot of unit cell volume for RE_3InSe_6.

In the previous single-crystal structure determinations of RE_3InSe_6 (*RE* = Pr, Sm, Gd), an orthorhombic U_3ScS_6-type structure in space group *Pnnm* was established, containing two In sites at 2*a* (0, 0, 0) and 2*c* (0, 1/2, 0).[16–18] Single crystals of the La, Ce, and Nd members have now been prepared (through use of a KBr flux) and analyzed. Although Nd_3InSe_6 is isostructural to the previously known members, La_3InSe_6 and Ce_3InSe_6 feature a subtle difference. The general framework is the same, consisting of In-centred polyhedra arranged in linear stacks aligned along the *c*-direction and separated by the RE^{3+} cations as well as isolated Se^{2-} anions interacting through ionic bonds (**Figure 2-2**). One stack is constructed by sharing *trans* edges of octahedra centred by the In2 atoms at 2*c* (0, 1/2, 0), as in the previously determined structures. This motif is reminiscent of the chains of edge-sharing octahedra found in rutile. However, another stack consists of half-occupied In1 sites at 4*e* (0, 0, *z*), where *z* is about 0.1 to 0.2, in tetrahedral coordination. The occurrence of this set of split sites is incontrovertible: any attempts to refine structural models in

which the In atoms are placed in 2*a* (0, 0, 0) instead of 4*e* (0, 0, *z*) resulted in significant residual electron density adjacent to them. The splitting becomes less severe on proceeding from La_3InSe_6 to Ce_3InSe_6, and eventually the split sites at 4*e* merge into a single one at 2*a*, attaining octahedral coordination, on proceeding to Nd_3InSe_6 (**Figure 2-3a**). In retrospect, this trend could have been foreshadowed by the early structure determination of Pr_3InSe_6, in which the In1 site at 2*a* exhibits an anomalously large displacement parameter, 4.4 times greater than that of the In2 site at 2*c*.[16,17] This displacement parameter gradually decreases on proceeding from Nd_3InSe_6 to Gd_3InSe_6, although even here, the displacement ellipsoid is prolate-shaped and elongated along the *c*-direction.[18] The In–Se distances to the In1 site become increasingly more irregular on proceeding from La_3InSe_6 (2.54–2.57 Å within an $InSe_4$ tetrahedron) to Nd_3InSe_6 (2.54–2.87 Å within an $InSe_6$ octahedron). The In–Se distances to the In2 site within an octahedron are more regular, remaining relatively unchanged on proceeding from La_3InSe_6 (2.73–2.88 Å) to Nd_3InSe_6 (2.74–2.75 Å). These In–Se distances lie within the typical range of 2.4–2.9 Å found in other compounds.[4]

There are three *RE* sites, each surrounded by Se atoms in high coordination numbers. The *RE*1 site is centred within what could be described alternatively as a monocapped trigonal prism or a capped octahedron (CN7), whereas the *RE*2 and *RE*3 sites are situated within bicapped trigonal prisms (CN8) (**Figure 2-3(b)**). The *RE*–Se distances are normal; for example, the La–Se distances of 3.0–3.3 Å in La_3InSe_6 are within the typical range of 2.9–3.4 Å found in other compounds.[4]

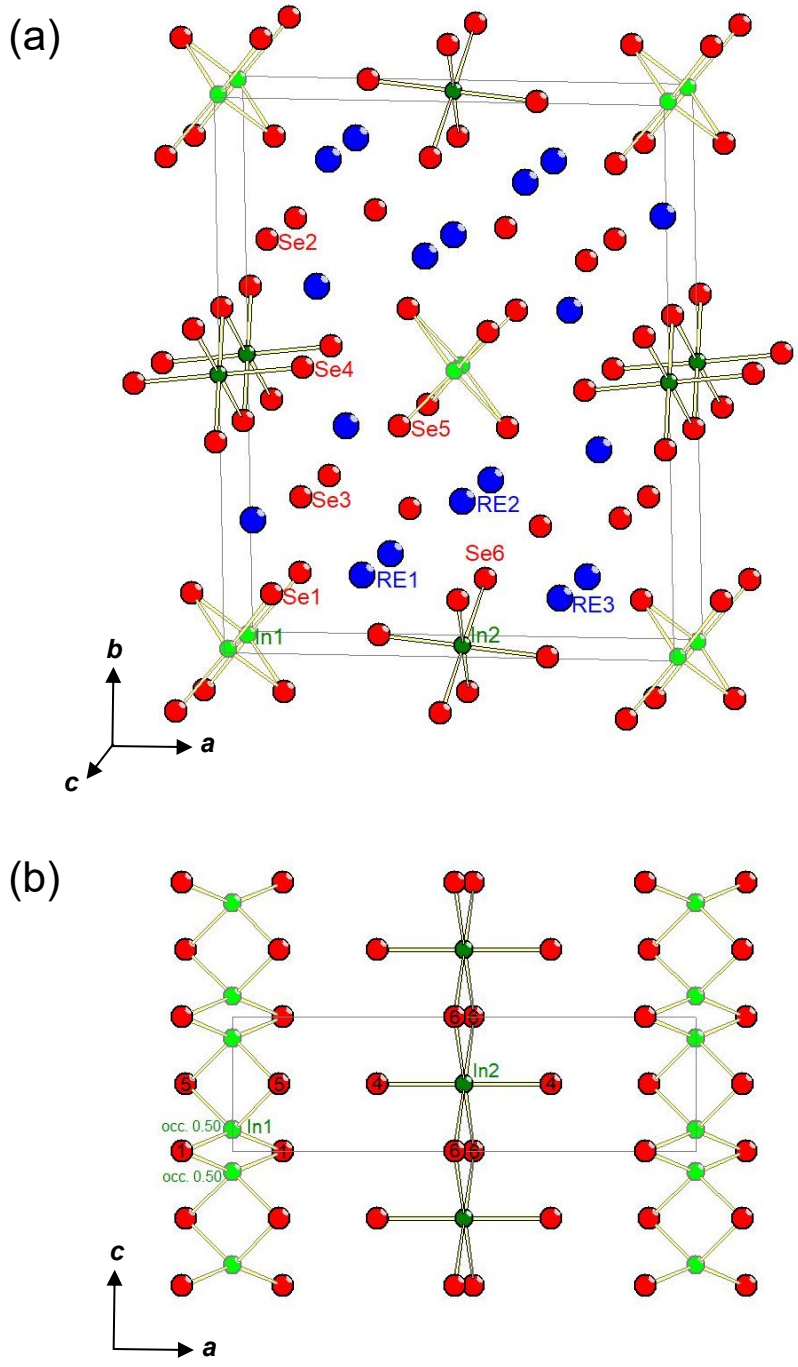

Figure 2-2. Structure of RE_3InSe_6 (*RE* = La, Ce) highlighting the connectivity of $InSe_4$ tetrahedra and $InSe_6$ octahedra. (a) Unit cell contents viewed down the *c*-direction. (b) Slice parallel to (010) plane, viewed down the *b*-direction.

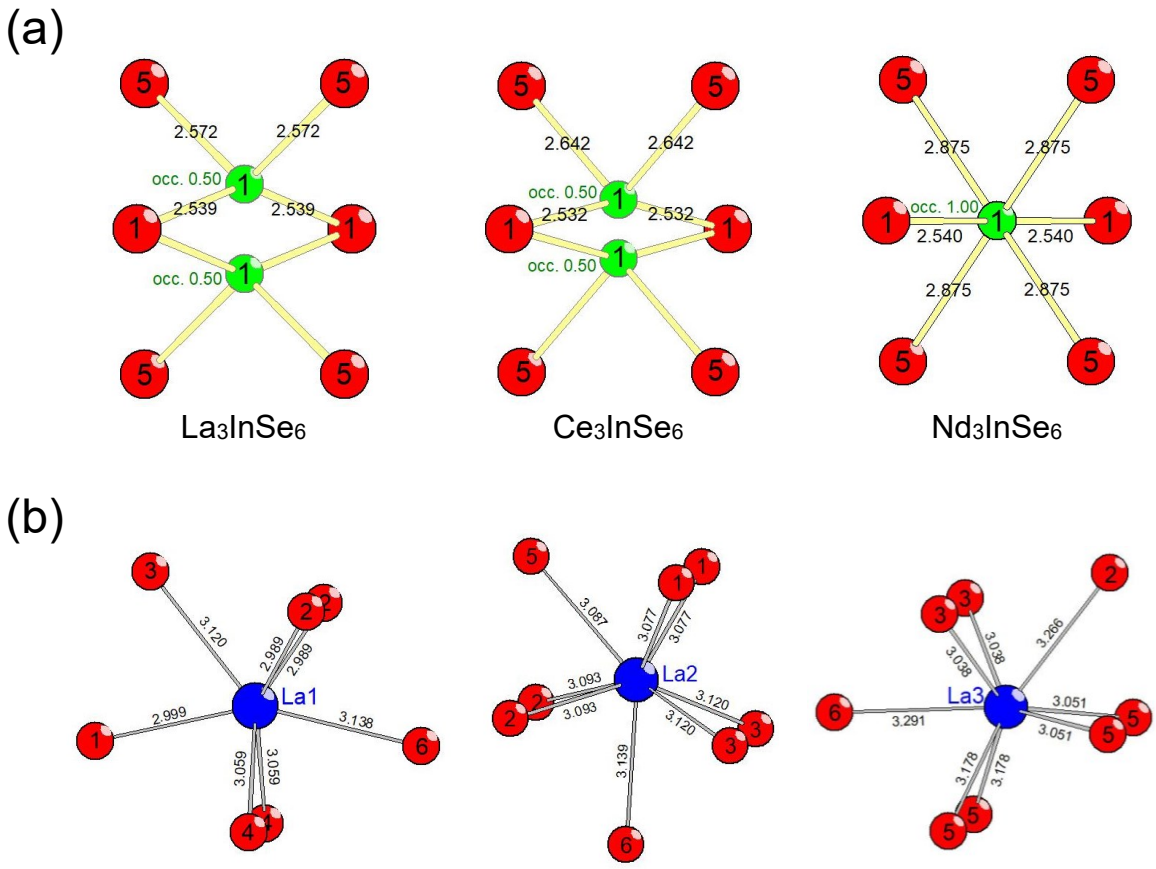

Figure 2-3. (a) Environment around In1 atoms, which reside in half-occupied split sites in La_3InSe_6 and Ce_3InSe_6, but merge into a fully occupied site in Nd_3InSe_6. (b) Coordination around La sites in La_3InSe_6. Distances are indicated in Å.

Given that the sulfides RE_3InS_6 have been reported to form both noncentrosymmetric (La_3InS_6-type, $P2_12_12$) and centrosymmetric structures (U_3ScS_6-type, *Pnnm*),[9–15] the latter corresponding to the one adopted by the selenides RE_3InSe_6 presented here, it is helpful to develop a unified picture of structural relationships. As was astutely noted by Guittard and co-workers, the La_3InS_6-type structure could be regarded as a small distortion of the U_3ScS_6-type structure in which one of the In atoms is displaced away from the centre of an octahedron towards one of the edges so that it becomes effectively four-coordinate.[10] However, what is remarkable is that the displacement is cooperative and always in the same direction, along a polar twofold rotation axis, resulting in isolated tetrahedra. The structure of La_3InSe_6 and Ce_3InSe_6 determined here

corresponds to the occurrence of disordered displacements in opposite directions, so that there is no loss of the mirror symmetry, on average, and the space group remains unchanged (**Figure 2-4**). This conclusion resolves the ambiguity about the structural assignment of RE_3InS_6 compounds, which have generally been assumed to adopt the noncentrosymmetric La_3InS_6-type structure even without verification from single-crystal diffraction experiments. Depending on the synthetic conditions and the quality of the crystal, it is conceivable that both ordered La_3InS_6-type or disordered U_3ScS_6-type structures (exhibiting partially occupied split In sites) are possible. We did attempt to refine the structure of La_3InSe_6 in space group $P2_12_12$ with twinning invoked; however, the split sites still remained. This result suggests that the In disorder occurs at a length scale smaller than typical twin domains, or that pairs of edge-sharing $InSe_4$ tetrahedra may be present.

For RE_3InSe_6, the simple charge-balanced formulation $(RE^{3+})_3(In^{3+})(Se^{2-})_6$ agrees well with the bond valence sums (bvs) evaluated for all atoms,[26] with no deviations greater than 0.3 from expected values (**Table 2-6**), and is consistent with the absence of homoatomic bonds in the structure. Close inspection of the bvs provides further insight for the site preference of the In atoms. Although placing the In1 atom hypothetically within the unsplit octahedral site (2a) in La_3InSe_6 would allow it to become less overbonded (bvs of 3.08), this would be at the expense of causing overbonding in the adjacent Se1 atoms (bvs of 2.35) and underbonding in the Se5 atoms (bvs of 1.74). Furthermore, on progressing from La_3InSe_6 to Nd_3InSe_6, there are opposing trends of increasing deviations in the bvs of the *RE* atoms while the bvs of the In atoms approach the ideal value of 3.0. This observation suggests that the range of permissible *RE* substituents in the RE_3InSe_6 series represents a balance of optimum *RE*–Se and In–Se bonding.

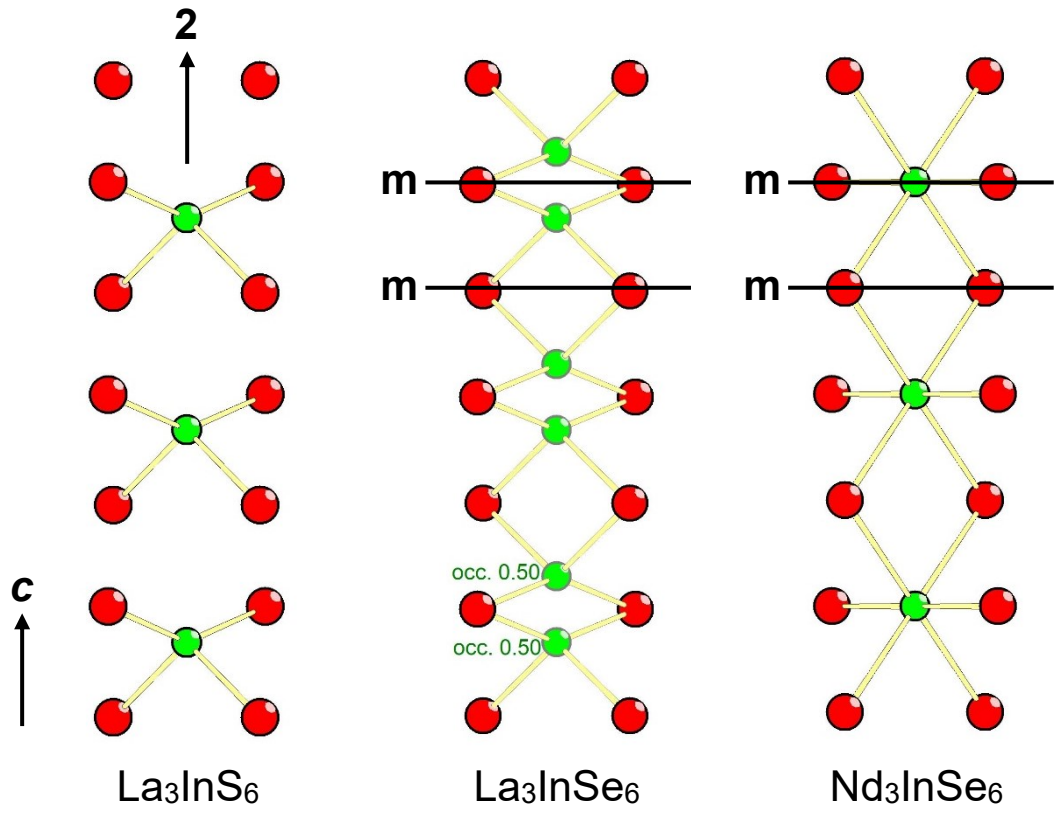

Figure 2-4. Comparison of In-centred tetrahedra or octahedra arranged in linear stacks aligned along the *c*-direction in La_3InS_6, La_3InSe_6, and Nd_3InSe_6. Symmetry elements (twofold rotation axis and mirror planes) are indicated.

Table 2-6. Bond valence sums in RE_3InSe_6 (*RE* = La, Ce, Nd).

	La_3InSe_6	Ce_3InSe_6	Nd_3InSe_6
*RE*1	3.06	3.28	3.32
*RE*2	3.02	3.29	3.31
*RE*3	2.84	3.00	2.98
In1	3.31	3.19	3.00
In2	2.69	2.76	2.85
Se1	2.13	2.30	2.35
Se2	2.03	2.18	2.19
Se3	1.97	2.11	2.11
Se4	1.95	2.05	2.05
Se5	2.08	2.04	1.90
Se6	1.76	1.86	1.93

For La_3InSe_6, the charge-balanced formulation indicated above implies closed-shell electron configurations for all atoms. Electronic structure calculations were performed using the LMTO method on an ordered model of La_3InSe_6 (**Figure 2-5**). As expected, the density of states (DOS) curve shows a band gap. This gap is direct and occurs at the Brillouin zone centre, as indicated by the band dispersion diagram (**Figure A2-3**). (A calculation was also performed using the VASP method, giving similar results, not shown here, that confirm essentially a direct band gap of about 0.85 eV.) Filled In- and Se-based states dominate the valence band, which extends from −5.3 eV to the Fermi level, whereas empty La-based states are found mostly in the conduction band. As evaluated by the crystal orbital Hamilton population (−COHP) curves, both La−Se and In−Se bonding is optimized, with all bonding levels filled up to the Fermi level (**Figure 2-5**).

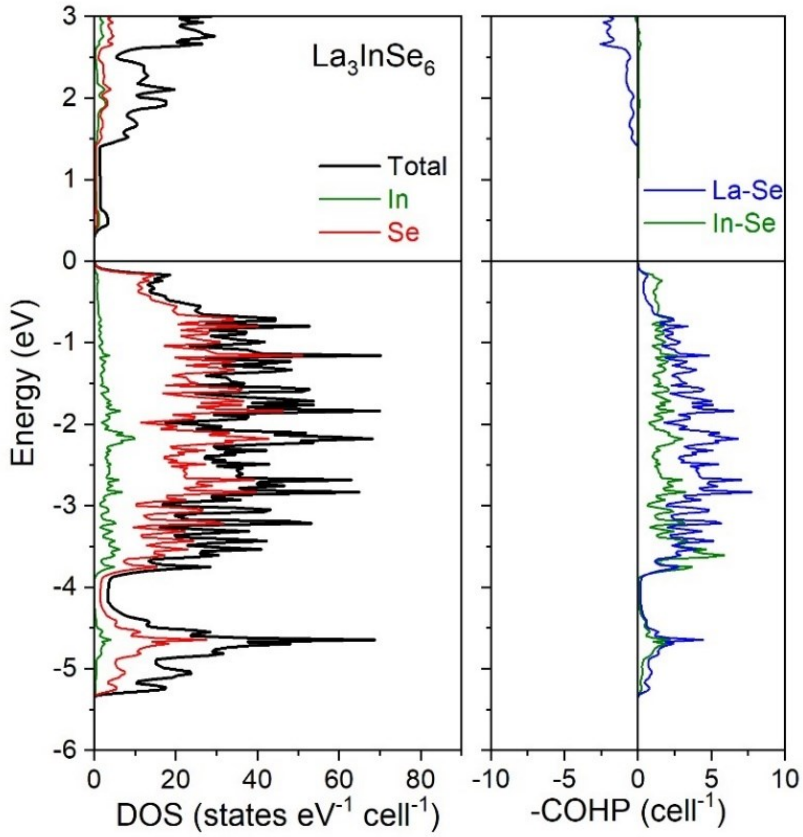

Figure 2-5. Density of states (DOS) and crystal orbital Hamilton population (−COHP) curves for La_3InSe_6.

UV-vis-NIR diffuse reflectance spectra were measured for all RE_3InSe_6 compounds and converted into optical absorption spectra (shown for La_3InSe_6 in **Figure 2-6**, and for all other compounds in **Figure A2-4**). The optical band gaps, as extracted from the absorption edges, are relatively constant at 1.2−1.4 eV for the entire series. These values are consistent with the black colour observed for single crystals of these compounds, and they are similar to the 0.9−1.4 eV band gaps reported for $REInSe_3$.[27] (Without appropriate corrections applied, computed band gaps obtained from routine DFT calculations, such as described for La_3InSe_6 above, are typically underestimated and cannot be considered to be reliable.[28])

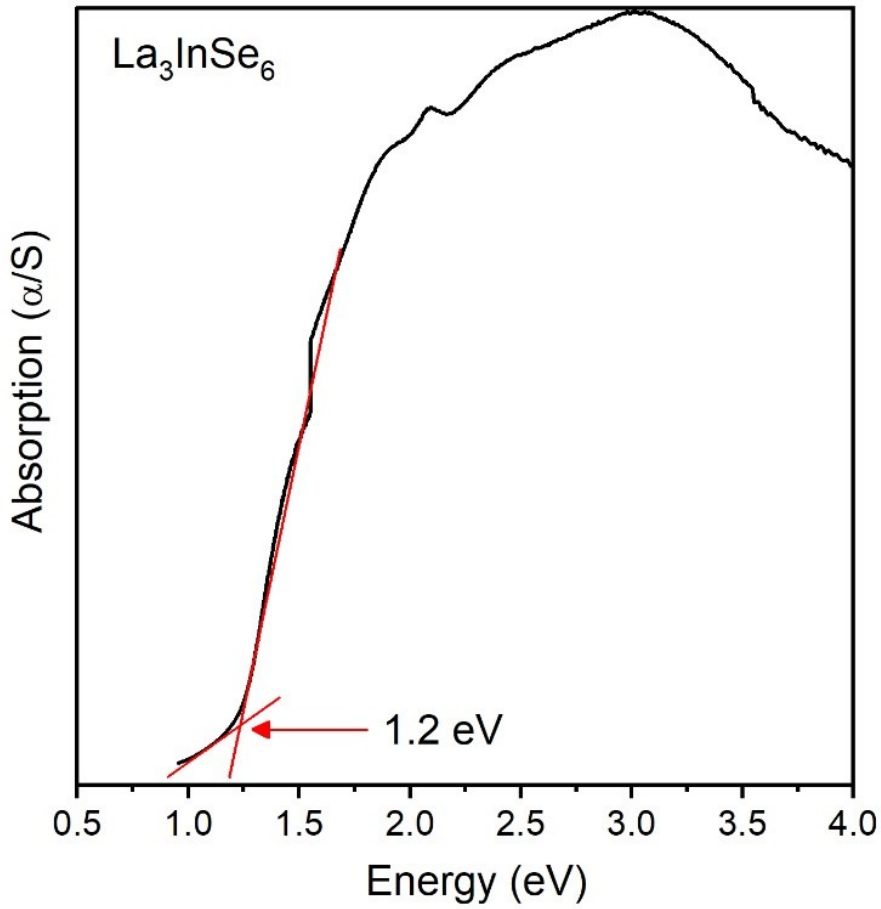

Figure 2-6. Optical absorption spectrum for La_3InSe_6.

Magnetic measurements were made on La_3InSe_6 and Nd_3InSe_6. Weak temperature-independent paramagnetism (on the order of 10^{-5} emu/mol) was observed for La_3InSe_6, but a Curie tail that appears at low temperatures suggests that the positive magnetic susceptibility is likely a result of magnetic impurities (**Figure A2-5**). For Nd_3InSe_6, no magnetic ordering transitions were observed down to 2 K, and the linear portion of the inverse magnetic susceptibility (above 20 K) was fit to the Curie-Weiss law, $\chi = C / (T - \theta_p)$ (**Figure 2-7**). The effective magnetic moment evaluated from the Curie constant, $\mu_{eff} = (8C)^{1/2}$, is 6.70(2) μ_B per formula unit. Given that Nd

atoms are the only source of unpaired electrons, the magnetic moment, evaluated from $\mu_{eff} = (3\mu_{RE}^2)^{1/2}$, was found to be 3.87(1) μ_B per Nd atom, in good agreement with the free-ion value of 3.62 μ_B expected for Nd^{3+} species (with an electron configuration of $4f^3$). The paramagnetic Weiss constant was −19(1) K, indicating weak antiferromagnetic coupling of the Nd atoms, which are 4 Å apart.

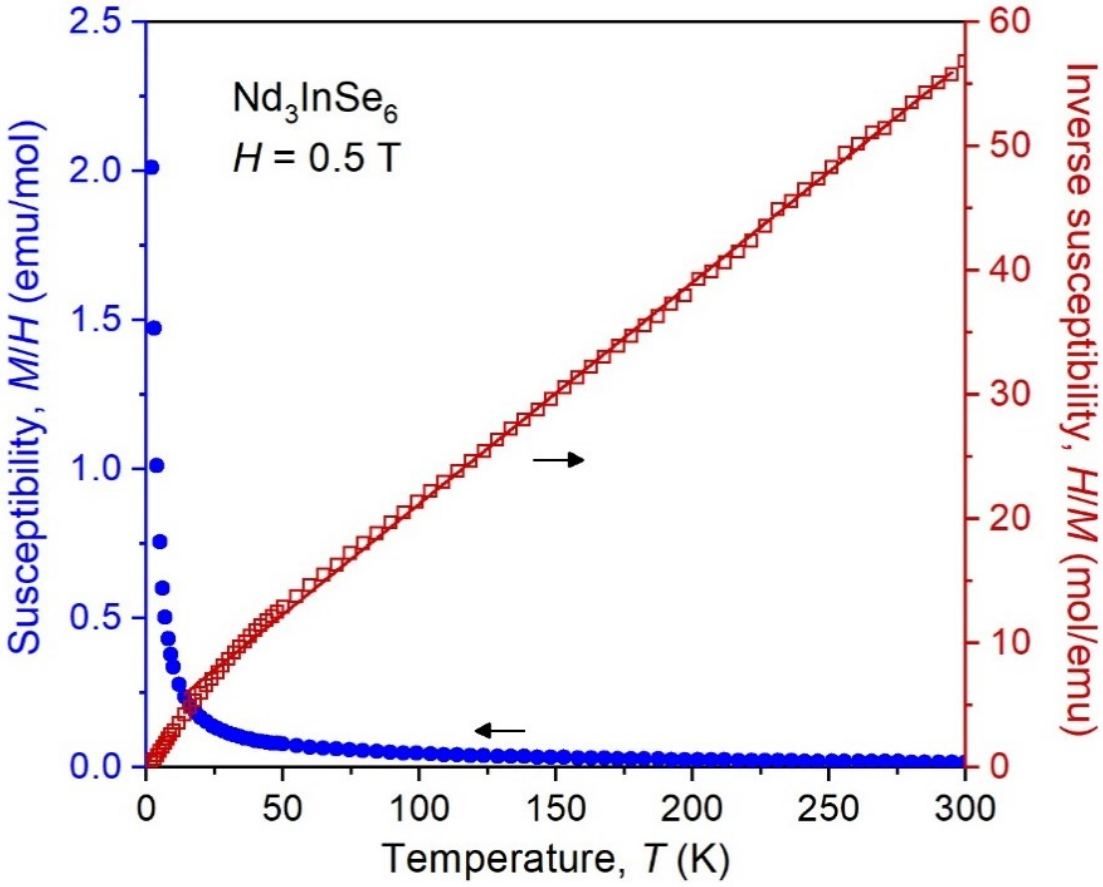

Figure 2-7. Magnetic susceptibility and its inverse for Nd_3InSe_6.

2.4. Conclusions

The preparation and characterization of all possible members in RE_3InSe_6 clarifies the structural trends that were not previously apparent in these selenides and the related sulfides RE_3InS_6. In particular, the noncentrosymmetric La_3InS_6-type ($P2_12_12$) and centrosymmetric U_3ScS_6-type structures (*Pnnm*) form a continuum in which one of the In atoms can be gradually displaced between tetrahedral and octahedral sites. The displacement can be ordered, as manifested in identically oriented tetrahedra in the La_3InS_6-type structure, or disordered, as manifested in split tetrahedral sites that are half-occupied in the U_3ScS_6-type structure. Because powder XRD patterns are not easily capable of discerning which of these features occurs, it would be worthwhile to reexamine other members of the sulfides RE_3InS_6 more carefully by single-crystal X-ray diffraction. All members of RE_3InSe_6 exhibit band gaps in the range of 1.2−1.4 eV, which matches closely with the optimal band gap to attain maximum efficiency in single-junction solar cells, and electronic structure calculations suggest that the band gap in La_3InSe_6 is a direct one. It would thus be worthwhile to evaluate these selenides, particularly La_3InSe_6, as potential candidates for photovoltaic materials.

2.5. References

(1) Mitchell, K.; Ibers, J. A. *Chem. Rev.* **2002**, *102*, 1929–1952.

(2) Alemi, A.; Klein, A.; Meyer, G.; Dolatyari, M.; Babalou, A. *Z. Anorg. Allg. Chem.* **2011**, *637*, 87–93.

(3) Chi, Y.; Guo, S.-P.; Xue, H.-G. *RSC Adv.* **2017**, *7*, 5039–5045.

(4) Villars, P.; Cenzual, K. *Pearson's Crystal Data – Crystal Structure Database for Inorganic Compounds,* Release 2019/20, ASM International, Materials Park, OH, USA.

(5) Lozac'h, A. M.; Jaulmes, S.; Guittard, M. *C. R. Seances Acad. Sci., Ser. C* **1971**, *272*, 1123–1126.

(6) Jaulmes, S.; Laruelle, P. *Acta Crystallogr. Sect. B Struct. Crystallogr. Cryst. Chem.* **1973**, *29*, 352–354.

(7) Loireau-Lozac'h, A. M.; Guittard, M.; Flahaut, J. *Mater. Res. Bull.* **1977**, *12*, 881–886.

(8) Zhang, M.-J.; Li, B.-X.; Liu, B.-W.; Fan, Y.-H.; Li, X.-G.; Zeng, H.-Y.; Guo, G.-C. *Dalton Trans.* **2013**, *42*, 14223–14229.

(9) Carré, D.; Guittard, M.; Adolphe, C. *Acta Crystallogr. Sect. B Struct. Crystallogr. Cryst. Chem.* **1978**, *34*, 3499–3501.

(10) Guittard, M.; Carré, D.; Kabré, T. S. *Mater. Res. Bull.* **1978**, *13*, 279–286.

(11) Aliev, O. M. *Izv. Akad. Nauk. SSSR – Neorg. Mater.* **1980**, *16*, 1514–1518.

(12) Akhmedova, D. A.; Agaev, A. B.; Rustamov, P. G. *Zh. Neorg. Khim.* **1992**, *37*, 461–464.

(13) Ivashchenko, I. A.; Kozak, V. S.; Olekseyuk, I. D.; Daszkiewicz, M.; Halyan, V. V.; Tishchenko, P. V.; Shemet, V. Y.; Gulay, L. D. *J. Solid State Chem.* **2020**, *288*, 121339.

(14) Messain, D.; Carré, D.; Laruelle, P. *Acta Crystallogr. Sect. B Struct. Crystallogr. Cryst. Chem.* **1977**, *33*, 2540–2542.

(15) Gulay, L. D.; Daszkiewicz, M.; Huch, M. R. *J. Solid State Chem.* **2008**, *181*, 2626–2632.

(16) Aleandri, L. E.; Ibers, J. A. *J. Solid State Chem.* **1989**, *79*, 107–111.

(17) Aleandri, L. E.; Ibers, J. A. *J. Solid State Chem.* **1989**, *81*, 317.

(18) Tougait, O.; Ibers, J. A. *Inorg. Chem.* **2000**, *39*, 1790–1794.

(19) Huch, M. R.; Gulay, L. D.; Olekseyuk, I. D. *J. Alloys Compd.* **2007**, *439*, 156–161.

(20) Coelho, A. A. *TOPAS–Academic, Version 6*, Coelho Software, Brisbane, Australia, 2007.

(21) Sheldrick, G. M. *Acta Crystallogr. Sect. A: Found. Crystallogr.* **2008**, *64*, 112–122.

(22) Gelato, L. M.; Parthé, E. *J. Appl. Crystallogr.* **1987**, *20*, 139–143.

(23) Tank, R.; Jepsen, O.; Burkhardt, A.; Andersen, O. K. *TB-LMTO-ASA Program, Version 4.7*, Max-Planck-Institut für Festkörperforschung: Stuttgart, Germany, 1998.

(24) Dronskowski, R.; Bloechl, P. E. *J. Phys. Chem.* **1993**, *97*, 8617–8624.

(25) Kortüm, G. *Reflectance Spectroscopy*; Springer, New York, 1969.

(26) Brese, N. E.; O'Keeffe, M. *Acta Crystallogr. Sect. B Struct. Sci.* **1991**, *47*, 192–197.

(27) Fedorchenko, V. P.; Lashkarev, G. V. *Izv. Akad. Nauk. SSSR – Neorg. Mater.* **1974**, *10*, 1177–1183.

(28) Mori-Sánchez, P.; Cohen, A. J.; Yang, W. *Phys. Rev. Lett.* **2008**, *100*, 146401.

Chapter 3.

Semiconducting Sm_3GaSe_5O with trigonal bipyramidal $GaSe_5$ units

A version of this chapter has been published.

Mishra, V.; Mumbaraddi, D.; Iyer, A. K.; Yin, W.; Mar, A. J. Solid State Chem. ***2022****, 308, 122901.*

3.1. Introduction

Inorganic solids consisting of more than one type of anion, termed mixed-anion compounds, offer new opportunities for expanding structural diversity and varying physical properties.[1,2] Given the long-held dominance of oxides in solid state chemistry, it is not surprising that many of these mixed-anion compounds have been investigated in conjunction with oxide anions. Perhaps the most well known of these are various layered rare-earth oxypnictides and oxychalcogenides.[3–7] Other combinations of anions, such as chalcogenide halides, are also possible.[8]

Although descriptions of crystal structures typically focus on the connectivity of coordination polyhedra centred by cations, changing the perspective to anions can lead to new insight. Krivovichev and co-workers have drawn attention to anion-centred tetrahedra, which can be used to build up structures in a complementary way to cation-centred polyhedra, and also serve as robust units that influence bonding interactions, with implications for geochemical transport of certain metals.[9] In this way, many oxypnictides and oxychalcogenides can be viewed in terms of separate blocks or slabs: one that typically contains O-centred tetrahedra exhibiting more ionic bonding character, and one that contains the *Pn* or *Ch* anions exhibiting more covalent bonding

character. Assertions are then often made in the literature that physical properties, such as band gaps, can be "tuned" or controlled in a rational fashion by taking appropriate combinations of the more insulating O-containing blocks and the more semiconducting *Pn*- or *Ch*-containing blocks.

Quaternary rare-earth oxychalcogenides *RE*–*M*–*Ch*–O in which *M* is a d- or p-block metal or metalloid include attractive candidates for transparent semiconductors (LaCuSO),[10] ionic conductors (LaAgSO),[11] thermoelectrics and superconductors (LaBiCh_2O),[12,13] and photocatalysts ($Sm_2Ti_2S_2O_5$, $LaInS_2O$).[14,15] These compounds remain relatively few. If *M* is restricted to the group-13 metals Ga and In, the previously reported representatives are *REMCh*$_2$O (*M* = Ga, In; *Ch* = S, Se),[16–20] $RE_4Ga_2Ch_5O_4$ (*Ch* = S, Se),[18,21,22] $RE_4Ga_{1.33}S_4O_4$,[18] $La_{3.33}Ga_6S_{12}O_2$,[23] La_3GaS_5O,[24] $La_5In_3S_9O_3$,[20] and $La_{10}In_6S_{17}O_6$.[25] Most of these compounds are oxysulfides, and where *RE* substitution was investigated, these were generally limited to the early members (La–Nd).

A reasonable hypothesis is that new oxychalcogenides could be derived from parent chalcogenides in which O atoms substitute for *Ch* atoms within crystallographically inequivalent sites. Various RE_3MCh_6 (*M* = Ga, In; *Ch* = S, Se) compounds are known which could serve as such a platform.[26] In the course of these investigations, the new oxyselenide Sm_3GaSe_5O was identified. We report its rational preparation and describe its crystal structure in terms of cation- and anion-centred units. The optical band gap of this compound was measured and compared with predictions from electronic structure calculations.

3.2. Experimental

3.2.1. Synthesis

Freshly filed *RE* metal pieces (99.9%, Hefa), Ga chunks (99.9%, Alfa-Aesar), Se powder (99.99%, Sigma-Aldrich), and RE_2O_3 powder (99.99%, Alfa-Aesar) were used as obtained.

Ga_2Se_3 was prepared from a stoichiometric reaction of elemental Ga and Se, placed within evacuated and sealed fused-silica tubes, at 950 °C.

The oxyselenide Sm_3GaSe_5O was first identified in attempts to prepare hypothetical solid solutions $RE_3MCh_{6-x}O_x$ (M = Ga, In; Ch = S, Se). Subsequently, in optimized syntheses, Sm_3GaSe_5O was prepared from mixtures of Sm_2O_3, Sm, Ga_2Se_3, and Se in a molar ratio of 2:14:3:21, with a total mass of 300 mg. To compensate for slight volatilization losses of the chalcogen, a 5% weight excess of Se was added. The mixtures were cold-pressed into pellets and placed into fused-silica tubes (9-mm diameter, 15-cm length), which were evacuated and sealed. The tubes were placed in a furnace where they were heated to 950 °C over 24 h, held at this temperature for 72 h, cooled to 400 °C over 96 h, and then cooled to room temperature by shutting off the furnace. Attempts to prepare analogues with earlier *RE* members (La–Nd) under these conditions were unsuccessful. Similarly, when these reactions were extended to later *RE* components beyond Sm and up to Lu, the products consisted mostly of binary selenides.

Single crystals of Sm_3GaSe_5O extracted from the reaction products were black, needle-shaped, and long (up to 1 mm) (**Figure A3-1(a)**). They were initially screened on a JEOL JSM-6010LA InTouchScope scanning electron microscope operated with an accelerating voltage of 15 kV. Energy-dispersive X-ray (EDX) analyses were performed on several points on these single crystals, with acquisition times of 60 s each. Although oxygen is normally problematic to quantify by EDX analysis, the observed average composition (in mol %) of 32% Sm, 10% Ga, 45% Se, and 13% O was in good agreement with expectations (30% Sm, 10% Ga, 50% Se, 10% O). As a further check, the crystals were also examined on a Zeiss Sigma 300 VP field emission scanning electron microscope operated with an accelerating voltage of 15 kV and equipped with a Bruker Quantax 600 system with dual X-Flash 6/60 detectors, which are well suited to give reliable light

element analysis. The average composition from this analysis was found to be 28% Sm, 9% Ga, 51% Se, and 12% O (**Figure A3-1(b)**), confirming the results above.

Powder X-ray diffraction (XRD) patterns on ground samples were collected on a Bruker D8 Advance diffractometer equipped with a Cu $K\alpha_1$ radiation source operated at 40 kV and 40 mA. The patterns were recollected after several months and showed no changes, indicating that the samples are air-stable. Rietveld refinements were performed using the program GSAS-II,[27] with a 12-term Chebyshev polynomial applied to fit the background (**Table A3-1**).

3.2.2. Structure determination

Intensity data were collected on a single crystal of Sm_3GaSe_5O at room temperature on a Bruker PLATFORM diffractometer equipped with a SMART APEX II CCD area detector and a graphite-monochromated Mo $K\alpha$ radiation source, using ω scans at 7–8 different ϕ angles with a frame width of 0.3° and an exposure time of 15 s per frame. Face-indexed numerical absorption corrections were applied. Structure solution and refinement were carried out with use of the SHELXTL (version 2018/3) program package.[28]

The centrosymmetric monoclinic space group $P2_1/m$ was chosen on the basis of Laue symmetry, intensity statistics, and systematic absences. The initial positions of all Sm, Ga, and Se atoms were located by direct methods, and the O atoms were located in subsequent difference maps. Atomic positions were standardized with the program STRUCTURE TIDY.[29] Refinements proceeded in a straightforward fashion, with no evidence for disorder or partial occupancy. The final refinement led to reasonable atomic displacement parameters, sensible bond lengths, and good agreement factors. **Table 3-1** lists crystal data, **Table 3-2** lists atomic and displacement parameters, and **Table 3-3** lists interatomic distances. CCDC 2123893 contains the supplementary

crystallographic data for this paper. These data can be obtained free of charge from the Cambridge Crystallographic Data Centre via www.ccdc.cam.ac.uk/structures.

Table 3-1. Crystallographic data for Sm_3GaSe_5O.

formula	Sm_3GaSe_5O
formula mass (amu)	931.57
space group	$P2_1/m$ (No. 11)
a (Å)	11.0042(9)
b (Å)	3.9761(3)
c (Å)	21.2458(17)
β (deg.)	96.2436(14)
V (Å^3)	924.07(13)
Z	4
T (K)	296(2)
ρ_{calcd} (g cm^{-3})	6.696
crystal dimensions (mm)	0.34 × 0.04 × 0.02
μ(Mo $K\alpha$) (mm^{-1})	41.29
transmission factors	0.053–0.465
2θ limits	3.72–66.14°
data collected	$-16 \le h \le 16$, $-6 \le k \le 6$, $-32 \le l \le 32$
no. of data collected	13318
no. of unique data, including $F_o^2 < 0$	3865 (R_{int} = 0.057)
no. of unique data, with $F_o^2 > 2\sigma(F_o^2)$	3004
no. of variables	121
$R(F)$ for $F_o^2 > 2\sigma(F_o^2)$ [a]	0.037
$R_w(F_o^2)$ [b]	0.085
goodness of fit	1.07
$(\Delta\rho)_{max}$, $(\Delta\rho)_{min}$ (e Å^{-3})	5.30, –2.74

[a] $R(F) = \sum||F_o| - |F_c|| / \sum|F_o|$. [b] $R_w(F_o^2) = [\sum[w(F_o^2 - F_c^2)^2] / \sum wF_o^4]^{1/2}$; $w^{-1} = [\sigma^2(F_o^2) + (Ap)^2 + Bp]$, where $p = [\max(F_o^2,0) + 2F_c^2] / 3$.

Table 3-2. Atomic coordinates [a] and equivalent isotropic displacement parameters for Sm_3GaSe_5O.

Atom	*x*	*y*	*z*	U_{eq} (Å^2) [b]
Sm1	0.05843(5)	¼	0.84100(3)	0.01432(11)
Sm2	0.20568(5)	¼	0.51221(3)	0.01294(11)
Sm3	0.46060(5)	¼	0.89052(3)	0.01405(11)
Sm4	0.56631(5)	¼	0.56644(2)	0.01078(10)
Sm5	0.81041(5)	¼	0.98064(3)	0.01381(11)
Sm6	0.91175(5)	¼	0.64324(3)	0.01328(11)
Ga1	0.29140(14)	¼	0.22795(6)	0.0222(3)
Ga2	0.69158(11)	¼	0.29314(5)	0.0133(2)
Se1	0.03409(9)	¼	0.07082(5)	0.01325(19)
Se2	0.04389(10)	¼	0.24582(5)	0.01314(19)
Se3	0.18809(9)	¼	0.72276(5)	0.01300(19)
Se4	0.29886(9)	¼	0.33979(5)	0.01193(19)
Se5	0.38626(9)	¼	0.03199(5)	0.01241(19)
Se6	0.51907(10)	¼	0.21157(5)	0.0153(2)
Se7	0.63436(9)	¼	0.39687(5)	0.01271(19)
Se8	0.73998(11)	¼	0.83807(5)	0.0178(2)
Se9	0.74262(10)	¼	0.11139(5)	0.0151(2)
Se10	0.96872(9)	¼	0.42515(5)	0.01222(19)
O1	0.4056(6)	¼	0.4857(3)	0.0115(13)
O2	0.7806(6)	¼	0.5479(3)	0.0098(13)

[a] All atoms are located in Wyckoff position 2*e*.

[b] U_{eq} is defined as one-third of the trace of the orthogonalized U_{ij} tensor.

Table 3-3. Interatomic distances (Å) in Sm_3GaSe_5O.

Sm1–Se2 (×2)	2.8584(9)	Sm5–Se1 (×2)	2.9125(9)
Sm1–Se1 (×2)	2.9856(9)	Sm5–Se5 (×2)	2.9295(9)
Sm1–Se3	3.0208(12)	Sm5–Se1	2.9502(12)
Sm1–Se9 (×2)	3.0475(9)	Sm5–Se9	2.9537(12)
Sm1–Se8	3.4980(14)	Sm5–Se8	3.0437(12)
Sm2–Se10	3.0285(12)	Sm6–Se10 (×2)	2.8651(8)
Sm2–Se10 (×2)	3.1563(9)	Sm6–Se2 (×2)	3.0816(9)
Sm2–Se7 (×2)	3.1690(9)	Sm6–Se4 (×2)	3.1041(9)
Sm2–O1	2.330(7)	Sm6–Se3	3.3142(12)
Sm2–O2 (×2)	2.376(4)	Sm6–O2	2.356(7)
Sm3–Se6 (×2)	2.9686(9)	Ga1–Se4	2.3686(16)
Sm3–Se5 (×2)	2.9831(9)	Ga1–Se8 (×2)	2.4359(10)
Sm3–Se9 (×2)	2.9892(9)	Ga1–Se6	2.5667(19)
Sm3–Se5	3.1996(12)	Ga1–Se2	2.7906(19)
Sm3–Se8	3.3821(14)	Ga2–Se7	2.3568(16)
Sm4–Se4 (×2)	3.0790(9)	Ga2–Se6	2.4272(16)
Sm4–Se7 (×2)	3.1323(9)	Ga2–Se3 (×2)	2.4326(9)
Sm4–O1 (×2)	2.313(2)		
Sm4–O1	2.325(7)		
Sm4–O2	2.433(7)		

3.2.3. Electronic structure calculations

First-principles calculations were performed using the projected augmented wave (PAW) method as implemented in the Vienna ab initio simulation package (VASP)[30–32] to determine the electronic structure and density of states (DOS) of Sm_3GaSe_5O. Exchange and correlation were treated in this density functional theory (DFT) method by the generalized gradient approximation, as parameterized by Perdew, Burke, and Ernzerhof (PBE).[33–35] The recommended standard PAW potentials (Sm_3, Ga_d, Se, and O) were used, with the plane-wave basis cutoff energy set to 500 eV. A 9 × 25 × 5 Monkhorst-Pack *k*-mesh was chosen to sample the first Brillouin zone. The convergence criteria were set to 10^{-8} eV for electronic optimization, and -2×10^{-2} eV for ionic relaxation. Chemical bonding was examined by evaluating crystal orbital Hamilton populations (–COHP), electron localization functions (ELF), and Bader charges, using the program LOBSTER (version 3.2.0).[36–40]

3.2.4. Diffuse reflectance spectroscopy

The optical diffuse reflectance spectrum for a ground sample of Sm_3GaSe_5O was measured from 200 nm (6.2 eV) to 1400 nm (0.9 eV) on a Cary 5000 UV-vis-NIR spectrophotometer equipped with a diffuse reflectance accessory. An optical polytetrafluoroethylene disc with >98% reflectivity in the range of 250 to 2200 nm was used as a reflectance standard. The reflectance spectra were converted to optical absorption spectra using the Kubelka-Munk function, $F(R) = \alpha/S = (1-R)^2/2R$, where α is the Kubelka–Munk absorption coefficient, S is the scattering coefficient, and R is the reflectance.[41]

3.3. Results and discussion

Initial attempts were made to prepare oxychalcogenides by substituting O for S or Se atoms in the ternary rare-earth chalcogenides RE_3MCh_6 (M = Ga, In; Ch = S, Se).[26] There are still gaps in knowledge within these series; in particular, it is curious that no members of the RE_3GaSe_6 series have yet been found. Thus, the discovery of the oxyselenide Sm_3GaSe_5O was a surprising result. Sm_3GaSe_5O was obtained as a majority phase (~83% by mass) through reaction of Sm_2O_3, Sm, Ga_2Se_3, and Se at 950 °C, in the presence of Sm_2SeO_2 (**Figure 3-1**). Regrinding and reheating treatments may help improve the purity of the sample, but we note that small amounts of Sm_2SeO_2 tended to deposit on the other side of the fused-silica tube, making it difficult to control the correct composition. Substitution with other *RE* metals was unsuccessful under similar heating conditions.

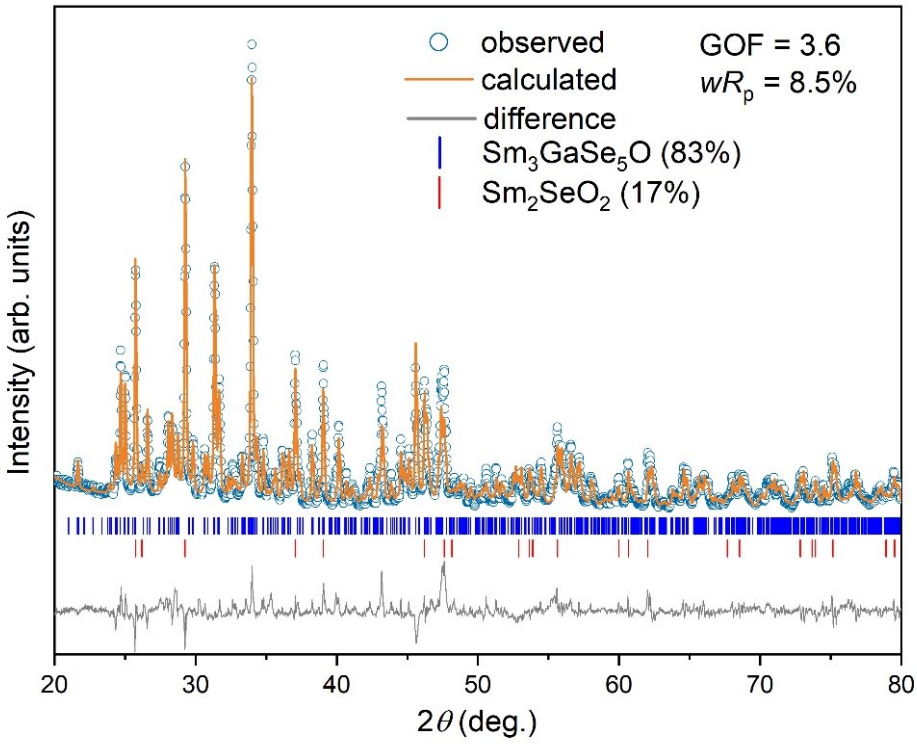

Figure 3-1. Powder XRD pattern and Rietveld refinement of a sample of Sm_3GaSe_5O.

The crystal structure of Sm_3GaSe_5O is monoclinic (space group $P2_1/m$) and contains six Sm, two Ga, ten Se, and two O sites, all lying on mirror planes (Wyckoff position 2*e*). It is convenient to describe the structure in terms of three types of building blocks which stack along the *c*-direction and extend along the *b*-direction: Sm−Se, Sm−O, and Ga−Se (**Figure 3-2**). The Sm−Se blocks also extend along the *a*-direction, forming corrugated two-dimensional slabs oriented parallel to the *ab*-plane, whereas the Sm−O and Ga−Se blocks are interrupted along the *a*-direction, forming only one-dimensional strips or ribbons. These building blocks are invoked to facilitate description, but of course, they are not really isolated from each other, but linked together through additional Sm−Se bonds. The Sm1, Sm3, and Sm5 atoms (within the Sm−Se blocks) are surrounded exclusively by Se atoms, whereas the Sm2, Sm4, and Sm6 atoms (within the Sm−O blocks) are surrounded by both Se and O atoms. Their coordination geometries are monocapped and bicapped trigonal prisms (CN7 and 8) (**Figure A3-2**). Among the Se atoms, one of them (Se10) does not easily fit into these building blocks. The coordination geometries around the Se atoms are tetrahedra and square pyramids (CN4 and 5) (**Figure A3-3**).

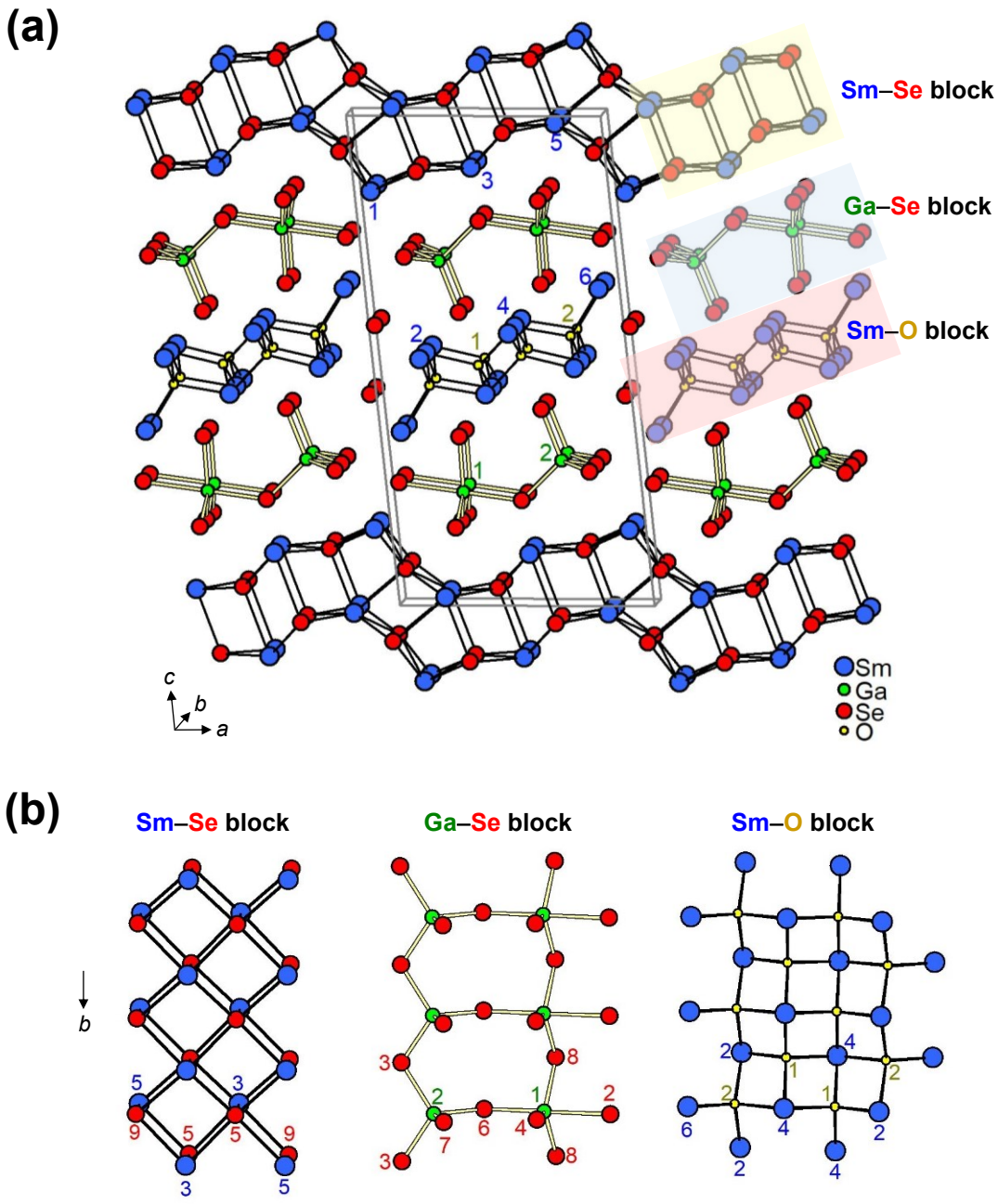

Figure 3-2. (a) Structure of Sm_3GaSe_5O in terms of (b) Sm–Se, Ga–Se, and Sm–O blocks that extend along the *b*-direction. The numbered labels identify some key crystallographically inequivalent sites for Sm (blue), Ga (green), Se (red), and O (yellow) atoms.

The Sm–Se blocks are built from Sm and Se atoms arranged in cubes, and they are essentially distorted fragments of the rocksalt-type structure, which is adopted by SmSe and other rare-earth monochalcogenides. The Sm–Se distances of 2.93–3.20 Å within these blocks are similar to the 3.1 Å distances found in SmSe.[42] The Sm–O blocks are built from edge-sharing O-centred tetrahedra, four across the width of the strips, and can be considered to be fragments of two-dimensional layers more commonly encountered in oxychalcogenides, such as *RE*Cu*Ch*O with the ZrCuSiAs-type structure.[3,6] Similar one-dimensional strips of various widths are found in La_3GaS_5O, $La_{10}In_6S_{17}O_6$, and related oxychalcogenides.[24,25] The Sm–O distances of 2.31–2.43 Å are distinctly shorter than the Sm–Se distances, and agree with distances found in similar O-centred tetrahedra found in any of the polymorphic forms of Sm_2O_3.[43]

The Ga–Se blocks are perhaps the most unusual feature of the structure. They are built by linking corners of two types of polyhedra with Ga surrounded by Se atoms in tetrahedral geometry (CN4), which is expected, and in trigonal bipyramidal geometry (CN5), which is noteworthy. Related examples of five-coordinate GaO_5 units are rare (occurring in a few compounds such as $GaInO_3$ and $Zn_6Ga_2O_9$)[44,45] and GaS_5 units have not yet been found; to our knowledge, the observation of five-coordinate $GaSe_5$ units is new. The Ga–Se distances are 2.36–2.43 Å within the $GaSe_4$ tetrahedra and 2.37–2.79 Å within the $GaSe_5$ trigonal bipyramids. Given that typical Ga–Se distances lie in the range of 2.3 to 2.5 Å, it will be important to evaluate if the longer distances found within the $GaSe_5$ units are significant, as discussed later.

Although the original hypothesis was that oxychalcogenides RE_3MCh_5O could be derived from existing ternary chalcogenides, there is no close relationship between Sm_3GaSe_5O and RE_3MCh_6 (*M* = Ga, In; *Ch* = S, Se).[26] Instead, the structure of Sm_3GaSe_5O is of a new type. It is isopointal to the $CeTmS_3$- and $Tb_3In_5S_{12}$-type structures, which have the same space group

($P2_1/m$), similar cell parameters, and same Wyckoff sequence (e^{20}), but with quite different atomic coordinates and local coordination environments.[46,47] The only other oxychalcogenide with an analogous chemical formula is La_3GaS_5O,[24] which has an orthorhombic structure with similar cell dimensions as in Sm_3GaSe_5O, but the connectivity of the building blocks is completely different (Figure 3-3). In place of Sm–Se slabs lying on the *ab* plane and Sm–O strips lying halfway between the former in Sm_3GaSe_5O, there are now heterogeneous slabs built from both La–S and La–O blocks lying on these planes in La_3GaS_5O. Moreover, the strips of linked $GaSe_4$ tetrahedra and $GaSe_5$ trigonal bipyramids in Sm_3GaSe_5O give way to isolated chains of GaS_5 tetrahedra in La_3GaS_5O.

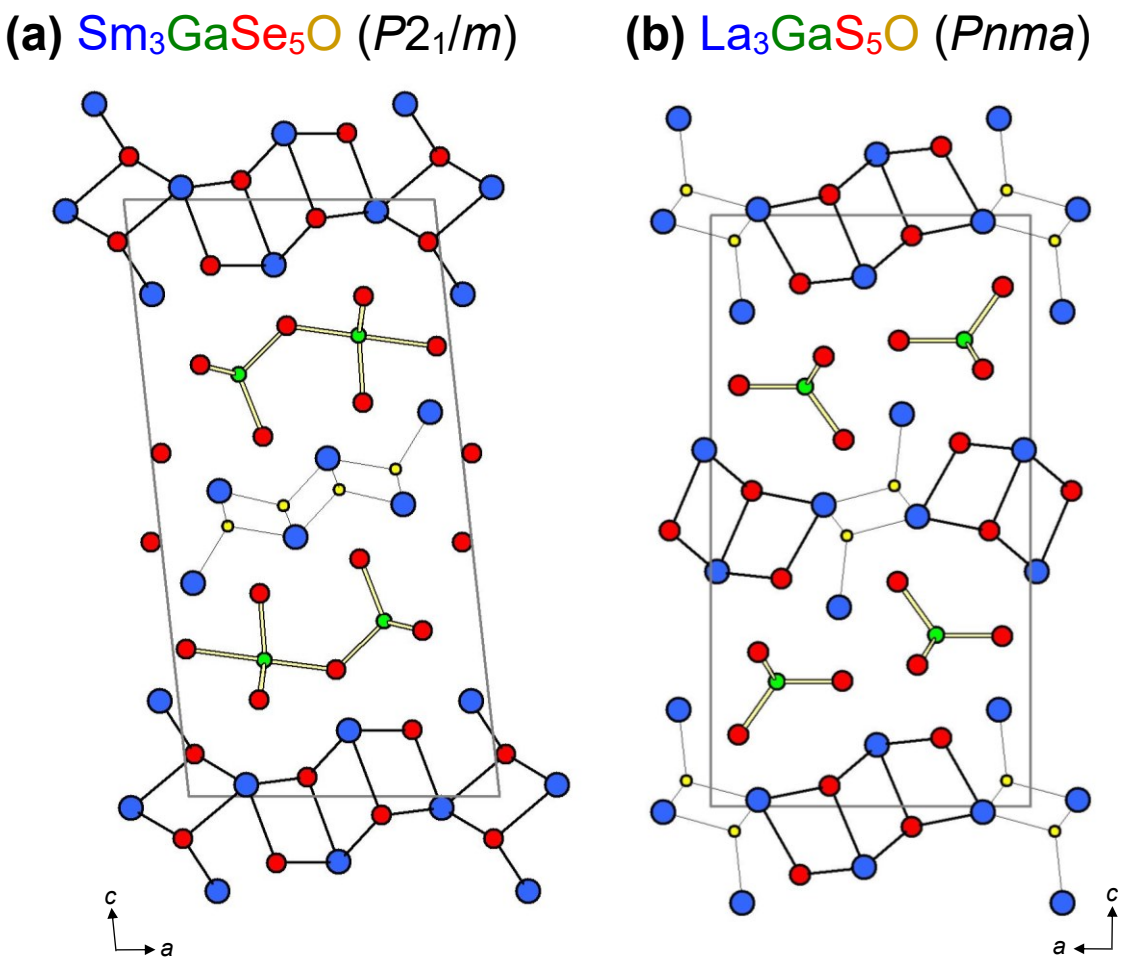

Figure 3-3. Comparison of structures of (a) Sm_3GaSe_5O and (b) La_3GaS_5O, highlighting the different connectivity of building blocks.

The charge-balanced formulation, $(Sm^{3+})_3(Ga^{3+})(Se^{2-})_5(O^{2-})$, is consistent with the presence of isolated ions in the structure, and agrees well with the bond valence sums,[48] which have the expected values for all atoms (**Table 3-4**). DFT calculations were performed to obtain the band dispersion, DOS, and –COHP curves for Sm_3GaSe_5O (**Figure 3-4**). Consistent with the closed-shell configurations for all atoms, the electronic band structure shows an energy gap of 0.67 eV between valence and conduction bands. As seen in the band dispersion diagram, the valence band maximum is located at the Brillouin zone centre but the conduction band minimum is slightly

shifted, indicating an indirect band gap. However, the bands are relatively flat in this region and the gap is nearly direct. The DOS diagram shows that filled Se 4p states largely contribute to the valence band (–4.5 to 0 eV), with mixing of Ga 4p and O 2p states, whereas empty Sm 5d states dominate the conduction band (above 0.7 eV). Inspection of the –COHP curves reveals that the opening of the energy gap is dictated by the separation of bonding and antibonding Ga–Se interactions, which are optimized. The Sm–O interactions are also optimized, but they do not affect states close to the Fermi level. The integrated –COHP (or –ICOHP) values (in eV/bond) are relatively small for the Sm–Se interactions (0.7 to 1.1) and just slightly larger for Sm–O interactions (1.1 to 1.4), indicating mostly ionic character in their bonding. Perhaps the most interesting results are the –ICOHP values for the Ga–Se interactions, which are strong for the typical 2.36–2.43 Å distances within the Ga2-centred tetrahedron (4.7 to 5.8) and remain appreciably large for the 2.37–2.79 Å distances within the Ga1-centred trigonal bipyramid (3.2 to 5.5) (**Figure 3-5**). In particular, the –COHP curve for the long apical Ga1–Se2 distance clearly shows the same profile of filled bonding and empty antibonding levels as the shorter Ga–Se contacts.

Table 3-4. Bond valence sums in Sm_3GaSe_5O.

Sm1	3.27	Se1	2.36
Sm2	2.87	Se2	2.12
Sm3	2.98	Se3	1.96
Sm4	3.24	Se4	2.11
Sm5	3.33	Se5	2.09
Sm6	3.12	Se6	2.09
Ga1	2.97	Se7	1.95
Ga2	2.96	Se8	2.00
O1	2.14	Se9	2.03
O2	1.80	Se10	2.10

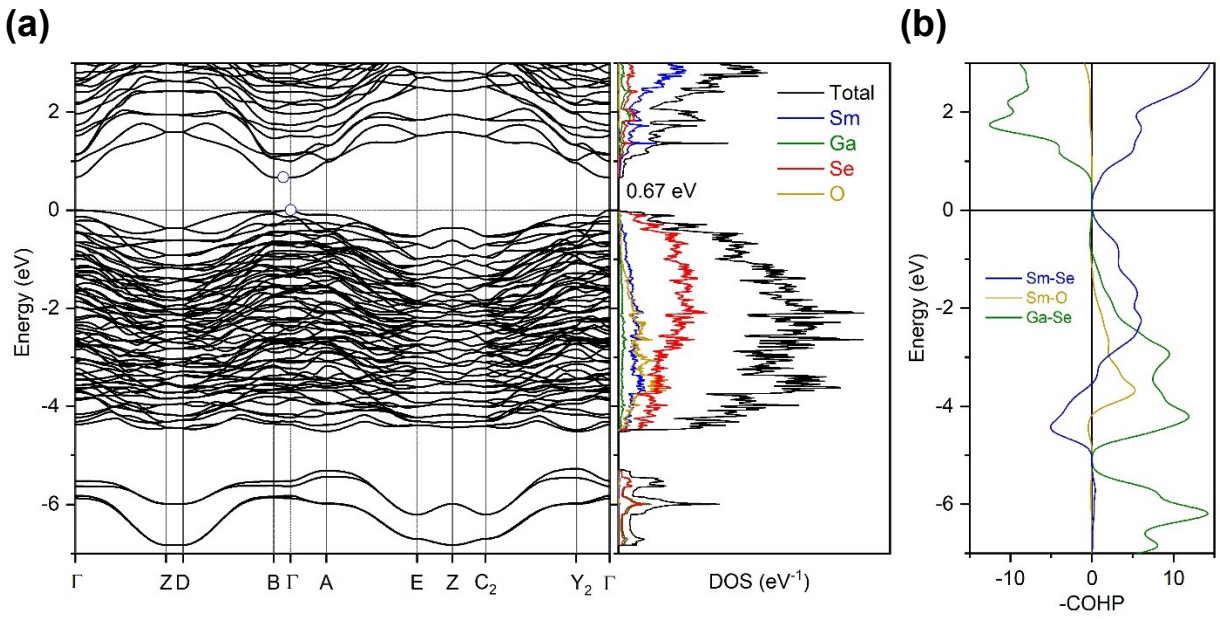

Figure 3-4. (a) Band dispersion and DOS for Sm_3GaSe_5O. The blue circles mark the valence band maximum and conduction band minimum. (b) –COHP curves for Sm–Se, Sm–O, and Ga–Se contacts, with positive values signifying bonding interactions and negative values signifying antibonding interactions.

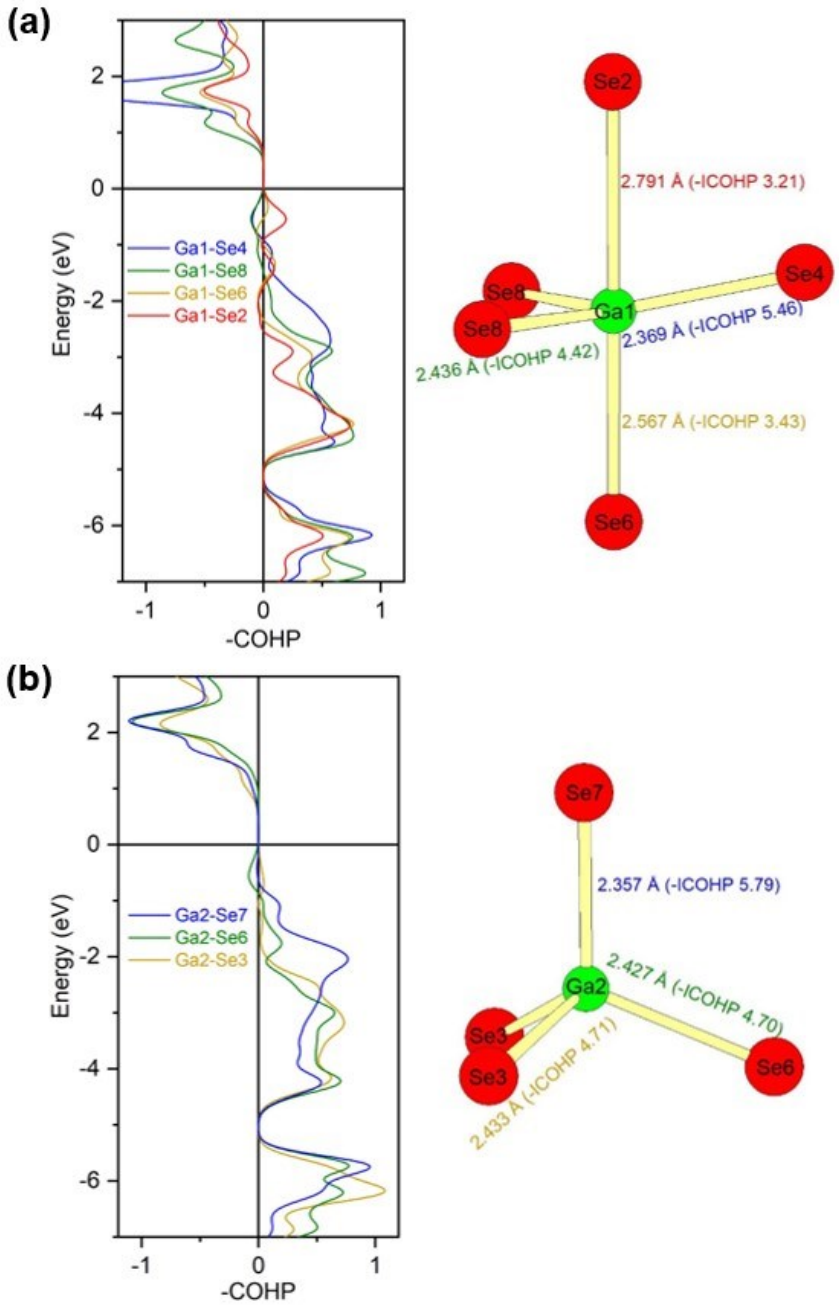

Figure 3-5. –COHP curves for individual Ga–Se contacts within (a) $GaSe_5$ trigonal bipyramids and (b) $GaSe_4$ tetrahedra in Sm_3GaSe_5O. The integrated COHP (–ICOHP) values (in eV/bond) are shown for these contacts.

To visualize the bonding character in Sm_3GaSe_5O in more detail, ELF plots were generated from the electronic structure (**Figure 3-6**). It is striking that the electron density can be clearly delineated into identifiable Sm–Se, Sm–O, and Ga–Se blocks, indicating that these units are not merely convenient for structural description, but exhibit distinctly different bonding character. The electron density is highly localized around the Sm and Se atoms within the Sm–Se blocks and around the Sm and O atoms within the Sm–O blocks, evident by the minima (blue colours) between these atoms. In contrast, the electron density is intermediate (green colours) and smeared between the Ga and Se atoms within the Ga–Se blocks. These features support the assertion of primarily ionic bonding character within the Sm–Se and Sm–O blocks, and covalent bonding character within the Ga–Se blocks. The Bader charges tend to be more extreme for the atoms participating in ionic bonding: 1.49+ to 1.61+ for Sm and 0.73– to 1.09– for Se atoms within the Sm–Se blocks; 1.65+ to 1.98+ for Sm and 1.38– for O atoms within the Sm–O blocks. These charges are more moderate for the atoms participating in covalent bonding: 0.84+ to 0.88+ for Ga and 0.77– to 0.92– for Se atoms within the Ga–Se blocks.

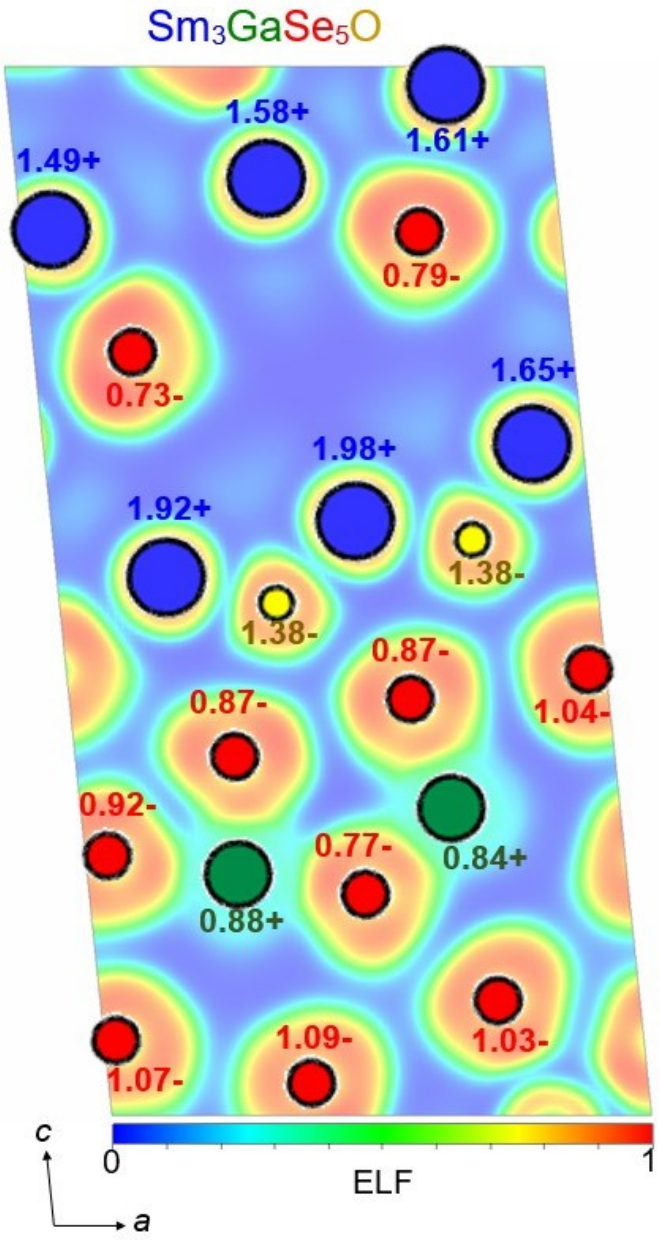

Figure 3-6. ELF and Bader charges for a slice of the Sm_3GaSe_5O structure parallel to the (010)-plane at $y = ¾$.

The optical diffuse reflectance spectrum measured for Sm_3GaSe_5O shows sharp peaks between 0.6 and 1.1 eV arising from f-f transitions of Sm atoms and an absorption edge near 1.3 eV, confirming the occurrence of a band gap (**Figure 3-7**). If an indirect gap is assumed, the band

gap extracted from the Tauc plot is 1.2 eV. This experimental band gap is higher than the value of 0.67 eV predicted from the DFT calculation, which tends to give inaccurate band gaps if the standard functionals are used, but it is consistent with the black colour of the compound. The sample does contain a small amount of Sm_2SeO_2, which has been reported to be "grey beige,"[49] suggestive of a larger band gap, with a minimum value of 2.3 eV as estimated from DFT calculations.[50] The optical spectrum would be dominated by the majority phase present in the sample and the conclusion of a small band gap for Sm_3GaSe_5O remains unchanged. To correct for the underestimation of the PBE-computed band gap, the calculations were repeated using the hybrid HSE06 functional, giving a computed band gap of 1.04 eV, in good agreement with the experimental value (**Figure A3-4**).

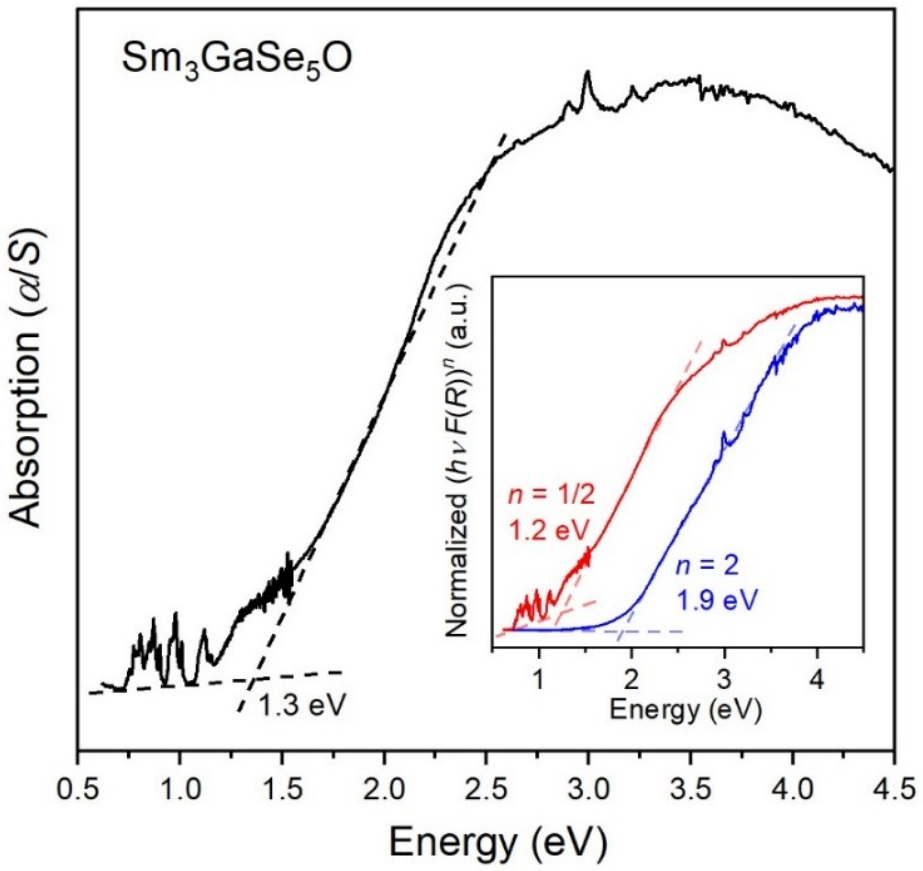

Figure 3-7. Optical diffuse reflectance spectrum for Sm_3GaSe_5O, with inset showing fittings assuming indirect (n = ½) or direct (n = 2) band gap.

3.4. Conclusions

The hypothesis that quaternary oxychalcogenides could be derived from ternary chalcogenides RE_3MCh_6 (M = Ga, In; Ch = S, Se) was tested. The new oxyselenide Sm_3GaSe_5O was synthesized but its structure is completely new and exhibits the unusual feature of $GaSe_5$ trigonal bipyramids, heretofore unreported. The oft-cited claim that oxychalcogenides can be viewed in terms of separate blocks – insulating O-containing and semiconducting *Ch*-containing ones – was evaluated by inspecting the ELF plots for Sm_3GaSe_5O, which showed a clear distinction between localized electron density around the atoms within the Sm–Se and Sm–O

blocks and shared electron density within the Ga−Se blocks. A nearly direct band gap is present in the DOS and is controlled largely by the separation of bonding and antibonding Ga−Se interactions. The measured band gap of 1.2 eV is relatively narrow compared to other related oxychalcogenides, which tend to be >2 eV, such as those found in the layered series *RE*Cu*Ch*O.[3] This band gap is close to desired values for maximum solar cell efficiency (cf. 1.1 eV for silicon) and suggests that Sm_3GaSe_5O may have potential as an optical material.

3.5. References

(1) Kageyama, H.; Hayashi, K.; Maeda, K.; Attfield, J. P.; Hiroi, Z.; Rondinelli, J. M.; Poeppelmeier, K. R. *Nat. Commun.* **2018**, *9*, 772.

(2) Harada, J. K.; Charles, N.; Poeppelmeier, K. R.; Rondinelli, J. M. *Adv. Mater.* **2019**, *31*, 1805295.

(3) Clarke, S. J.; Adamson, P.; Herkelrath, S. J. C.; Rutt, O. J.; Parker, D. R.; Pitcher, M. J.; Smura, C. F. *Inorg. Chem.* **2008**, *47*, 8473–8486.

(4) Hiramatsu, H.; Kamihara, Y.; Yanagi, H.; Ueda, K.; Kamiya, T.; Hirano, M.; Hosono, H. *J. Eur. Ceram. Soc.* **2009**, *29*, 245–253.

(5) Muir, S.; Subramanian, M. A. *Prog. Solid State Chem.* **2012**, *40*, 41–56.

(6) Luu, S. D. N.; Vaqueiro, P. *J. Materiomics* **2016**, *2*, 131–140.

(7) Tippireddy, S.; D S, P. K.; Das, S.; Mallik, R. C. *ACS Appl. Energy Mater.* **2021**, *4*, 2022–2040.

(8) Xiao, J.-R.; Yang, S.-H.; Feng, F.; Xue, H.-G.; Guo, S.-P. *Coord. Chem. Rev.* **2017**, *347*, 23–47.

(9) Krivovichev, S. V.; Mentré, O.; Siidra, O. I.; Colmont, M.; Filatov, S. K. *Chem. Rev.* **2013**, *113*, 6459–6535.

(10) Ueda, K.; Hiramatsu, H.; Hirano, M.; Kamiya, T.; Hosono, H. *Thin Solid Films* **2006**, *496*, 8–15.

(11) Wilmer, D.; Jorgensen, J. D.; Wuensch, B. J. *Solid State Ionics* **2000**, *136–137*, 961–966.

(12) Mizuguchi, Y.; Omachi, A.; Goto, Y.; Kamihara, Y.; Matoba, M.; Hiroi, T.; Kajitani, J.; Miura, O. *J. Appl. Phys.* **2014**, *116*, 163915.

(13) Chen, Y.; Cui, Y.; Pham, A.; Wang, Y.; Bhadbhade, M. M.; Wang, R.; Su, Y.; Hu, H.; Wen, Z.; Cheng, C.; Tan, T. T.; Li, S.; Zhao, Y. *J. Mater. Chem. C* **2019**, *7*, 586–591.

(14) Ishikawa, A.; Takata, T.; Kondo, J. N.; Hara, M.; Kobayashi, H.; Domen, K. *J. Am. Chem. Soc.* **2002**, *124*, 13547–13553.

(15) Miura, A.; Oshima, T.; Maeda, K.; Mizuguchi, Y.; Moriyoshi, C.; Kuroiwa, Y.; Meng, Y.; Wen, X.-D.; Nagao, M.; Higuchi, M.; Tadanaga, K. *J. Mater. Chem. A* **2017**, *5*, 14270–14277.

(16) Jaulmes, P. S. *Acta Crystallogr. B* **1978**, *34*, 2610–2612.

(17) Bénazeth, S.; Guittard, M.; Laruelle, P. *Acta Crystallogr. C* **1984**, *40*, 345–347.

(18) Guittard, M.; Bénazeth, S.; Dugué, J.; Jaulmes, S.; Palazzi, M.; Laruelle, P.; Flahaut, J. *J. Solid State Chem.* **1984**, *51*, 227–238.

(19) Ito, H.; Miura, A.; Goto, Y.; Mizuguchi, Y.; Moriyoshi, C.; Kuroiwa, Y.; Azuma, M.; Liu, J.; Wen, X.-D.; Nishioka, S.; Maeda, K.; Masubuchi, Y.; Rosero-Navarro, N. C.; Tadanaga, K. *Dalton Trans.* **2019**, *48*, 12272–12278.

(20) Kabbour, H.; Cario, L.; Moëlo, Y.; Meerschaut, A. *J. Solid State Chem.* **2004**, *177*, 1053–1059.

(21) Dugué, J.; Guittard, M. *Acta Crystallogr. B* **1982**, *38*, 2368–2371.

(22) Bénazeth, S.; Laruelle, P.; Guittard, M. *J. Solid State Chem.* **1989**, *78*, 148–153.

(23) Mazurier, A.; Guittard, M.; Jaulmes, S. *Acta Crystallogr. B* **1982**, *38*, 379–382.

(24) Jaulmes, S.; Mazurier, A.; Guittard, M. *Acta Crystallogr. C* **1983**, *39*, 1594–1597.

(25) Gastaldi, L.; Carré, D.; Pardo, M. P. *Acta Crystallogr. B* **1982**, *38*, 2365–2367.

(26) Mishra, V.; Mumbaraddi, D.; Iyer, A. K.; Mar, A. *J. Solid State Chem.* **2021**, *297*, 122096.

(27) Toby, B. H.; Von Dreele, R. B. *J. Appl. Crystallogr.* **2013**, *46*, 544–549.

(28) Sheldrick, G. M. *Acta Crystallogr. A: Found. Crystallogr.* **2008**, *64*, 112–122.

(29) Gelato, L. M.; Parthé, E. *J. Appl. Crystallogr.* **1987**, *20*, 139–143.

(30) Kresse, G.; Furthmüller, J. *Phys. Rev. B* **1996**, *54*, 11169–11186.

(31) Kresse, G.; Joubert, D. *Phys. Rev. B* **1999**, *59*, 1758–1775.

(32) Blöchl, P. E. *Phys. Rev. B* **1994**, *50*, 17953–17979.

(33) Perdew, J. P.; Burke, K.; Ernzerhof, M. *Phys. Rev. Lett.* **1996**, *77*, 3865–3868.

(34) Hohenberg, P.; Kohn, W. *Phys. Rev.* **1964**, *136*, B864–B871.

(35) Kohn, W.; Sham, L. J. *Phys. Rev.* **1965**, *140*, A1133–A1138.

(36) Dronskowski, R.; Blöchl, P. E. *J. Phys. Chem.* **1993**, *97*, 8617–8624.

(37) Deringer, V. L.; Tchougréeff, A. L.; Dronskowski, R. *J. Phys. Chem. A* **2011**, *115*, 5461–5466.

(38) Maintz, S.; Deringer, V. L.; Tchougréeff, A. L.; Dronskowski, R. *J. Comput. Chem.* **2013**, *34*, 2557–2567.

(39) Grin, Y.; Savin, A.; Silvi, B., The ELF perspective of chemical bonding. In *The Chemical Bond: Fundamental Aspects of Chemical Bonding*, Frenking, G.; Shaik, S., Eds.; Wiley-VCH: Weinheim, **2014**; pp 345–382.

(40) Maintz, S.; Deringer, V. L.; Tchougréeff, A. L.; Dronskowski, R. *J. Comput. Chem.* **2016**, *37*, 1030–1035.

(41) Kortüm, G. *Reflectance Spectroscopy*; Springer, New York, 1969.

(42) Le Bihan, T.; Darracq, S.; Heathman, S.; Benedict, U.; Mattenberger, K.; Vogt, O. *J. Alloys Compd.* **1995**, *226*, 143–145.

(43) Villars, P.; Cenzual, K., *Pearson's Crystal Data – Crystal Structure Database for Inorganic Compounds*, Release 2021/22, ASM International: Materials Park, OH, USA.

(44) Shannon, R. D.; Prewitt, C. T. *J. Inorg. Nucl. Chem.* **1968**, *30*, 1389–1398.

(45) Michiue,Y.; Kimizuka, N.; Kanke, Y. *Acta Crystallogr. B* **2008**, *64*, 521–526.

(46) Rodier, N. *Bull. Soc. Fr. Minéral. Cristallogr.* **1973**, *96*, 350–355.

(47) Carre, D. *Acta Crystallogr. B* **1977**, *33*, 1163–1166.

(48) Brese, N. E.; O'Keeffe, M. *Acta Crystallogr. Sect. B Struct. Sci.* **1991**, *47*, 192–197.

(49) Guittard, M.; Flahaut, J.; Domange, L. *Acta Crystallogr.* **1966**, *21*, 832.

(50) Jain, A.; Ong, S. P.; Hautier, G.; Chen, W.; Richards, W. D.; Dacek, S.; Cholia, S.; Gunter, D.; Skinner, D.; Ceder, G.; Persson, K. A. *APL Mater.* **2013**, *1*, 011002.

Chapter 4.

$La_4Ga_2Se_6O_3$: A rare-earth oxyselenide built from one-dimensional strips

A version of this chapter has been published.

Mishra, V.; Zabolotnii, A.; Mar, A. Inorg. Chem. ***2022****, 61, 12458–12465.*

4.1. Introduction

Among mixed-anion compounds,[1–3] quaternary rare-earth oxychalcogenides *RE*–*M*–*Ch*–O (where *M* is a d- or p-block metal or metalloid) form a diverse group that hold promise for many materials applications.[4–8] Well-known examples include transparent semiconductors (LaCuSO),[9] ionic conductors (LaAgSO),[10] photocatalysts ($Sm_2Ti_2S_2O_5$),[11] and thermoelectrics ($LaBiS_2O$).[12] The consideration of such oxychalcogenides as potential thermoelectric materials is relatively recent.[7] They are hypothesized to be suitable candidates because they may show intermediate characteristics desirable for thermoelectric applications, being more resistant to thermal degradation than chalcogenides while maintaining narrower band gaps than oxides.

The presence of two types of anions is presumed to give greater variability in structures, which may lead to the impression that unrestricted control over properties is possible. A more nuanced assessment of known oxychalcogenides reveals that there are limitations in the types of structures adopted.[13–15] For example, contrary to naive expectations, it is unusual for an oxychalcogenide to be derived from an existing oxide or chalcogenide in which one anion simply substitutes for another. Rather, oxychalcogenides often exhibit unique structure types that are not easily predictable. Layered structures (such as the ZrCuSiAs-type adopted by LaCuSO) are

perhaps the most familiar, but by no means are they the only ones possible.[4,5] One pattern is clear: there is often, but not always, a segregation of more ionic *RE*–O and more covalent *M*–*Ch* substructures, a phenomenon peculiar to oxychalcogenides which has been described as an example of "selective bonding" and which can be understood in terms of hard-soft acid-base concepts.[6] The coordination polyhedra around the *RE* atoms typically contain a variable number of O and *Ch* atoms, and serve as the link between the two substructures. Layered oxychalcogenides have been proposed to be advantageous for thermoelectric properties because the confinement of electrical conduction to the *M*–*Ch* substructure would increase the Seebeck coefficient and the low-dimensionality of the structure would lower thermal conductivity.[7] To extend this hypothesis, it is natural to wonder how oxychalcogenides built from one-dimensional motifs, which are not as common, would perform.

Many oxysulfides have now been characterized, but the corresponding oxyselenides are not as numerous and not necessarily isostructural. For example, within the gallium-containing systems *RE*–Ga–*Ch*–O, the known oxysulfides are $LaGaS_2O$,[16] $RE_4Ga_2S_5O_4$,[13,17] $RE_4Ga_{1.33}S_4O_4$,[13] $La_{3.33}Ga_6S_{12}O_2$,[18] and La_3GaS_5O,[19] whereas the known oxyselenides are limited to $LaGaSe_2O$,[13,20] $La_4Ga_{1.9}Se_{4.8}O_4$,[21] and Sm_3GaSe_5O.[22] The oxysulfides $LaGaS_2O$ and La_3GaS_5O have been evaluated for photocatalytic activity.[23]

As part of ongoing investigations to discover new rare-earth oxychalcogenides *RE*–*M*–*Ch*–O, we report here the synthesis and characterization of the oxyselenide $La_4Ga_2Se_6O_3$. To test the assumption that the structure can be separated into more ionic La–O and more covalent Ga–Se parts, the bonding character was examined through electronic structure calculations. The transport properties were also calculated to assess whether this compound is a worthy candidate as a thermoelectric material.

4.2. Experimental

4.2.1. Synthesis

Starting materials were freshly filed La pieces (99.9%, Hefa), Ga chunks (99.9%, Alfa-Aesar), Se powder (99.99%, Sigma-Aldrich), and La_2O_3 powder (99.99%, Alfa-Aesar). Ga_2Se_3 was prepared by combining Ga and Se in stoichiometric amounts, placing the mixture in evacuated fused-silica tubes, and heating at 950 °C.

$La_4Ga_2Se_6O_3$ was first obtained during attempts to prepare other rare-earth analogues of recently discovered Sm_3GaSe_5O.[22] A mixture of La_2O_3, La, Ga_2Se_3, and Se in a molar ratio of 2:14:3:21, corresponding to a nominal composition of La_3GaSe_5O, with a total mass of 400 mg was combined with 50 mg of NaCl acting as a flux. A 5% weight excess of Se was also added to compensate for volatilization losses. The combined precursors were cold-pressed into a pellet and transferred to a fused-silica tube (12-mm diameter, 15-cm length) which was evacuated, sealed, and placed in a furnace. The tube was heated to 950 °C over 24 h, held at this temperature for 72 h, cooled to 400 °C over 96 h, and then cooled to room temperature by shutting off the furnace. After the NaCl flux was removed by washing with water and methanol, very thin, black, needle-shaped crystals were extracted from the reaction product (**Figure A4-1**). These crystals were examined on a Zeiss Sigma 300 VP field emission scanning electron microscope operated with an accelerating voltage of 15 kV and equipped with a Bruker Quantax 600 system with dual X-Flash 6/60 detectors, which enable light elements to be analyzed. From energy-dispersive X-ray analysis, the average composition of these crystals was 23% La, 11% Ga, 42% Se, and 24% O, in reasonable agreement with the chemical formula $La_4Ga_2Se_6O_3$ (27% La, 13% Ga, 40% Se, 20% O). Although the reaction product is multiphase, this compound can be obtained reproducibly following the procedure described. When the reaction was repeated using exactly the same

conditions as above, but without NaCl added, the resulting product contained $La_4Ga_2Se_6O_3$ as the major phase (~93%), with the remainder being accounted by GaSe and other unidentified phases (**Figure A4-2**).

A rational synthesis route was attempted by reacting stoichiometric amounts of La_2O_3, La, Ga_2Se_3, and Se in a molar ratio of 1:2:1:3, corresponding to a nominal composition of $La_4Ga_2Se_6O_3$, with a total mass of 300 mg and a 5% weight excess of Se, but no NaCl added. The same heating profile with a holding temperature of 950 °C was used as before. Unfortunately, the targeted oxychalcogenide was not obtained. Heating at other temperatures between 850 and 950 °C, as well as regrinding and reheating, resulted in complex multiphase mixtures without the desired compound. Substitution of other *RE* metals for La was also unsuccessful. From the observations of the synthetic experiments conducted so far, it can be inferred that $La_4Ga_2Se_6O_3$ is likely an incongruently melting phase, and efforts are ongoing to improve its synthesis.

4.2.2. Structure determination

Intensity data were collected on a single crystal of $La_4Ga_2Se_6O_3$ at room temperature on a Bruker PLATFORM diffractometer equipped with a SMART APEX II CCD area detector and a graphite-monochromated Mo $K\alpha$ radiation source, using ω scans at 8 different ϕ angles with a frame width of 0.3° and an exposure time of 15 s per frame. Face-indexed numerical absorption corrections were applied. Structure solution and refinement were carried out with use of the SHELXTL (version 2018/3) program package.[24]

On the basis of the Laue symmetry 2/*m*, systematic absences indicating the presence of *C*-centring and a *c*-glide plane perpendicular to the *b*-axis, intensity statistics (mean $|E^2-1| = 1.10$) suggestive of centrosymmetry, and a reasonable error of merging ($R_{int} = 0.05$), the monoclinic

space group *C*2/*c* was chosen. The La, Ga, and Se atoms were located by direct methods, and the O atoms were subsequently found in difference electron density maps. Atomic positions were standardized with the program STRUCTURE TIDY[25] and the structure refinement was straightforward. However, the ADDSYM routine as implemented in PLATON[26] suggested the possible presence of missing symmetry elements (mirror and additional glide planes), leading to the orthorhombic space group *Ibam* after cell transformation. Careful inspection reveals that these symmetry operations are violated by the location of the Ga atoms in the structure, and confirms that the monoclinic space group *C*2/*c* is indeed correct. As discussed later, this lower symmetry is understandable when structural relationships are examined more closely.

Table 4-1 lists crystal data, **Table 4-1** lists atomic and displacement parameters, and **Table 4-2** lists interatomic distances. CCDC 2177628 contains the supplementary crystallographic data, which can be obtained free of charge via www.ccdc.cam.ac.uk/data_request/cif, or by emailing data_request@ccdc.cam.ac.uk.

Table 4-1. Crystallographic data for $La_4Ga_2Se_6O_3$.

formula	$La_4Ga_2Se_6O_3$
formula mass (amu)	1216.84
space group	*C*2/*c* (No. 15)
a (Å)	21.2832(13)
b (Å)	11.6272(7)
c (Å)	6.0006(4)
β (deg.)	106.3430(10)
V (Å^3)	1424.93(15)
Z	4
T (K)	296(2)
ρ_{calcd} (g cm^{-3})	5.672
crystal dimensions (mm)	0.12 × 0.05 × 0.04
μ(Mo *K*α) (mm^{-1})	30.75
transmission factors	0.141–0.509
2θ limits	3.99–66.50°
data collected	$-32 \le h \le 32$, $-17 \le k \le 17$, $-9 \le l \le 9$
no. of data collected	10386
no. of unique data, including $F_o^2 < 0$	2729 (R_{int} = 0.049)
no. of unique data, with $F_o^2 > 2\sigma(F_o^2)$	2028
no. of variables	70
$R(F)$ for $F_o^2 > 2\sigma(F_o^2)$ [a]	0.041
$R_w(F_o^2)$ [b]	0.106
goodness of fit	1.10
$(\Delta\rho)_{max}$, $(\Delta\rho)_{min}$ (e Å^{-3})	3.43, –2.86

[a] $R(F) = \sum||F_o| - |F_c|| / \sum|F_o|$. [b] $R_w(F_o^2) = [\sum[w(F_o^2 - F_c^2)^2] / \sum wF_o^4]^{1/2}$; $w^{-1} = [\sigma^2(F_o^2) + (Ap)^2 + Bp]$, where $p = [\max(F_o^2,0) + 2F_c^2] / 3$.

Table 4-2. Atomic coordinates and equivalent isotropic displacement parameters for $La_4Ga_2Se_6O_3$.

atom	Wyckoff position	*x*	*y*	*z*	U_{eq} (Å^2) [a]
La1	8*f*	0.06899(2)	0.10733(3)	0.57312(7)	0.01004(11)
La2	8*f*	0.20646(2)	0.10649(3)	0.20936(7)	0.01015(11)
Ga	8*f*	0.12989(4)	0.40598(7)	0.02988(14)	0.01444(18)
Se1	8*f*	0.07217(3)	0.23695(7)	0.07708(12)	0.01392(16)
Se2	8*f*	0.24405(4)	0.35881(6)	0.24192(12)	0.01377(16)
Se3	8*f*	0.37562(5)	0.10461(6)	0.37174(14)	0.01943(18)
O1	8*f*	0.1405(2)	0.0017(5)	0.3950(8)	0.0124(10)
O2	4*e*	0	0.0022(6)	¼	0.0100(13)

[a] U_{eq} is defined as one-third of the trace of the orthogonalized U_{ij} tensor.

Table 4-3. Interatomic distances (Å) in $La_4Ga_2Se_6O_3$.

La1–Se1	3.2537(8)	La2–Se1	3.1341(8)
La1–Se1	3.3540(8)	La2–Se2	3.1878(8)
La1–Se1	3.3624(8)	La2–Se2	3.1955(8)
La1–Se3	3.5351(9)	La2–Se3	3.4553(10)
La1–O2	2.404(4)	La2–O1	2.362(5)
La1–O2	2.410(4)	La2–O1	2.371(5)
La1–O1	2.425(5)	Ga–Se1	2.3765(11)
La1–O1	2.449(5)	Ga–Se3	2.3828(11)
La2–Se2	3.0327(8)	Ga–Se3	2.3949(11)
La2–Se2	3.0521(8)	Ga–Se2	2.4664(12)

4.2.3. Calculations

Electronic structure calculations were performed on $La_4Ga_2Se_6O_3$ with the projected augmented wave (PAW) method using the Vienna ab initio simulation package (VASP).[27] Exchange and correlation were treated in this density functional theory (DFT) method by the generalized gradient approximation, as parameterized by Perdew, Burke, and Ernzerhof.[28] Standard PAW potentials (La, Ga_d, Se, and O) were used. The plane-wave basis cutoff energy was set to 550 eV. The first Brillouin zone was sampled by a $8 \times 12 \times 25$ *k*-mesh. The convergence criteria were set to 10^{-8} eV for electronic optimization, and -2×10^{-2} eV for ionic relaxation. Crystal orbital Hamilton populations (−COHP), crystal orbital bond index (COBI), electron localization functions (ELF), and Bader charges were determined using the program LOBSTER (version 4.1.0).[29–32]

Phonon calculations were carried out using the Phonopy code, which applies the modified Parlinski-Li-Kawazoe method to compute force constants.[33] A $1 \times 1 \times 2$ supercell, with dimensions of ~$22 \times 12 \times 12$ Å, was used to determine the phonon band dispersion and density of states.

Transport properties were calculated using the BoltzTraP2 code, which applies the constant relaxation time approximation to interpolate the band structure obtained by DFT calculations.[34]

4.2.4. Diffuse reflectance spectroscopy

The optical diffuse reflectance spectrum for $La_4Ga_2Se_6O_3$ was measured from 200 nm (6.2 eV) to 1500 nm (0.8 eV) on a Cary 5000 UV-vis-NIR spectrophotometer equipped with a diffuse reflectance accessory. An optical polytetrafluoroethylene disc with >98% reflectivity in the range of 250 to 2200 nm was used as a reflectance standard. The absorption spectrum was generated

from the optical reflectance data using using the Kubelka-Munk function, $F(R) = \alpha/S = (1-R)^2/2R$, where α is the Kubelka–Munk absorption coefficient, S is the scattering coefficient, and R is the reflectance.[35]

4.3. Results and discussion

$La_4Ga_2Se_6O_3$ is a new oxyselenide in the La–Ga–Se–O system, in which the only other previously known quaternary phases are $LaGaSe_2O$,[13,20] $La_4Ga_{1.9}Se_{4.8}O_4$,[21] and Sm_3GaSe_5O.[22] It crystallizes in monoclinic space group $C2/c$ with two La, one Ga, three Se, and two O sites (**Figure 4-1**). The structure consists of familiar building motifs common to other oxychalcogenides. The O atoms are centred within tetrahedra formed by the La atoms, and these OLa_4 tetrahedra share edges to form one-dimensional strips, three tetrahedra wide, that extend down the *c*-direction. These strips can be regarded as fragments cut out from the much more prevalent two-dimensional slabs built from fluorite-type blocks, found in layered oxychalcogenides such as LaCuSO and layered oxypnictides such as LaFeAsO.[4] Parallel to these strips, pairs of zigzag chains built from corner-sharing $GaSe_4$ tetrahedra also extend down this direction. These La–O and Ga–Se building blocks are connected via the La atoms. There are four Se and four O atoms around La1, or six Se and two O atoms around La2, in coordination environments (CN8) that are quite irregular so that terminology such as square antiprismatic or bicapped trigonal prismatic can be regarded at best as approximations (**Figure A4-3**). All interatomic distances (La–Se, 3.1–3.5 Å; La–O, 2.4–2.5 Å; Ga–Se, 2.4–2.5 Å) are consistent with usual values.[36]

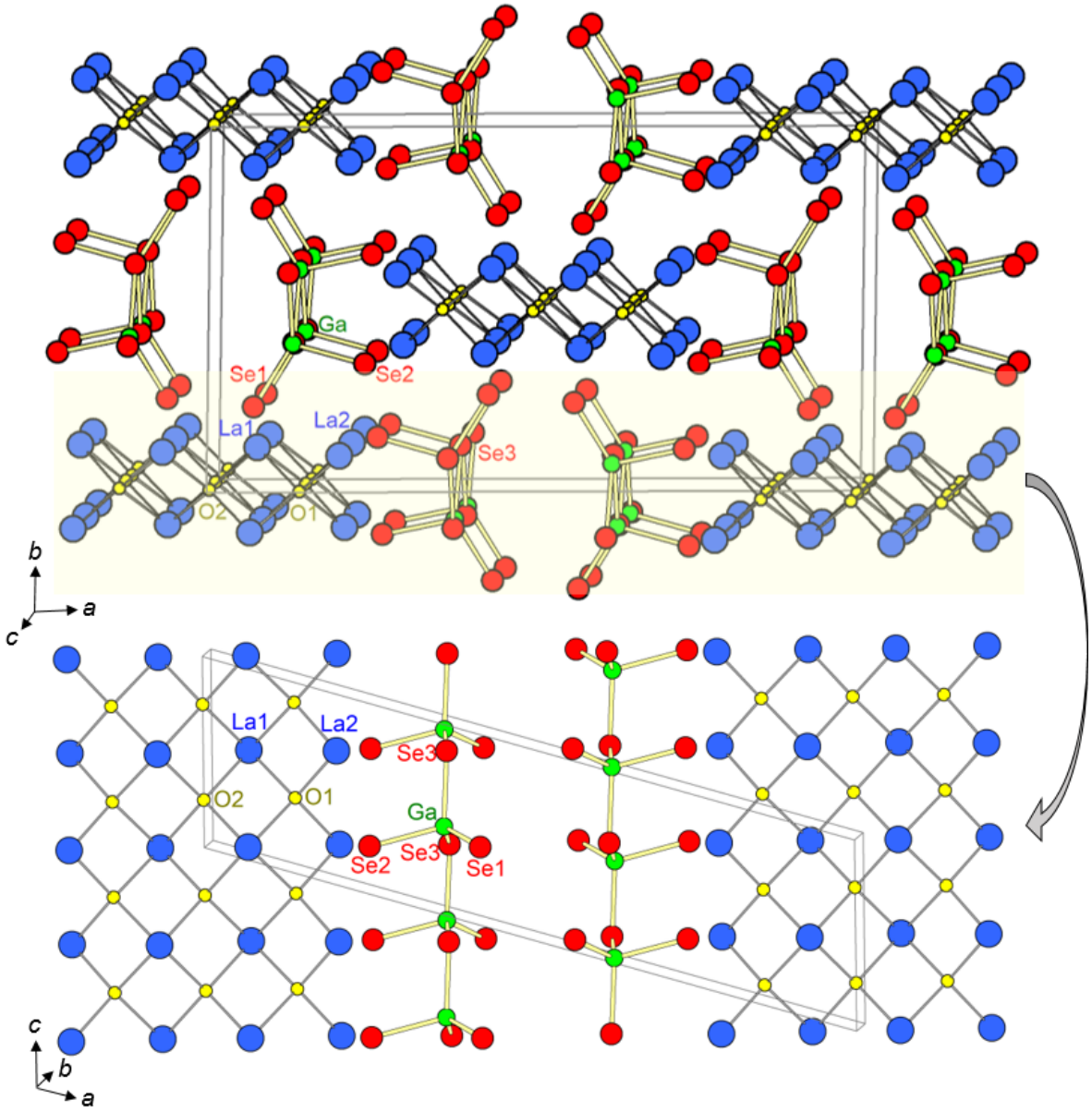

Figure 4-1. Structure of $La_4Ga_2Se_6O_3$ in terms of La–O and Ga–Se blocks.

The structure type of $La_4Ga_2Se_6O_3$ is new, but it is closely related to the orthorhombic structure of $La_4As_2S_6O_3$ (space group *Ibam*) (**Figure A4-4**).[37] In both cases, the chalcogen atoms are arranged in triangles that stack along the short *c*-axis repeat of 6 Å. The Ga atoms occupy tetrahedral sites between Se_3 triangles in an ordered fashion in $La_4Ga_2Se_6O_3$; in contrast, the As

atoms half-occupy trigonal pyramidal sites between S_3 triangles in a random fashion in $La_4As_2S_6O_3$, by virtue of the unphysically short distances (1.3 Å) caused by mirror symmetry perpendicular to *c*-axis (**Figure 4-2**). The more irregular coordination geometry around the nominally trivalent As atoms in $La_4As_2S_6O_3$ can be attributed to stereochemically active lone pairs which point toward void spaces between the stacks of S_3 triangles.

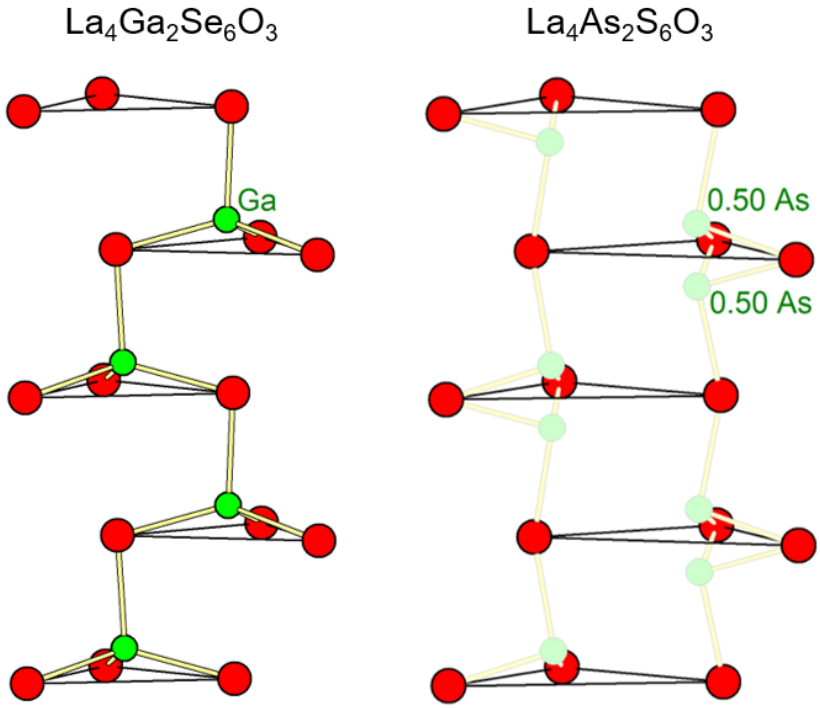

Figure 4-2. Arrangement of $GaSe_4$ tetrahedra in $La_4Ga_2Se_6O_3$, which contains fully occupied Ga sites, compared with arrangement of AsS_3 trigonal pyramids in $La_4As_2S_6O_3$, which contains half-occupied As sites.

Like other oxychalcogenides, $La_4Ga_2Se_6O_3$ is expected to be a semiconductor, in accordance with the charge-balanced formulation $(La^{3+})_4(Ga^{3+})_2(Se^{2-})_6(O^{2-})_3$, which is supported by bond valence sums[38] evaluated to be 2.8–3.1 for La, 3.0 for Ga, 1.8–2.1 for Se, and 2.1–2.2 for O atoms. The optical diffuse reflectance spectrum shows an absorption edge near 1.8 eV (**Figure 4-3**). Fitting to Tauc plots gives a band gap of 1.7 eV if direct, or 2.7 eV if indirect. DFT

calculations were also performed to evaluate the band gap of $La_4Ga_2Se_6O_3$ independently to ascertain which of these values is correct, and to ensure that the measurements were unaffected by the small amount of GaSe, which has an indirect band gap of 2.0 eV,[39] in the sample. In good agreement with the experimental results and the observed black colour of $La_4Ga_2Se_6O_3$ crystals, the calculated band dispersion and DOS reveal a band gap of 1.75 eV, which is direct, with the valence band maximum and conduction band minimum located at the Brillouin zone centre (**Figure 4-4(a)**). Many flat bands are located close to the Fermi level, suggesting a high electron effective mass. As seen in the –COHP and COBI curves, optimization of Ga–Se bonding interactions largely controls the band gap, with all bonding levels filled below the Fermi level and all antibonding levels empty above (**Figure 4-4(b)**).

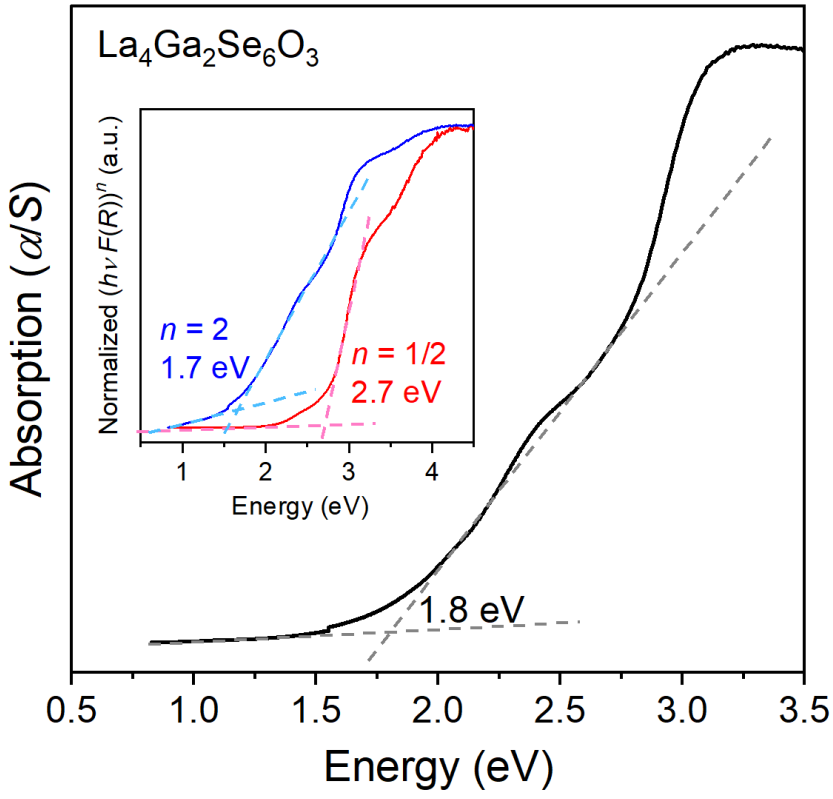

Figure 4-3. Optical diffuse reflectance spectrum for $La_4Ga_2Se_6O_3$. The inset shows fittings assuming that the band gap is direct ($n = 2$) or indirect ($n = ½$).

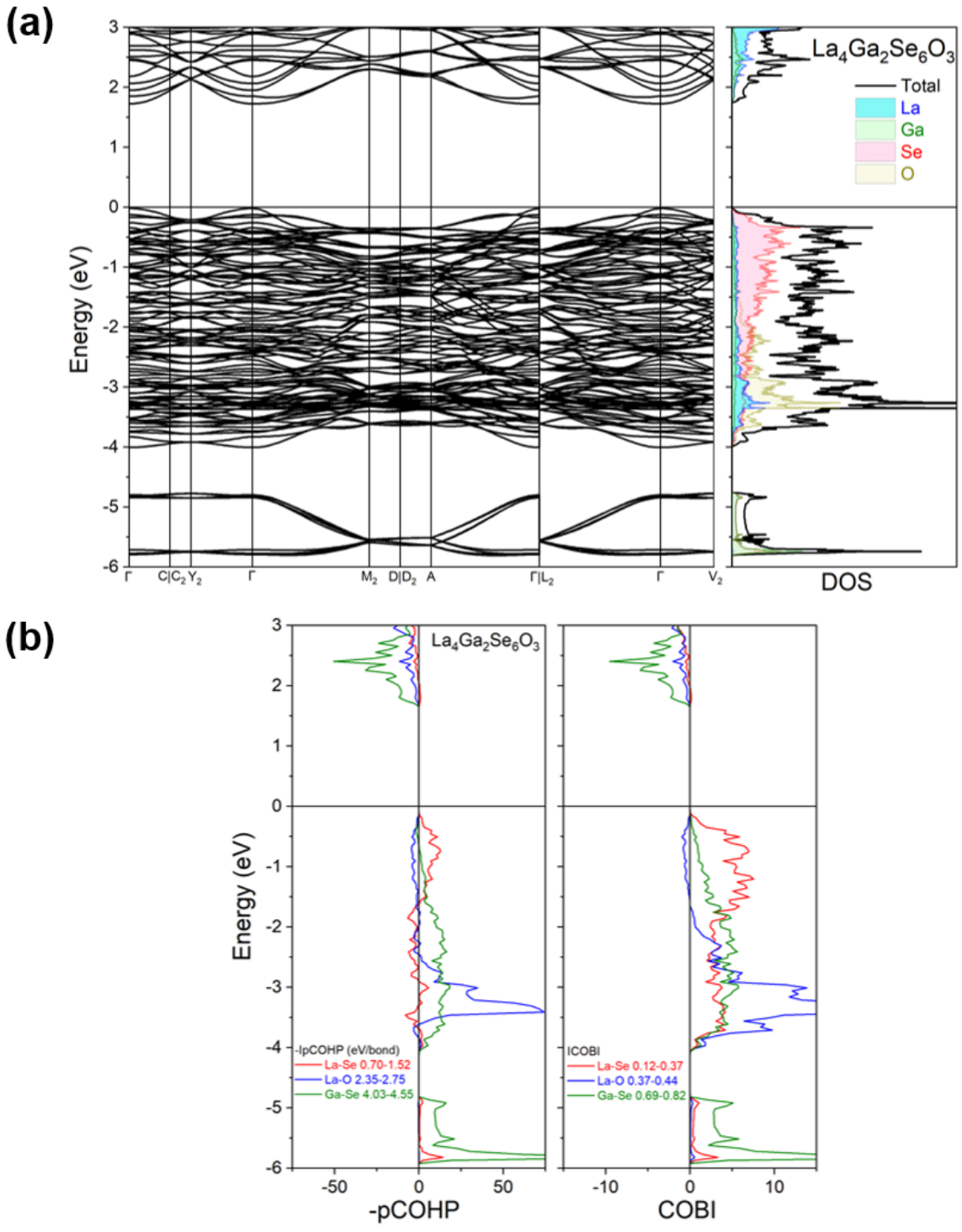

Figure 4-4. (a) Band dispersion and DOS for $La_4Ga_2Se_6O_3$. (b) –COHP and COBI curves for La–Se, La–O, and Ga–Se contacts (positive values are bonding interactions and negative values are antibonding interactions). Integrated –COHP and COBI values are provided in eV/bond.

As gauged by the integrated COBI values (ICOBI in eV/bond), the bonding character is largely ionic for the La–Se (0.12–0.37) and La–O contacts (0.37–0.44), but largely covalent for the Ga–Se contacts (0.69–0.82). This distinction is clearly visualized in the ELF plots, which show that the electron density is highly localized around the La and O atoms, separated by minima (blue) from the other atoms, whereas the electron density is intermediate and shared in the region (green) between the Ga and Se atoms (**Figure 4-5**). Moreover, the Bader charges are more extreme for the La (1.87+ to 1.99+) and O atoms (1.37– to 1.39–), but much less so for the Ga (0.66+) and Se atoms (0.52– to 1.01–). These results confirm the notion, often assumed but rarely quantified, that the bonding in oxychalcogenides can be separated into more ionic vs. more covalent substructures.

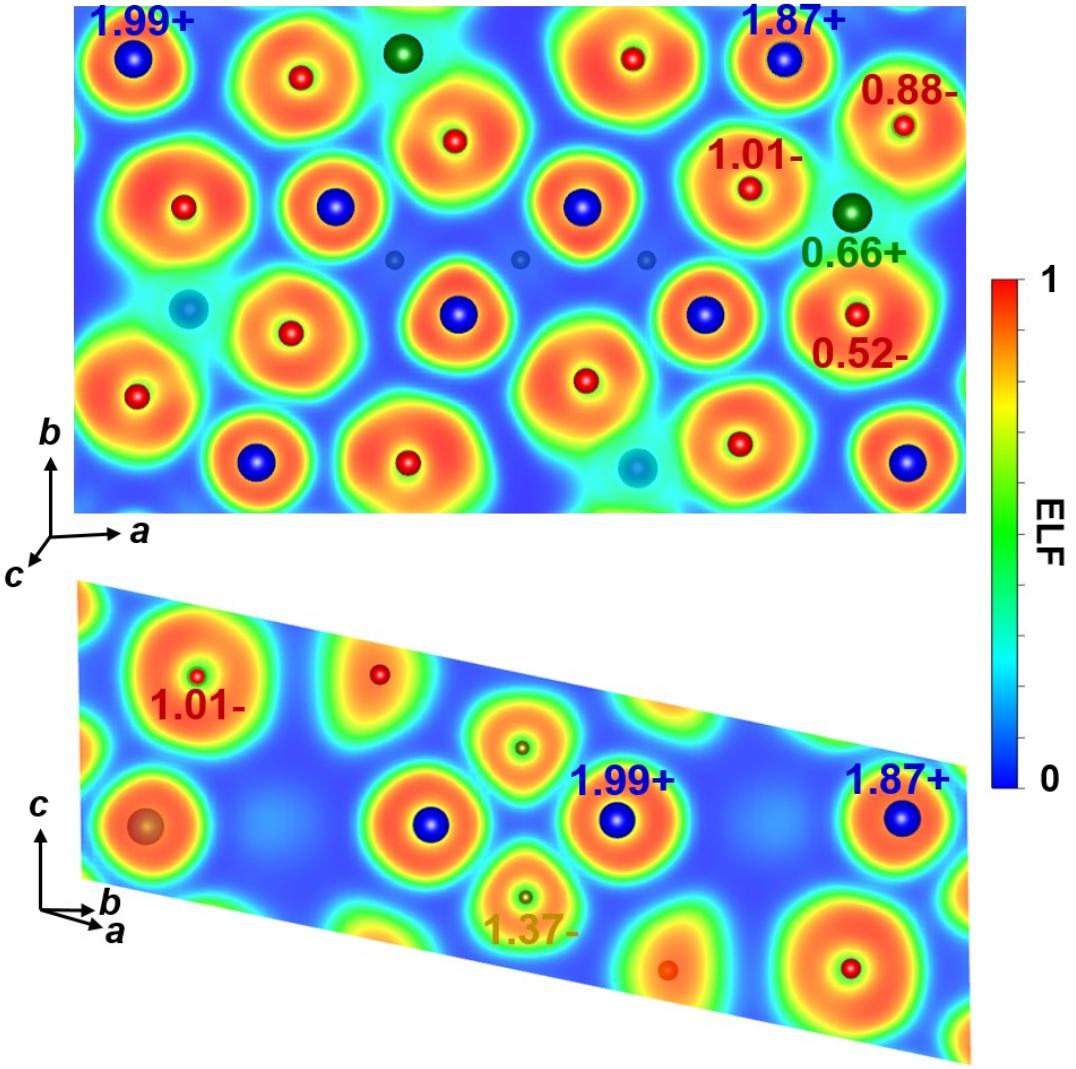

Figure 4-5. ELF and Bader charges for slices of $La_4Ga_2Se_6O_3$ taken parallel to $(10\bar{1})$ (top) and $(2\bar{1}0)$ (bottom).

The phonon band dispersion and DOS show a distinct separation between the lower frequency acoustic vibrations (< 300 cm^{-1}) and higher frequency optical vibrations, which attain a maximum frequency of 477 cm^{-1} (**Figure 4-6**). No imaginary frequencies are found, indicating that the structure is dynamically stable. The acoustic modes involve contributions from the heavier

La, Ga, and Se atoms, whereas the optical modes are dominated by the lighter O atoms, similar to other oxychalcogenides and oxypnictides.

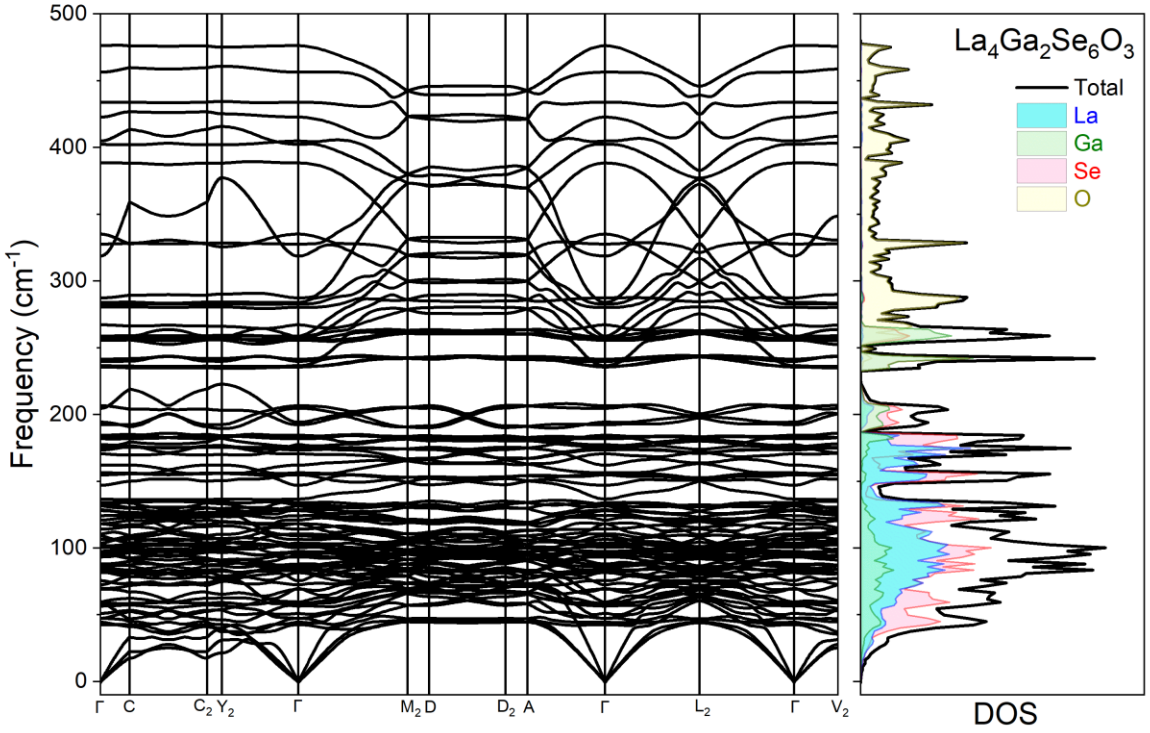

Figure 4-6. Phonon dispersion and DOS for $La_4Ga_2Se_6O_3$.

Given that $La_4Ga_2Se_6O_3$ is a semiconductor with a large effective mass near the Fermi level, it is worthwhile evaluating its potential as a thermoelectric material, whose efficiency is proportional to the power factor, $PF = S^2\sigma$, where S is the Seebeck coefficient (or thermopower) and σ is the electrical conductivity. Semi-classical Boltzmann transport theory was applied within the constant relaxation time approximation, allowing properties such as the power factor and thermal conductivity to be determined relative to the relaxation time τ_o, which should be obtained by experiment. The Seebeck coefficients were calculated at different temperatures from 300 to 900 K, within a chemical potential range μ of ±1.8 eV, relative to the Fermi level at 0 eV (**Figure**

4-7(a)). The most extreme values are $S = \pm 1.6$ mV K^{-1}, occurring at 300 K for $\mu = \pm 0.4$ eV, where negative S or positive μ implies electron doping (n-type) and positive S or negative μ implies hole doping (p-type). The electrical conductivity reaches slightly higher values for n-type than p-type doping (**Figure 4-7(b)**). Combining the dependence of the Seebeck coefficient and electrical conductivity results in maxima in the power factor at $\mu = \pm 0.9$ eV, again slightly higher for n-doping (**Figure 4-7(c)**). These maxima in the power factor increase monotonically with higher temperature (**Figure 4-7(d)**). Relaxation times are difficult to compute reliably, but if typical values of 10^{-15} to 10^{-14} s^{-1} are assumed, then the predicted power factor of ~10^{-4} to 10^{-3} W K^{-2} m^{-1} s^{-1} is competitive, with other oxychalcogenides.[7] To confirm these thermoelectric properties experimentally, there remain some challenges to be resolved, including the need to improve the phase purity and the tendency of oxychalcogenide samples to crack upon sintering.

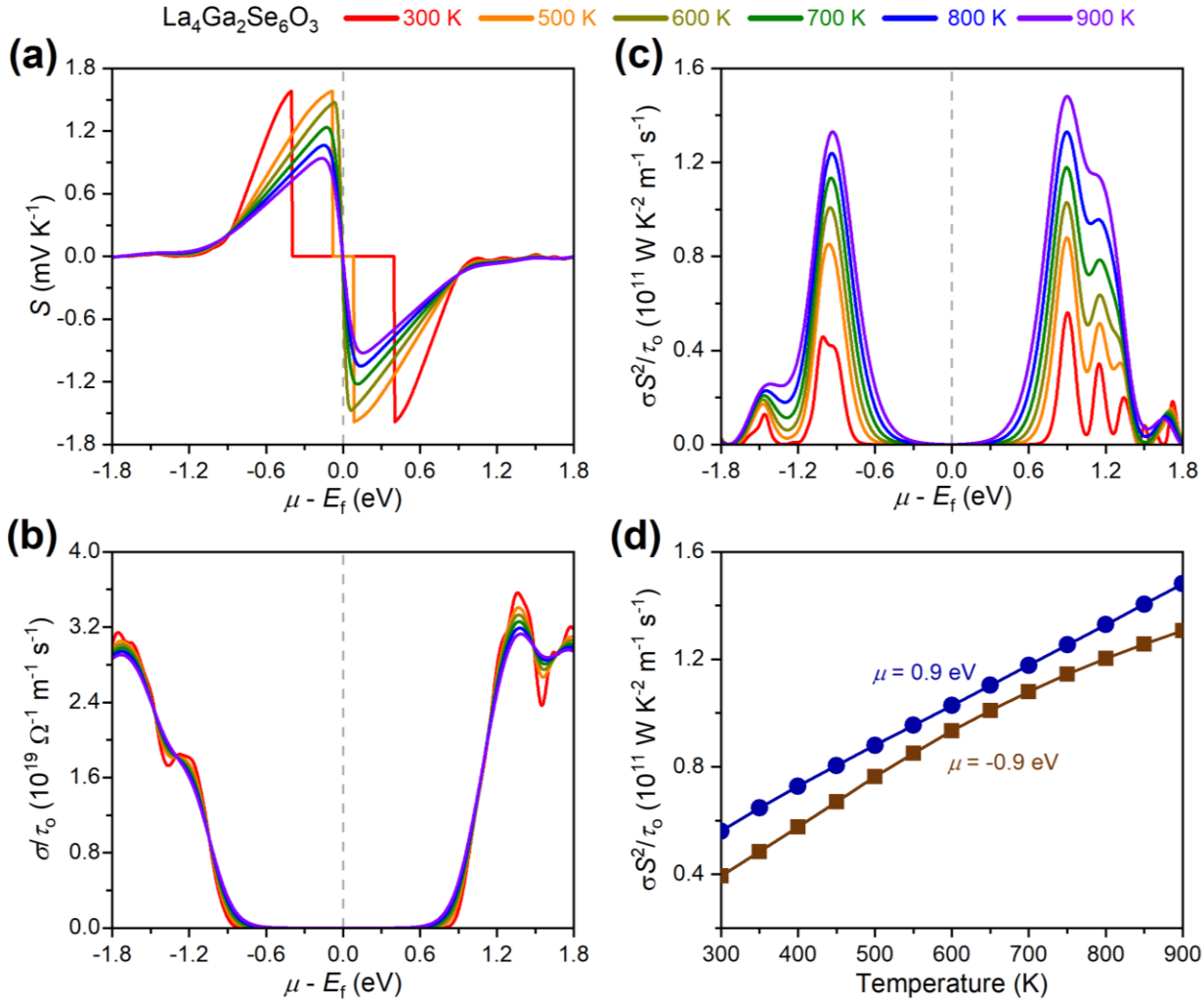

Figure 4-7. Dependence of (a) Seebeck coefficient, (b) electrical conductivity, and (c) power factor on chemical potential at different temperatures for $La_4Ga_2Se_6O_3$. The maxima in the power factor, at $\mu = \pm 0.9$ eV, are plotted as a function of temperature in (d).

4.4. Conclusions

The new structure type adopted by the oxyselenide $La_4Ga_2Se_6O_3$ illustrates the continuing theme of segregated blocks of more ionic (La–O) vs. more covalent (Ga–Se) bonding character typical of oxychalcogenides, as visualized in ELF plots and quantified by COBI analysis. This compound is a direct band gap semiconductor predicted to have transport properties comparable to other oxychalcogenides, with a thermoelectric power factor that could be enhanced through n-doping, possibly through substitution of Ga with Ge or O with F.

4.5. References

(1) Kageyama, H.; Hayashi, K.; Maeda, K.; Attfield, J. P.; Hiroi, Z.; Rondinelli, J. M.; Poeppelmeier, K. R. *Nat. Commun.* **2018**, *9*, 772.

(2) Harada, J. K.; Charles, N.; Poeppelmeier, K. R.; Rondinelli, J. M. *Adv. Mater.* **2019**, *31*, 1805295.

(3) Tripathi, T. S.; Karppinen, M. *Adv. Mater. Interfaces* **2021**, *8*, 2100146.

(4) Clarke, S. J.; Adamson, P.; Herkelrath, S. J. C.; Rutt, O. J.; Parker, D. R.; Pitcher, M. J.; Smura, C. F. *Inorg. Chem.* **2008**, *47*, 8473–8486.

(5) Luu, S. D. N.; Vaqueiro, P. *J. Materiomics* **2016**, *2*, 131–140.

(6) Larquet, C.; Carenco, S. *Front. Chem.* **2020**, *8*, 179.

(7) Tippireddy, S.; Prem Kumar, D. S.; Das, S.; Malik, R. C. *ACS Appl. Energy Mater.* **2021**, *4*, 2022–2040.

(8) Orr, M.; Hebberd, G. R.; McCabe, E. E.; Macaluso, R. T. *ACS Omega* **2020**, *7*, 8209–8218.

(9) Ueda, K.; Inoue, S.; Hirose, S.; Kawazoe, H.; Hosono, H. *Appl. Phys. Lett.* **2020**, *77*, 2701–2703.

(10) Palazzi, M.; Carcaly, C.; Flahaut, J. *J. Solid State Chem.* **1980**, *35*, 150–155.

(11) Ishikawa, A.; Takata, T.; Kondo, J. N.; Hara, M.; Kobayashi, H.; Domen, K. *J. Am. Chem. Soc.* **2002**, *124*, 13547–13553.

(12) Mizuguchi, Y.; Omachi, A.; Goto, Y.; Kamihara, Y.; Matoba, M.; Hiroi, T.; Kajitani, J.; Miura, O. *J. Appl. Phys.* **2014**, *116*, 163915.

(13) Guittard, M.; Bénazeth, S.; Dugué, J.; Jaulmes, S.; Palazzi, M.; Laruelle, P.; Flahaut, J. *J. Solid State Chem.* **1984**, *51*, 227–238.

(14) Carré, D.; Guittard, M.; Jaulmes, S.; Mazurier, A.; Palazzi, M.; Pardo, M. P.; Laruelle, P.; Flahaut, J. *J. Solid State Chem.* **1984**, *55*, 287–292.

(15) Figueiredo, M. O. *Inorg. Chim. Acta* **1987**, *140*, 161–164.

(16) Jaulmes, S. *Acta Crystallogr. Sect. B* **1978**, *34*, 2610–2612.

(17) Dugué, J.; Guittard, M. *Acta Crystallogr. Sect. B* **1982**, *38*, 2368–2371.

(18) Mazurier, A.; Guittard, M.; Jaulmes, S. *Acta Crystallogr. Sect. B* **1982**, *38*, 379–382.

(19) Jaulmes, S.; Mazurier, A.; Guittard, M. *Acta Crystallogr. Sect. C* **1983**, *39*, 1594–1597.

(20) Bénazeth, S.; Guittard, M.; Laruelle, P. *Acta Crystallogr. Sect. C* **1984**, *40*, 345–347.

(21) Bénazeth, S.; Laruelle, P.; Guittard, M. *J. Solid State Chem.* **1989**, *78*, 148–153.

(22) Mishra, V.; Mumbaraddi, D.; Iyer, A. K.; Yin, W.; Mar, A. *J. Solid State Chem.* **2022**, *308*, 122901.

(23) Ogisu, K.; Ishikawa, A.; Shimodaira, Y.; Takata, T.; Kobayashi, H.; Domen, K. *J. Phys. Chem. C* **2008**, *112*, 11978–11984.

(24) Sheldrick, G. M. *Acta Crystallogr., Sect. A: Found. Crystallogr.* **2008**, *64*, 112–122.

(25) Gelato, L. M.; Parthé, E. *J. Appl. Crystallogr.* **1987**, *20*, 139–143.

(26) Spek, A. L. *Acta Crystallogr., Sect. D* **2009**, *65*, 148–155.

(27) Hafner, J. *J. Comput. Chem.* **2008**, *29*, 2044–2078.

(28) Perdew, J. P.; Burke, K.; Ernzerhof, M. *Phys. Rev. Lett.* **1996**, *77*, 3865–3868.

(29) Deringer, V. L.; Tchougréeff, A. L.; Dronskowski, R. *J. Phys. Chem. A* **2011**, *115*, 5461–5466.

(30) Maintz, S.; Deringer, V. L.; Tchougréeff, A.L.; Dronskowski, R. *J. Comput. Chem.* **2013**, *34*, 2557–2567.

(31) Grin, Y.; Savin, A.; Silvi, B. The ELF perspective of chemical bonding. In *The Chemical Bond: Fundamental Aspects of Chemical Bonding*; Frenking, G., Shaik, S., Eds.; Wiley-VCH, Weinheim, 2014, pp. 345−382.

(32) Maintz, S.; Deringer, V. L.; Tchougréeff, A. L.; Dronskowski, R. *J. Comput. Chem.* **2016**, *37*, 1030–1035.

(33) Togo, A.; Tanaka, I. *Scr. Mater.* **2015**, *28*, 1−5.

(34) Madsen, G. K. H.; Carrete, J.; Verstraete, M. J. *Comput. Phys. Commun.* **2018**, *231*, 140–145.

(35) Kortüm, G. *Reflectance Spectroscopy*; Springer, New York, 1969.

(36) Villars, P.; Cenzual, K. *Pearson's Crystal Data – Crystal Structure Database for Inorganic Compounds,* Release 2021/22, ASM International, Materials Park, OH, USA.

(37) Palazzi, M.; Jaulmes, S. *Acta Crystallogr., Sect. B* **1981**, *37*, 1340−1342.

(38) Brese, N. E.; O'Keeffe, M. *Acta Crystallogr., Sect. B: Struct. Sci.* **1991**, *47*, 192–197.

(39) Bube, R. H.; Lind, E. L. *Phys. Rev.* **1959**, *115*, 1159–1164.

Chapter 5.

Structure and optical properties of $RE_4Ga_2Se_7O_2$ (*RE* = Pr, Nd) containing trigonal bipyramidal $GaSe_5$ units

5.1. Introduction

Introducing more than one type of anion in a solid state compound offers greater flexibility to control chemical and physical properties, by taking advantage of the different electronegativities, sizes, polarizabilities, and oxidation states of various nonmetals. Such mixed-anion compounds could consist of various combinations of oxide, halide (F, Cl, Br), chalcogenide (S, Se, Te), or pnictide anions (P, As, Sb).[1–8] Rare-earth oxysufides RE_2SO_2, used as phosphors for cathode ray tubes, were among the earliest examples of mixed-anion compounds. Various quaternary rare-earth oxychalcogenides *RE*–*M*–*Ch*–O (*M* = d- or p-block metals or metalloids) have attracted wide attention as thermoelectrics (LaBiCh_2O),[5] transparent semiconductors (LaCuSO),[9] superconductors ($LaO_{1-x}BiS_2$),[10] ionic conductors (LaAgSO),[11] and photocatalysis ($Sm_2Ti_2S_2O_5$,[12] $LaInS_2O$).[13]

As part of ongoing investigations on oxychalcogenides as candidates for optical and thermoelectric materials, we have focused on the quaternary systems *RE*–*M*–*Ch*–O (*M* = Ga, In; *Ch* = S, Se). Previously known compounds in these systems include *REMCh*$_2$O (*M* = Ga, In; *Ch* = S, Se),[14–18] $RE_4Ga_2Ch_5O_4$ (*Ch* = S, Se),[16,19,20] $RE_4Ga_{1.33}S_4O_4$,[16] $La_{3.33}Ga_6S_{12}O_2$,[21] La_3GaS_5O,[22] $La_5In_3S_9O_3$,[18] $La_{10}In_6S_{17}O_6$,[23] and Sm_3GaSe_5O.[24] Most of these compounds are oxysulfides, whereas the corresponding oxyselenides are much less numerous. The compound Sm_3GaSe_5O was discovered inadvertently as a result of targeting the hypothetical solid solutions $RE_3MCh_{6-x}O_x$,

based on the existence of the ternary phases RE_3MCh_6.[24] It is becoming clear that such oxychalcogenides cannot be extrapolated in a simple way from parent chalcogenides, and that more complex structure-building principles are at play in these mixed-anion systems. In particular, there is a preference of the *RE* and O atoms to be bonded together in recurring structural motifs involving ORE_4 tetrahedra.

Here we report the synthesis of the oxyselenides $RE_4Ga_2Se_7O_2$ (*RE* = Pr, Nd) and their structure determination. To evaluate their potential as optical and thermoelectric materials, their optical band gaps were measured and their transport coefficients were predicted from DFT calculations.

5.2. Experimental

5.2.1. Synthesis

The oxyselenides $RE_4Ga_2Se_7O_2$ (*RE* = Pr, Nd) were initially identified in the course of targeting hypothetical solid solutions $RE_3MCh_{6-x}O_x$ (*M* = Ga, In; *Ch* = S, Se). Rational syntheses were subsequently developed. Starting materials were freshly filed *RE* pieces (Pr, Nd; 99.9%, Hefa), PrO_2 or Nd_2O_3 powders (99.99%, Sigma Aldrich), Ga chunks (99.9%, Alfa Aesar), and Se powder (99.99%, Sigma Aldrich). Ga_2Se_3 was prepared by heating a stoichiometric mixture of Ga and Se at 950 °C in sealed fused-silica tubes.

For $Pr_4Ga_2Se_7O_2$, a mixture of Pr, PrO_2, Ga_2Se_3, and Se in the molar ratio of 3:1:1:4 was prepared; for $Nd_4Ga_2Se_7O_2$, a mixture of Nd, Nd_2O_3, Ga_2Se_3, and Se in the molar ratio of 8:2:3:12 was prepared. The total mass of each mixture was 300 mg, with a 5% weight excess of Se added to compensate for volatilization losses. The mixtures were pressed into pellets and placed in fused-silica tubes (12-mm diameter, 15-cm length), which were evacuated and sealed. For growth of

single crystals, the tubes were heated to 950 °C in 24 h, held there for 72 h, cooled to 400 °C in 96 h, and then cooled to room temperature by shutting off the furnace. Thin, needle-shaped, dark brown single crystals of $Pr_4Ga_2O_2Se_7$ and $Nd_4Ga_2O_2Se_7$ were found in the products (**Figure A5-1**) and examined on a Zeiss Sigma 300 VP field emission scanning electron microscope operated with an accelerating voltage of 15 kV and equipped with a Bruker Quantax 600 system with dual X-Flash 6/60 detectors. Energy-dispersive X-ray (EDX) analysis indicates an average composition (in atomic %) of 24–25% *RE*, 10–11% Ga, 46–47% Se, and 16–19% O, in good agreement with expectations (27% *RE*, 13% Ga, 47% Se, 13% O). For preparation of phase-pure samples, the tubes were heated to 950 °C in 18 h, held there for 48 h, and cooled to room temperature in 18 h. Powder X-ray diffraction (XRD) patterns were collected on a Bruker D8 Advance X-ray diffractometer equipped with a Cu $K\alpha_1$ radiation source operated at 40 kV and 40 mA. XRD patterns recollected after a few months are unchanged, confirming that the samples are air-stable (**Figure 5-1**). Attempts were made to synthesize other *RE* analogues of these compounds under the same conditions as described above, but were unsuccessful.

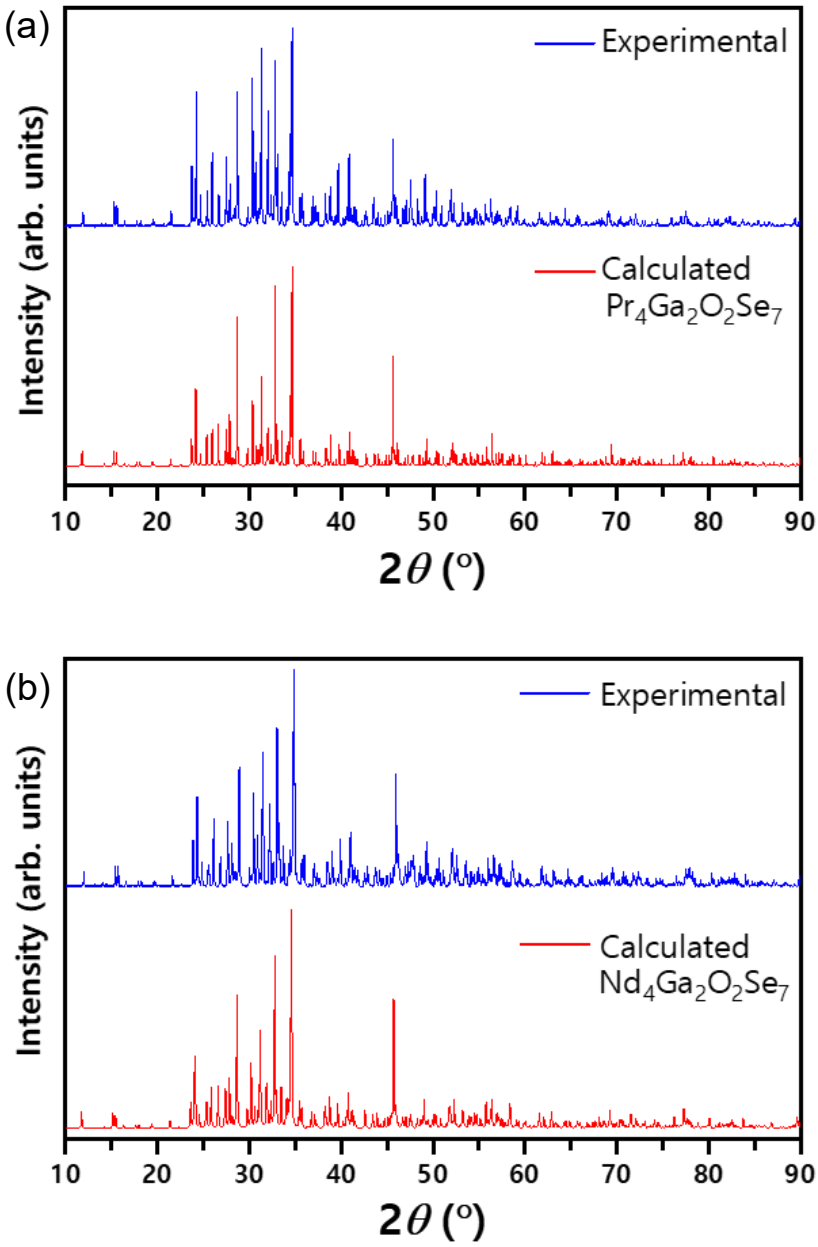

Figure 5-1. Powder XRD patterns of (a) $Pr_4Ga_2Se_7O_2$ and (b) $Nd_4Ga_2Se_7O_2$.

5.2.2. Structure determination

Intensity data were collected on single crystals of $Pr_4Ga_2Se_7O_2$ and $Nd_4Ga_2Se_7O_2$ at room temperature on a Bruker PLATFORM diffractometer equipped with a SMART APEX II CCD area detector and a graphite-monochromated Mo Kα radiation source, using ω scans at 7–8 different ϕ angles with a frame width of 0.3° and an exposure time 60 s per frame. Absorption corrections were applied. Structure solution and refinement were carried out with use of the SHELXTL (version 2018/3) program package.[25]

On the basis of Laue symmetry, intensity statistics, and systematic absences, the orthorhombic space group *Pnma* was chosen. The locations of four *RE*, two Ga, and seven Se atoms were located by direct methods. Two additional peaks were found in difference electron density maps and assigned as O atoms. Refinements were straightforward, with no indication for disorder. Atomic positions were standardized with the program STRUCTURE TIDY.[26] Crystal data, atomic and displacement parameters, and interatomic distances are listed in **Table 5-1** to **Table 5-3**.

Table 5-1. Crystallographic data for $Pr_4Ga_2Se_7O_2$ and $Nd_4Ga_2Se_7O_2$.

formula	$Pr_4Ga_2Se_7O_2$	$Nd_4Ga_2Se_7O_2$
formula mass (amu)	1287.80	1301.12
space group	*Pnma* (No. 62)	*Pnma* (No. 62)
a (Å)	11.721(2)	11.683(2)
b (Å)	3.9882(7)	3.9667(7)
c (Å)	29.644(5)	29.581(5)
V (Å^3)	1385.8(4)	1301.12
Z	4	4
T (K)	296	296
ρ_{calcd} (g cm^{-3})	6.173	6.304
crystal dimensions (mm)	0.080 × 0.020 × 0.011	0.169 × 0.027 × 0.019
μ(Mo $K\alpha$) (mm^{-1})	35.976	37.302
2θ limits	2.74–59.28°	3.75–59.64°
data collected	$-16 \le h \le 16$, $-5 \le k \le 5$, $-41 \le l \le 41$	$-32 \le h \le 32$, $-10 \le k \le 10$, $-18 \le l \le 18$
no. of data collected	19586	37878
no. of unique data, including $F_o^2 < 0$	2228 (R_{int} = 0.1268)	2232 (R_{int} = 0.1476)
no. of unique data, with $F_o^2 > 2\sigma(F_o^2)$	1499	1640
no. of variables	91	91
$R(F)$ for $F_o^2 > 2\sigma(F_o^2)$ [a]	0.0514	0.0408
$R_w(F_o^2)$ [b]	0.1171	0.0852
goodness of fit	1.033	1.031
$(\Delta\rho)_{max}$, $(\Delta\rho)_{min}$ (e Å^{-3})	2.895, –3.777	2.512, –3.322

[a] $R(F) = \sum||F_o| - |F_c|| / \sum|F_o|$. [b] $R_w(F_o^2) = [\sum[w(F_o^2 - F_c^2)^2] / \sum wF_o^4]^{1/2}$; $w^{-1} = [\sigma^2(F_o^2) + (Ap)^2 + Bp]$, where $p = [\max(F_o^2,0) + 2F_c^2]/3$.

Table 5-2. Atomic coordinates and equivalent isotropic displacement parameters for $Pr_4Ga_2Se_7O_2$ and $Nd_4Ga_2Se_7O_2$.[a]

atom	*x*	*y*	*z*	U_{eq} (Å^2) [b]
$Pr_4Ga_2Se_7O_2$				
Pr1	0.23596(9)	¼	0.05905(3)	0.0146(2)
Pr2	0.36342(9)	¼	0.66841(4)	0.0149(2)
Pr3	0.49675(11)	¼	0.81644(4)	0.0228(3)
Pr4	0.53559(9)	¼	0.55117(3)	0.0134(2)
Ga1	0.0938(2)	¼	0.43178(8)	0.0183(5)
Ga2	0.3600(2)	¼	0.29650(8)	0.0193(5)
Se1	0.02883(19)	¼	0.56221(10)	0.0308(6)
Se2	0.04544(18)	¼	0.24153(7)	0.0175(4)
Se3	0.15274(19)	¼	0.35578(7)	0.0221(5)
Se4	0.2293(2)	¼	0.76663(7)	0.0226(5)
Se5	0.26155(18)	¼	0.47666(7)	0.0171(4)
Se6	0.32097(17)	¼	0.15734(7)	0.0158(4)
Se7	0.45826(18)	¼	0.36766(6)	0.0156(4)
O1	0.0531(10)	¼	0.0273(4)	0.010(2)
O2	0.3425(12)	¼	0.5893(4)	0.016(3)
$Nd_4Ga_2Se_7O_2$				
Nd1	0.23483(7)	¼	0.05879(3)	0.01310(17)
Nd2	0.36539(7)	¼	0.66795(3)	0.01344(17)
Nd3	0.50007(8)	¼	0.81498(3)	0.0213(2)
Nd4	0.53512(7)	¼	0.55101(3)	0.01246(17)
Ga1	0.09313(15)	¼	0.43170(6)	0.0175(3)
Ga2	0.35536(15)	¼	0.29763(6)	0.0182(4)
Se1	0.03008(15)	¼	0.56236(8)	0.0345(5)
Se2	0.04269(13)	¼	0.24066(5)	0.0165(3)
Se3	0.14957(14)	¼	0.35491(5)	0.0207(3)
Se4	0.23044(15)	¼	0.76575(6)	0.0216(3)
Se5	0.26164(13)	¼	0.47636(5)	0.0155(3)
Se6	0.31871(13)	¼	0.15716(5)	0.0142(3)
Se7	0.45704(13)	¼	0.36813(5)	0.0144(3)
O1	0.0539(8)	¼	0.0280(3)	0.0115(19)
O2	0.3445(9)	¼	0.5886(3)	0.015(2)

[a] All atoms are located in Wyckoff position 4*c*. [b] U_{eq} is defined as one-third of the trace of the orthogonalized U_{ij} tensor.

Table 5-3. Interatomic distances (Å) in $Pr_4Ga_2Se_7O_2$ and $Nd_4Ga_2Se_7O_2$.

	$Pr_4Ga_2Se_7O_2$	$Nd_4Ga_2Se_7O_2$
*RE*1–Se1 (×2)	3.404(2)	3.3895(16)
*RE*1–Se5 (×2)	3.1532(18)	3.1434(14)
*RE*1–Se6	3.079(2)	3.0705(18)
*RE*2–Se2 (×2)	3.1330(19)	3.1166(14)
*RE*2–Se4	3.309(3)	3.295(2)
*RE*2–Se6 (×2)	2.9589(17)	2.9431(13)
*RE*2–Se7 (×2)	3.0803(18)	3.0621(14)
*RE*3–Se1	3.617(3)	3.645(3)
*RE*3–Se2 (×2)	3.0253(18)	3.0027(13)
*RE*3–Se3 (×2)	2.8994(19)	2.8957(14)
*RE*3–Se4	3.465(3)	3.470(2)
*RE*3–Se4	3.673(3)	3.598(2)
*RE*3–Se6 (×2)	3.0241(18)	3.0159(14)
*RE*4–Se5 (×2)	3.2110(19)	3.1980(14)
*RE*4–Se7 (×2)	3.1259(16)	3.1086(14)
Ga1–Se1 (×2)	2.4646(19)	2.4570(15)
Ga1–Se3	2.357(3)	2.365(2)
Ga1–Se5	2.374(3)	2.371(2)
Ga2–Se2	2.449(3)	2.464(2)
Ga2–Se3	2.998(3)	2.941(2)
Ga2–Se4 (×2)	2.4199(19)	2.4141(15)
Ga2–Se7	2.403(3)	2.400(2)
*RE*1–O1	2.340(12)	2.308(9)
*RE*1–O1 (×2)	2.372(7)	2.360(5)
*RE*2–O2	2.358(12)	2.360(9)
*RE*4–O1	2.335(12)	2.346(9)
*RE*4–O1 (×2)	2.358(6)	2.341(5)
*RE*4–O2	2.530(14)	2.489(10)

5.2.3. Calculations

Electronic structure calculations were performed on $Pr_4Ga_2Se_7O_2$ and $Nd_4Ga_2Se_7O_2$ using the projected augmented wave method as implemented in the Vienna ab initio simulation package (VASP).[27–29] The generalized gradient approximation (GGA) was used to treat the exchange and correlation in the density functional theory (DFT) used in VASP, as parameterized by Perdew, Burke, and Ernzerhof.[30–32] The recommended standard PAW potentials Pr_3, Nd_3 Se, Ga_d, and O were used with the plane-wave basis cutoff energy set to 550 eV. A 12 × 35 × 5 gamma centered *k*-mesh was chosen to sample the first Brillouin zone. The convergence criteria for electronic relaxation were set to 10^{-8} eV and $|-2\times10^{-2}|$ for ionic relaxation. Electron localization function (ELF) plots were prepared using VESTA.[33,34] Bader analysis was performed to evaluate the charges on atoms.[35–37] Chemical bonding was examined by assessing crystal orbital Hamilton populations (–COHP) and crystal orbital bond index (COBI) using the program local-orbital basis suite toward electronic structure (LOBSTER *version* 4.1.0).[38–40] Transport properrties were calculated using the Boltztrap2 code, with the constant relaxation time approximation applied to interpolate the band structure obtained by DFT calculations.[41]

5.2.4. Diffuse reflectance spectroscopy

Optical diffuse reflectance spectra for $Pr_4Ga_2O_2Se_7$ and $Nd_4Ga_2O_2Se_7$ were measured on from 200 nm (6.2 eV) to 1400 nm (0.8 eV) on a Cary 5000 UV-vis-NIR spectrophotometer equipped with a diffuse reflectance accessory. An optical polytetrafluorethylene disc with >98% reflectivity in the range of 250–2200 nm was used as a reflectance standard. The reflectance spectra were converted to absorption spectra using the Kubelka-Munk function, $F(R) = \alpha/S = (1–$

$R)^2/2R$, where α is the Kubelka–Munk absorption coefficient, S is the scattering coefficient, and R is the reflectance.

5.3. Results and discussion

The oxyselenides $Pr_4Ga_2Se_7O_2$ and $Nd_4Ga_2Se_7O_2$ were prepared by reactions at 950 °C. They crystallize in orthorhombic space group *Pnma* and contain four *RE,* two Ga, seven Se, and two O sites, all lying on mirror planes. The structure can be described in terms of three building blocks that extend along the *b*-direction: *RE*–O, *RE*–Se, and Ga–Se (**Figure 5-2**). The *RE*–O blocks consist of edge-sharing RE_4O tetrahedra, four units thick. Within these blocks, the three types of *RE* atoms are coordinated by Se and O atoms in bicapped trigonal prismatic geometry (CN8). The *RE*–Se blocks are really just one-dimensional confacial columns of $RESe_6$ trigonal prisms (CN6) extending along the *b*-direction. The Ga–Se blocks are particularly interesting, consisting of $GaSe_4$ tetrahedra connected to $GaSe_5$ trigonal bipyramids. Coordination environments are shown in further detail in **Figure A5-2** and **Figure A5-3**.

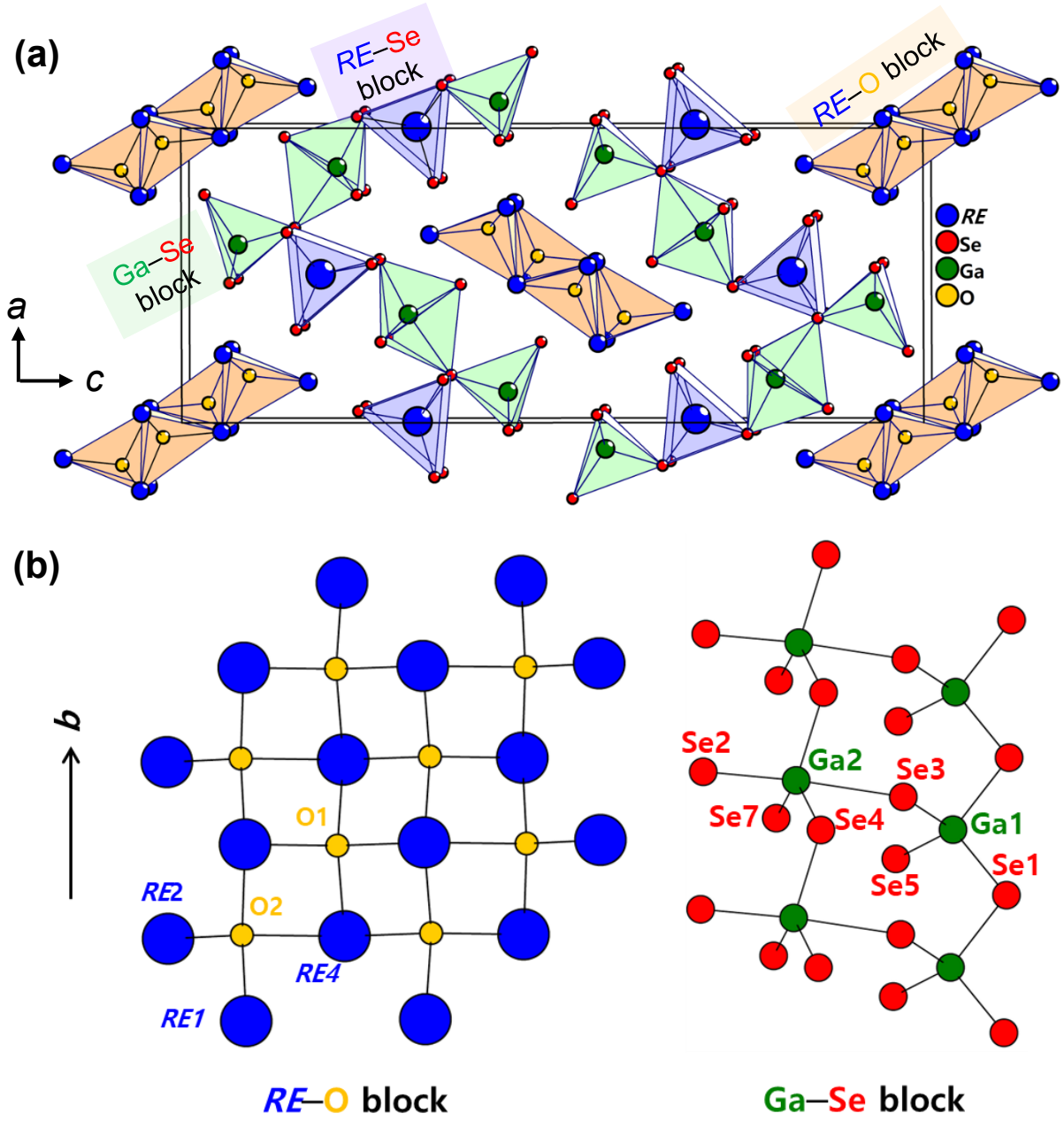

Figure 5-2. (a) Crystal structure of $RE_4Ga_2Se_7O_2$ (*RE* = Pr, Nd) built of (b) *RE*–O (left) and Ga–Se (right) blocks that extend along the *b*-direction.

The RE_4O tetrahedra are a recurring theme in oxychalcogenides, occuring as a group of four units here, or as two-dimensional layers in *RE*Cu*Ch*O (ZrCuSiAs-type structure).[1,4] Such fragments with varying widths have been reported in Sm_3GaSe_5O,[24] $La_{10}In_6S_{17}O_6$,[23] and related

oxychalcogenides. The *RE*–O bond distances are 2.34–2.53 Å in $Pr_4Ga_2Se_7O_2$ and 2.30–2.50 Å in $Nd_4Ga_2Se_7O_2$, similar to distances found in various forms of RE_2O_3.[42]

The Ga–Se blocks are the most unusual feature in the structure. The coordination geometry around Ga1 is a regular tetrahedron (CN4), with Ga–Se distances of 2.37–2.47 Å in $Pr_4Ga_2Se_7O_2$ and 2.37–2.46 Å in $Nd_4Ga_2Se_7O_2$, in accordance with expectations. However, it is remarkable that Ga2 is surrounded by five Se atoms in a trigonal bipyramidal geometry (CN5). The only other example of such $GaSe_5$ units is found in Sm_3GaSe_5O, reported in Chapter 3.[24] The Ga–Se distances in these trigonal bipyramids are significantly longer, 2.40–3.00 Å for $Pr_4Ga_2Se_7O_2$ and 2.40–2.94 Å for $Nd_4Ga_2Se_7O_2$. An analysis of these longer distances is discussed below.

Electronic band structure calculations show an energy gap between the valence band maxima, located slightly off the Brillouin zone centre, and the conduction band minima, located at the zone centre, indicating that these compounds are predicted to be indirect semiconductors (**Figure A5-4**). However, because the topmost valence bands are quite flat near the zone centre, the gap is nearly direct. The calculated band gaps are 0.98 eV for $Pr_4Ga_2Se_7O_2$ and 1.10 eV for $Nd_4Ga_2Se_7O_2$. The valence band extends from –4.4 to 0 eV and consists of mixing of Se 4p with Ga 4p and O 2p states, whereas the conduction band extends from 1.0 eV upwards and consists of mixing of *RE* 5d with Ga 4s and Se 4p states, as seen in the projected DOS plots (**Figure 5-3**). As is typical of valence-precise compounds, the band gap arises from the optimization of bonding interactions: all bonding Ga–Se states are filled and all antibonding Ga–Se states are empty. In contrast, the *RE*–O and *RE*–Se interactions do not have significant contributions near the Fermi level; instead, they are expected to have more ionic character. Accordingly, the –ICOHP values are largest for the more covalent Ga–Se interactions, and relatively low for the more ionic *RE*–O and *RE*–Se interactions. The degree of covalent character can be further quantified by inspection

of COBI values, which range from 1 for covalent to 0 for covalent interactions. In agreement with expectations, the integrated COBI values are high for the Ga–Se interactions (0.7–0.9) but low for the *RE*–O and *RE*–Se interactions (0.1–0.2).

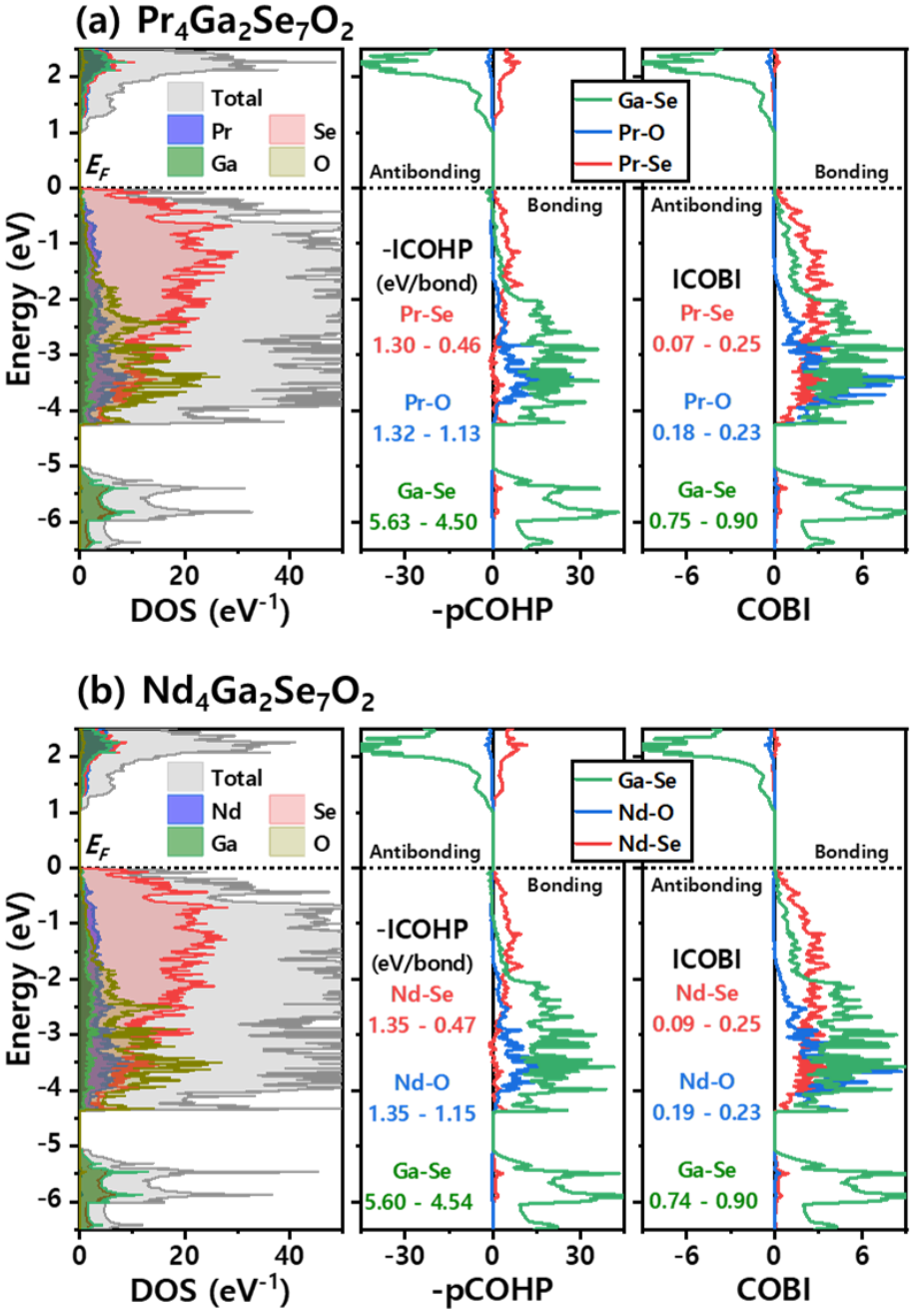

Figure 5-3. DOS (left), –COHP (center), and COBI (right) curves for (a) $Pr_4Ga_2Se_7O_2$ and (b) $Nd_4Ga_2Se_7O_2$. Positive values of –COHP and COBI signify bonding interactions whereas negative values represent antibonding interactions.

The Ga–Se interactions are the strongest in the structure (**Figure 5-4**). Within the $GaSe_4$ tetrahedra, the –ICOHP values are the largest (4.50–5.45 eV/bond for $Pr_4Ga_2Se_7O_2$, 4.53–5.48 eV/bond for $Nd_4Ga_2Se_7O_2$) for typical Ga–Se distances of 2.37–2.47 Å. Within the $GaSe_5$ trigonal bipyramids, these –ICOHP values are large (4.70–5.02 eV/bond) for the shorter Ga–Se distances of 2.40–2.45 Å, and they are still significant (1.32 eV/bond for $Pr_4Ga_2Se_7O_2$, 1.48 eV/bond for $Nd_4Ga_2Se_7O_2$) for the longer axial Ga–Se distances of 2.99 Å and 2.94 Å, respectively. From these values, perhaps the Ga atoms within these trigonal bipyramids are better described as having CN 4+1.

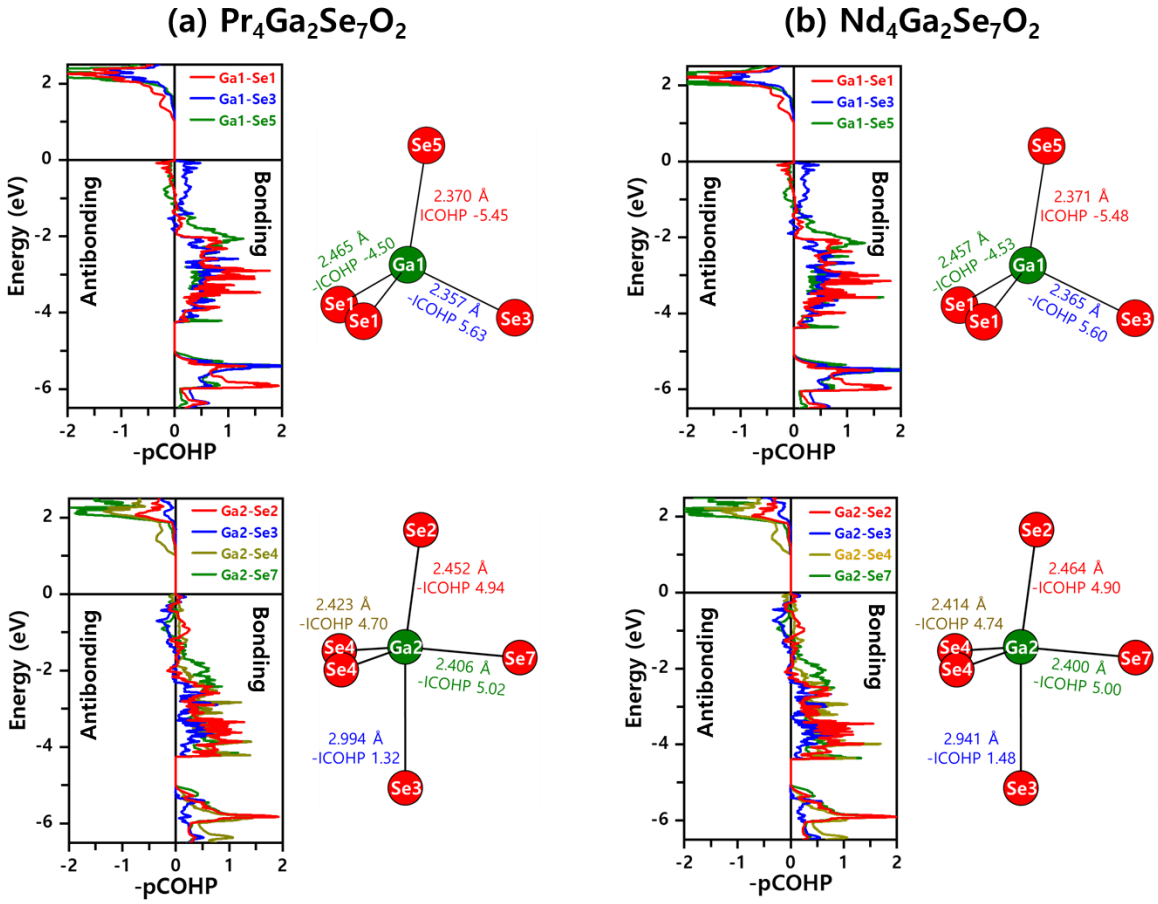

Figure 5-4. –COHP curves for each Ga–Se contacts within Ga1 tetrahedra and Ga2 trigonal bipyramids within (a) $Pr_4Ga_2Se_7O_2$ and (b) $Nd_4Ga_2Se_7O_2$.

To visualize the chemical bonding in further detail, and to test the assertion that the structures of rare-earth oxychalcogenides can be separated into more ionic vs. more covalent building blocks, ELF plots were extracted from the electronic structure calculations (**Figure 5-5**). Minima (blue colours) are evident between *RE* and O atoms, and between *RE* and Se atoms, indicating that the electron density tends to be localized within these atoms rather than being shared in the region between them, consistent with ionic bonding character. In contrast, intermediate values of electron density (blue-green colours) are found between Ga and Se atoms, consistent with covalent bonding character. These results are also consistent with the ICOBI values presented earlier. The calculated Bader charges (**Table 5-4**) are not as extreme as suggested by the charge-balanced formulation $(RE^{3+})_4(Ga^{3+})_2(Se^{2-})_7(O^{2-})_2$, but they tend to be larger for the *RE* and O atoms, which participate in ionic bonds, and less so for the Ga and Se atoms, which participate in covalent bonds.

Table 5-4. Bader charges in $RE_4Ga_2Se_7O_2$.

	RE	Ga	Se	O
$Pr_4Ga_2Se_7O_2$	1.96+ to 1.65+	0.79+ to 0.86+	1.14– to 0.72–	1.39– to 1.35–
$Nd_4Ga_2Se_7O_2$	1.97+ to 1.63+	0.84+ to 0.88+	1.11– to 0.73–	1.39– to 1.36–

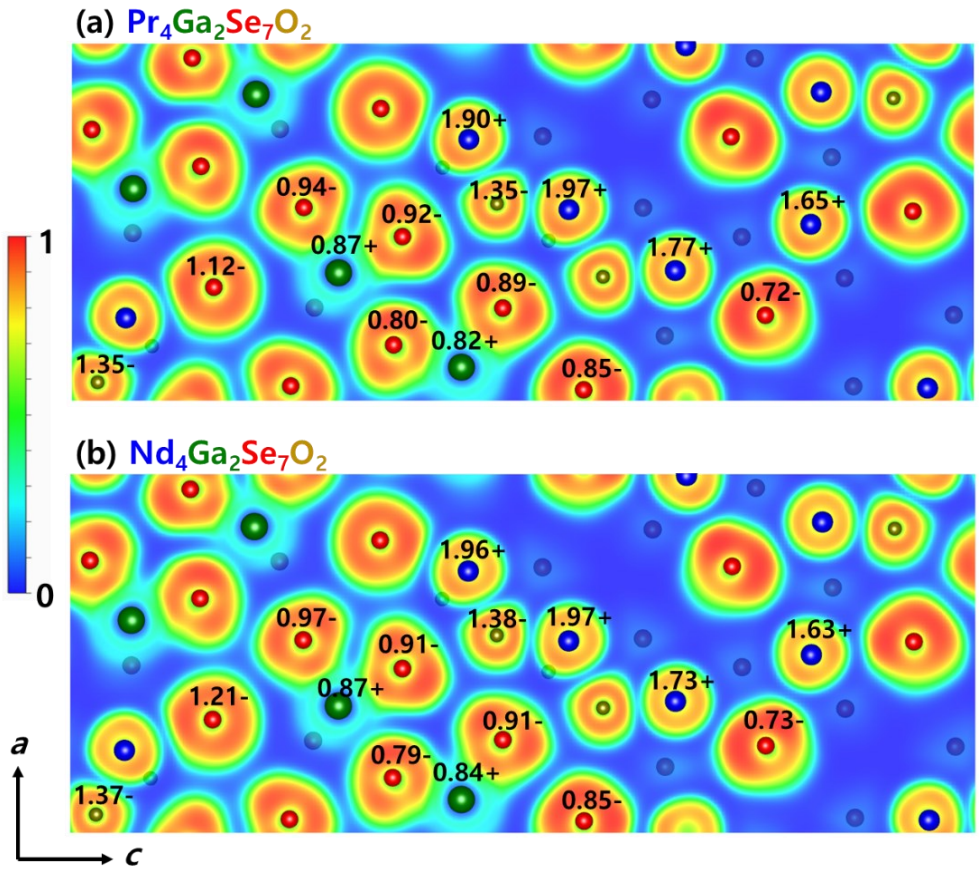

Figure 5-5. ELF plots and Bader charges for a slice along the (010) plane at y = ¼ for (a) $Pr_4Ga_2Se_7O_2$ and (a) $Nd_4Ga_2Se_7O_2$.

Optical diffuse reflectance spectra were collected on phase-pure powder samples of these compounds (**Figure 5-6**). The sharp edges in the curve for $Nd_4Ga_2Se_7O_2$ arise from f-f transitions of Nd atoms. The band gaps extracted from Tauc plots, which were fitted with the assumption of a direct band gap, are 1.68 eV for $Pr_4Ga_2Se_7O_2$ and 1.74 eV for $Nd_4Ga_2Se_7O_2$, consistent with the dark brown colour of both samples. These are larger than the values predicted using standard functionals in DFT calculations, presented above, which tend to underestimate band gaps. When the DFT calculations were repeated using a hybrid HSE06 functional (with an HF to PBE ratio of 25:75), the calculated band gaps of 1.52 eV for $Pr_4Ga_2Se_7O_2$ and 1.58 eV for $Nd_4Ga_2Se_7O_2$ are in better agreement with the experimental values (**Figure A5-5**).

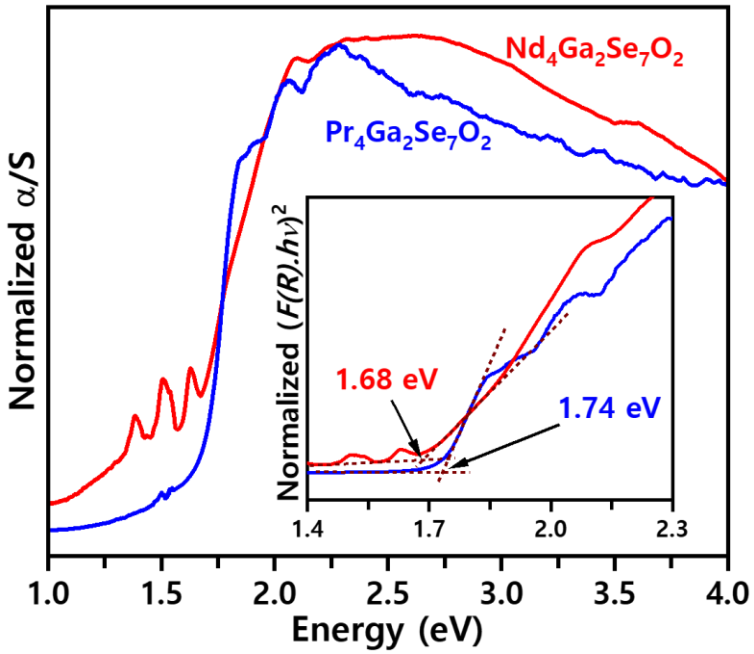

Figure 5-6. Optical absorbance spectra of $Pr_4Ga_2Se_7O_2$ and $Nd_4Ga_2Se_7O_2$ converted from diffuse reflectance spectra. The inset shows Tauc plots and fits assuming direct band gaps.

It is of interest to evaluate $Pr_4Ga_2Se_7O_2$ and $Nd_4Ga_2Se_7O_2$ as potential thermoelectric materials, given that they are semiconductors and have high effective masses, as judged by the presence of flat bands in the band dispersion plots. Thermal transport coefficients were calculated from the electronic band structure within a range of temperatures from 300 to 1500 K, at increments of 100 K (**Figure 5-7**and **Figure 5-8**). Maximum values of the Seebeck coefficients S are listed, with positive chemical potential μ or negative S signifying electron doping (n-type), and negative μ or positive signifying hole doping (p-type) (**Table 5-5**). As the temperature increases, the Seebeck coefficient decreases, shifting away from $\mu = 0$. At $S = 0$, the chemical potential range narrows to ±0.5 eV at all temperatures, attributed to easier electronic excitations. The tempeature dependence of chemical potential and relaxation time, as well as the occurrence of greater scattering at high temperatures, should be taken into account if experimental measurements are made.

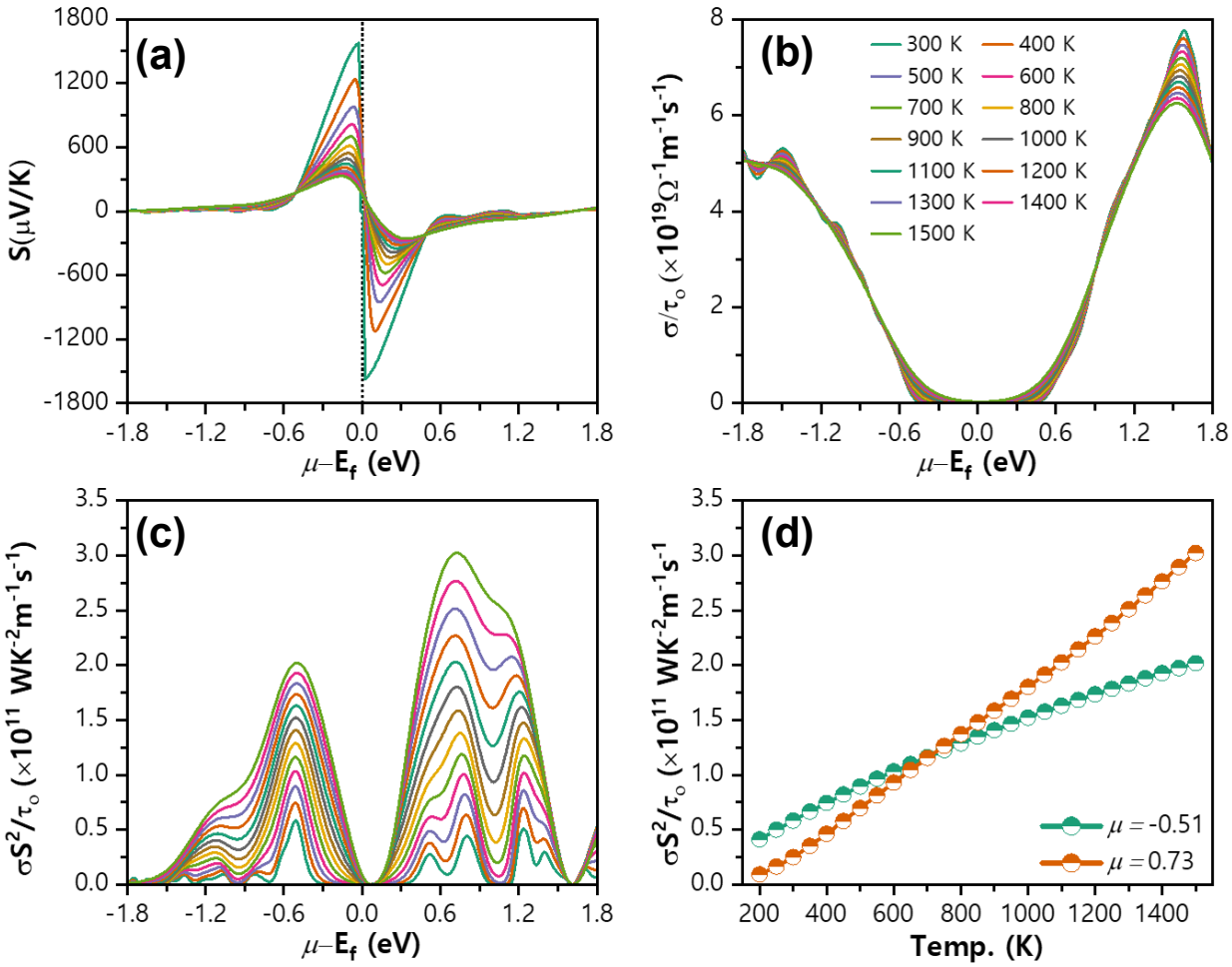

Figure 5-7. $Pr_4Ga_2Se_7O_2$: Temperature dependence of (a) Seebeck coefficient, (b) electronic conductivity over relaxation time (σ/τ_0), (c) power factor over relaxation time ($\sigma S^2/\tau_0$) with chemical potential. (d) The maxima in the power factor are plotted as function of temperature at $\mu = +0.73$ and -0.51.

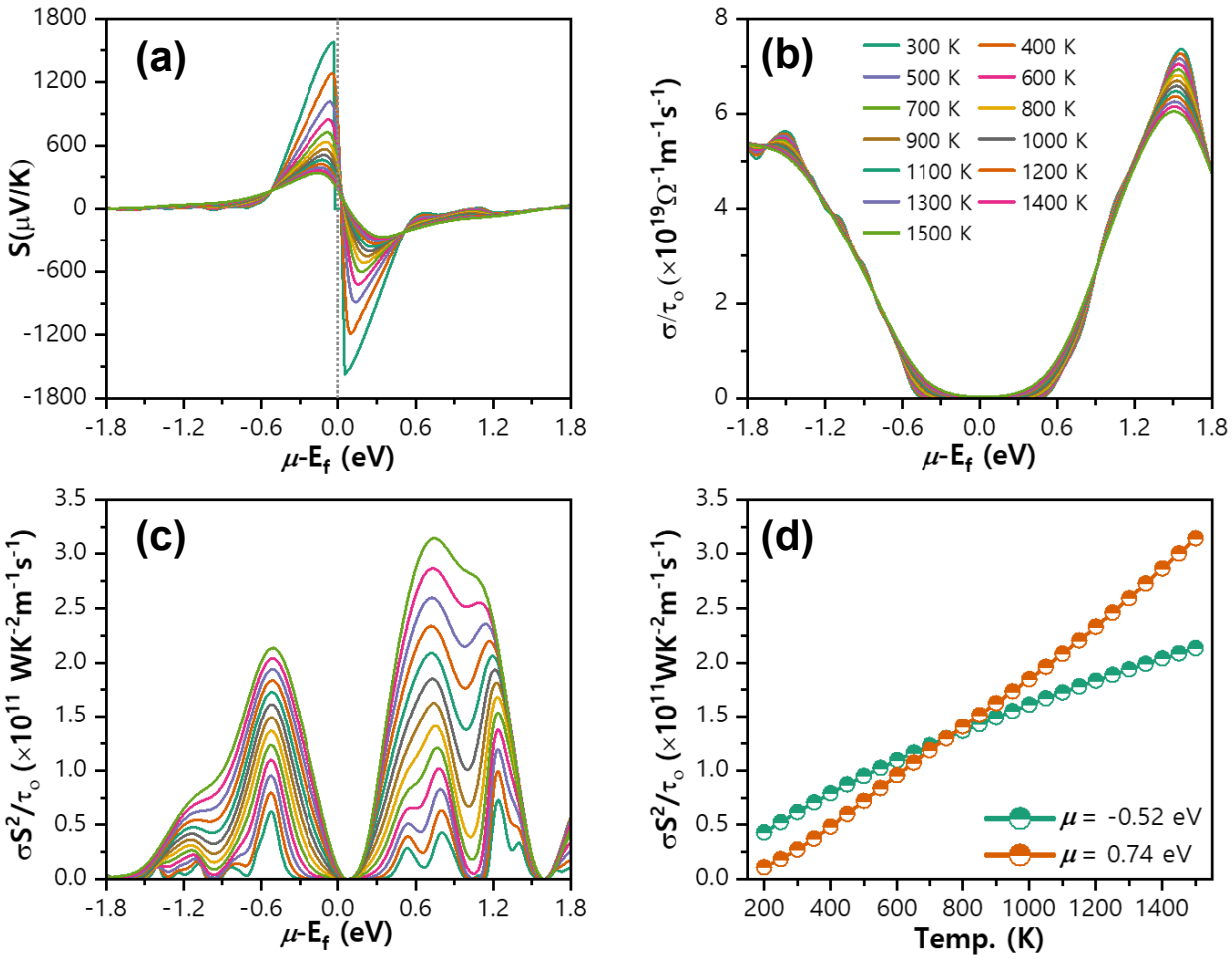

Figure 5-8. $Nd_4Ga_2Se_7O_2$: Temperature dependence of (a) Seebeck coefficient, (b) electronic conductivity over relaxation time (σ/τ_0), (c) power factor over relaxation time ($\sigma S^2/\tau_0$) with chemical potential. (d) The maxima in the power factor are plotted as function of temperature at $\mu = +0.73$ and -0.51.

Table 5-5. Maximum calculated Seebeck coefficients at 300 K.

	Seebeck coefficient S (μV/K)	Chemical potential μ (eV)
$Pr_4Ga_2Se_7O_2$	+S = 1578	–0.03
	–S = 1575	+0.03
$Nd_4Ga_2Se_7O_2$	+S = 1578	–0.03
	–S = 1573	+0.05

The thermoelectric figure of merit ZT is directly proportional to the power factor, $PF = \sigma S^2$. The electronic and thermal conductivities can be calculated within respect to relaxation time using Boltzmann transport theory within the constant relaxation time approximation. From the plots of electronic conductivity, the maximum value of σ/τ_0 is significantly larger for n-type than for p-type doping. The power factor curves show two maxima, corresponding to $+\mu$ and $-\mu$, at all temperatures, and these are also larger for n-type doping ($+\mu$). The maximum power factor increases with higher temperature, more so within the $+\mu$ than the $-\mu$ regions. At lower temperatures (<800 K), within the $+\mu$ region, the power factor curves split into two maxima. The highest power factors are attained at μ = –0.51 and +0.73 for $Pr_4Ga_2Se_7O_2$ and at μ = –0.52 and +0.74 for $Nd_4Ga_2Se_7O_2$, and their temperature dependences are plotted (**Figure 5-7d**, **Figure 5-8d,** and **Table 5-6**). These plots enable realistic power factors to be predicted if the scattering time is measured experimentally for these compounds. If typical values of 10^{-15}–10^{-14} s^{-1} for relaxation time are assumed, the calculated power factors are 10^{-4} to 10^{-3} W K^{-2} m^{-1} s^{-1}, which are similar to those found in other oxychalcogenides.[5,43]

Table 5-6. Minimum and maximum calculated power factors (10^{11} $W \cdot K^{-2} \cdot m^{-1} \cdot s^{-1}$).

	$Pr_4Ga_2Se_7O_2$		$Nd_4Ga_2Se_7O_2$	
	μ = 0.73 eV	μ = –0.51 eV	μ = 0.74 eV	μ = –0.52 eV
300 K	0.25	0.58	0.27	0.62
1500 K	3.02	2.02	3.14	2.14

5.4 Conclusions

The oxyselenides $Pr_4Ga_2Se_7O_2$ and $Nd_4Ga_2Se_7O_2$ adopt a new structure type, and contain unusual $GaSe_5$ trigonal bipyramids, only the second instance observed of such units. The segregation into more ionic *RE*–O and Ga–Se blocks, as quantified by electronic structure calculations, reinforces this recurring theme found in many oxychalcogenides. These compounds are semiconductors with nearly direct band gaps of 1.7 eV, dictated by the crossover of bonding to antibonding Ga–Se interactions at the Fermi level. Calculations of thermal transport properties indicate higher power factors for positive chemical potentials within a temperature range of 300 to 1500 K. This implies that n-type doping could be applied to enhance the power factors.

5.4. References

(1) Clarke, S. J.; Adamson, P.; Herkelrath, S. J. C.; Rutt, O. J.; Parker, D. R.; Pitcher, M. J.; Smura, C. F. *Inorg. Chem.* **2008**, *47*, 8473−8486.

(2) Hiramatsu, H.; Kamihara, Y.; Yanagi, H.; Ueda, K.; Kamiya, T.; Hirano, M.; Hosono, H. *J. Eur. Ceram. Soc.* **2009**, *29*, 245–253.

(3) Muir, S.; Subramanian, M. A. *Prog. Solid State Chem.* **2012**, *40*, 41–56.

(4) Luu, S. D. N.; Vaqueiro, P. *J. Materiomics* **2016**, *2*, 131–140.

(5) Tippireddy, S.; D S, P. K.; Das, S.; Mallik, R. C. *ACS Appl. Energy Mater.* **2021**, *4*, 2022–2040.

(6) Orr, M.; Hebberd, G. R.; McCabe, E. E.; Macaluso, R. T. *ACS Omega* **2022**, *7*, 8209–8218.

(7) Recham, N.; Chotard, J. N.; Dupont, L.; Delacourt, C.; Walker, W.; Armand, M.; Tarascon, J. M. *Nat. Mater.* **2010**, *9*, 68–74.

(8) Jansen, M.; Letschert, H. P. *Nature* **2000**, *404*, 980–982.

(9) Ueda, K.; Hiramatsu, H.; Hirano, M.; Kamiya, T.; Hosono, H. *Thin Solid Films* **2006**, *496*, 8–15.

(10) Chen, Y.; Cui, Y.; Pham, A.; Wang, Y.; Bhadbhade, M. M.; Wang, R.; Su, Y.; Hu, H.; Wen, Z.; Cheng, C.; Tan, T. T.; Li, S.; Zhao, Y. *J. Mater. Chem. C* . **2019**, *7*, 586–591.

(11) Wilmer, D.; Jorgensen, J. D.; Wuensch, B. J. *Solid State Ion.* **2000**, *136–137*, 961–966.

(12) Ishikawa, A.; Takata, T.; Kondo, J. N.; Hara, M.; Kobayashi, H.; Domen, K. *J. Am. Chem. Soc.* **2002**, *124*, 13547–13553.

(13) Miura, A.; Oshima, T.; Maeda, K.; Mizuguchi, Y.; Moriyoshi, C.; Kuroiwa, Y.; Meng, Y.; Wen, X.-D.; Nagao, M.; Higuchi, M.; Tadanaga, K. *J. Mater. Chem. A* **2017**, *5*, 14270–14277.

(14) Jaulmes, S. *Acta Crystallogr. B* **1978**, *34*, 2610–2612.

(15) Bénazeth, S.; Guittard, M.; Laruelle, P. *Acta Crystallogr. C* **1984**, *40*, 345–347.

(16) Guittard, M.; Benazeth, S.; Dugué, J.; Jaulmes, S.; Palazzi, M.; Laruelle, P.; Flahaut, J. *J. Solid State Chem.* **1984**, *51*, 227–238.

(17) Ito, H.; Miura, A.; Goto, Y.; Mizuguchi, Y.; Moriyoshi, C.; Kuroiwa, Y.; Azuma, M.; Liu, J.; Wen, X.-D.; Nishioka, S.; Maeda, K.; Masubuchi, Y.; Rosero-Navarro, N. C.; Tadanaga, K. *Dalton Trans.* **2019**, *48*, 12272–12278.

(18) Kabbour, H.; Cario, L.; Moëlo, Y.; Meerschaut, A. *J. Solid State Chem.* **2004**, *177*, 1053–1059.

(19) Dugué, J.; Guittard, M. *Acta Crystallogr. B* **1982**, *38*, 2368–2371.

(20) Bénazeth, S.; Laruelle, P.; Guittard, M. *J. Solid State Chem.* **1989**, *78*, 148–153.

(21) Mazurier, A.; Guittard, M.; Jaulmes, S. *Acta Crystallogr. B* **1982**, *38*, 379–382.

(22) Jaulmes, S.; Mazurier, A.; Guittard, M. *Acta Crystallogr. B* **1983**, *39*, 1594–1597.

(23) Gastaldi, L.; Carre, D.; Pardo, M. *Acta Crystallogr. B* **1982**, *38*, 2365–2367.

(24) Mishra, V.; Mumbaraddi, D.; Iyer, A. K.; Yin, W.; Mar, A. *J. Solid State Chem.* **2022**, *308*, 122901.

(25) Sheldrick, G. M. *Acta Crystallogr. A: Found. Crystallogr.* **2008**, *64*, 112–122.

(26) Gelato, L. M.; Parthé, E. *J. Appl. Crystallogr.* **1987**, *20*, 139–143.

(27) Kresse, G.; Furthmüller, J. *Phys. Rev. B* **1996**, *54*, 11169–11186.

(28) Kresse, G.; Joubert, D. *Phys. Rev. B* **1999**, *59*, 1758–1775.

(29) Blöchl, P. E. *Phys. Rev. B* **1994**, *50*, 17953–17979.

(30) Perdew, J. P.; Burke, K.; Ernzerhof, M. *Phys. Rev. Lett.* **1996**, *77*, 3865–3868.

(31) Hohenberg, P.; Kohn, W. *Phys. Rev.* **1964**, *136*, B864–B871.

(32) Kohn, W.; Sham, L. J. *Phys. Rev.* **1965**, *140*, A1133–A1138.

(33) Momma, K.; Izumi, F. *J. Appl. Crystallogr.* **2011**, *44*, 1272–1276.

(34) Grin, Y.; Savin, A.; Silvi, B. The ELF Perspective of Chemical Bonding. In *The Chemical Bond: Fundamental Aspects of Chemical Bonding*, Frenking, G.; Shaik, S Eds. Wiley-VCH: Weinheim, 2014; pp 345–380.

(35) Henkelman, G.; Arnaldsson, A.; Jónsson, H. *J. Comput. Mater. Sci.* **2006**, *36*, 354–360.

(36) Sanville, E.; Kenny, S. D.; Smith, R.; Henkelman, G. *J. Comput. Mater. Sci.* **2007**, *28*, 899–908.

(37) Tang, W.; Sanville, E.; Henkelman, G. *J. Condens. Matter Phys.* **2009**, *21*, 084204.

(38) Deringer, V. L.; Tchougréeff, A. L.; Dronskowski, R. *J. Phys. Chem. A* **2011**, *115*, 5461–5466.

(39) Maintz, S.; Deringer, V. L.; Tchougréeff, A. L.; Dronskowski, R. *J. Comput. Chem.* **2016**, *37*, 1030–1035.

(40) Müller, P. C.; Ertural, C.; Hempelmann, J.; Dronskowski, R. *J. Phys. Chem. C* **2021**, *125*, 7959–7970.

(41) Madsen, G. K. H.; Carrete, J.; Verstraete, M. J. *Comput. Phys. Commun.* **2018**, 231, 140–145.

(42) Villars, P.; Cenzual, K. *Pearson's Crystal Data – Crystal Structure Database for Inorganic Compounds,* Release 2022/23, ASM International, Materials Park, OH, USA.

(43) Mishra, V.; Zabolotnii, A.; Mar, A. *Inorg. Chem.* **2022**, *61*, 12458–12465.

Chapter 6.

Conclusions

The central theme of this thesis has been to discover new ternary chalcogenides and quaternary oxychalcogenides. In pursuit of these objectives, the series of ternary selenides RE_3InSe_6 were characterized. Consistent with their charge-balanced formulation, these compounds are semiconductors. A hypothesis was formulated that quaternary oxychalcogenides could be derived from these ternary compounds by substituting *Ch* for O atoms. Following this idea, the solid solutions RE_3GaSe_5O were targeted. Although the hypothesis was not fulfilled, four new compounds were found: Sm_3GaSe_5O, $La_4Ga_2Se_6O_3$, $Pr_4Ga_2Se_7O_2$, and $Nd_4Ga_2Se_7O_2$, which are intrinsic semiconductors. $La_4Ga_2Se_6O_3$ contains expected structural features, whereas $Pr_4Ga_2Se_7O_2$, $Nd_4Ga_2Se_7O_2$, and Sm_3GaSe_5O contain unprecedented $GaSe_5$ trigonal bipyramids. These findings suggest that preparing new oxychalcogenides from existing chalcogenides or oxides by substituting anion for another is not straightforward.

The band gaps for all compounds range from 1.2 to 1.8 eV, which are close to the desired values for solar cell and photocatalytic applications. Electronic structure calculations were helpful in providing insight on the type of band gap and on the bonding character in these oxychalcogenides. In particular, the assertion of more ionic character in *RE*–O blocks and more covalent character in *M*–*Ch* blocks within oxychalcogenides was supported.

6.1. Ternary selenides

In Chapter 2, the compounds RE_3InSe_6 were investigated, as part of a larger context of ternary chalcogenides RE_3MCh_6 (*RE* = rare-earth metal; *M* = Ga, In, Tl; *Ch* = S, Se, Te) which had been previously identified, but were incompletely characterized. Only four members of the sulfides RE_3GaS_6 were previously known, and the corresponding selenides RE_3GaSe_6 were unknown. Attempts to prepare early *RE* members of RE_3GaS_6 were unsuccessful, yielding $RE_3Ga_{1.67}S_7$ instead. The sulfides RE_3InS_6 had been known for nearly all *RE* components, but the selenides RE_3InSe_6 had been restricted to only three members. An unexpected outcome was that these selenides show subtle structural differences, adopting the U_3ScS_6-type instead of the La_3InS_6-type found for the sulfides. The difference was traced to gradual transitions in the coordination of In atoms, from tetrahedral to octahedral geometry, as manifested by split half-occupied sites merging into a single site.

Prior to this work, the only characterization of these compounds was limited to structural assignments, with details most unconfirmed except for cell parameters. Because most chalcogenides are expected to be semiconductors, optical spectra were obtained to extract their band gaps. Attempts to extend the RE_3InSe_6 series showed that these compounds form up to *RE* = Tb. The band gaps are direct, as indicated by electronic structure calculations. The *RE* atoms carry localized magnetic moments.

6.2. Quaternary oxyselenides

These quaternary compounds resulted from attempts to prepare derivatives of RE_3MCh_6 by substituting O for *Ch* atoms. Although Sm_3GaSe_5O seems to have a formula related to RE_3MCh_6, the structures are completely unrelated. A major technical challenge in the structural characterization common to all these oxyselenides is the tendency for these compounds to grow as very thin, needled-shaped crytals. The $GaSe_5$ trigonal bipyramidal unit present in Sm_3GaSe_5O contains longer Ga–Se bonds than normally observed, but they are still significant, as supported by COHP values in electronic structure calculations. The calculated optical band gap is 1.2 eV and it is nearly direct, consistent with flat bands near the Fermi level. Although attempts were made to extend the *RE* substitution in RE_3GaSe_5O, only this one member could be prepared.

$La_4Ga_2Se_6O_3$ adopts a new structure type containing the usual motifs of $GaSe_4$ tetrahedra. Even though it was prepared from a nominally loaded composition of La_3GaSe_5O, which is a known phase, these compounds have unrelated structures. Rational synthesis of $La_4Ga_2Se_6O_3$ was unsuccessful, even after repeated heating and grinding. It is becoming apparent that the "design" of oxychalcogenides from existing oxides or chalcogenides is not easy, beause of these synthetic challenges. Moreover, the structural features of oxychalcogenides are still not easy to predict. An indirect band gap of 1.8 eV was measured and calculated for $La_4Ga_2Se_6O_3$.

$Pr_4Ga_2Se_7O_2$ and $Nd_4Ga_2Se_7O_2$ were obtained after attempted *RE* substitutions of $RE_4Ga_2Se_6O_3$ and RE_3GaSe_5O. Again, they adopt a new structure type, exhibiting $GaSe_5$ units as observed in Sm_3GaSe_5O. Subequently, a rational synthesis route was developed, enabling phase-pure samples to be prepared reproducibly. These compounds are semiconductors with nearly direct band gaps of 1.7 eV.

The structures of many existing rare-earth oxychalcogenides can be described as a combination of more ionic *RE*–O and more covalent *M*–*Ch* blocks, but the degree of ionic vs. covalent bonding character has never been quantified. Applying the recently developed concept of crystal orbital bond index shows that this description is remarkably apt. Analysis of ELF plots also provides visual confirmation of this distinction between ionic and covalent bonding character, as manifested by highly localized electron density around the *RE* and *Ch* atoms, in contrast to the shared electron density between *M* and *Ch* atoms.

Recent proposals that oxychalcogenides could be good candidates as thermoelectric materials were tested by performing calculations of thermal transport properties on $La_4Ga_2Se_6O_3$, $Pr_4Ga_2Se_7O_2$, and $Nd_4Ga_2Se_7O_2$. These compounds are predicted to be competitive with other oxychalcogenides in terms of their thermoelectric properties.

6.3. Future directions

The results in this thesis suggest that much more remains to be discovered among chalcogenides, which have been extensively studied by many group over the past two decades, and oxychalcogenides, which have barely been investigated. Although sulfides and selenides are usually expected to form isostructural compounds, tellurides are distinct. It would be worthwhile targeting, for example, $RE_3M\mathrm{Te}_6$, with anticipation that they are not likely to be related to the corresponding sulfides or selenides.

Despite many efforts to expand solid state compounds beyond oxides, mixed-anion compounds remain relatively few. Many other quaternary oxychalcogenides *RE*–*M*–*Ch*–O, with other components *M* besides group-13 elements, are worthwhile investigating. As a starting point,

similar compositions could be attempted, but as this thesis has shown, surprises will no doubt be in store.

The oxyselenides prepared here tend to have lower band gaps than other oxychalcogenides known in the literature. Because narrow band gaps are desirable for thermoelectric materials, this observation portends well for oxyselenides as a promising class of compounds to continue investigating. The intermediate characteristics imparted by the *RE*–O and *M*–*Ch* blocks offers additional degrees of flexibility for modifying electrical and thermal properties. In fact, the physical properties of many existing oxychalcogenides are still unknown, so even reproducing their syntheses and evaluating these properties are important tasks to complete. Because the band gap values, which range from 1.2 to 1.8 eV, overlap with the solar spectrum, a potential new application of these oxychalcogenides is as photovoltaic materials.

Bibliography

(1) West, A. R. *Basic Solid State Chemistry*, 2nd ed.; Wiley: New York, 1999.

(2) Villars, P.; Cenzual, K. *Pearson's Crystal Data – Crystal Structure Database for Inorganic Compounds,* Release 2022/23, ASM International, Materials Park, OH, USA.

(3) Mitchell, K.; Ibers, J. A. *Chem. Rev.* **2002**, *102*, 1929–1952.

(4) Cody, J. A.; Mansuetto, M. F.; Pell, M. A.; Chien, S.; Ibers, J. A. *J. Alloys Compd.* **1995**, *219*, 59–62.

(5) Mar, A.; Jobic, S.; Ibers, J. A. *J. Am. Chem. Soc.* **1992**, *114*, 8963–8971.

(6) Rouxel, J. *Acc. Chem. Res.* **1992**, *25*, 328–336.

(7) Rahman, A.; Khan, M. M. *New J. Chem.* **2021**, *45*, 19622–19635.

(8) Choi, Y. I.; Lee, S.; Kim, S. K.; Kim, Y.-I.; Cho, D. W.; Khan, M. M.; Sohn, Y. *J. Alloys Compd.* **2016**, *675*, 46–56.

(9) Tsai, M.-L.; Su, S.-H.; Chang, J.-K.; Tsai, D.-S.; Chen, C.-H.; Wu, C.-I.; Li, L.-J.; Chen, L.-J.; He, J.-H. *ACS Nano* **2014**, *8*, 8317–8322.

(10) Tsai, D.-S.; Lien, D.-H.; Tsai, M.-L.; Su, S.-H.; Chen, K.-M.; Ke, J.-J.; Yu, Y.-C.; Li, L.-J.; He, J.-H. *IEEE J. Sel. Top. Quantum Electron.* **2014**, *20*, 30–35.

(11) Woods-Robinson, R.; Han, Y.; Zhang, H.; Ablekim, T.; Khan, I.; Persson, K. A.; Zakutayev, A. *Chem. Rev.* **2020**, *120*, 4007–4055.

(12) Yin, J.; Jin, J.; Lin, H.; Yin, Z.; Li, J.; Lu, M.; Guo, L.; Xi, P.; Tang, Y.; Yan, C.-H. *Adv. Sci.* **2020**, *7*, 1903070.

(13) Huang, J.; Wei, Z.; Liao, J.; Ni, W.; Wang, C.; Ma, J. *J. Energy Chem.* **2019**, *33*, 100–124.

(14) Zogg, H.; Maissen, C.; Masek, J.; Hoshino, T.; Blunier, S.; Tiwari, A. N. *Semicond Sci. Technol.* **1991**, *6*, C36–C41.

(15) Fischer, Ø.; Odermatt, R.; Bongi, G.; Jones, H.; Chevrel, R.; Sergent, M. *Phys. Lett. A* **1973**, *45*, 87–88.

(16) Matthias, B. T.; Marezio, M.; Corenzwit, E.; Cooper, A. S.; Barz, H. E. *Science* **1972**, *175*, 1465–1466.

(17) Francis, J. D. S.; Rice, T. M. *Phys. Today* **1979**, *32*, 32–38.

(18) Zhou, J.; Liu, Y.; Zhang, S.; Zhou, T.; Guo, Z. *InfoMat.* **2020**, *2*, 437–465.

(19) Boyd, G.; Kasper, H.; McFee, J. *IEEE J. Quantum Electron.* **1971**, *7*, 563–573.

(20) Shi, Y.; Sturm, C.; Kleinke, H. *J. Solid State Chem.* **2019**, *270*, 273–279.

(21) Balaram, V. *Geosci. Front.* **2019**, *4*, 1285–1303.

(22) Wall, F. Rare earth elements. In *Critical Metals Handbook*, Gunn G., Ed.; Wiley, 2014; pp 312–339.

(23) Petit, L.; Szotek, Z.; Lüders, M.; Svane, A. *J. Phys. Condens. Matter* **2016**, *28*, 223001.

(24) Wachter, P. *Crit. Rev. Solid State Mater. Sci.* **1972**, *3*, 189–241.

(25) Kumta, P.N., Risbud, S.H. *J. Mater. Sci*. **1994**, *29*, 1135–1158.

(26) Liu, W.; Zhang, Z.; Ji, J.; Liu, Y.; Li, J.; Wang, X.; Lei, H.; Chen, G.; Zhang, Q. *Chinese Phys. Lett.* **2018**, *35*, 117501.

(27) Meng, F.; Hughbanks, T. *Inorg. Chem.* **2001**, *40*, 2482–2483.

(28) Holtzberg, F.; McGuire, T. R.; Methfessel, S.; Suits, J. C. *Phys. Rev. Lett.* **1964**, *13*, 18–21.

(29) Chen, H.-Y.; Zhang, Y.-Y.; Yang, Y.-F.; Guo, S.-P. *J. Alloys Compd.* **2021**, *868*, 159112.

(30) Chen, M.-C.; Li, L.-H.; Chen, Y.-B.; Chen, L. *J. Am. Chem. Soc.* **2011**, *133*, 4617–4624.

(31) Alemi, A.; Klein, A.; Meyer, G.; Dolatyari, M.; Babalou, A. *Z. Anorg. Allg. Chem* **2011**, *637*, 87–93.

(32) Chi, Y.; Guo, S.-P.; Xue, H.-G. *RSC Adv.* **2017**, *7*, 5039–5045.

(33) He, J.; Wang, Z.; Zhang, X.; Cheng, Y.; Gong, Y.; Lai, X.; Zheng, C.; Lin, J.; Huang, F. *RSC Adv.* **2015**, *5*, 52629–52635.

(34) Lozac'h, A. M.; Jaulmes, S.; Guittard, M. *C. R. Seances Acad. Sci., Ser. C* **1971**, *272*, 1123–1126.

(35) Jaulmes, S.; Laruelle, P. *Acta Crystallogr. Sect. B Struct. Crystallogr. Cryst. Chem.* **1973**, *29*, 352–354.

(36) Loireau-Lozac'h, A. M.; Guittard, M.; Flahaut, J. *Mater. Res. Bull.* **1977**, *12*, 881–886.

(37) Zhang, M.-J.; Li, B.-X.; Liu, B.-W.; Fan, Y.-H.; Li, X.-G.; Zeng, H.-Y.; Guo, G.-C. *Dalton Trans.* **2013**, *42*, 14223–14229.

(38) Carré, D.; Guittard, M.; Adolphe, C. *Acta Crystallogr. Sect. B Struct. Crystallogr. Cryst. Chem.* **1978**, *34*, 3499–3501.

(39) Guittard, M.; Carré, D.; Kabré, T. S. *Mater. Res. Bull.* **1978**, *13*, 279–286.

(40) Aliev, O. M. *Izv. Akad. Nauk. SSSR, Neorg. Mater.* **1980**, *16*, 1514–1518.

(41) Akhmedova, D. A.; Agaev, A. B.; Rustamov, P. G. *Zh. Neorg. Khim.* **1992**, 37, 461–464.

(42) Ivashchenko, I.; Kozak, V.; Olekseyuk, I.; Daszkiewicz, M.; Halyan, V.; Tishchenko, P.; Shemet, V. Y.; Gulay, L. *J. Solid State Chem.* **2020**, *288*, 121339-1–121339-7.

(43) Messain, D.; Carré, D.; Laruelle, P. *Acta Crystallogr. Sect. B Struct. Crystallogr. Cryst. Chem.* **1977**, *33*, 2540–2542.

(44) Gulay, L. D.; Daszkiewicz, M.; Huch, M. R. *J. Solid State Chem.* **2008**, *181*, 2626–2632.

(45) Aleandri, L. E.; Ibers, J. A. *J. Solid State Chem.* **1989**, *79*, 107–111.

(46) Aleandri, L. E.; Ibers, J. A. *J. Solid State Chem.* **1989**, *81*, 317.

(47) Tougait, O.; Ibers, J. A. *Inorg. Chem.* **2000**, *39*, 1790–1794.

(48) Huch, M. R.; Gulay, L. D.; Olekseyuk, I. D. *J. Alloys Compd.* **2007**, *439*, 156–161.

(49) Rao, C. N. R.; Raveau, B. *Acc. Chem. Res.* **1989**, *22*, 106–113.

(50) Jacobson, A. J. *Chem. Mater.* **2010**, *22*, 660–674.

(51) Kamihara, Y.; Hiramatsu, H.; Hirano, M.; Kawamura, R.; Yanagi, H.; Kamiya, T.; Hosono, H. *J. Am. Chem. Soc.* **2006**, *128*, 10012–10013.

(52) Kamihara, Y.; Watanabe, T.; Hirano, M.; Hosono, H. *J. Am. Chem. Soc.* **2008**, *130*, 3296–3297.

(53) Ueda, K.; Hiramatsu, H.; Ohta, H.; Hirano, M.; Kamiya, T.; Hosono, H. *Phys. Rev. B* **2004**, *69*, 155305.

(54) Clarke, S. J.; Adamson, P.; Herkelrath, S. J. C.; Rutt, O. J.; Parker, D. R.; Pitcher, M. J.; Smura, C. F. *Inorg. Chem.* **2008**, *47*, 8473–8486.

(55) Schwerdtfeger, P.; Nagle, J. K. *Mol. Phys.* **2019**, *117*, 1200–1225.

(56) Slater, J. C. *J. Chem. Phys.* **1964**, *41*, 3199–3204.

(57) Pearson, R. G. *J. Chem. Educ.* **1968**, *45*, 581 and 643.

(58) Cárdenas, C.; Ayers, P. W. *Phys. Chem. Chem. Phys.* **2013**, 15, 13959–13968.

(59) Ebbinghaus, S. G.; Abicht, H.-P.; Dronskowski, R.; Müller, T.; Reller, A.; Weidenkaff, A. *J. Prog. Solid State Chem.* **2009**, *37*, 173–205.

(60) Tsujimoto, Y.; Yamaura, K.; Takayama-Muromachi, E. *J Appl. Sci.* **2012**, *2*, 206–219.

(61) Stock, C.; McCabe, E. *J. Condens. Matter Phys.* **2016**, *28*, 453001.

(62) Luu, S. D.; Vaqueiro, P. *J. Materiomics* **2016**, *2*, 131–140.

(63) Hiramatsu, H.; Yanagi, H.; Kamiya, T.; Ueda, K.; Hirano, M.; Hosono, H. *Chem. Mater.* **2008**, *20*, 326–334.

(64) Ueda, K.; Hiramatsu, H.; Hirano, M.; Kamiya, T.; Hosono, H. *Thin Solid Films* **2006**, *496*, 8–15.

(65) Wilmer, D.; Jorgensen, J. D.; Wuensch, B. J. *Solid State Ionics* **2000**, *136–137*, 961–966.

(66) Hiramatsu, H.; Kamihara, Y.; Yanagi, H.; Ueda, K.; Kamiya, T.; Hirano, M.; Hosono, H. *J. Eur. Ceram. Soc.* **2009**, *29*, 245–253.

(67) Tippireddy, S.; Prem Kumar, D. S.; Das, S.; Mallik, R. C. *ACS Appl. Energy Mater.* **2021**, *4*, 2022–2040.

(68) Muir, S.; Subramanian, M. A. *Prog. Solid State Chem.* **2012**, *40*, 41–56.

(69) Orr, M.; Hebberd, G. R.; McCabe, E. E.; Macaluso, R. T. *ACS Omega* **2022**, *7*, 8209–8218.

(70) Li, Z.; Xiao, C.; Xie, Y. *Appl. Phys. Rev.* **2022**, *9*, 011303.

(71) Nakai, I.; Koto, K.; Nagashima, K.; Morimoto, N. *Chem. Lett.* **1977**, *6*, 275–276.

(72) Sabelli, C.; Nakai, I.; Katsura, S. *Am. Miner.* **1988**, *73*, 398–404.

(73) Zhao, F.; Yuan, M.; Zhang, W.; Gao, S. *J. Am. Chem. Soc.* **2006**, *128*, 11758–11759.

(74) Yang, L.; Cai, Z.; Hao, L.; Xing, Z.; Dai, Y.; Xu, X.; Pan, S.; Duan, Y.; Zou, J. *ACS Appl. Mater. Interfaces* **2017**, *9*, 22518–22529.

(75) Strobel, S.; Choudhury, A.; Dorhout, P. K.; Lipp, C.; Schleid, T. *Inorg. Chem.* **2008**, *47*, 4936–4944.

(76) Johnson, V.; Jeitschko, W. *J. Solid State Chem.* **1974**, *11*, 161–166.

(77) Pöttgen, R.; Johrendt, D. *Z. Naturforsch. B* **2008**, *63*, 1135–1148.

(78) Céolin, R.; Rodier, N. *Acta Crystallogr. Sect. B Struct. Crystallogr. Cryst. Chem.* **1976**, *32*, 1476–1479.

(79) Pardo, M. P.; Céolin, R.; Guittard, M. *C. R. Seances Acad. Sci., Ser. C* **1976**, *283*, 735–738.

(80) Si, Q.; Rabello, S.; Ingersent, K.; Smith, J. L. *Nature* **2001**, *413*, 804–808.

(81) Nagao, M.; Miura, A.; Ueta, I.; Watauchi, S.; Tanaka, I. *Solid State Commun.* **2016**, *245*, 11–14.

(82) Higashinaka, R.; Asano, T.; Nakashima, T.; Fushiya, K.; Mizuguchi, Y.; Miura, O.; Matsuda, T. D.; Aoki, Y. *J. Phys. Soc. Jpn.* **2014**, *84*, 023702.

(83) Tanaka, M.; Nagao, M.; Matsumoto, R.; Kataoka, N.; Ueta, I.; Tanaka, H.; Watauchi, S.; Tanaka, I.; Takano, Y. *J. Alloys Compd.* **2017**, *722*, 467–473.

(84) Mizuguchi, Y.; Demura, S.; Deguchi, K.; Takano, Y.; Fujihisa, H.; Gotoh, Y.; Izawa, H.; Miura, O. *J. Phys. Soc. Jpn.* **2012**, *81*, 114725.

(85) Xing, J.; Li, S.; Ding, X.; Yang, H.; Wen, H.-H. *Phys. Rev. B* **2012**, *86*, 214518.

(86) Jha, R.; Kumar, A.; Kumar Singh, S.; Awana, V. P. S. *J. Supercond. Novel Magn.* **2013**, *26*, 499–502.

(87) Demura, S.; Mizuguchi, Y.; Deguchi, K.; Okazaki, H.; Hara, H.; Watanabe, T.; Denholme, S. J.; Fujioka, M.; Ozaki, T.; Fujihisa, H.; Gotoh, Y.; Miura, O.; Yamaguchi, T.; Takeya, H.; Takano, Y. *J. Phys. Soc. Jpn.* **2013**, *82*, 033708.

(88) Yazici, D.; Huang, K.; White, B. D.; Chang, A. H.; Friedman, A. J.; Maple, M. B. *Philos. Mag.* **2013**, *93*, 673–680.

(89) Tomita, T.; Ebata, M.; Soeda, H.; Takahashi, H.; Fujihisa, H.; Gotoh, Y.; Mizuguchi, Y.; Izawa, H.; Miura, O.; Demura, S.; Deguchi, K.; Takano, Y. *J. Phys. Soc. Jpn.* **2014**, *83*, 063704.

(90) Mizuguchi, Y.; Miura, A.; Nishida, A.; Miura, O.; Tadanaga, K.; Kumada, N.; Lee, C. H.; Magome, E.; Moriyoshi, C.; Kuroiwa, Y. *J Appl. Phys.* **2016**, *119*, 155103.

(91) Mizuguchi, Y. *Chem. Rec.* **2016**, *16*, 633–651.

(92) Guittard, M.; Bénazeth, S.; Dugué, J.; Jaulmes, S.; Palazzi, M.; Laruelle, P.; Flahaut, J. *J. Solid State Chem.* **1984**, *51*, 227–238.

(93) Kabbour, H.; Cario, L.; Moëlo, Y.; Meerschaut, A. *J. Solid State Chem.* **2004**, *177*, 1053–1059.

(94) Gastaldi, L.; Carré, D.; Pardo, M. P. *Acta Crystallogr. Sect. B Struct. Crystallogr. Cryst. Chem.* **1982**, *38*, 2365–2367.

(95) Kabbour, H.; Sayede, A.; Saitzek, S.; Lefèvre, G.; Cario, L.; Trentesaux, M.; Roussel, P. *Chem. Commun.* **2020**, *56*, 1645–1648.

(96) Miura, A.; Oshima, T.; Maeda, K.; Mizuguchi, Y.; Moriyoshi, C.; Kuroiwa, Y.; Meng, Y.; Wen, X.-D.; Nagao, M.; Higuchi, M.; Tadanaga, K. *J. Mater. Chem. A* **2017**, *5*, 14270–14277.

(97) Ito, H.; Miura, A.; Goto, Y.; Mizuguchi, Y.; Moriyoshi, C.; Kuroiwa, Y.; Azuma, M.; Liu, J.; Wen, X.-D.; Nishioka, S.; Maeda, K.; Masubuchi, Y.; Rosero-Navarro, N. C.; Tadanaga, K. *Dalton Trans.* **2019**, *48*, 12272–12278.

(98) Weiland, A.; Frith, M. G.; Lapidus, S. H.; Chan, J. Y. *Chem. Mater.* **2021,** *33*, 7657–7664.

(99) Kanatzidis, M. G. *Inorg. Chem.* **2017**, *56*, 3158–3173.

(100) Shoemaker, D. P.; Chung, D. Y.; Mitchell, J. F.; Bray, T. H.; Soderholm, L.; Chupas, P. J.; Kanatzidis, M. G. *J. Am. Chem. Soc.* **2012**, *134*, 9456–9463.

(101) Massa, W. *Crystal Structure Determination*, 2nd ed.; Springer: Berlin, 2004.

(102) Mishra, V.; Subbarao, U.; Roy, S.; Sarma, S. C.; Mumbaraddi, D.; Sarkar, S.; Peter, S. C. *Inorg. Chem.* **2018**, *57*, 12576–12587.

(103) Mishra, V.; Mumbaraddi, D.; Iyer, A. K.; Mar, A., *J. Solid State Chem.* **2021**, *297*, 122096.

(104) Else, H. *Nature* **2022**, *608*, 461.

(105) Mishra, V.; Mumbaraddi, D.; Iyer, A. K.; Yin, W.; Mar, A. *J. Solid State Chem.* **2022**, *308*, 122901.

(106) Mishra, V.; Zabolotnii, A.; Mar, A. *Inorg. Chem.* **2022**, *61*, 12458–12465.

(107) Russ, J. C. *Fundamentals of Energy Dispersive X-ray Analysis*; Butterworth: London, 1984.

(108) Mishra, V.; Oliynyk, A. O.; Subbarao, U.; Sarma, S. C.; Mumbaraddi, D.; Roy, S.; Peter, S. C. *Cryst. Growth Des.* **2018**, *18*, 6091–6099.

(109) Mishra, V.; Iyer, A. K.; Mumbaraddi, D.; Oliynyk, A. O.; Zuber, G.; Boucheron, A.; Dmytriv, G.; Bernard, G. M.; Michaelis, V. K.; Mar, A. *J. Solid State Chem.* **2020**, *292*, 121703.

(110) Mumbaraddi, D.; Mishra, V.; Lidin, S.; Mar, A. *J. Solid State Chem.* **2022**, *311*, 123157.

(111) Jomaa, M.; Mishra, V.; Mumbaraddi, D.; Chaudhary, M.; Dmytriv, G.; Michaelis, V. K.; Mar, A. *J. Solid State Chem.* **2022**, *306*, 122792.

(112) Jomaa, M.; Mishra, V.; Chaudhary, M.; Mumbaraddi, D.; Michaelis, V. K.; Mar, A. *J. Solid State Chem.* **2022**, *314*, 123372.

(113) Kubelka, P.; Munk, F. *Z. Tech. Phys.* **1931**, *12*, 259–274.

(114) Urbach, F. *Phys. Rev.* **1953**, *92*, 1324–1324.

(115) *Properties of Crystalline Silicon*, 4th ed.; Hull, R., Ed.; INSPEC: London, 1999.

(116) Bloch, F. *Z. Phys.* **1929**, *52*, 555–600.

(117) Kohn, W.; Sham, L. J. *Phys. Rev.* **1965**, *140*, A1133–A1138.

(118) Born, M.; Oppenheimer, R. *Ann. Phys.* **1927**, *389*, 457–484.

(119) Perdew, J. P.; Burke, K.; Ernzerhof, M. *Phys. Rev. Lett.* **1996**, *77*, 3865–3868.

(120) Perdew, J. P.; Ernzerhof, M.; Burke, K. *Chem. Phys.* **1996**, *105*, 9982–9985.

(121) Müller, P. C.; Ertural, C.; Hempelmann, J.; Dronskowski, R. *J. Phys. Chem. C* **2021**, *125*, 7959–7970.

(122) Wiberg, K. B. *Tetrahedron* **1968**, *24*, 1083–1096.

(123) Mayer, I. *Chem. Phys. Lett.* **1983**, *97*, 270–274.

(124) Mitchell, K.; Ibers, J. A. *Chem. Rev.* **2002**, *102*, 1929–1952.

(125) Alemi, A.; Klein, A.; Meyer, G.; Dolatyari, M.; Babalou, A. *Z. Anorg. Allg. Chem.* **2011**, *637*, 87–93.

(126) Chi, Y.; Guo, S.-P.; Xue, H.-G. *RSC Adv.* **2017**, *7*, 5039–5045.

(127) Villars, P.; Cenzual, K. *Pearson's Crystal Data – Crystal Structure Database for Inorganic Compounds,* Release 2019/20, ASM International, Materials Park, OH, USA.

(128) Lozac'h, A. M.; Jaulmes, S.; Guittard, M. *C. R. Seances Acad. Sci., Ser. C* **1971**, *272*, 1123–1126.

(129) Jaulmes, S.; Laruelle, P. *Acta Crystallogr. Sect. B Struct. Crystallogr. Cryst. Chem.* **1973**, *29*, 352–354.

(130) Loireau-Lozac'h, A. M.; Guittard, M.; Flahaut, J. *Mater. Res. Bull.* **1977**, *12*, 881–886.

(131) Zhang, M.-J.; Li, B.-X.; Liu, B.-W.; Fan, Y.-H.; Li, X.-G.; Zeng, H.-Y.; Guo, G.-C. *Dalton Trans.* **2013**, *42*, 14223–14229.

(132) Carré, D.; Guittard, M.; Adolphe, C. *Acta Crystallogr. Sect. B Struct. Crystallogr. Cryst. Chem.* **1978**, *34*, 3499–3501.

(133) Guittard, M.; Carré, D.; Kabré, T. S. *Mater. Res. Bull.* **1978**, *13*, 279–286.

(134) Aliev, O. M. *Izv. Akad. Nauk. SSSR – Neorg. Mater.* **1980**, *16*, 1514–1518.

(135) Akhmedova, D. A.; Agaev, A. B.; Rustamov, P. G. *Zh. Neorg. Khim.* **1992**, *37*, 461–464.

(136) Ivashchenko, I. A.; Kozak, V. S.; Olekseyuk, I. D.; Daszkiewicz, M.; Halyan, V. V.; Tishchenko, P. V.; Shemet, V. Y.; Gulay, L. D. *J. Solid State Chem.* **2020**, *288*, 121339.

(137) Messain, D.; Carré, D.; Laruelle, P. *Acta Crystallogr. Sect. B Struct. Crystallogr. Cryst. Chem.* **1977**, *33*, 2540–2542.

(138) Gulay, L. D.; Daszkiewicz, M.; Huch, M. R. *J. Solid State Chem.* **2008**, *181*, 2626–2632.

(139) Aleandri, L. E.; Ibers, J. A. *J. Solid State Chem.* **1989**, *79*, 107–111.

(140) Aleandri, L. E.; Ibers, J. A. *J. Solid State Chem.* **1989**, *81*, 317.

(141) Tougait, O.; Ibers, J. A. *Inorg. Chem.* **2000**, *39*, 1790–1794.

(142) Huch, M. R.; Gulay, L. D.; Olekseyuk, I. D. *J. Alloys Compd.* **2007**, *439*, 156–161.

(143) Coelho, A. A. *TOPAS–Academic, Version 6*, Coelho Software, Brisbane, Australia, 2007.

(144) Sheldrick, G. M. *Acta Crystallogr. Sect. A: Found. Crystallogr.* **2008**, *64*, 112–122.

(145) Gelato, L. M.; Parthé, E. *J. Appl. Crystallogr.* **1987**, *20*, 139–143.

(146) Tank, R.; Jepsen, O.; Burkhardt, A.; Andersen, O. K. *TB-LMTO-ASA Program, Version 4.7*, Max-Planck-Institut für Festkörperforschung: Stuttgart, Germany, 1998.

(147) Dronskowski, R.; Bloechl, P. E. *J. Phys. Chem.* **1993**, *97*, 8617–8624.

(148) Kortüm, G. *Reflectance Spectroscopy*; Springer, New York, 1969.

(149) Brese, N. E.; O'Keeffe, M. *Acta Crystallogr. Sect. B Struct. Sci.* **1991**, *47*, 192–197.

(150) Fedorchenko, V. P.; Lashkarev, G. V. *Izv. Akad. Nauk. SSSR – Neorg. Mater.* **1974**, *10*, 1177–1183.

(151) Mori-Sánchez, P.; Cohen, A. J.; Yang, W. *Phys. Rev. Lett.* **2008**, *100*, 146401.

(152) Kageyama, H.; Hayashi, K.; Maeda, K.; Attfield, J. P.; Hiroi, Z.; Rondinelli, J. M.; Poeppelmeier, K. R. *Nat. Commun.* **2018**, *9*, 772.

(153) Harada, J. K.; Charles, N.; Poeppelmeier, K. R.; Rondinelli, J. M. *Adv. Mater.* **2019**, *31*, 1805295.

(154) Clarke, S. J.; Adamson, P.; Herkelrath, S. J. C.; Rutt, O. J.; Parker, D. R.; Pitcher, M. J.; Smura, C. F. *Inorg. Chem.* **2008**, *47*, 8473–8486.

(155) Hiramatsu, H.; Kamihara, Y.; Yanagi, H.; Ueda, K.; Kamiya, T.; Hirano, M.; Hosono, H. *J. Eur. Ceram. Soc.* **2009**, *29*, 245–253.

(156) Muir, S.; Subramanian, M. A. *Prog. Solid State Chem.* **2012**, *40*, 41–56.

(157) Luu, S. D. N.; Vaqueiro, P. *J. Materiomics* **2016**, *2*, 131–140.

(158) Tippireddy, S.; D S, P. K.; Das, S.; Mallik, R. C. *ACS Appl. Energy Mater.* **2021**, *4*, 2022–2040.

(159) Xiao, J.-R.; Yang, S.-H.; Feng, F.; Xue, H.-G.; Guo, S.-P. *Coord. Chem. Rev.* **2017**, *347*, 23–47.

(160) Krivovichev, S. V.; Mentré, O.; Siidra, O. I.; Colmont, M.; Filatov, S. K. *Chem. Rev.* **2013**, *113*, 6459–6535.

(161) Ueda, K.; Hiramatsu, H.; Hirano, M.; Kamiya, T.; Hosono, H. *Thin Solid Films* **2006**, *496*, 8–15.

(162) Wilmer, D.; Jorgensen, J. D.; Wuensch, B. J. *Solid State Ionics* **2000**, *136–137*, 961–966.

(163) Mizuguchi, Y.; Omachi, A.; Goto, Y.; Kamihara, Y.; Matoba, M.; Hiroi, T.; Kajitani, J.; Miura, O. *J. Appl. Phys.* **2014**, *116*, 163915.

(164) Chen, Y.; Cui, Y.; Pham, A.; Wang, Y.; Bhadbhade, M. M.; Wang, R.; Su, Y.; Hu, H.; Wen, Z.; Cheng, C.; Tan, T. T.; Li, S.; Zhao, Y. *J. Mater. Chem. C* **2019**, *7*, 586–591.

(165) Ishikawa, A.; Takata, T.; Kondo, J. N.; Hara, M.; Kobayashi, H.; Domen, K. *J. Am. Chem. Soc.* **2002**, *124*, 13547–13553.

(166) Miura, A.; Oshima, T.; Maeda, K.; Mizuguchi, Y.; Moriyoshi, C.; Kuroiwa, Y.; Meng, Y.; Wen, X.-D.; Nagao, M.; Higuchi, M.; Tadanaga, K. *J. Mater. Chem. A* **2017**, *5*, 14270–14277.

(167) Jaulmes, P. S. *Acta Crystallogr. B* **1978**, *34*, 2610–2612.

(168) Bénazeth, S.; Guittard, M.; Laruelle, P. *Acta Crystallogr. C* **1984**, *40*, 345–347.

(169) Guittard, M.; Bénazeth, S.; Dugué, J.; Jaulmes, S.; Palazzi, M.; Laruelle, P.; Flahaut, J. *J. Solid State Chem.* **1984**, *51*, 227–238.

(170) Ito, H.; Miura, A.; Goto, Y.; Mizuguchi, Y.; Moriyoshi, C.; Kuroiwa, Y.; Azuma, M.; Liu, J.; Wen, X.-D.; Nishioka, S.; Maeda, K.; Masubuchi, Y.; Rosero-Navarro, N. C.; Tadanaga, K. *Dalton Trans.* **2019**, *48*, 12272–12278.

(171) Kabbour, H.; Cario, L.; Moëlo, Y.; Meerschaut, A. *J. Solid State Chem.* **2004**, *177*, 1053–1059.

(172) Dugué, J.; Guittard, M. *Acta Crystallogr. B* **1982**, *38*, 2368–2371.

(173) Bénazeth, S.; Laruelle, P.; Guittard, M. *J. Solid State Chem.* **1989**, *78*, 148–153.

(174) Mazurier, A.; Guittard, M.; Jaulmes, S. *Acta Crystallogr. B* **1982**, *38*, 379–382.

(175) Jaulmes, S.; Mazurier, A.; Guittard, M. *Acta Crystallogr. C* **1983**, *39*, 1594–1597.

(176) Gastaldi, L.; Carré, D.; Pardo, M. P. *Acta Crystallogr. B* **1982**, *38*, 2365–2367.

(177) Mishra, V.; Mumbaraddi, D.; Iyer, A. K.; Mar, A. *J. Solid State Chem.* **2021**, *297*, 122096.

(178) Toby, B. H.; Von Dreele, R. B. *J. Appl. Crystallogr.* **2013**, *46*, 544–549.

(179) Sheldrick, G. M. *Acta Crystallogr. A: Found. Crystallogr.* **2008**, *64*, 112–122.

(180) Gelato, L. M.; Parthé, E. *J. Appl. Crystallogr.* **1987**, *20*, 139–143.

(181) Kresse, G.; Furthmüller, J. *Phys. Rev. B* **1996**, *54*, 11169–11186.

(182) Kresse, G.; Joubert, D. *Phys. Rev. B* **1999**, *59*, 1758–1775.

(183) Blöchl, P. E. *Phys. Rev. B* **1994**, *50*, 17953–17979.

(184) Perdew, J. P.; Burke, K.; Ernzerhof, M. *Phys. Rev. Lett.* **1996**, *77*, 3865–3868.

(185) Hohenberg, P.; Kohn, W. *Phys. Rev.* **1964**, *136*, B864–B871.

(186) Kohn, W.; Sham, L. J. *Phys. Rev.* **1965**, *140*, A1133–A1138.

(187) Dronskowski, R.; Blöchl, P. E. *J. Phys. Chem.* **1993**, *97*, 8617–8624.

(188) Deringer, V. L.; Tchougréeff, A. L.; Dronskowski, R. *J. Phys. Chem. A* **2011**, *115*, 5461–5466.

(189) Maintz, S.; Deringer, V. L.; Tchougréeff, A. L.; Dronskowski, R. *J. Comput. Chem.* **2013**, *34*, 2557–2567.

(190) Grin, Y.; Savin, A.; Silvi, B., The ELF perspective of chemical bonding. In *The Chemical Bond: Fundamental Aspects of Chemical Bonding*, Frenking, G.; Shaik, S., Eds.; Wiley-VCH: Weinheim, **2014**; pp 345–382.

(191) Maintz, S.; Deringer, V. L.; Tchougréeff, A. L.; Dronskowski, R. *J. Comput. Chem.* **2016**, *37*, 1030–1035.

(192) Kortüm, G. *Reflectance Spectroscopy*; Springer, New York, 1969.

(193) Le Bihan, T.; Darracq, S.; Heathman, S.; Benedict, U.; Mattenberger, K.; Vogt, O. *J. Alloys Compd.* **1995**, *226*, 143–145.

(194) Villars, P.; Cenzual, K., *Pearson's Crystal Data – Crystal Structure Database for Inorganic Compounds*, Release 2021/22, ASM International: Materials Park, OH, USA.

(195) Shannon, R. D.; Prewitt, C. T. *J. Inorg. Nucl. Chem.* **1968**, *30*, 1389–1398.

(196) Michiue,Y.; Kimizuka, N.; Kanke, Y. *Acta Crystallogr. B* **2008**, *64*, 521–526.

(197) Rodier, N. *Bull. Soc. Fr. Minéral. Cristallogr.* **1973**, *96*, 350–355.

(198) Carre, D. *Acta Crystallogr. B* **1977**, *33*, 1163–1166.

(199) Brese, N. E.; O'Keeffe, M. *Acta Crystallogr. Sect. B Struct. Sci.* **1991**, *47*, 192–197.

(200) Guittard, M.; Flahaut, J.; Domange, L. *Acta Crystallogr.* **1966**, *21*, 832.

(201) Jain, A.; Ong, S. P.; Hautier, G.; Chen, W.; Richards, W. D.; Dacek, S.; Cholia, S.; Gunter, D.; Skinner, D.; Ceder, G.; Persson, K. A. *APL Mater.* **2013**, *1*, 011002.

(202) Kageyama, H.; Hayashi, K.; Maeda, K.; Attfield, J. P.; Hiroi, Z.; Rondinelli, J. M.; Poeppelmeier, K. R. *Nat. Commun.* **2018**, *9*, 772.

(203) Harada, J. K.; Charles, N.; Poeppelmeier, K. R.; Rondinelli, J. M. *Adv. Mater.* **2019**, *31*, 1805295.

(204) Tripathi, T. S.; Karppinen, M. *Adv. Mater. Interfaces* **2021**, *8*, 2100146.

(205) Clarke, S. J.; Adamson, P.; Herkelrath, S. J. C.; Rutt, O. J.; Parker, D. R.; Pitcher, M. J.; Smura, C. F. *Inorg. Chem.* **2008**, *47*, 8473–8486.

(206) Luu, S. D. N.; Vaqueiro, P. *J. Materiomics* **2016**, *2*, 131–140.

(207) Larquet, C.; Carenco, S. *Front. Chem.* **2020**, *8*, 179.

(208) Tippireddy, S.; Prem Kumar, D. S.; Das, S.; Malik, R. C. *ACS Appl. Energy Mater.* **2021**, *4*, 2022–2040.

(209) Orr, M.; Hebberd, G. R.; McCabe, E. E.; Macaluso, R. T. *ACS Omega* **2020**, *7*, 8209–8218.

(210) Ueda, K.; Inoue, S.; Hirose, S.; Kawazoe, H.; Hosono, H. *Appl. Phys. Lett.* **2020**, *77*, 2701–2703.

(211) Palazzi, M.; Carcaly, C.; Flahaut, J. *J. Solid State Chem.* **1980**, *35*, 150–155.

(212) Ishikawa, A.; Takata, T.; Kondo, J. N.; Hara, M.; Kobayashi, H.; Domen, K. *J. Am. Chem. Soc.* **2002**, *124*, 13547–13553.

(213) Mizuguchi, Y.; Omachi, A.; Goto, Y.; Kamihara, Y.; Matoba, M.; Hiroi, T.; Kajitani, J.; Miura, O. *J. Appl. Phys.* **2014**, *116*, 163915.

(214) Guittard, M.; Bénazeth, S.; Dugué, J.; Jaulmes, S.; Palazzi, M.; Laruelle, P.; Flahaut, J. *J. Solid State Chem.* **1984**, *51*, 227–238.

(215) Carré, D.; Guittard, M.; Jaulmes, S.; Mazurier, A.; Palazzi, M.; Pardo, M. P.; Laruelle, P.; Flahaut, J. *J. Solid State Chem.* **1984**, *55*, 287–292.

(216) Figueiredo, M. O. *Inorg. Chim. Acta* **1987**, *140*, 161–164.

(217) Jaulmes, S. *Acta Crystallogr. Sect. B* **1978**, *34*, 2610–2612.

(218) Dugué, J.; Guittard, M. *Acta Crystallogr. Sect. B* **1982**, *38*, 2368–2371.

(219) Mazurier, A.; Guittard, M.; Jaulmes, S. *Acta Crystallogr. Sect. B* **1982**, *38*, 379–382.

(220) Jaulmes, S.; Mazurier, A.; Guittard, M. *Acta Crystallogr. Sect. C* **1983**, *39*, 1594–1597.

(221) Bénazeth, S.; Guittard, M.; Laruelle, P. *Acta Crystallogr. Sect. C* **1984**, *40*, 345–347.

(222) Bénazeth, S.; Laruelle, P.; Guittard, M. *J. Solid State Chem.* **1989**, *78*, 148–153.

(223) Mishra, V.; Mumbaraddi, D.; Iyer, A. K.; Yin, W.; Mar, A. *J. Solid State Chem.* **2022**, *308*, 122901.

(224) Ogisu, K.; Ishikawa, A.; Shimodaira, Y.; Takata, T.; Kobayashi, H.; Domen, K. *J. Phys. Chem. C* **2008**, *112*, 11978–11984.

(225) Sheldrick, G. M. *Acta Crystallogr., Sect. A: Found. Crystallogr.* **2008**, *64*, 112–122.

(226) Gelato, L. M.; Parthé, E. *J. Appl. Crystallogr.* **1987**, *20*, 139–143.

(227) Spek, A. L. *Acta Crystallogr., Sect. D* **2009**, *65*, 148–155.

(228) Hafner, J. *J. Comput. Chem.* **2008**, *29*, 2044–2078.

(229) Perdew, J. P.; Burke, K.; Ernzerhof, M. *Phys. Rev. Lett.* **1996**, *77*, 3865–3868.

(230) Deringer, V. L.; Tchougréeff, A. L.; Dronskowski, R. *J. Phys. Chem. A* **2011**, *115*, 5461–5466.

(231) Maintz, S.; Deringer, V. L.; Tchougréeff, A.L.; Dronskowski, R. *J. Comput. Chem.* **2013**, *34*, 2557–2567.

(232) Grin, Y.; Savin, A.; Silvi, B. The ELF perspective of chemical bonding. In *The Chemical Bond: Fundamental Aspects of Chemical Bonding*; Frenking, G., Shaik, S., Eds.; Wiley-VCH, Weinheim, 2014, pp. 345–382.

(233) Maintz, S.; Deringer, V. L.; Tchougréeff, A. L.; Dronskowski, R. *J. Comput. Chem.* **2016**, *37*, 1030–1035.

(234) Togo, A.; Tanaka, I. *Scr. Mater.* **2015**, *28*, 1–5.

(235) Madsen, G. K. H.; Carrete, J.; Verstraete, M. J. *Comput. Phys. Commun.* **2018**, *231*, 140–145.

(236) Kortüm, G. *Reflectance Spectroscopy*; Springer, New York, 1969.

(237) Villars, P.; Cenzual, K. *Pearson's Crystal Data – Crystal Structure Database for Inorganic Compounds,* Release 2021/22, ASM International, Materials Park, OH, USA.

(238) Palazzi, M.; Jaulmes, S. *Acta Crystallogr., Sect. B* **1981**, *37*, 1340–1342.

(239) Brese, N. E.; O'Keeffe, M. *Acta Crystallogr., Sect. B: Struct. Sci.* **1991**, *47*, 192–197.

(240) Bube, R. H.; Lind, E. L. *Phys. Rev.* **1959**, *115*, 1159–1164.

(241) Clarke, S. J.; Adamson, P.; Herkelrath, S. J. C.; Rutt, O. J.; Parker, D. R.; Pitcher, M. J.; Smura, C. F. *Inorg. Chem.* **2008**, *47*, 8473–8486.

(242) Hiramatsu, H.; Kamihara, Y.; Yanagi, H.; Ueda, K.; Kamiya, T.; Hirano, M.; Hosono, H. *J. Eur. Ceram. Soc.* **2009**, *29*, 245–253.

(243) Muir, S.; Subramanian, M. A. *Prog. Solid State Chem.* **2012**, *40*, 41–56.

(244) Luu, S. D. N.; Vaqueiro, P. *J. Materiomics* **2016**, *2*, 131–140.

(245) Tippireddy, S.; D S, P. K.; Das, S.; Mallik, R. C. *ACS Appl. Energy Mater.* **2021**, *4*, 2022–2040.

(246) Orr, M.; Hebberd, G. R.; McCabe, E. E.; Macaluso, R. T. *ACS Omega* **2022**, *7*, 8209–8218.

(247) Recham, N.; Chotard, J. N.; Dupont, L.; Delacourt, C.; Walker, W.; Armand, M.; Tarascon, J. M. *Nat. Mater.* **2010**, *9*, 68–74.

(248) Jansen, M.; Letschert, H. P. *Nature* **2000**, *404*, 980–982.

(249) Ueda, K.; Hiramatsu, H.; Hirano, M.; Kamiya, T.; Hosono, H. *Thin Solid Films* **2006**, *496*, 8–15.

(250) Chen, Y.; Cui, Y.; Pham, A.; Wang, Y.; Bhadbhade, M. M.; Wang, R.; Su, Y.; Hu, H.; Wen, Z.; Cheng, C.; Tan, T. T.; Li, S.; Zhao, Y. *J. Mater. Chem. C* . **2019**, *7*, 586–591.

(251) Wilmer, D.; Jorgensen, J. D.; Wuensch, B. J. *Solid State Ion.* **2000**, *136–137*, 961–966.

(252) Ishikawa, A.; Takata, T.; Kondo, J. N.; Hara, M.; Kobayashi, H.; Domen, K. *J. Am. Chem. Soc.* **2002**, *124*, 13547–13553.

(253) Miura, A.; Oshima, T.; Maeda, K.; Mizuguchi, Y.; Moriyoshi, C.; Kuroiwa, Y.; Meng, Y.; Wen, X.-D.; Nagao, M.; Higuchi, M.; Tadanaga, K. *J. Mater. Chem. A* **2017**, *5*, 14270–14277.

(254) Jaulmes, S. *Acta Crystallogr. B* **1978**, *34*, 2610–2612.

(255) Bénazeth, S.; Guittard, M.; Laruelle, P. *Acta Crystallogr. C* **1984**, *40*, 345–347.

(256) Guittard, M.; Benazeth, S.; Dugué, J.; Jaulmes, S.; Palazzi, M.; Laruelle, P.; Flahaut, J. *J. Solid State Chem.* **1984**, *51*, 227–238.

(257) Ito, H.; Miura, A.; Goto, Y.; Mizuguchi, Y.; Moriyoshi, C.; Kuroiwa, Y.; Azuma, M.; Liu, J.; Wen, X.-D.; Nishioka, S.; Maeda, K.; Masubuchi, Y.; Rosero-Navarro, N. C.; Tadanaga, K. *Dalton Trans.* **2019**, *48*, 12272–12278.

(258) Kabbour, H.; Cario, L.; Moëlo, Y.; Meerschaut, A. *J. Solid State Chem.* **2004**, *177*, 1053–1059.

(259) Dugué, J.; Guittard, M. *Acta Crystallogr. B* **1982**, *38*, 2368–2371.

(260) Bénazeth, S.; Laruelle, P.; Guittard, M. *J. Solid State Chem.* **1989**, *78*, 148–153.

(261) Mazurier, A.; Guittard, M.; Jaulmes, S. *Acta Crystallogr. B* **1982**, *38*, 379–382.

(262) Jaulmes, S.; Mazurier, A.; Guittard, M. *Acta Crystallogr. B* **1983**, *39*, 1594–1597.

(263) Gastaldi, L.; Carre, D.; Pardo, M. *Acta Crystallogr. B* **1982**, *38*, 2365–2367.

(264) Mishra, V.; Mumbaraddi, D.; Iyer, A. K.; Yin, W.; Mar, A. *J. Solid State Chem.* **2022**, *308*, 122901.

(265) Sheldrick, G. M. *Acta Crystallogr. A: Found. Crystallogr.* **2008**, *64*, 112–122.

(266) Gelato, L. M.; Parthé, E. *J. Appl. Crystallogr.* **1987**, *20*, 139–143.

(267) Kresse, G.; Furthmüller, J. *Phys. Rev. B* **1996**, *54*, 11169–11186.

(268) Kresse, G.; Joubert, D. *Phys. Rev. B* **1999**, *59*, 1758–1775.

(269) Blöchl, P. E. *Phys. Rev. B* **1994**, *50*, 17953–17979.

(270) Perdew, J. P.; Burke, K.; Ernzerhof, M. *Phys. Rev. Lett.* **1996**, *77*, 3865–3868.

(271) Hohenberg, P.; Kohn, W. *Phys. Rev.* **1964**, *136*, B864–B871.

(272) Kohn, W.; Sham, L. J. *Phys. Rev.* **1965**, *140*, A1133–A1138.

(273) Momma, K.; Izumi, F. *J. Appl. Crystallogr.* **2011**, *44*, 1272–1276.

(274) Grin, Y.; Savin, A.; Silvi, B. The ELF Perspective of Chemical Bonding. In *The Chemical Bond: Fundamental Aspects of Chemical Bonding*, Frenking, G.; Shaik, S Eds. Wiley-VCH: Weinheim, 2014; pp 345–380.

(275) Henkelman, G.; Arnaldsson, A.; Jónsson, H. *J. Comput. Mater. Sci.* **2006**, *36*, 354–360.

(276) Sanville, E.; Kenny, S. D.; Smith, R.; Henkelman, G. *J. Comput. Mater. Sci.* **2007**, *28*, 899–908.

(277) Tang, W.; Sanville, E.; Henkelman, G. *J. Condens. Matter Phys.* **2009**, *21*, 084204.

(278) Deringer, V. L.; Tchougréeff, A. L.; Dronskowski, R. *J. Phys. Chem. A* **2011**, *115*, 5461–5466.

(279) Maintz, S.; Deringer, V. L.; Tchougréeff, A. L.; Dronskowski, R. *J. Comput. Chem.* **2016**, *37*, 1030–1035.

(280) Müller, P. C.; Ertural, C.; Hempelmann, J.; Dronskowski, R. *J. Phys. Chem. C* **2021**, *125*, 7959–7970.

(281) Madsen, G. K. H.; Carrete, J.; Verstraete, M. J. *Comput. Phys. Commun.* **2018**, 231, 140–145.

(282) Villars, P.; Cenzual, K. *Pearson's Crystal Data – Crystal Structure Database for Inorganic Compounds,* Release 2022/23, ASM International, Materials Park, OH, USA.

(283) Mishra, V.; Zabolotnii, A.; Mar, A. *Inorg. Chem.* **2022**, *61*, 12458–12465.

(284) Cretu, C.; van der Lingen, E. *Gold Bull.* **1999**, *32*, 115–126.

(285) Wolff, I. M. *Endeavour* **1995**, *19*, 16–19.

(286) Corti, C. W. In *The Santa Fe Symposium on Jewelry Manufacturing Technology*, 2004; Bell, E., Ed.; Met-Chem Research, Albuquerque. 2004; pp 121–134.

(287) Klotz, U. E. *Gold Bull.* **2010**, *43*, 4–10.

(288) Fischer-Bühner, J.; Basso, A.; Poliero, M. *Gold Bull.* **2010**, *43*, 11–20.

(289) Liu, J.; Liu, Y.; Gong, P.; Li, Y.; Moore, K. M.; Scanley, E.; Walker, F.; Broadbridge, C. C.; Schroers, J. *Gold Bull.* **2015**, *48*, 111–118.

(290) Steinemann, S. G.; Wolf, W.; Podloucky, R. Color and Optical Properties. In *Intermetallic Compounds – Principles and Practice*, Vol. 3; Westbrook, J.H., Fleischer, R.L., Eds.; Wiley, New York 2002, pp 231–244.

(291) van der Lingen, E. *J. S. Afr. Inst. Min. Metall.* **2014**, *114*, 137–144.

(292) Steinemann, S. G.; Anongba, P. N. B.; Podloucky, R. *J. Phase Equilib.* **1997**, *18*, 655–662.

(293) Cahn, R. W. *Nature* **1998**, *396*, 523–524.

(294) Keast, V. J.; Birt, K.; Koch, C. T.; Supansomboon, S.; Cortie, M. B. *Appl. Phys. Lett.* **2011**, *99*, 111908.

(295) Furrer, A.; Seita, M.; Spolenak, R. *Acta Mater.* **2013**, *61*, 2874–2883.

(296) Hurly, J.; Wedepohl, P. T. *J. Mater. Sci.* **1993**, *28*, 5648–5653.

(297) Nomerovannaya, L. V.; Kirillova, M. M.; Shaikin, A. B. *Phys. Status Solidi B* **1980**, *102*, 715–720.

(298) Jeong, Y. B.; Kim, J. T.; Hong, S. H.; Lee, H. D.; Choi, S. Y.; Kim, K. B. *Mater. Des.* **2019**, *175*, 107814-1–107814-11.

(299) Eberz, U.; Seelentag, W.; Schuster, H.-U. *Z. Naturforsch. B Chem. Sci.* **1980**, *35*, 1341–1343.

(300) Drews, J.; Eberz, U.; Schuster, H.-U. *J. Less Common. Met.* **1986**, *116*, 271–278.

(301) Czybulka, A.; Petersen, A.; Schuster, H.-U. *J. Less Common. Met.* **1990**, *161*, 303–312.

(302) Dmytriv, G.; Pauly, H.; Ehrenberg, H.; Pavlyuk, V.; Vollmar, E. *J. Solid State Chem.* **2005**, *178*, 2825–2831.

(303) Villars, P.; Cenzual, K. *Pearson's Crystal Data – Crystal Structure Database for Inorganic Compounds,* Release 2018/19, ASM International, Materials Park, OH, USA.

(304) Kraus, W.; Nolze, G. *J. Appl. Crystallogr.* **1996**, *29*, 301–303.

(305) Long, N. H.; Akai, H. *J. Phys. Condens. Matter* **2007**, *19*, 365232-1–365232-8.

(306) Dupke, S.; Eckert, H.; Winter, F.; Pöttgen, R. *Prog. Solid State Chem.* **2014**, *42*, 57–64.

(307) Hunt, R. W. G.; Pointer, M. R. *Measuring Colour*. 4th ed.; Wiley, Chichester 2011.

(308) Huheey, J. E.; Keiter, E. A.; Keiter, R. L. *Inorganic Chemistry: Principles of Structure and Reactivity*, 4th ed.; Harper Collins, New York, 1993.

(309) Burdick, G. A. *Phys. Rev.* **1963**, *129*, 138–150.

(310) Rangel, T.; Kecik, D.; Trevisanutto, P. E.; Rignanese, G. M.; Van Swygenhoven, H.; Olevano, V. *Phys. Rev. B* **2012**, *86*, 125125-1–125125-10.

(311) Saeger, K. E.; Rodies, J. *Gold Bull.* **1977**, *10*, 10–14.

Appendix 1.

Coloured intermetallic compounds $LiCu_2Al$ and $LiCu_2Ga$

A version of this appendix has been published.

Mishra, V.; Iyer, A. K.; Mumbaraddi, D.; Oliynyk, A. O.; Zuber, G.; Boucheron, A.; Dmytriv, G.; Bernard, G. M.; Michaelis, V. K.; Mar, A. J. Solid State Chem. ***2020****, 292, 121703.*

A1.1. Introduction

Metallic substances, which encompass many elements, alloys, and intermetallic compounds, possess varied physical and chemical properties which make them useful in many applications such as structural, magnetic, superconducting, and catalytic materials. Among these properties, however, colour is unusual and highly prized, as exemplified by the widespread use of gold (as well as various alloys with copper, silver, and other metals) in jewellery and decorative coatings, a multibillion dollar global industry.[1–6] Apart from gold and its alloys, intermetallic compounds can also exhibit colour, but exceedingly rarely: out of 10^5–10^6 known intermetallic compounds, only ~10^2 have been reported to be coloured.[7,8] They include binary (e.g., dark blue $CoSi_2$,[9] purple $AuAl_2$ ("purple plague"),[10–12] yellow $PtAl_2$,[13] red PdIn,[14] light yellow $MgCu_2$,[15] ternary (various Li- or Mg-containing intermetallics),[16–19] and quaternary phases (e.g., LiMgPdSn).[16]

Given the presence of highly delocalized electrons, typical metallic substances have uniformly high optical reflectivity in the visible region of the electromagnetic spectrum, resulting in their characteristic lustrous appearance. In contrast, the few exceptions that exhibit colour do so because they have absorption edges that fall within the visible region, corresponding to

electronic transitions in the range of 1.5–3.0 eV. The electronic conditions for the appearance of colour can be related to chemical and structural features: (i) the presence of sharp peaks in the density of states (DOS), which lead to distinct absorption edges, requires high space group symmetry; (ii) the placement of the Fermi level such that these states with high DOS are completely filled, generally requires late transition metals; and (iii) the fulfilment of the dipole selection rule ($\Delta l = \pm 1$) requires strong mixing of metal d and metalloid s/p states.[7,8] It is not a coincidence that many previously known coloured intermetallics are Zintl phases with cubic structures, because they are a special class of intermetallic compounds that satisfy normal valence rules, resulting in the presence of a pseudogap in the DOS that separate filled bonding from empty antibonding levels.[16–19] This situation can be contrasted with semiconductors, which exhibit colour because there is a finite energy gap, not a pseudogap, in the DOS.

The majority of known coloured intermetallics contain precious metals (e.g., Pd, Pt, Ag, Au), usually in combination with Li or Mg. The appearance of colour in such compounds was typically noted as a side observation and not a targeted property. It would be desirable to discover new coloured intermetallics prepared with less expensive components, through a more directed approach with an aim to understand how the colour arises from structural and electronic features. We hypothesize that the ternary systems Li–Cu–*X* (*X* = group 13–15 metals or metalloids) may be fruitful to find such compounds, given the requirements described above. Inspection of these systems reveals several existing coloured intermetallics (**Table A1-1**), such as $LiCu_2Si$, $LiCu_2Ge$, Li_2CuGe, and Li_2CuSn,[20] suggesting that more can be expected.

Here we report the preparation of $LiCu_2Al$ and $LiCu_2Ga$, their structural characterization by powder X-ray diffraction, and their optical reflectance spectra. ^{7}Li nuclear magnetic resonance spectroscopy was performed to resolve ambiguities in locating the Li atoms, which scatter X-rays

weakly, by diffraction methods alone. Electronic structure calculations were also carried out to gain insight on the origin of colour in these compounds.

Table A1-1. Colours in Li–Cu–*X* (*X* = Group 13–15 metals or metalloids) system.

		$Li_{2.5-2.6}Cu_{0.4}N$ black, blue $Li_{2.25}Cu_{0.43}N$ golden
$Li_6Cu_{9.6}Al_{11.4}$ dark silvery gray $Li_4Cu_{6.58}Al_{2.42}$ dark silvery gray $Li_4Cu_{4.2}Al_{4.8}$ dark gray $Li_{1.67}Cu_{1.67}Al_{3.33}$ gray	$Li_{13}Cu_{14.22}Si_{12.78}$ gray $Li_{7.3}CuSi_3$ bluish gray Li_7CuSi_2 silvery gray $LiCu_2Si$ red violet LiCuSi gray	$Li_{5.25}Cu_{3.75}P_6$ black blue Li_2CuP black $LiCu_2P_2$ black
	Li_2CuGe red brown $LiCu_2Ge$ red violet $LiCu_{0.5}Ge_{0.5}$ copper brown	Li_2CuAs gray
	Li_2CuSn dark violet, red violet, pink Li_2CuSn_2 light purple $LiCu_2Sn$ violet	Li_2CuSb gray

A1.2. Experimental

A1.2.1. Synthesis

Starting materials were Li rod (99.5%, Cerac), Cu shot (99.5%, Alfa Aesar), Al powder (99.97%, Cerac), and Ga ingot (99.99% Alfa Aesar). All manipulations were performed in an argon-filled glove box. The Li rod was scraped to remove surface oxides prior to use and cut into pieces of the desired mass. Mixtures of Li, Cu, and Al or Ga were combined in a molar ratio of 1:2:1 in a total mass of 0.200 g and placed within tantalum tubes, which were welded shut in a Centorr 5TA tri-arc furnace on a water-cooled copper hearth under an argon atmosphere. The samples were placed in a water-cooled Ambrell EASYHEAT 5060LI 6.0 kW induction heater where they were subjected to a frequency of 157 kHz and a current of 138 A for 18 min under

argon atmosphere within a copper coil of 5-cm diameter. Based on optical pyrometer measurements, the temperature attained was estimated to be between 800 and 900 °C. These are the optimum conditions that yield the most consistent results in terms of phase purity and uniform colour.

A1.2.2.Characterization

Energy-dispersive X-ray (EDX) analysis on the products, which were examined on a JEOL JSM-6010LA scanning electron microscope, confirmed the 2:1 ratio of Cu to Al or Ga, but Li is undetectable by this technique. Powder X-ray diffraction (XRD) patterns were collected on an Inel diffractometer equipped with a curved position-sensitive detector (CPS 120) and a Cu $K\alpha_1$ radiation source operated at 40 kV and 20 mA. The patterns were analyzed using the program PowderCell (version 2.3).[21]

Optical reflectance spectra were measured for $LiCu_2Al$ and $LiCu_2Ga$ from 200 nm (6.2 eV) to 1500 nm (0.83 eV) on an Agilent Cary 5000 UV-vis-NIR spectrophotometer equipped with a reflectance accessory. For comparison, spectra were also measured for elemental gold (99.999%, Materion) and various Au–Ag–Cu alloys that have been reported to be coloured and have been marketed commercially.[1] The alloys were prepared by reactions of the elemental components, which were arc-melted under an argon atmosphere in an Edmund Bühler MAM-1 arc melter. All samples were polished to obtain flat surfaces. The spectra were normalized, with a compacted pellet of $BaSO_4$ used as a 100% reflectance standard.

Magnetic measurements on ground, freshly synthesized samples were carried out on a Quantum Design 9T-PPMS magnetometer under an applied field of 3 T between 2 and 300 K. Magnetic susceptibility values were corrected for contributions from the sample holder.

Solid-state ^{7}Li nuclear magnetic resonance (NMR) spectra were acquired on a Bruker Avance 500 MHz (B_o = 11.75 T) NMR spectrometer equipped with a 4-mm magic angle spinning (MAS) probe operating in double resonance mode. Powdered samples were packed into 4-mm outside diameter ZrO_2 rotors with Kel-F caps; spectra were acquired on non-spinning samples. A Hahn echo pulse sequence with a 90° pulse width of 3.6 μs, an interpulse delay of 24.6 μs, and a recycle delay of 0.5 s were applied; 6400 to 13100 transients were co-added. The spectra were referenced by setting the ^{7}Li peak of a 1.0-M LiCl(aq) solution to 0.0 ppm.

A1.2.3. Electronic structure calculations

Pseudo-potential, first-principles electronic structure calculations were performed using the program Akai-KKR, with the Korringa-Kohn-Rostoker (KKR) Green function method combined with the local density approximation and the coherent potential approximation.[22] This method is suitable and convenient for structures exhibiting atomic disorder. To attain an accurate ground state, 400 *k*-points were used in the first Brillouin zone and the condition for convergence was set to 1×10^{-6} eV for the total energy.

A1.3. Results and discussion

Initial investigations of the Li–Cu–*X* (*X* = group 13–15 metals or metalloids) system were carried out by high frequency induction melting of mixtures of the elements. They revealed that many samples with nominal composition $LiCu_2X$ exhibit colour. For example, $LiCu_2In$ and $LiCu_2Sb$ exhibit a golden yellow colour, but unfortunately the samples degrade rapidly in air. The most consistent results were obtained for $LiCu_2Al$ and $LiCu_2Ga$, which are reported here. Uniform, homogeneously melted, phase-pure samples with the most intense colours were obtained

at optimized conditions of 157 kHz frequency, 138 A current, and 18 min heating time. $LiCu_2Al$ is red and $LiCu_2Ga$ is yellow. The colours remain intact for two to three days, gradually degrading so that the red colour of $LiCu_2Al$ turns to a darker shade and the yellow colour of $LiCu_2Ga$ fades. However, powder XRD patterns collected even after one year show virtually no change in the bulk samples (**Figure A1-1**), implying that the colour degradation observed after a few days is probably a surface phenomenon.

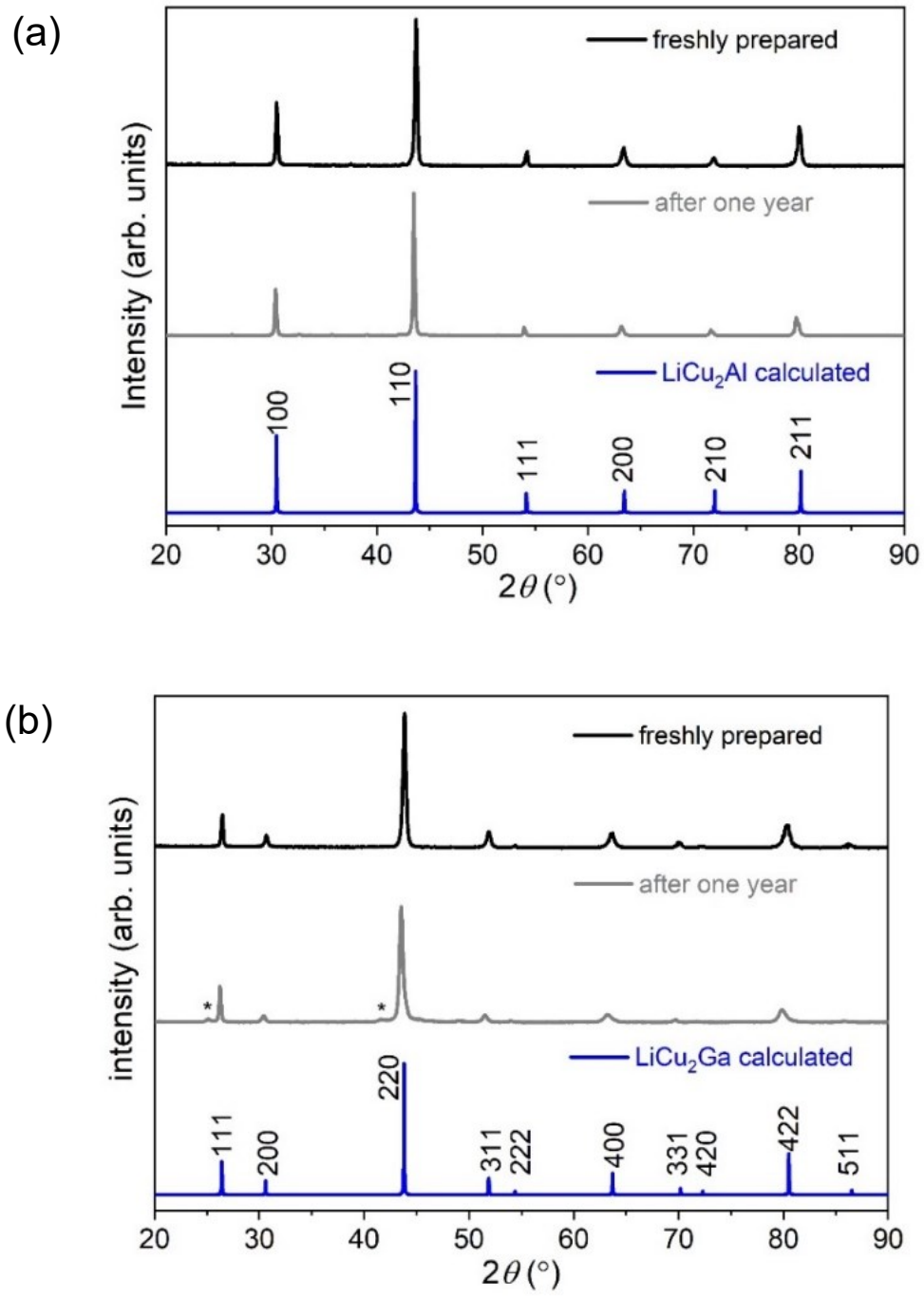

Figure A1-1. Powder XRD patterns for samples freshly prepared and after one year for (a) $LiCu_2Al$ and (b) $LiCu_2Ga$. The asterisks mark small unidentified peaks in the $LiCu_2Ga$ sample.

The structures of these compounds were deduced from their powder XRD patterns, which are relatively simple (**Figure A1-2**) and were indexed to cubic lattices (**Table A1-2**). $LiCu_2Al$ adopts a CsCl-type structure with a primitive cubic lattice (space group $Pm\bar{3}m$): Cu atoms occupy the 1a site at the corners of the unit cell, while Li and Al atoms are disordered over the 1b site at the centre of the unit cell (**Figure A1- 3(a)**). Following an alternative typical description of the CsCl-type structure, there are interpenetrating cubic arrays (not "lattices" or "sublattices," as sometimes described in the literature!) of Li/Al and Cu atoms. The XRD pattern of $LiCu_2Ga$ clearly shows additional peaks compared to that of $LiCu_2Al$ corresponding to a doubled unit cell length. $LiCu_2Ga$ adopts a Cu_2MnAl-type (full-Heusler) structure with a face-centred cubic lattice (space group $Fm\bar{3}m$): Cu atoms occupy the 8c site at ¼, ¼, ¼, while Li and Ga atoms are ordered over the 4b and 4a sites located at the edges, centre, and corners of the unit cell (**Figure A1- 3(b)**).

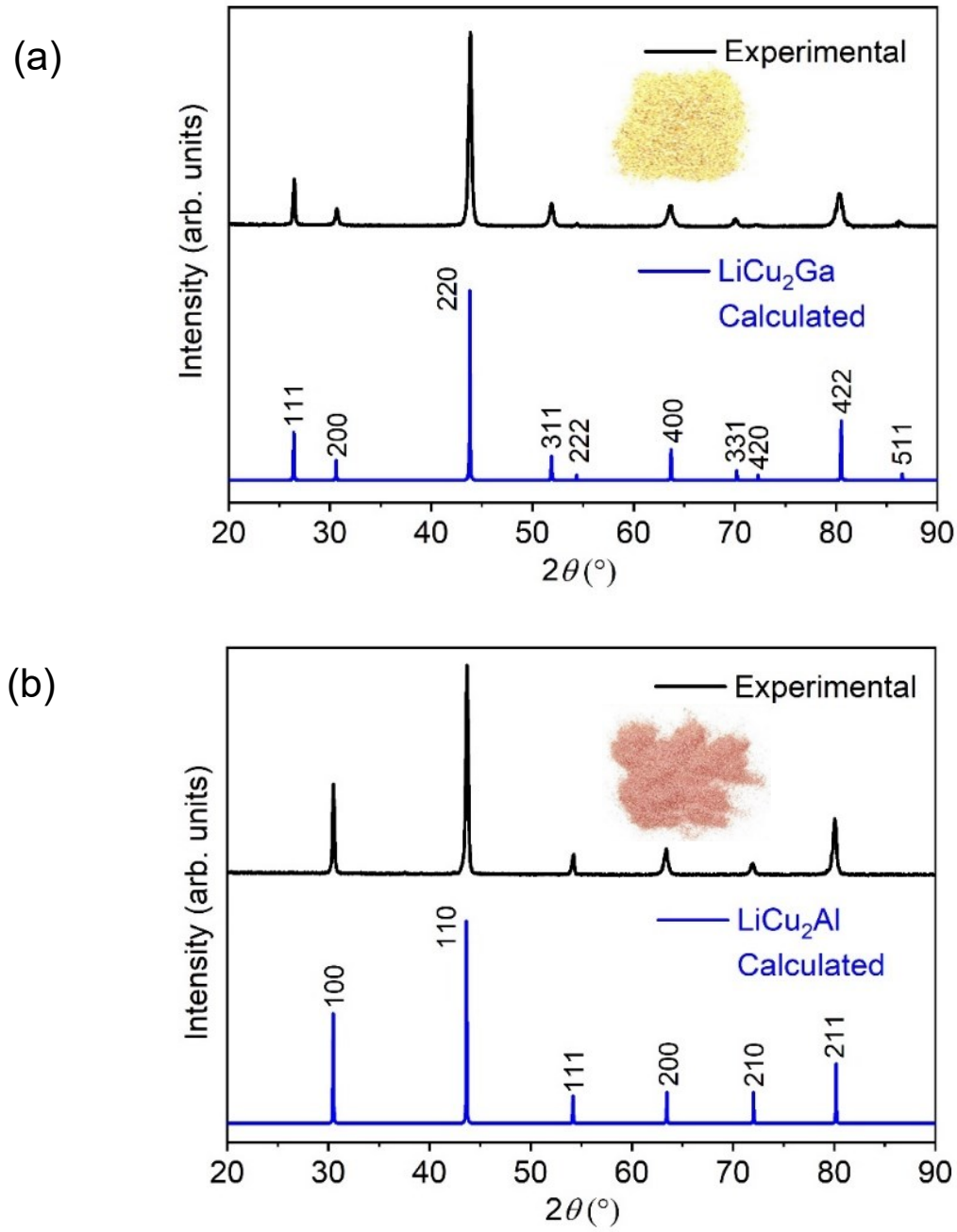

Figure A1-2. Powder XRD patterns and images of powder samples for (a) $LiCu_2Al$ and (b) $LiCu_2Ga$.

Table A1-2. Crystallographic data for $LiCu_2Al$ and $LiCu_2Ga$.

Crystal data		
formula	$Li_{0.5}CuAl_{0.5}$	$LiCu_2Ga$
formula mass (amu)	80.51	203.76
space group	$Pm\bar{3}m$ (No. 221)	$Fm\bar{3}m$ (No. 225)
a (Å)	2.9283(2)	5.8617(4)
V (Å^3)	25.110(5)	201.41(4)
Z	1	4
ρ_{calcd} (g cm^{-3})	5.254	6.632
Atomic coordinates		
Li	Li at 1*b* (½, ½, ½), occ. 0.5	Li at 4*b* (½, ½, ½)
Cu	Cu at 1*a* (0, 0, 0)	Cu at 8*c* (¼, ¼, ¼)
X	Al at 1*b* (½, ½, ½), occ. 0.5	Ga at 4*a* (0, 0, 0)

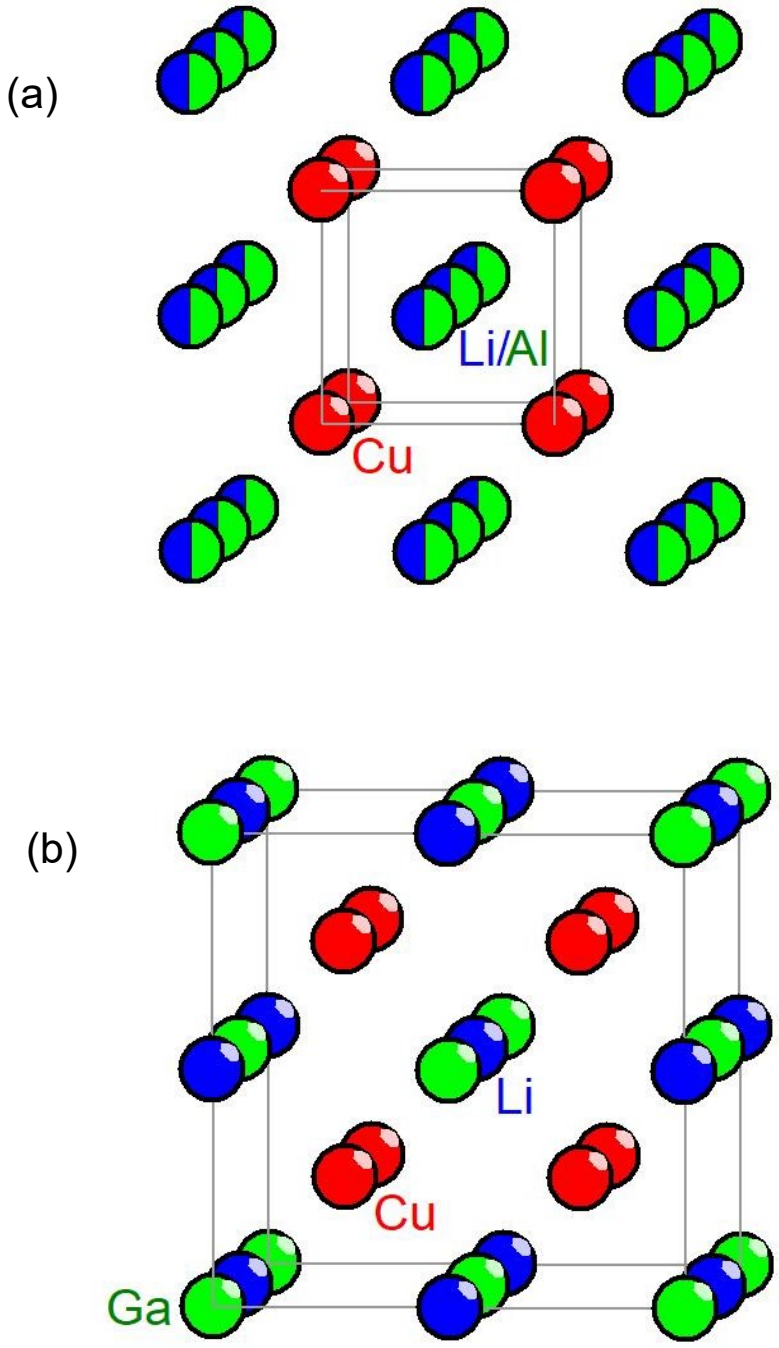

Figure A1- 3. Crystal structures of (a) $LiCu_2Al$ (CsCl-type) and (b) $LiCu_2Ga$ (Cu_2MnAl-type).

To complement the XRD results, and in particular, to confirm the occupation of Li atoms within one set of sites in the structures of $LiCu_2Al$ and $LiCu_2Ga$, solid state ^7Li NMR spectroscopy was also performed (**Figure A1-4**). Magnetic measurements were first carried out to reveal that the samples are diamagnetic (**Figure A1-5**) and thus contain no unpaired electrons, which would complicate the interpretation of the NMR spectra. The spectrum for $LiCu_2Al$ is dominated by a peak at 49 ppm, with a smaller peak (20% of the total intensity) at 0 ppm. The latter is typical of ionic Li, but the dominant peak is outside the typical Li chemical shift range, suggesting a Knight shift, a consequence of conduction electrons. Likewise, the ^7Li spectrum of $LiCu_2Ga$ is dominated by a peak at 48 ppm, with minor contributions totaling 5%, from peaks at 5 and 120 ppm. The occurrence of dominant peaks for both $LiCu_2Al$ and $LiCu_2Ga$ with the same chemical shift (within error) is consistent with the presence of similar chemical environments of eight nearest neighbour Cu atoms at 2.536–2.538 Å in a cubic geometry around the Li atoms in both structures. The ^7Li resonance for $LiCu_2Al$ (FWHM of 11 kHz) is significantly broader than that for $LiCu_2Ga$ (FWHM of 8 kHz), supporting the occurrence of Li/Al disorder in the former case, in which a random mixture of next-nearest neighbour Li and Al atoms in the second coordination sphere around each Li atom leads to a broadening. The ^7Li resonances in $LiCu_2Al$ and $LiCu_2Ga$ are shifted to high frequency relative to those (−1.6 to 3.3 ppm) in the half-Heusler compounds Li*MPn* (*M* = Mg, Zn, Cd; *Pn* = P, As, Sb, Bi);[23] as discussed above, the high frequency shifts for the compounds considered here are attributed to Knight shifts.

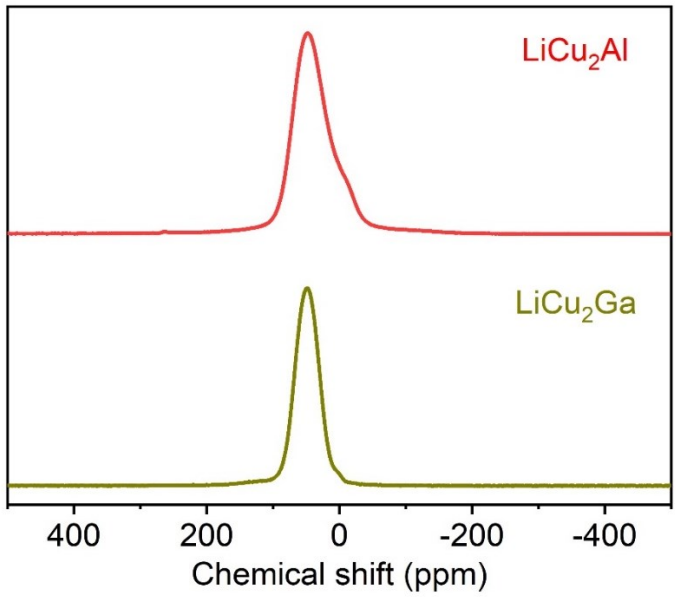

Figure A1-4. ^{7}Li NMR spectra of $LiCu_2Al$ and $LiCu_2Ga$.

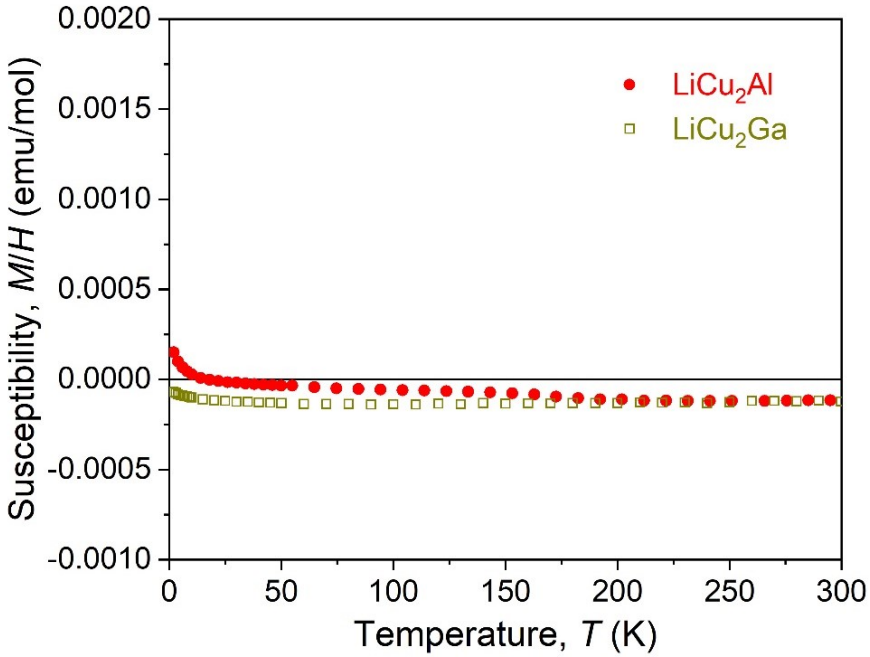

Figure A1-5. Magnetic susceptibility for $LiCu_2Al$ and $LiCu_2Ga$.

The optical reflectance spectra were measured on both ingot and powder samples. For $LiCu_2Al$, the spectra for the powder samples show somewhat different intensities; for $LiCu_2Ga$, the spectra are nearly the same for both types of samples (**Figure A1-6**). The spectra of the powder samples tend to suffer from decreased reflectivity after a few days. If the analysis is restricted to ingot samples, these spectra are consistent with the colours observed for $LiCu_2Al$ and $LiCu_2Ga$, and can be compared with that for high purity (99.999%) Au (**Figure A1-7**). In all cases, the reflectivity drops off abruptly at absorption edges of 2.4 eV for $LiCu_2Al$, 2.6 eV for Au, and 2.8 eV for $LiCu_2Ga$. The shift in absorption edge to higher energy agrees with the trend in colour, changing from red to yellow on progressing along this series. To assess the colours on more quantitative grounding, the optical reflectance was converted to coordinates in CIE 1931 colour space (with standard illuminant E)[24] and plotted on a chromaticity diagram (**Figure A1-8**). The plot shows both ingot and powder samples of $LiCu_2Al$ and $LiCu_2Ga$, in comparison to pure gold as well as a variety of commercial coloured gold alloys that were synthesized in our laboratory according to their reported compositions (**Table A1-3**). Despite the subjective terminology used to describe colours of gold alloys (e.g., green, yellow, rose, pink, red), their CIE *x* and *y* coordinates lie more or less within the same region of the diagram. An alternative interpretation is that human perception of colours is remarkably sensitive to small differences. $LiCu_2Al$ lies near the region of "pink" and $LiCu_2Ga$ near "orange" and "yellow" in this diagram. In particular, the colour coordinates for $LiCu_2Ga$ lie quite close to those for Au, consistent with their similar optical reflectivity profile. However, the average reflectance in the visible region is lower in $LiCu_2Ga$ (~22%) than Au (~50%).

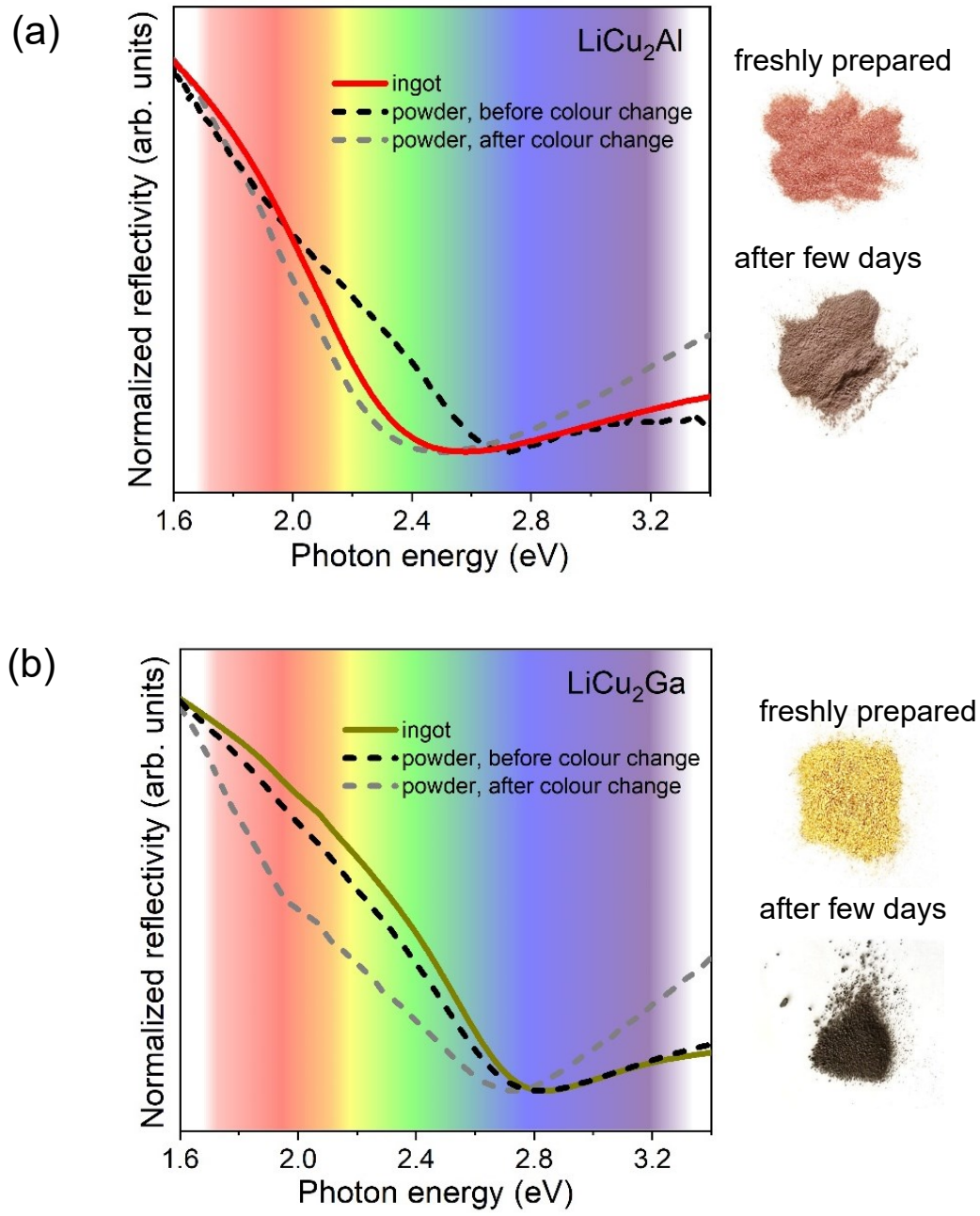

Figure A1-6. Optical reflectivity spectra for ingot vs. powder samples of (a) $LiCu_2Al$ and (b) $LiCu_2Ga$.

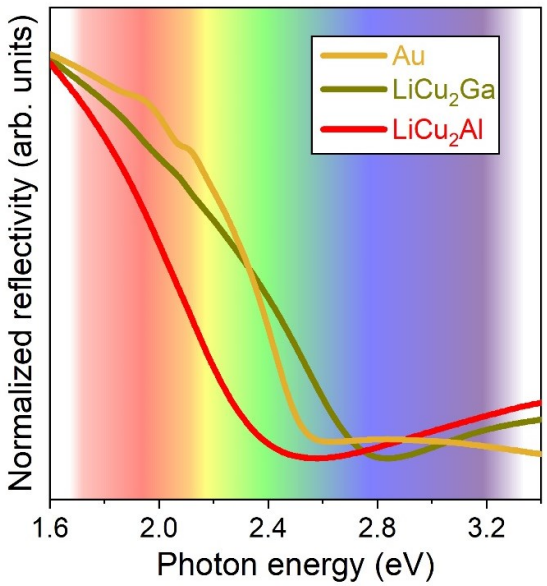

Figure A1-7. Optical reflectivity spectra for ingots of $LiCu_2Al$, $LiCu_2Ga$, and high purity Au (99.999%).

Table A1-3. Composition of coloured gold alloys prepared for comparison with $LiCu_2Al$ and $LiCu_2Ga$.

Description	**Composition**	**CIE 1931 *x***	**CIE 1931 *y***
Soft green gold	$Au_{75}Ag_{25}$	0.393	0.395
Light green gold	$Au_{75}Cu_{23}Cd_2$	0.368	0.362
Green gold	$Au_{75}Ag_{20}Cu_5$	0.370	0.363
Deep green gold	$Au_{75}Ag_{15}Cu_6Cd_4$	0.392	0.391
Yellow gold	$Au_{37.5}Ag_{42.5}Cu_{20}$	0.374	0.381
Yellow gold	$Au_{58.3}Ag_{30}Cu_{11.7}$	0.376	0.375
Yellow gold	$Au_{75}Ag_{15}Cu_{10}$	0.369	0.371
Rose gold	$Au_{37.5}Ag_{20}Cu_{42.5}$	0.401	0.379
Rose gold	$Au_{41.7}Ag_{20}Cu_{38.3}$	0.410	0.380
Rose gold	$Au_{91.7}Cu_{8.3}$	0.435	0.399
Pink gold	$Au_{75}Ag_5Cu_{20}$	0.400	0.376
Red gold	$Au_{75}Cu_{25}$	0.401	0.375

The electronic structures of $LiCu_2Al$ and $LiCu_2Ga$ can be examined in more detail. Because $LiCu_2Al$ and $LiCu_2Ga$ are related to the family of Heusler and half-Heusler compounds, which have hybridization gaps resulting from a clear separation of bonding and antibonding states, it is tempting to propose charge-balanced formulations $(Li^+)(Cu^+)_2(Al^{3-})$ and $(Li^+)(Cu^+)_2(Ga^{3-})$ which would allow them to be classified as Zintl phases. However, this assumption would be problematic because the electronegativity of Cu is the greatest or similar to that of Ga (cf., Pauling, $\chi_{Cu} = 1.90$, $\chi_{Ga} = 1.81$; Allred-Rochow, $\chi_{Cu} = 1.75$, $\chi_{Ga} = 1.82$) among the elemental components,[25] so it is no longer clear if such valence rules apply in these compounds. Nevertheless, these compounds resemble the majority of other known coloured intermetallic compounds, generally ternary phases (Li or Mg)–*M*–*X* (*M* = late transition metal; *X* = group 13–15 metal or metalloid)[16–19] for which an empirical rule has been proposed requiring a valence electron count of 7 or slightly less for colour to be exhibited.[7,8] For $LiCu_2Al$ and $LiCu_2Ga$, the electron count is 6 (per formula unit), which conforms to this electron counting rule.

From first-principles electronic structure calculations, the band dispersion diagrams for $LiCu_2Al$ and $LiCu_2Ga$ show a dense manifold of bands within a narrow energy range between –2.5 and –4.5 eV that originate from completely filled 3d states of the Cu atoms, overlaid on disperse bands resulting from mixing of Li 2s, Cu 4s/4p, and Al 3s/3p (or Ga 4s/4p) states (**Figure A1-9**). The electronic structure lacks the feature of a pseudogap near the Fermi level characteristic of typical Zintl phases, and instead resembles that of elemental copper or gold.[26,27] The origin of colour in $LiCu_2Al$ and $LiCu_2Ga$ is thus similar to that of copper or gold,[28] namely interband transitions from the filled Cu 3d states to the continuum of empty states above the Fermi level. The top of the Cu 3d band lies at about 2.5 eV below the Fermi level, in reasonably good agreement

with the absorption edges of 2.4 eV for $LiCu_2Al$ and 2.8 eV for $LiCu_2Ga$ observed in the optical reflectance spectra.

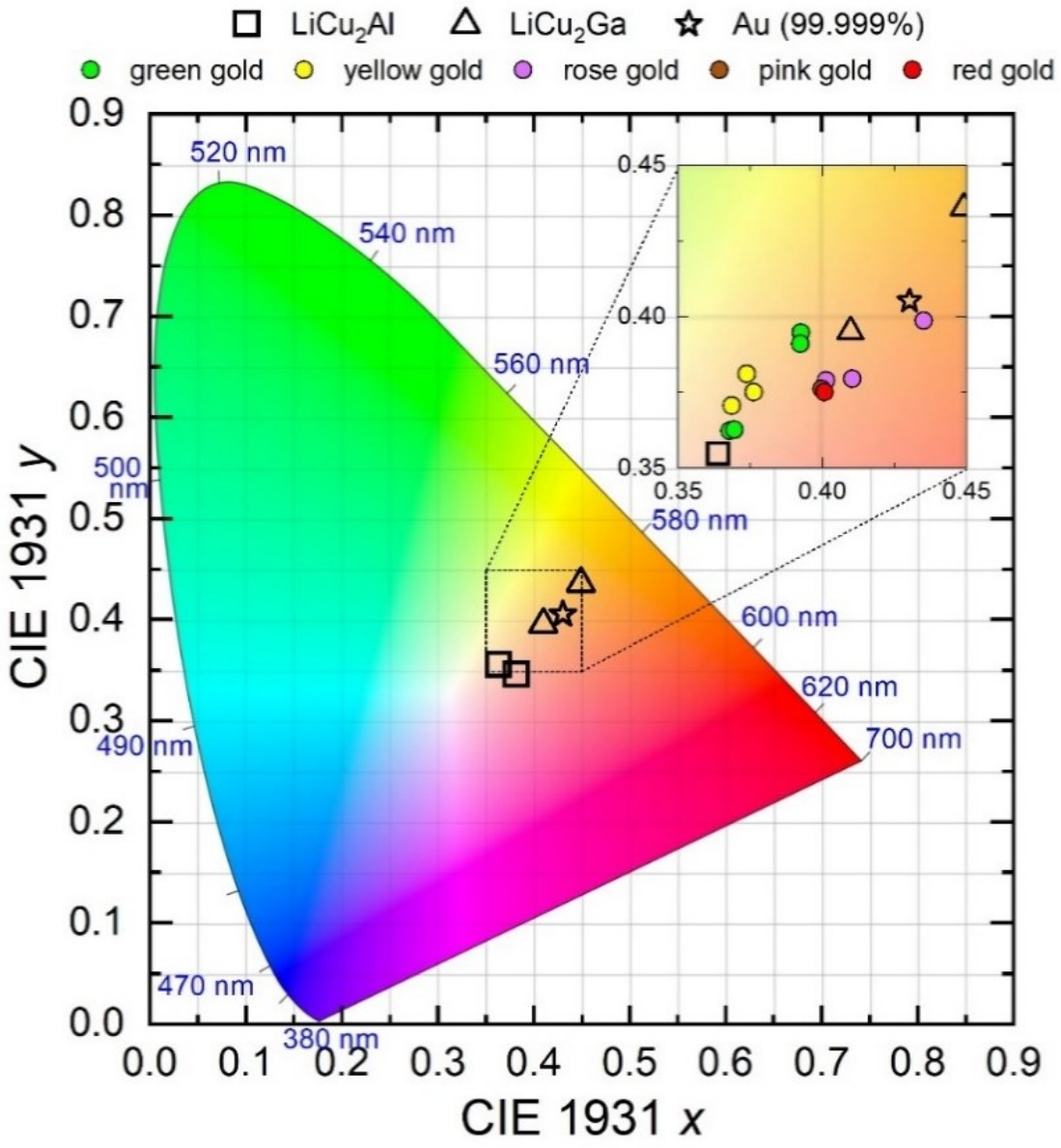

Figure A1-8. CIE 1931 coordinates for $LiCu_2Al$, $LiCu_2Ga$, Au, and various commercially known coloured gold-containing alloys.

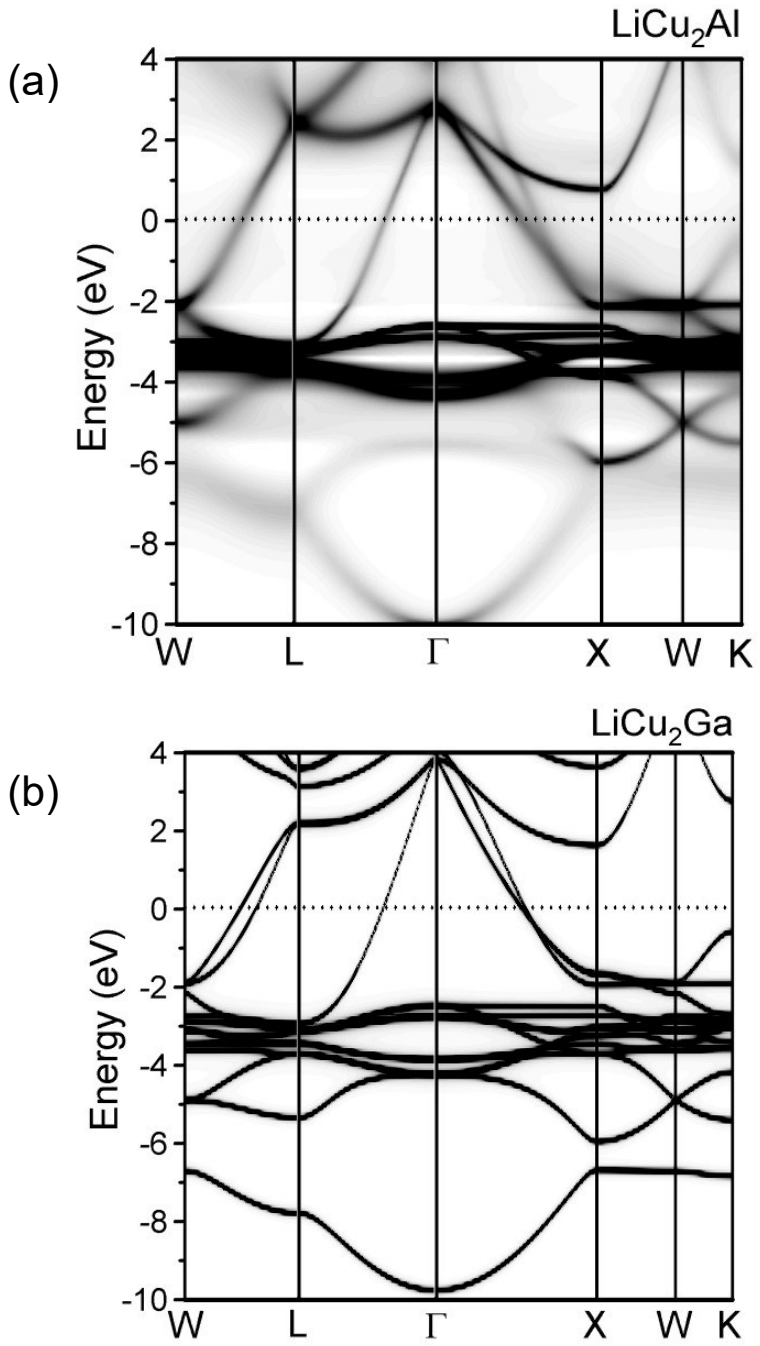

Figure A1-9. Band dispersion for (a) $LiCu_2Al$ and (b) $LiCu_2Ga$. In (a), the degree of blurring indicates states that are most strongly affected by disorder of Li and Al atoms in the crystal structure.

A1.4. Conclusions

$LiCu_2Al$ and $LiCu_2Ga$ were identified as unusual examples, still few, of intermetallic compounds that exhibit colour. Of these two compounds, $LiCu_2Ga$ is perhaps most interesting because its yellow colour resembles that of elemental gold, as confirmed by their optical reflectance spectra and quantification of CIE colour coordinates. The origin of the colour can be traced to electronic transitions from narrow, completely filled bands based on Cu 3d states to empty states above the Fermi level.

A1.5. References

(1) Cretu, C.; van der Lingen, E. *Gold Bull.* **1999**, *32*, 115–126.

(2) Wolff, I. M. *Endeavour* **1995**, *19*, 16–19.

(3) Corti, C. W. In *The Santa Fe Symposium on Jewelry Manufacturing Technology*, 2004; Bell, E., Ed.; Met-Chem Research, Albuquerque. 2004; pp 121–134.

(4) Klotz, U. E. *Gold Bull.* **2010**, *43*, 4–10.

(5) Fischer-Bühner, J.; Basso, A.; Poliero, M. *Gold Bull.* **2010**, *43*, 11–20.

(6) Liu, J.; Liu, Y.; Gong, P.; Li, Y.; Moore, K. M.; Scanley, E.; Walker, F.; Broadbridge, C. C.; Schroers, J. *Gold Bull.* **2015**, *48*, 111–118.

(7) Steinemann, S. G.; Wolf, W.; Podloucky, R. Color and Optical Properties. In *Intermetallic Compounds – Principles and Practice*, Vol. 3; Westbrook, J.H., Fleischer, R.L., Eds.; Wiley, New York 2002, pp 231–244.

(8) van der Lingen, E. *J. S. Afr. Inst. Min. Metall.* **2014**, *114*, 137–144.

(9) Steinemann, S. G.; Anongba, P. N. B.; Podloucky, R. *J. Phase Equilib.* **1997**, *18*, 655–662.

(10) Cahn, R. W. *Nature* **1998**, *396*, 523–524.

(11) Keast, V. J.; Birt, K.; Koch, C. T.; Supansomboon, S.; Cortie, M. B. *Appl. Phys. Lett.* **2011**, *99*, 111908.

(12) Furrer, A.; Seita, M.; Spolenak, R. *Acta Mater.* **2013**, *61*, 2874–2883.

(13) Hurly, J.; Wedepohl, P. T. *J. Mater. Sci.* **1993**, *28*, 5648–5653.

(14) Nomerovannaya, L. V.; Kirillova, M. M.; Shaikin, A. B. *Phys. Status Solidi B* **1980**, *102*, 715–720.

(15) Jeong, Y. B.; Kim, J. T.; Hong, S. H.; Lee, H. D.; Choi, S. Y.; Kim, K. B. *Mater. Des.* **2019**, *175*, 107814-1–107814-11.

(16) Eberz, U.; Seelentag, W.; Schuster, H.-U. *Z. Naturforsch. B Chem. Sci.* **1980**, *35*, 1341–1343.

(17) Drews, J.; Eberz, U.; Schuster, H.-U. *J. Less Common. Met.* **1986**, *116*, 271–278.

(18) Czybulka, A.; Petersen, A.; Schuster, H.-U. *J. Less Common. Met.* **1990**, *161*, 303–312.

(19) Dmytriv, G.; Pauly, H.; Ehrenberg, H.; Pavlyuk, V.; Vollmar, E. *J. Solid State Chem.* **2005**, *178*, 2825–2831.

(20) Villars, P.; Cenzual, K. *Pearson's Crystal Data – Crystal Structure Database for Inorganic Compounds,* Release 2018/19, ASM International, Materials Park, OH, USA.

(21) Kraus, W.; Nolze, G. *J. Appl. Crystallogr.* **1996**, *29*, 301–303.

(22) Long, N. H.; Akai, H. *J. Phys. Condens. Matter* **2007**, *19*, 365232-1–365232-8.

(23) Dupke, S.; Eckert, H.; Winter, F.; Pöttgen, R. *Prog. Solid State Chem.* **2014**, *42*, 57–64.

(24) Hunt, R. W. G.; Pointer, M. R. *Measuring Colour*. 4th ed.; Wiley, Chichester 2011.

(25) Huheey, J. E.; Keiter, E. A.; Keiter, R. L. *Inorganic Chemistry: Principles of Structure and Reactivity*, 4th ed.; Harper Collins, New York, 1993.

(26) Burdick, G. A. *Phys. Rev.* **1963**, *129*, 138–150.

(27) Rangel, T.; Kecik, D.; Trevisanutto, P. E.; Rignanese, G. M.; Van Swygenhoven, H.; Olevano, V. *Phys. Rev. B* **2012**, *86*, 125125-1–125125-10.

(28) Saeger, K. E.; Rodies, J. *Gold Bull.* **1977**, *10*, 10–14.

Appendix 2.

Supplementary Data for Chapter 2

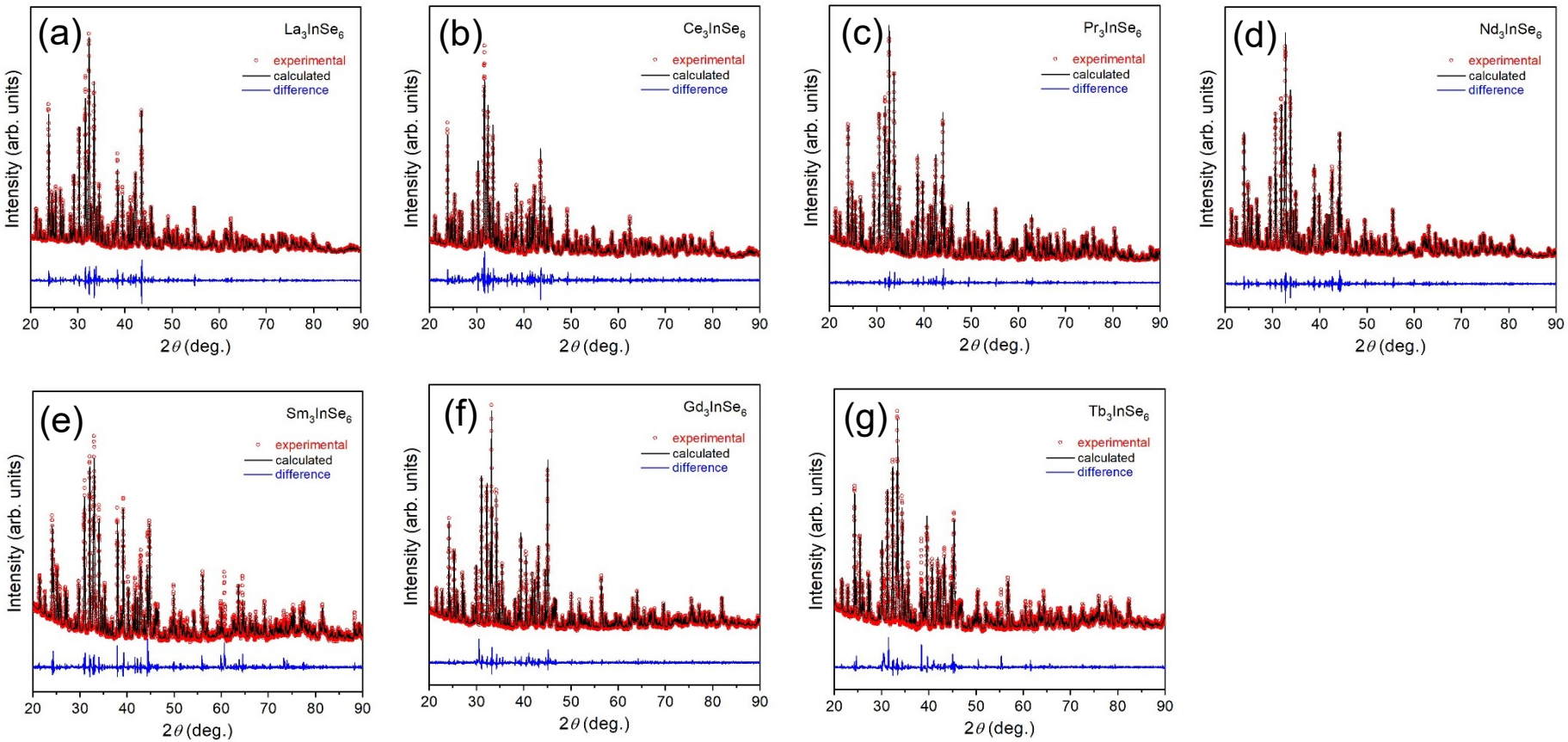

Figure A2-1. Powder XRD patterns fitted with Pawley method for RE_3InSe_6.

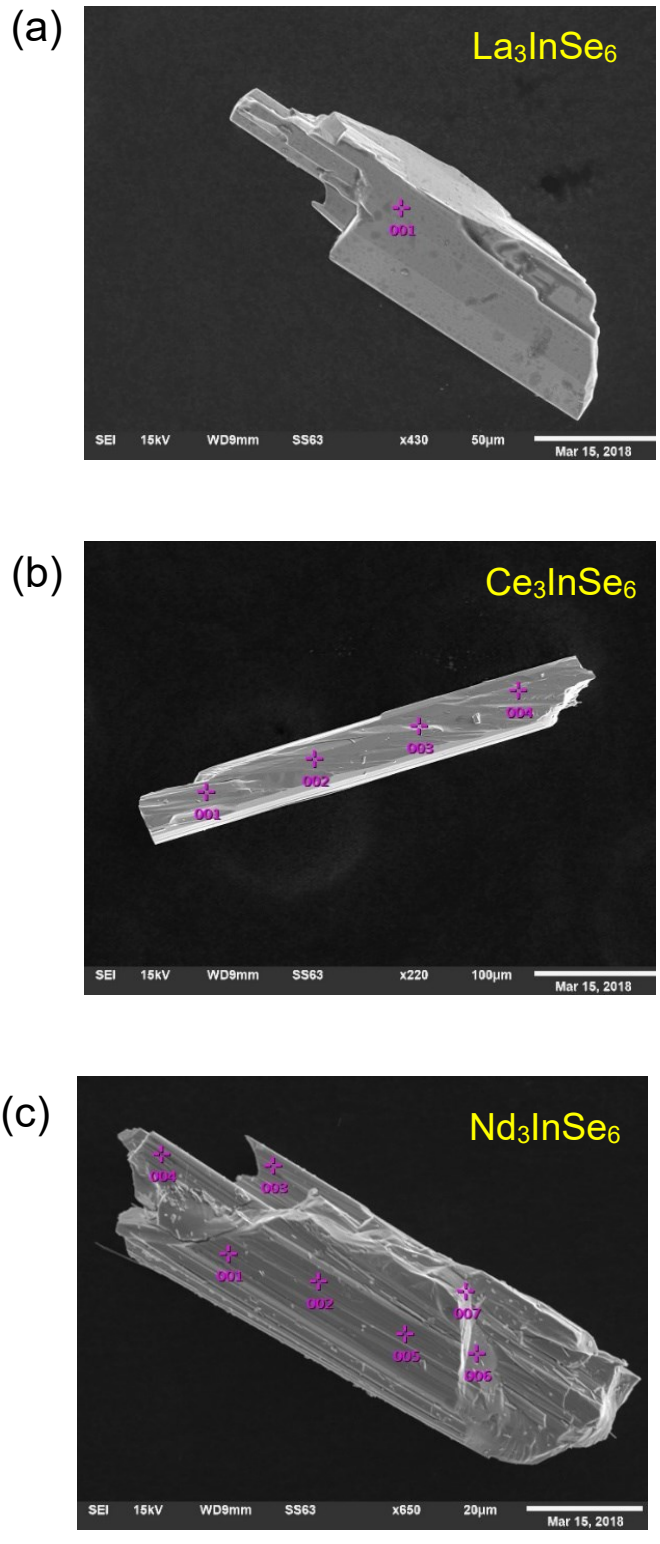

Figure A2-2. SEM images for RE_3InSe_6 (*RE* = La, Ce, Nd).

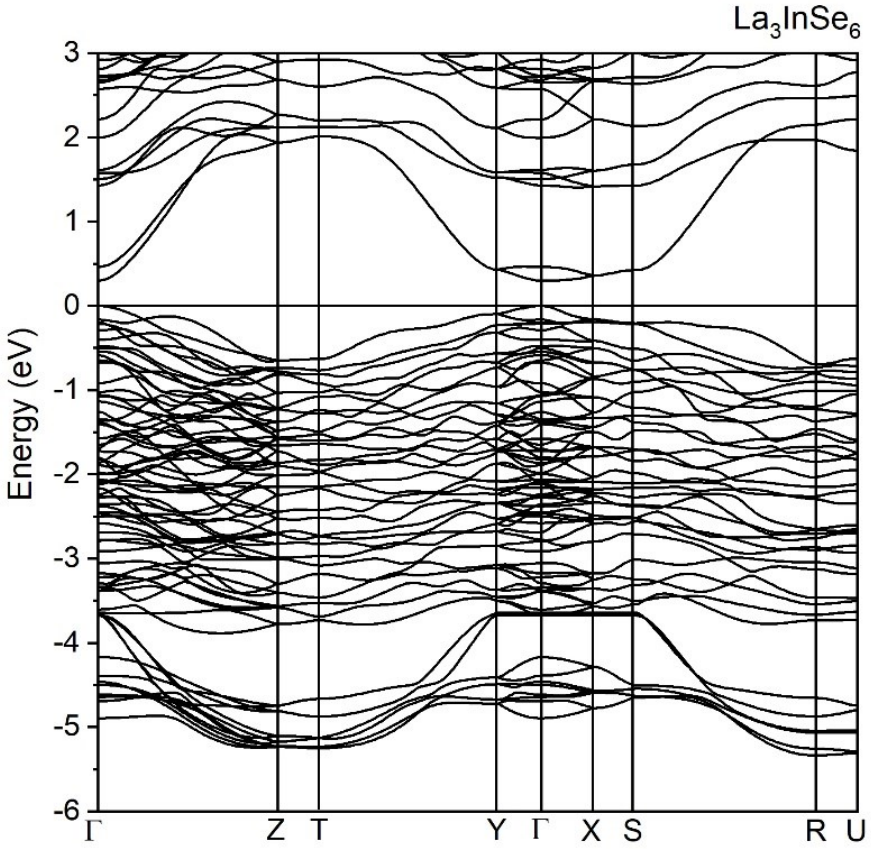

Figure A2-3. Band dispersion for La_3InSe_6.

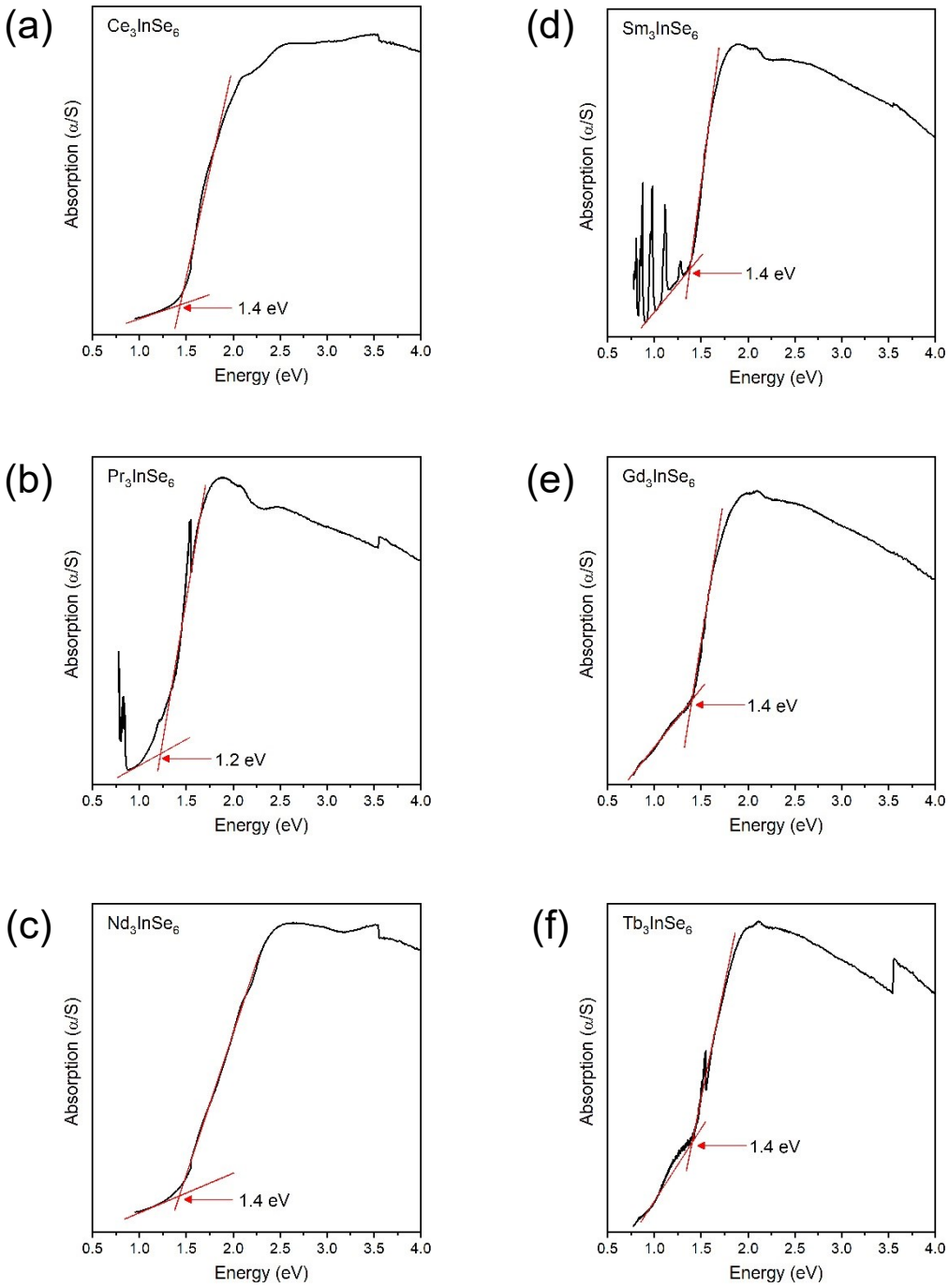

Figure A2-4. Optical absorption spectra for RE_3InSe_6 (*RE* = Ce, Pr, Nd, Sm, Gd, Tb).

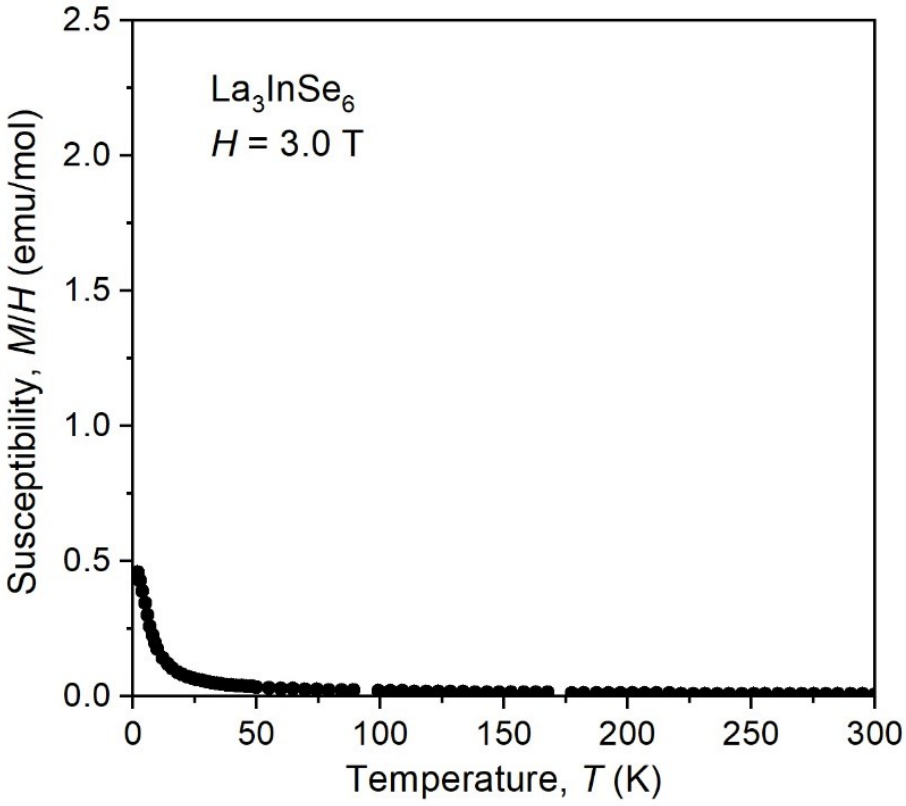

Figure A2-5. Magnetic susceptibility for La_3InSe_6.

Appendix 3.

Supplementary Data for Chapter 3

Table A3-1. Rietveld refinement of Sm_3GaSe_5O sample

phase	Sm_3GaSe_5O	Sm_2SeO_2
space group	$P2_1/m$ (No. 11)	$P\bar{3}m1$ (No. 164)
a (Å)	10.9778(5)	3.9255(3)
b (Å)	3.9762(1)	3.9255(3)
c (Å)	21.242(1)	6.9159(5)
β (deg.)	96.187(3)	90
V (Å^3)	921.82(4)	92.292(7)
Z	4	1
ρ_{calcd} (g cm^{-3})	6.713	7.408
phase weight fraction	0.831(4)	0.169(2)
no. of reflections	672	34
R_F	0.0674	0.0518
GOF	3.56	
R_p	0.0642	
wR_p	0.0847	

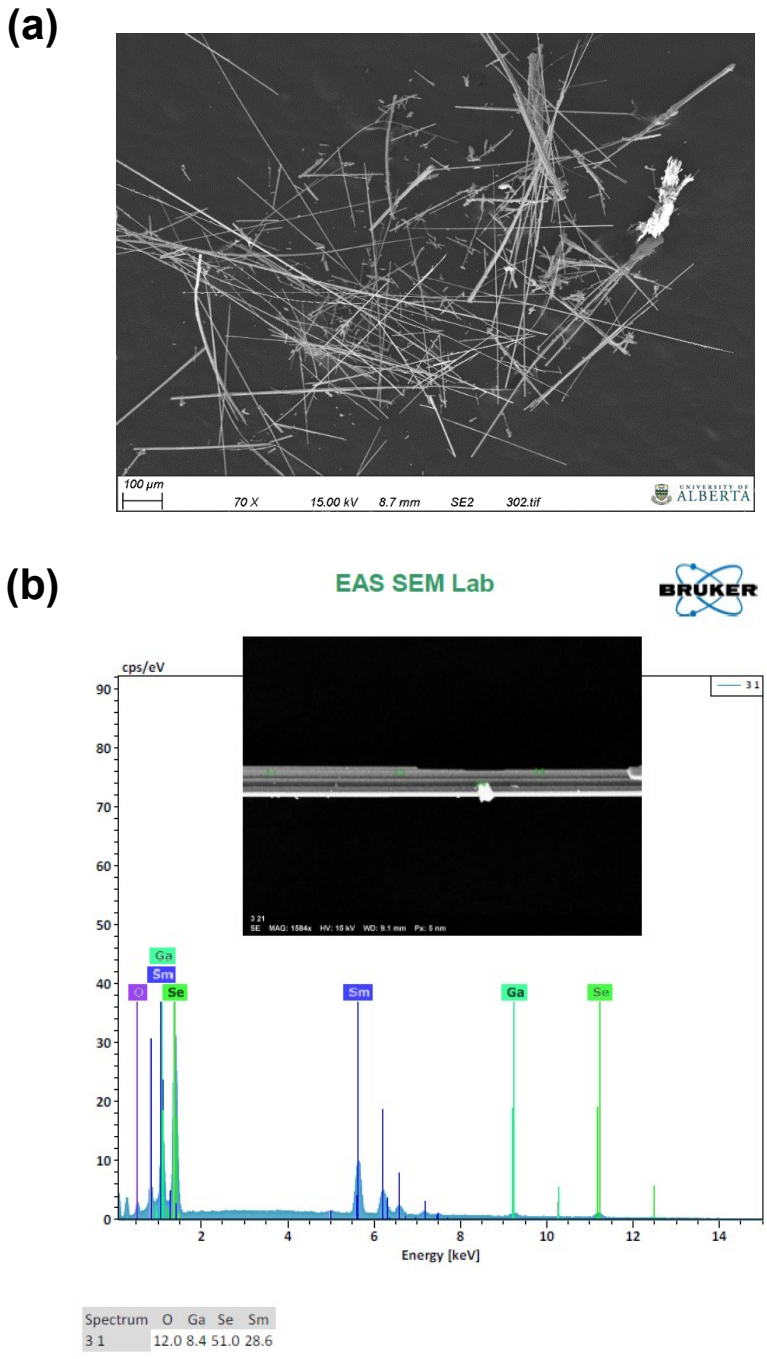

Figure A3-1. (a) SEM image of needle-shaped crystals of Sm_3GaSe_5O. (b) EDX spectrum for a representative crystal of Sm_3GaSe_5O

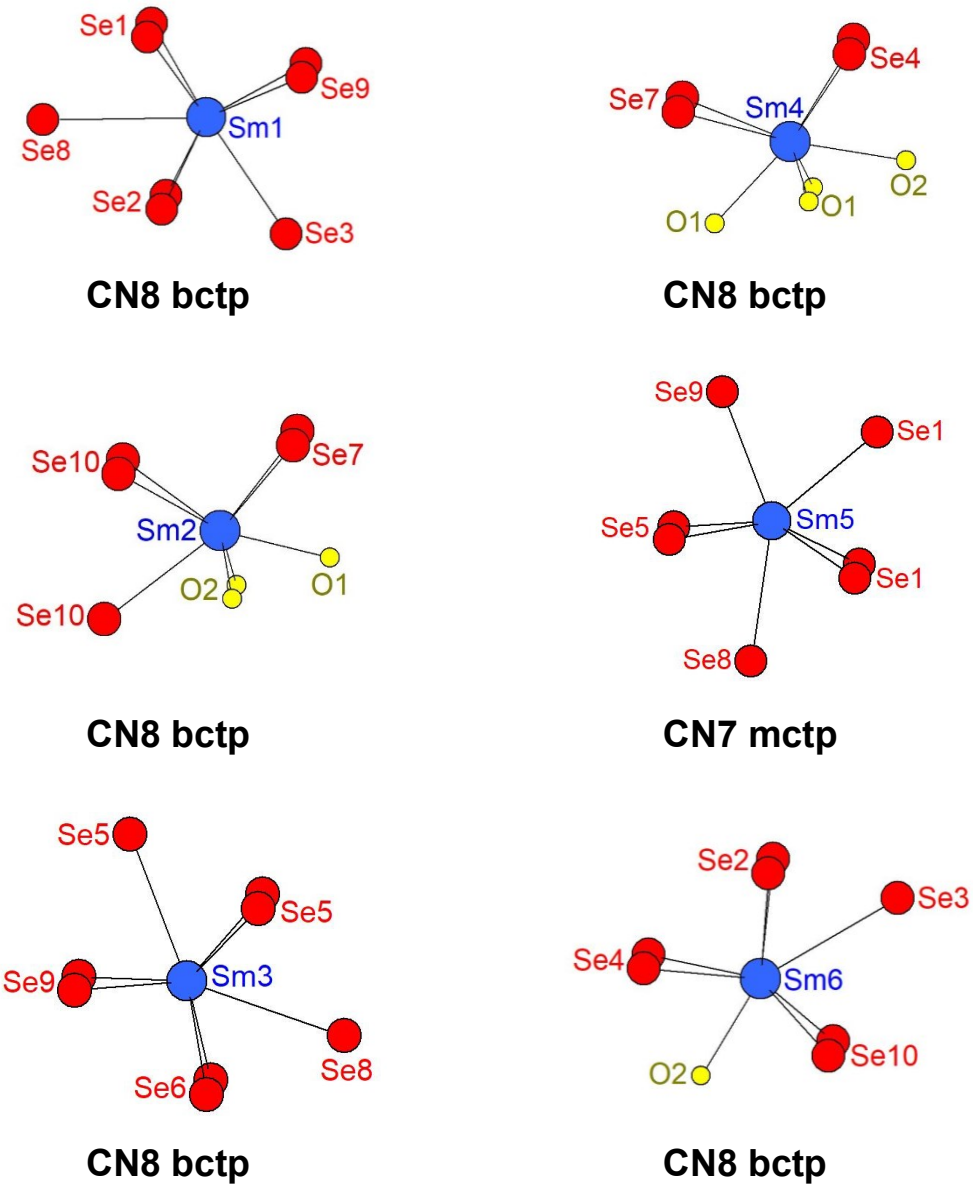

Figure A3-2. Coordination polyhedra around Sm atoms in Sm_3GaSe_5O

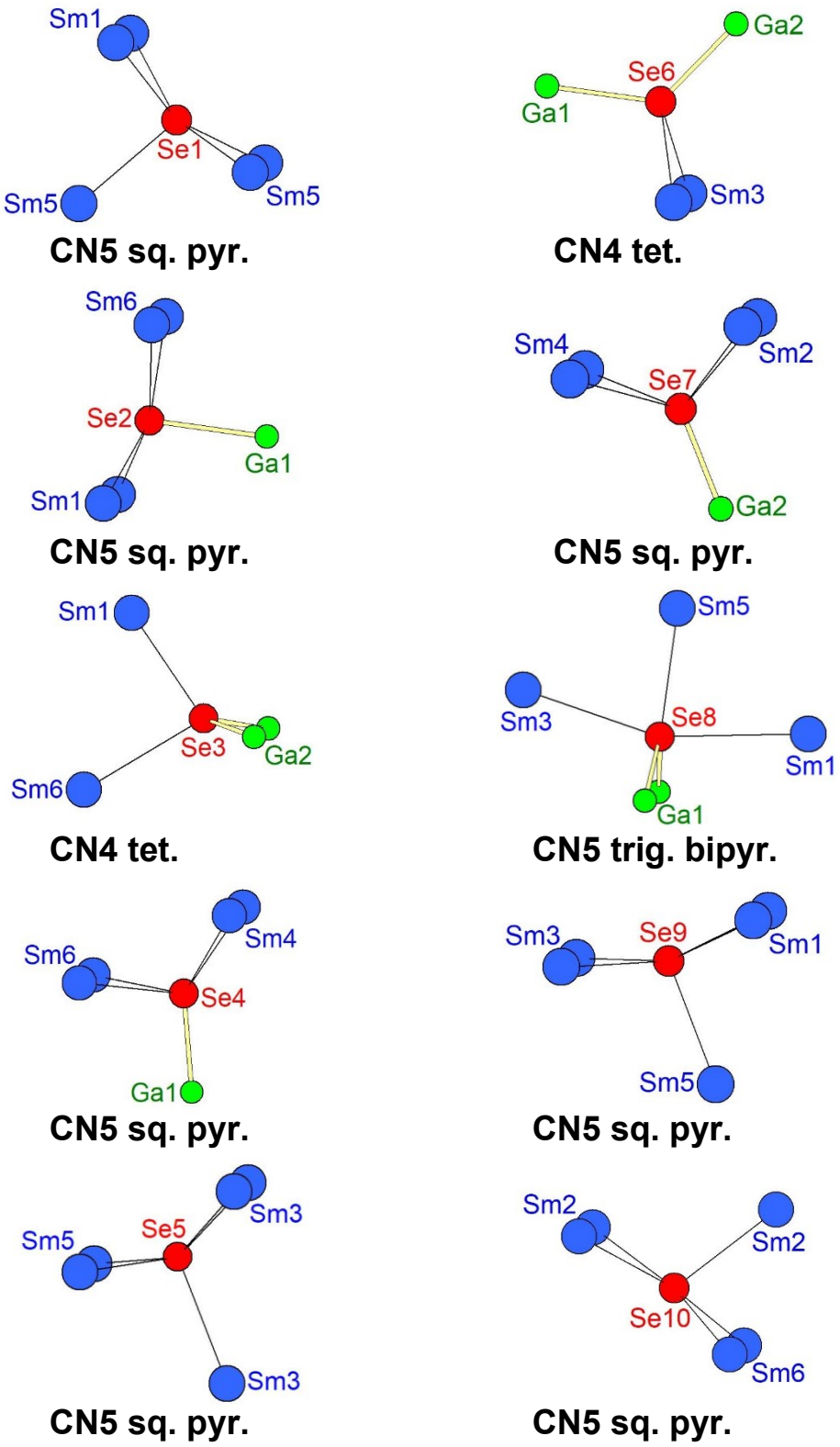

Figure A3-3. Coordination polyhedra around Se atoms in Sm_3GaSe_5O

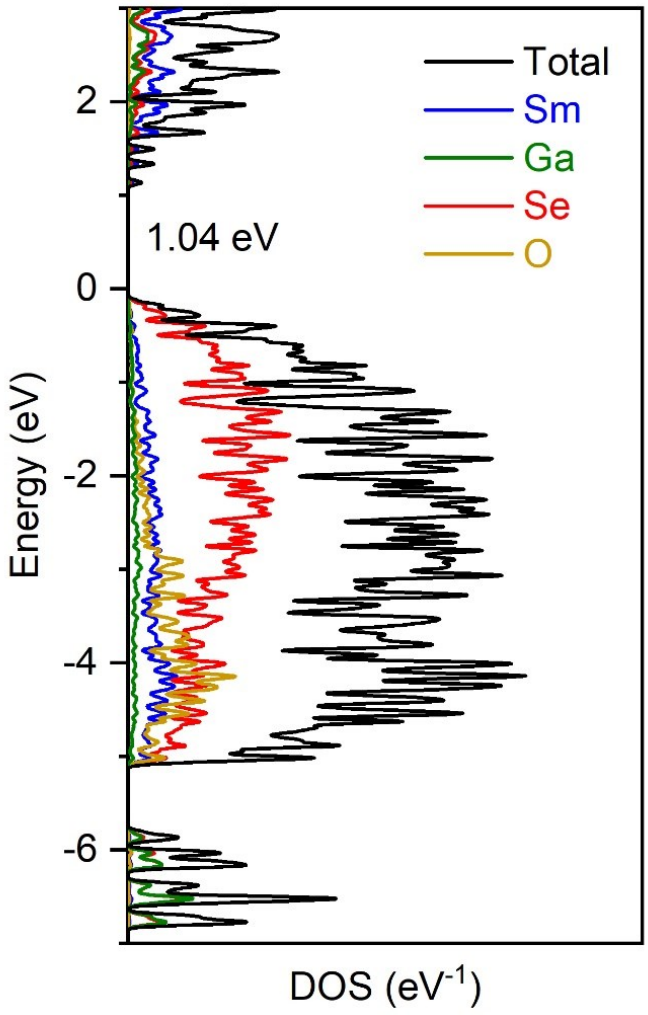

Figure A3-4. Density of states (DOS) for Sm_3GaSe_5O, obtained through DFT calculations with the HSE06 functional (PBE:Hartree-Fock (75:25)) applied to correct for the underestimation of the PBE band gap. A 3 × 8 × 2 gamma-centered k-mesh was chosen to sample the first Brillouin zone with the plane-wave basis cutoff energy set to 550 eV.

Appendix 4.

Supplementary Data for Chapter 4

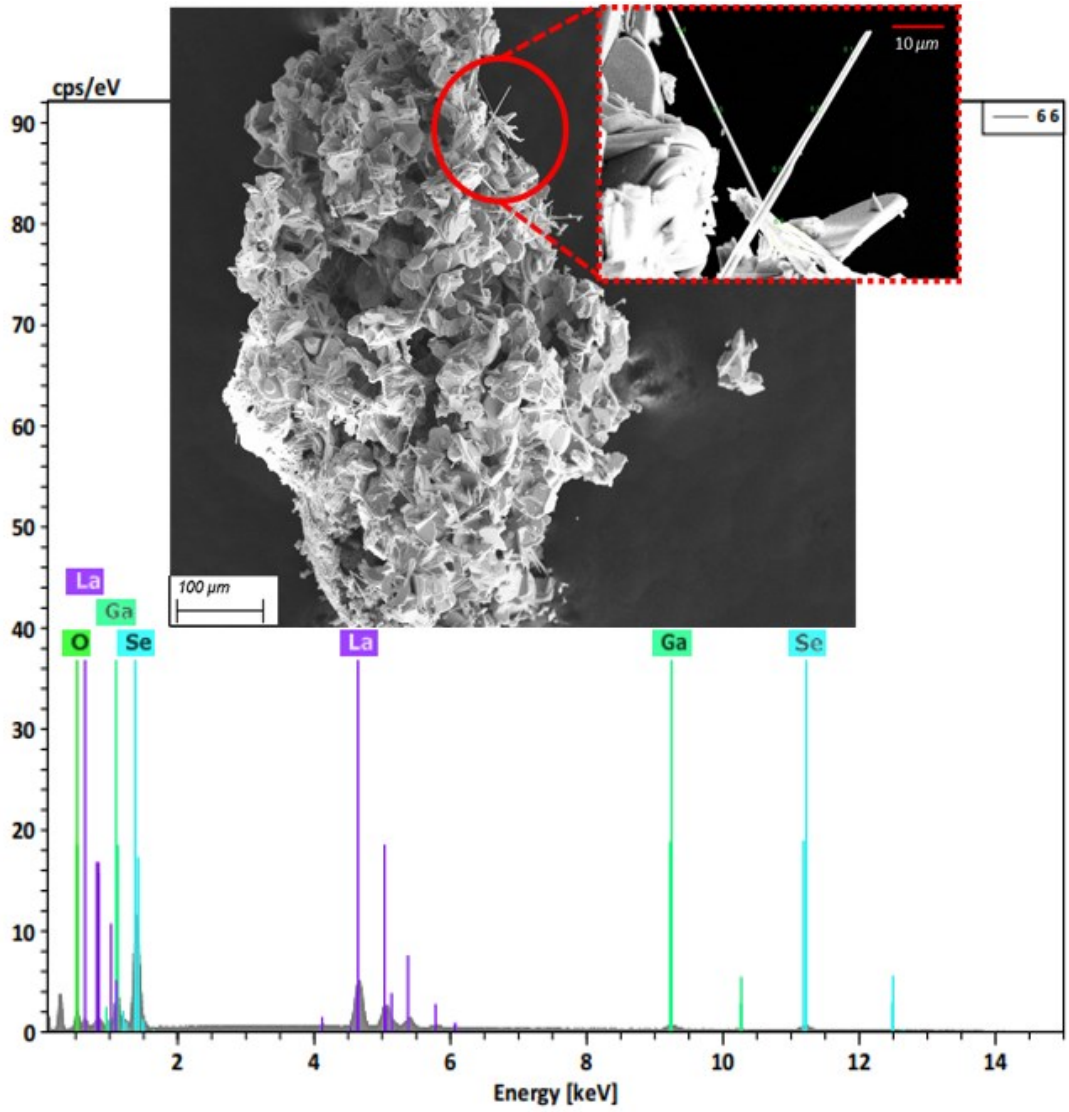

Spectrum	O	Ga	Se	La
6 6	18.9	11.1	44.8	25.2

Figure A4-1. SEM image and EDX analysis of typical needle-shaped crystals of $La_4Ga_2Se_6O_3$

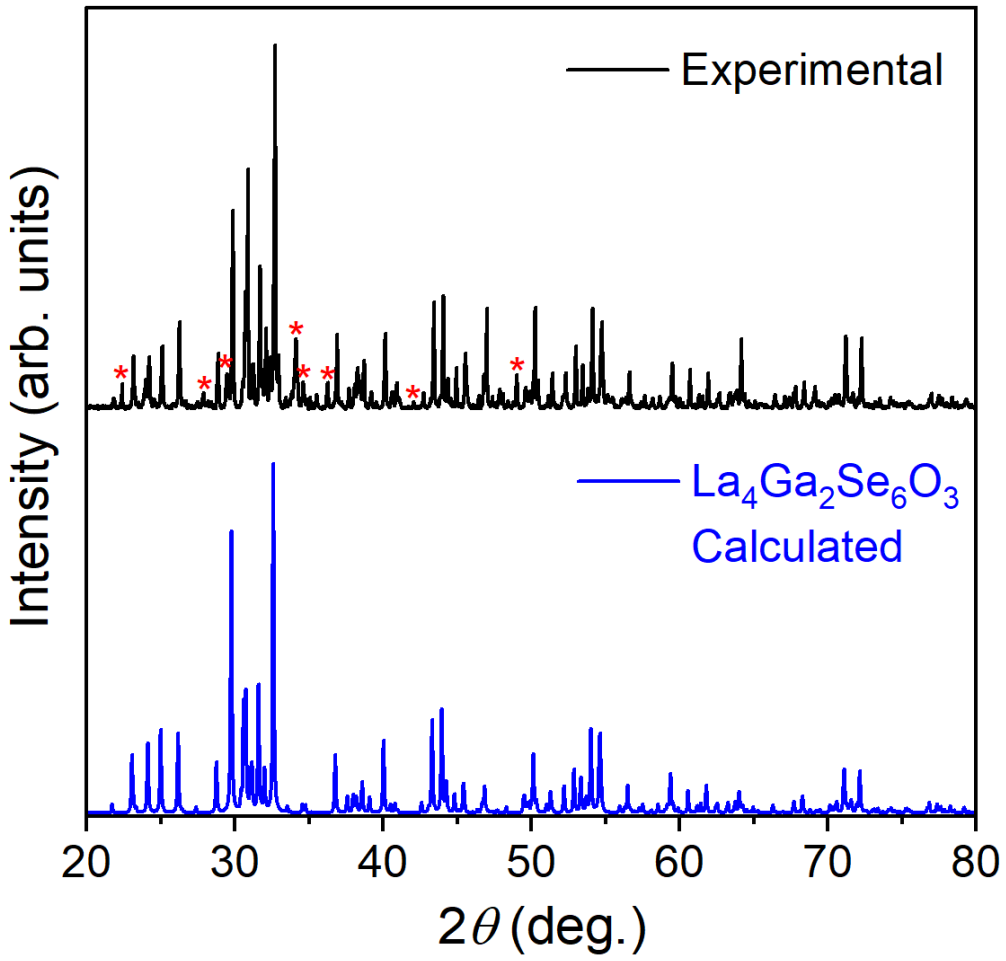

Figure A4-2. XRD pattern for a sample prepared from nominal composition of La_3GaSe_5O. The majority phase formed is $La_4Ga_2Se_6O_3$, and the minority phase is GaSe, which accounts for most of the additional peaks marked with asterisks

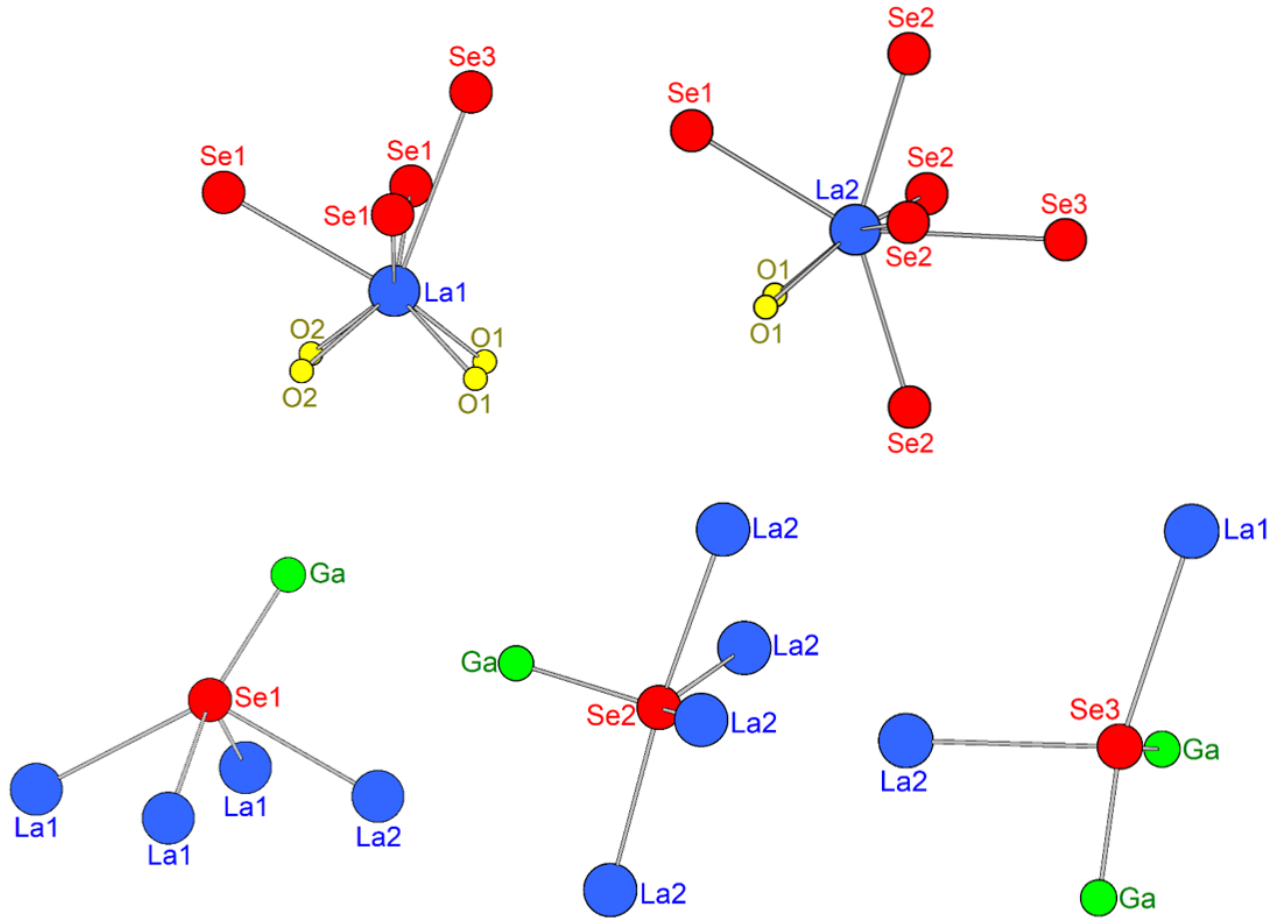

Figure A4-3. Coordination polyhedra around La and Se atoms in $La_4Ga_2Se_6O_3$

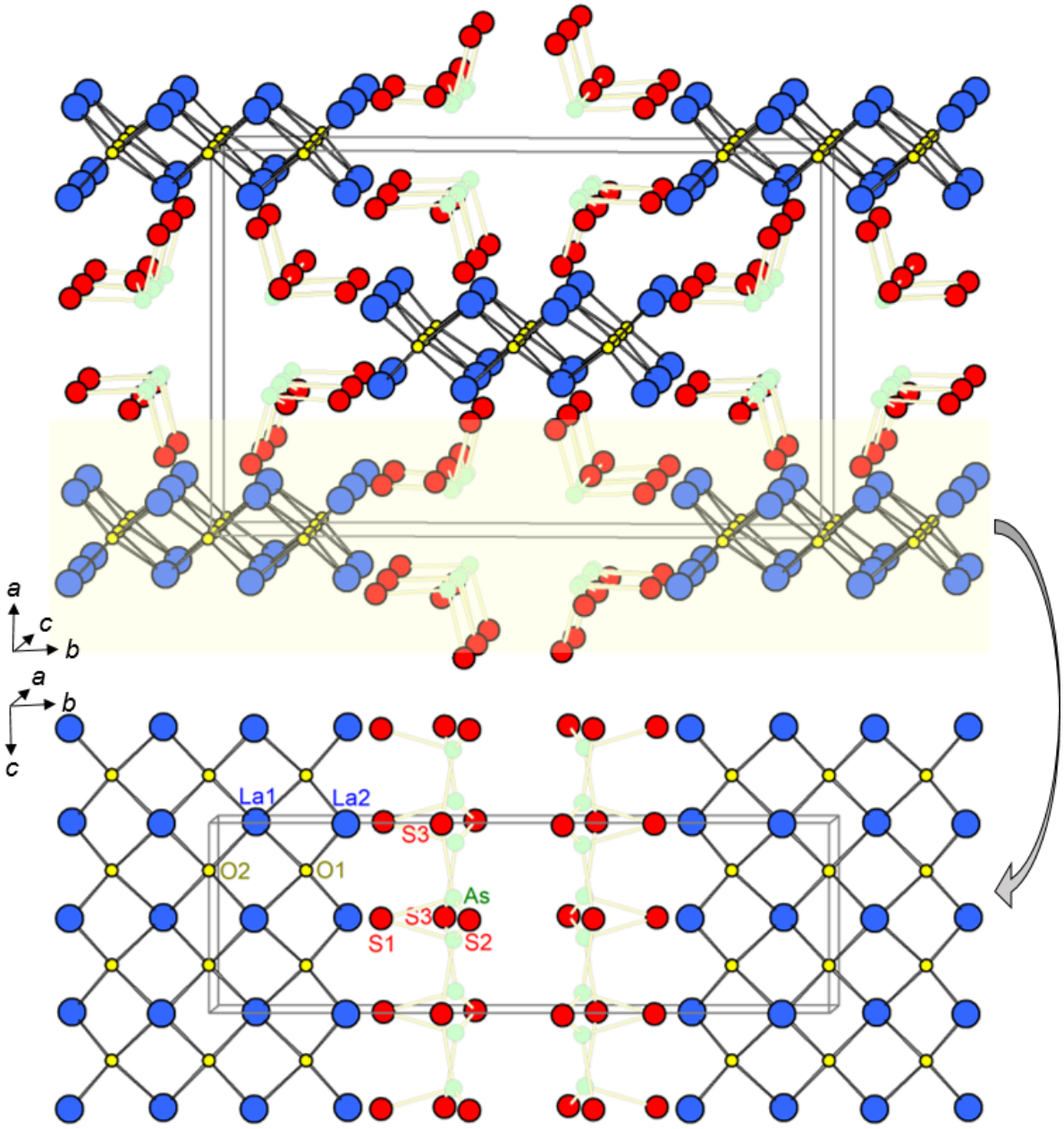

Figure A4-4. Orthorhombic structure of $La_4As_2S_6O_3$. The As sites are half-occupied

Appendix 5.

Supplementary Data for Chapter 5

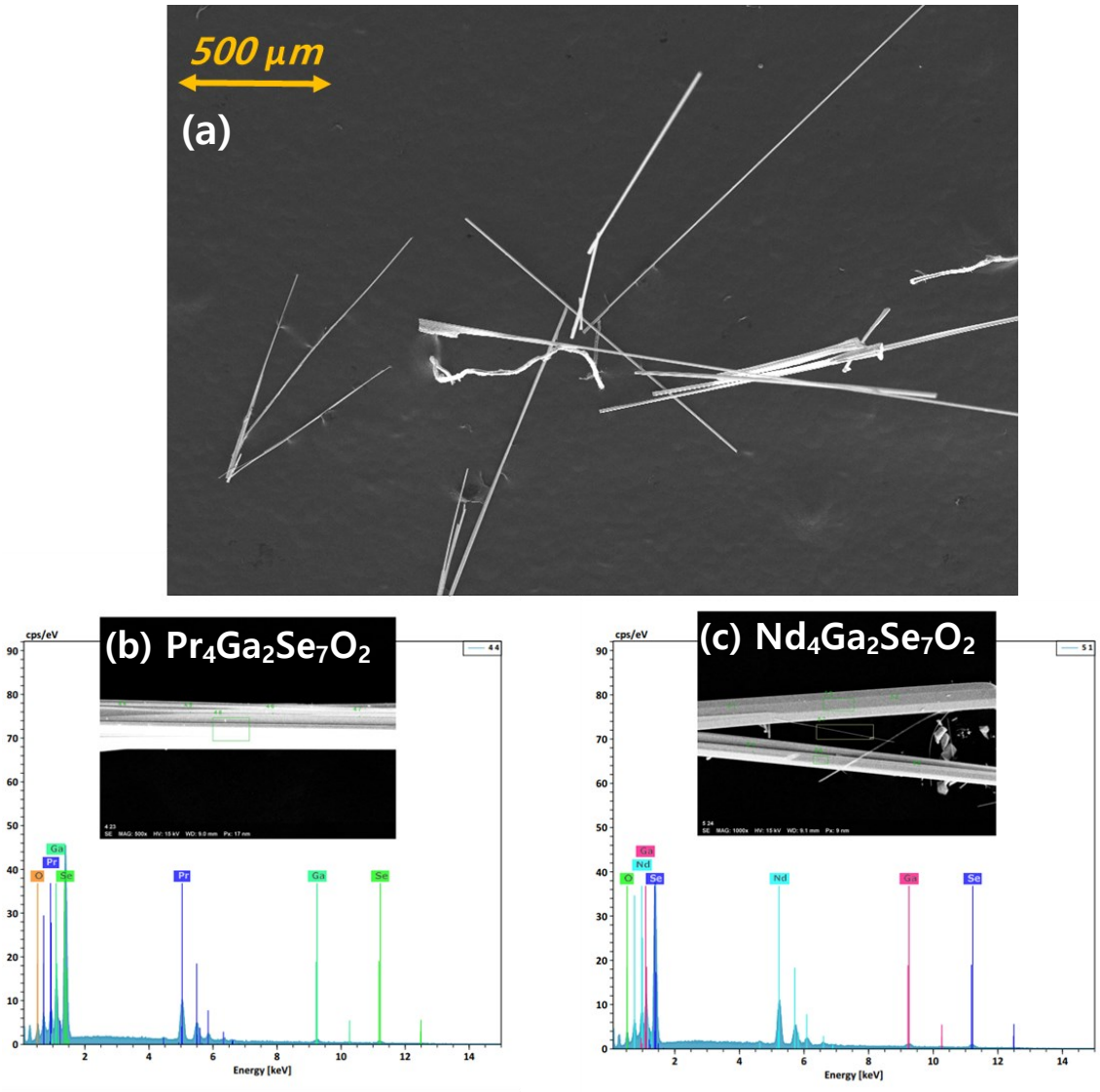

Figure A5-1. (a) Typical needle shaped large single crystals of $RE_4Ga_2Se_7O_2$, and EDX analysis on (b) $Pr_4Ga_2Se_7O_2$, and (c) $Nd_4Ga_2Se_7O_2$ single crystals.

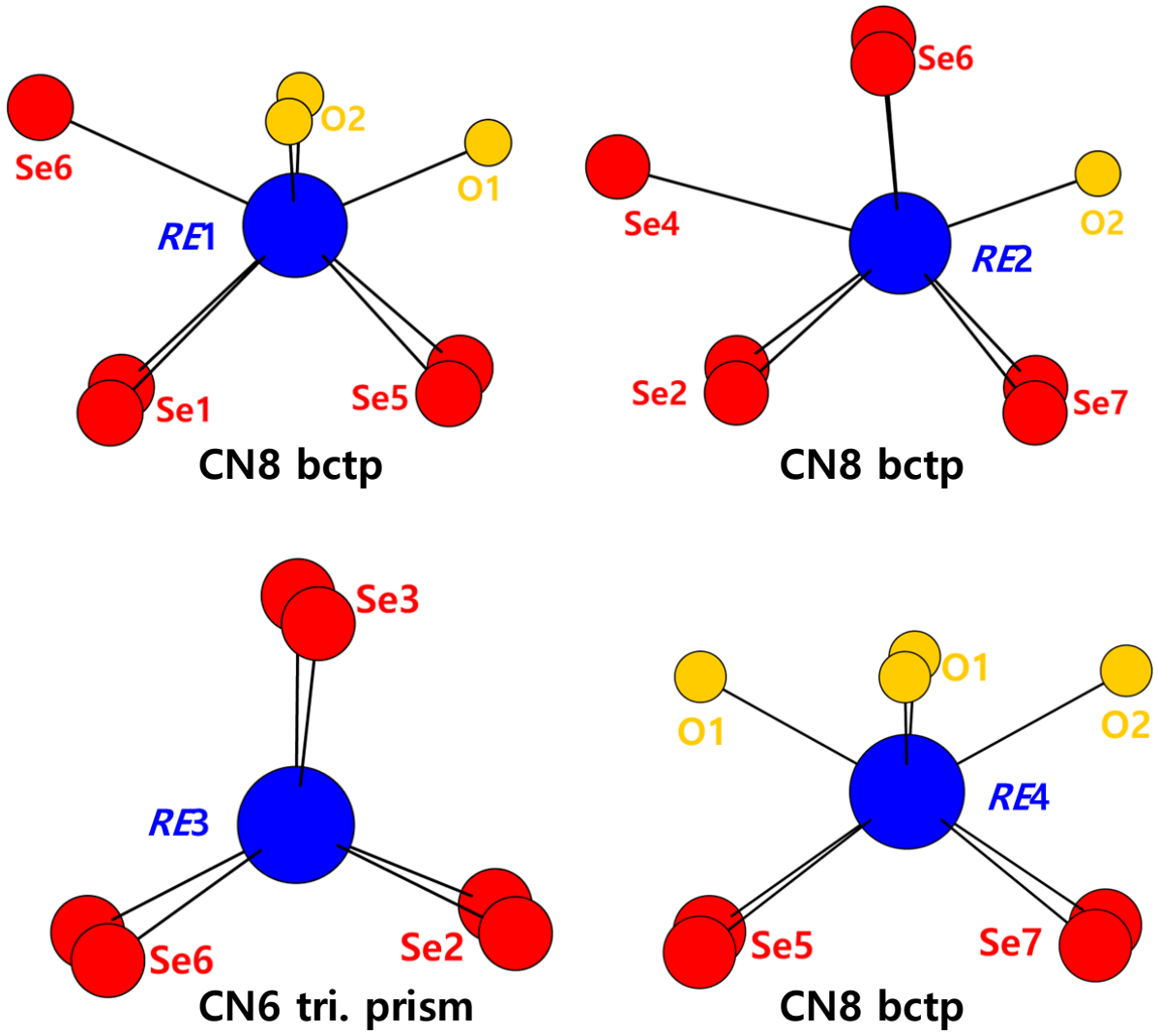

Figure A5-2. Coordination polyhedra around *RE* atoms in $RE_4Ga_2Se_7O_2$.

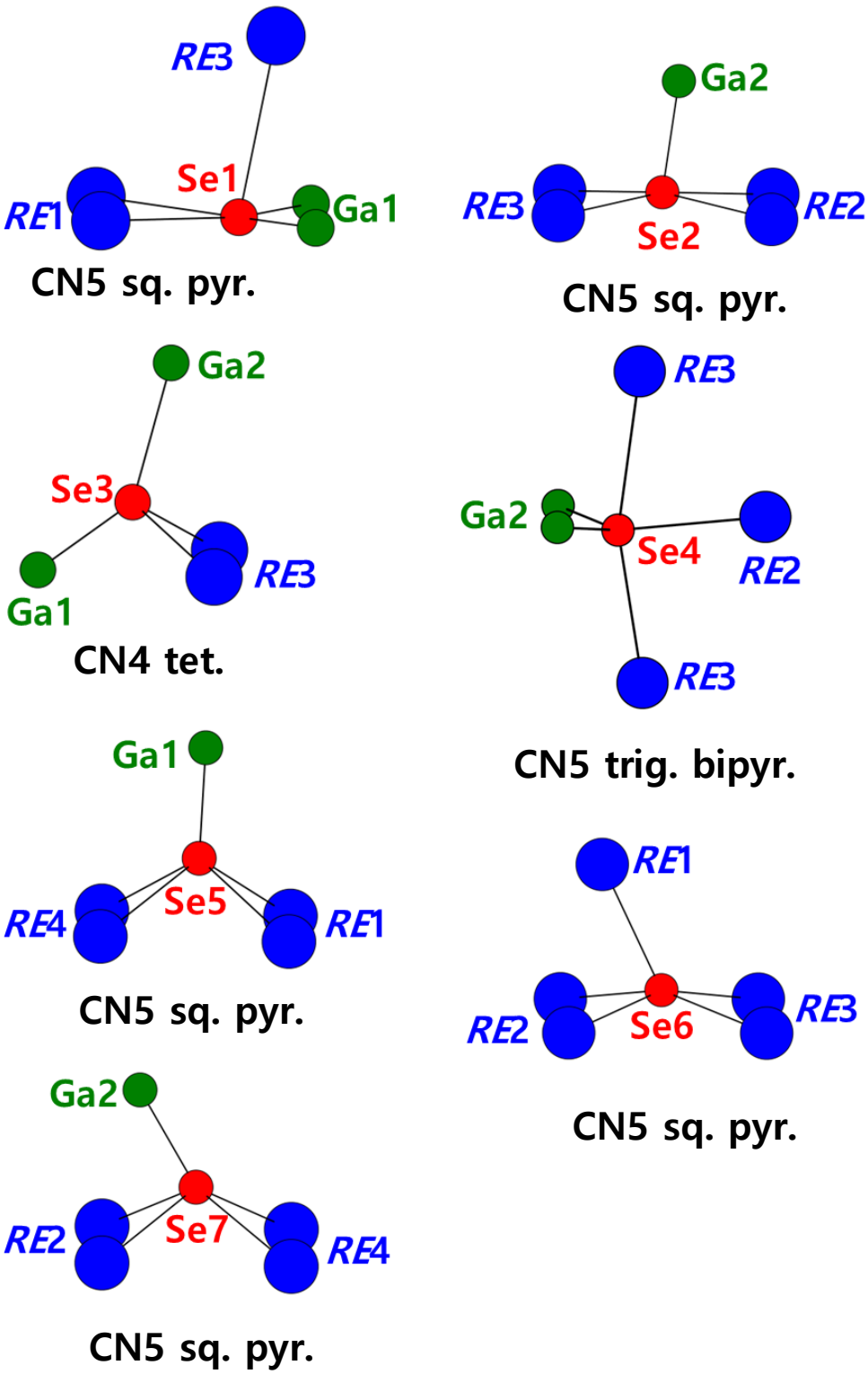

Figure A5-3. Coordination polyhedra around Se atoms in $RE_4Ga_2Se_7O_2$.

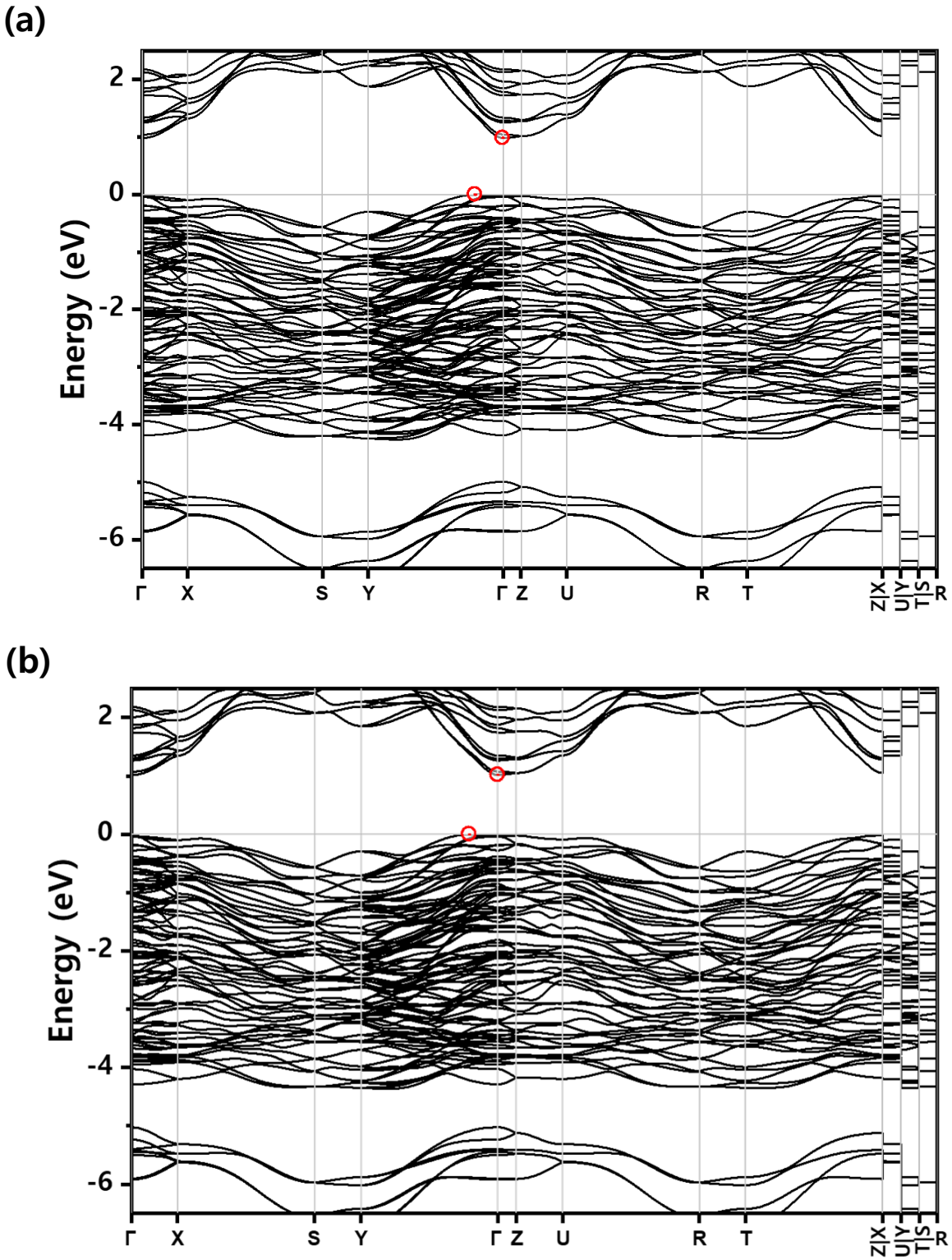

Figure A5-4. Band dispersion of (a) $Pr_4Ga_2Se_7O_2$ and (b) $Nd_4Ga_2Se_7O_2$. Red circles represent valence band minima and conduction band maxima, indicating nearly direct band gap.

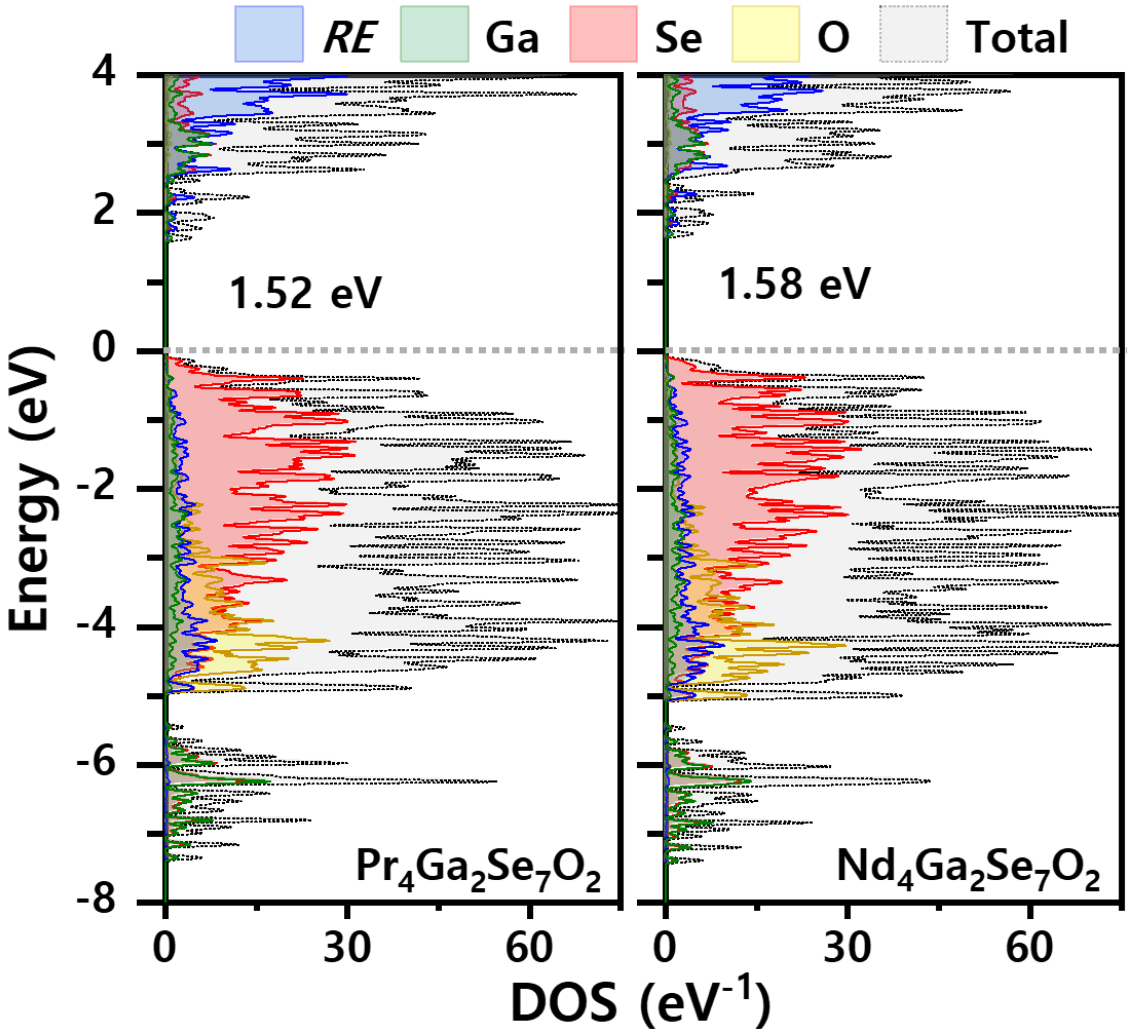

Figure A5-5. Density of states (DOS) for $Pr_4Ga_2Se_7O_2$ (left), and $Nd_4Ga_2Se_7O_2$ (right), calculated using HSE06 functional (PBE:Hartree-Fock (75:25)). A 3 × 8 × 1 gamma-centered *k*-mesh was chosen to sample the first Brillouin zone with the plane-wave basis cutoff energy set to 550 eV.